1-1-2014

Collective Flow And Azimuthally Differential Pion Femtoscopy With The Alice Experiment At The Lhc

Vera Reneee Loggins
Wayne State University,

COLLECTIVE FLOW AND AZIMUTHALLY DIFFERENTIAL PION FEMTOSCOPY WITH THE ALICE EXPERIMENT AT THE LHC

by

VERA LOGGINS

DISSERTATION

Submitted to the Graduate School

of Wayne State University,

Detroit, Michigan

in partial fulfillment of the requirements

for the degree of

DOCTOR OF PHILOSOPHY

2014

MAJOR: PHYSICS

Approved by:

_____

Advisor Date

_____

_____

_____

_____

DEDICATION

Dedicated to my mother Regina Loggins, my grandmother Carolyn Johnson, my sister Michelle Loggins, my minister Rev. Princess H. E. Scott, and in loving memory of overseer Bro. Arnett P. Scott, Jr. and my grandfather Willie Johnson Sr., for all the love and support and helping me to "dream the impossible dream....to reach the unreachable star!" — Joe Darion, Man of La Mancha

ACKNOWLEDGEMENTS

This work would not have been possible without a lot of help and support I received from many people. I would like to thank my advisor Sergei Voloshin for teaching me many physics courses and also guiding my research. I would also like to thank my PhD committee members, Professors Sean Gavin, Alexey Petrov, Claude Pruneau from the Department of Physics and Astronomy, and Daniel Frohardt from the Department of Mathematics for agreeing to serve on my dissertation committee. I want to thank members of the Relativistic Heavy Ion Group (RHIG) past and present for all their help with my questions and general understanding of heavy ion research, Professors Joern Putschke, Abhijit Majumder, Tom Cormier, Rene Bellwied, and Rosi Reed. In addition I would like to thank Monika Sharma, George Moschelli , Rajendra Pokharel, Alexandru Dobrin, Sarah LaPointe, Ron Belmont, Prabhat Pujahari and fellow graduate student Jocelyn Mlynarz. I would also like to thank and acknowledge the faculty who are not already acknowledged as committee members for their many lectures and guidance: Professors Jo Wadhera, Giovanni Bonvicini, Robert Harr, ZhiFeng Huang, Paul Keyes, Gavin Lawes, and Caroline Morgan. I would like to thank Scott Payson for help teaching the physics laboratory courses. I would like to thank Dawn Niedermiller, and Patricia Domanski for their assistance with physics outreach. I would also like to thank the staff, especially Delores Cowen, Audrey Rumbers, and Shere Davis for their kindness and support throughout my studies. And last, I would also like to thank the Chair of the Department of Physics and Astronomy Ratna Naik for her encouragement and guidance.

"Nothing in life is to be feared, it is only to be understood.

Now is the time to understand more, so that we may fear less."

– Marie Curie

TABLE OF CONTENTS

LIST OF FIGURES

LIST OF TABLES

Chapter 1

Introduction

1.1 Physics of Relativistic Heavy Ion Collisions

Up to 10^{-43} seconds after the Big Bang [1]-[4], the four fundamental forces of Nature, electromagnetic force, weak force, strong force, and gravity, had the same strength and were believed to be unified into one fundamental force. Around 10^{-43} seconds after the Big Bang [3, 4], gravity separated from the other forces that remain unified, and the earliest elementary particles begin to be created. At about 10^{-36} seconds after the Big Bang [3, 4], the strong force separated from the electroweak force (combined electromagnetic and weak forces) and the universe undergoes an exponential expansion, the cosmic inflation. It is during this time that the quark gluon plasma (QGP) formed [3, 4], in which quarks, (the most basic sub-particles) and their force carriers gluons are deconfined [5]. The prediction of the QGP, from the theory of quantum chromodynamics (QCD), was one of the primary motivations of our research field [6, 7], presented in detail in section 1.4. After the QGP formed, the temperature decreased and the universe continued to evolve, brief timeline shown in Figure 1.1. The research presented here is focused on studying the QGP properties by colliding nuclei at speeds close to the speed of light.

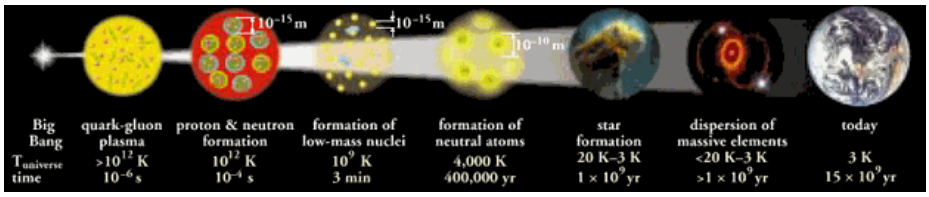

Figure 1.1: The timeline of the universe

1.2 Relativistic Heavy Ion Experiments

Our physics research is in the field of ultra-relativistic heavy-ion collisions, a field that connects high-energy elementary particle physics with nuclear physics [9]. *Heavy ions* refer to heavy atomic nuclei, and *ultra-relativistic* refers to particles or nuclei traveling close to the speed of light. High-energy particle physics deals with particles and their elementary interactions, whereas in the field of ultra-relativistic heavy ion collisions, nuclear/hadronic matter is analyzed with emphasis on phase transitions and the existence of the QGP and its properties [9].

The first experiments with ultra-relativistic heavy ions were performed at the Brookhaven National Laboratory (BNL) [10, 11] and at the European Organization for Nuclear Research (CERN) [12] in 1986. The Alternating Gradient Synchrotron (AGS) at BNL accelerated beams of ^{28}Si (Silicon) at 14 GeV per nucleon, and at CERN the Super Proton Synchrotron (SPS) accelerated ^{16}O (Oxygen) at 60 and 200 GeV per nucleon and ^{32}S (Sulfur) at 200 GeV in 1987. In 1995, the SPS at CERN collided ^{208}Pb (lead) beams at 158 GeV per nucleon. In 2000, the Relativistic Heavy Ion Collider (RHIC) at BNL collided ^{197}Au (gold) ions at 130 GeV, and from 2001-2004 at 200 GeV [13, 14]. In 2010, the Large Hadron Collider (LHC) at CERN ^{208}Pb ions were collided at 2.76 TeV. In 2015, the LHC will again collide ^{208}Pb ions at the top design energy of 5.5 TeV. The full list of $p + p$ and ultra-relativistic heavy ion experiments can be seen in Table 1.1. Further information on the LHC can be found in Chapter 2.

Table 1.1: $p+p$ and Ultra-relativistic Heavy Ion experiments

Year	Species	Synchrotron/Collider	Lab	Energy
1986	^{28}Si	AGS	BNL	14 GeV
1986	^{16}O			60 GeV
1986	^{16}O			200 GeV
1987	^{32}S			200 GeV
1990	^{32}S			60 GeV
1992	^{197}Au			11 GeV
1995	^{208}Pb			158 GeV
1999-2003	^{208}Pb	SPS	CERN	20, 30, 40, and 80 GeV
2000	Au+Au	RHIC	BNL	130 GeV
2001-2002	Au+Au			200 GeV
	p+p			200 GeV
2002-2003	d+Au			200 GeV
	p+p			200 GeV
2003-2004	p+p			200 GeV
	Au+Au			62.4 GeV
2004-2005	Cu+Cu			200 GeV
	Cu+Cu			62.4 GeV
	Cu+Cu			22.5 GeV
	p+p			200 GeV
2006	p+p			200 GeV
	p+p			62.4 GeV
2009	p+p	LHC	CERN	900 GeV
2009	p+p			2.36 TeV
2010	p+p			7 TeV
2010	Pb+Pb			2.76 TeV
2011	p+p			2.76 TeV
	Pb+Pb			2.76 TeV
2012	p+p			8 TeV
2013	p+Pb			5.05 TeV
2015	Pb+Pb			5.5 TeV

1.3 Standard Model

The Standard Model describes elementary matter particles (fermions) and gauge bosons that mediate the interactions between matter particles. It includes three interactions: electromagnetism, weak, and strong. The gravitational interaction is not included [15, 16]. Fermions, quarks and leptons, are arranged in three families. The quarks come in six flavors: up (u), down (d), charm (c), strange (s), top (t), and bottom (b).The heaviest quark is the t quark with a mass of 173 ± 0.27 GeV/c^2 [17] and the lightest quark is the u quark with a mass of 1.5-3.3 MeV/c^2 [15, 16]. Quarks are divided into two classes according to their electric charge: u, c, and t with charge $2/3$, and d, s, and b with charge $-1/3$. The leptons are the electron (e^-), muon (μ^-), tau (τ^-), and their neutrinos (ν_e, ν_μ, ν_τ). They are also divided into two classes according to electric charge: ν_e, ν_μ, and ν_τ with no charge, and e^-, μ^-, and τ^- with charge -1 [18], see Table 1.2. Quarks carry a color charge, as defined in QCD (red, green, and blue), whereas leptons are colorless (or color neutral). Quarks can interact through electromagnetic, weak, and strong interactions, while charged leptons interact by electromagnetic and weak interactions, and neutral leptons can only interact through weak interactions.

Table 1.2: Matter Particles in the Standard Model [18]

Quarks			Leptons		
Flavor	Mass	Charge	Flavor	Mass	Charge
u	1.5-3.3 MeV/c^2	$2/3$	ν_e	< 2 eV/c^2	0
d	3.5-6.0 MeV/c^2	$-1/3$	e^-	0.511 MeV/c^2	-1
c	$1.27^{+0.07}_{-0.11}$ GeV/c^2	$2/3$	ν_μ	< 0.19 MeV/c^2	0
s	105^{+25}_{-35} MeV/c^2	$-1/3$	μ^-	106 MeV/c^2	-1
t	171.3 ± 2.3 GeV/c^2	$2/3$	ν_τ	< 18.2 MeV/c^2	0
b	$4.20^{+0.17}_{-0.07}$ GeV/c^2	$-1/3$	τ^-	1.78 GeV/c^2	-1

The particles that mediate force are called gauge bosons. All of them have spin value 1 [18]. Eight gluons mediate the strong force. The $W^{\pm}$ and Z^0 bosons mediate the weak force, and the photon (γ) mediates the electromagnetic force.

Table 1.3: Gauge bosons and forces

Gauge Bosons		Force
	Mass	
Photon(γ)	0	Electromagnetic
$W^{\pm}$	80.4 GeV/c^2	Weak
Z^0	91.2 GeV/c^2	Weak
8 gluons (g)	0	Strong

1.4 Quantum Chromodynamics (QCD)

Historically, QCD began in 1963 with a proposal by Gell-Man and Zweig [7] suggesting that hadrons can be described by sub-particles inside hadrons (u, d, s quarks). In 1964, Greenberg [19], and in 1965, Han and Nambu [20], proposed that quarks have color charge, and interact by the exchange of eight gauge bosons (gluons). Asymptotic freedom in strong interactions was discovered by Gross, Politzer, and Wilczek [21, 22, 23]. This property stipulates that the interaction between particles at short distances or high momentum becomes weak. Color confinement, or confinement, states that quarks and gluons cannot be isolated [24]-[26]. Efforts to isolate or produce "bare" quarks have so far yielded null results.

The strength of the strong interaction is given by the QCD running coupling constant $\alpha_s(Q)$ [27], which depends on energy scale (Q).

$$\begin{aligned} \alpha_s(Q^2) &= \frac{1}{\beta_0 \ln(Q^2/\Lambda^2)} \\ \beta_0 &= \frac{33 - 2N_f}{12\pi} \\ \Lambda^2 &= \frac{\mu^2}{e^{1/(\beta_0 \alpha_s(\mu^2))}} \end{aligned} \tag{1.1}$$

where N_f is the number of flavor, and μ is a scale.

The running of the strong coupling constant calculated using lattice QCD calculations [27] as a function of Q is shown in Figure 1.2. As Q increases the strength of α_s decreases logarithmically.

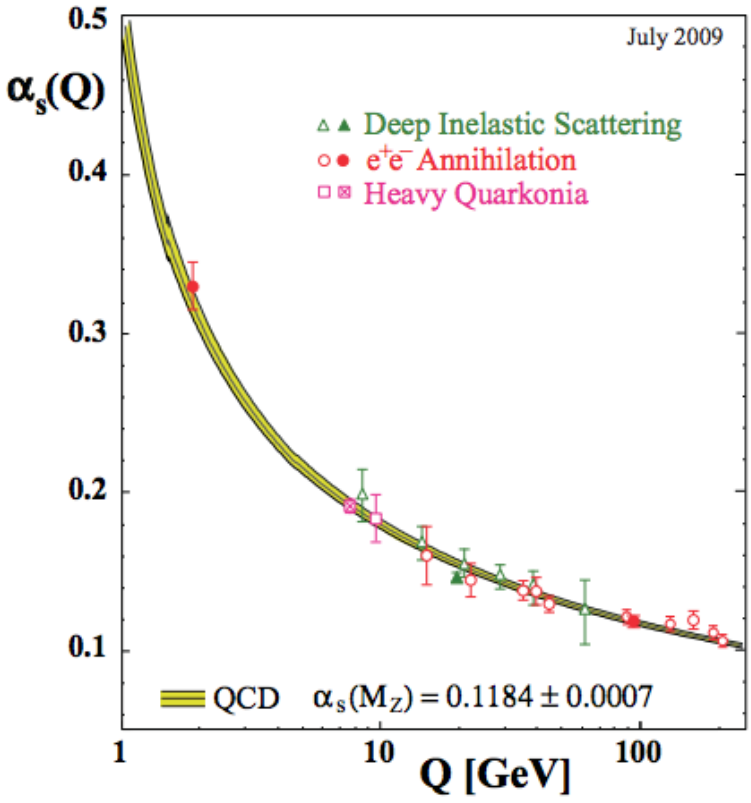

Figure 1.2: Summary of measurements of α_s as a function of the respective energy scale Q. The curves are QCD predictions for the combined world average value of $\alpha_s(M_{Z^0})$ [27]

QCD predicts a transition from a state of hadrons to a plasma of deconfined quarks and gluons, first named quark gluon plasma by Shuryak in 1978 [6], occurring at high energy density.

The QCD phase diagram, see Figure 1.3, shows the temperature T vs. baryon chemical potential μ, a measure of the imbalance between baryons and anti-baryons in the system. A high μ indicates a higher baryon density, whereas a low μ indicates no preference for baryons over anti-baryons. On the QCD phase diagram at $\mu = 0$ and $T = 0$, if the temperature is increased at $\mu = 0$, then there is a phase transition from a hadronic phase in which quarks are confined to the QGP in which quarks are deconfined and can move freely. High temperature T and low baryon density μ corresponds to the state of the early universe and at higher μ the state of heavy ion collisions.

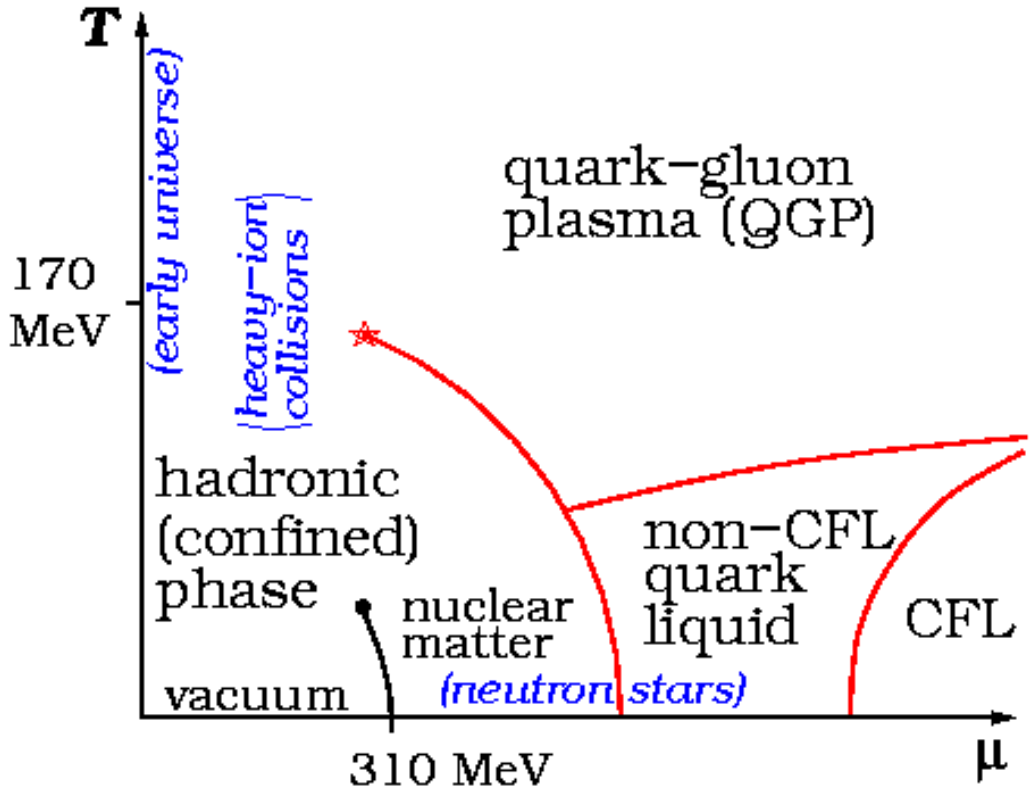

Figure 1.3:
QCD phase diagram. Temperature T vs. baryon chemical potential μ

1.5 Heavy Ion Collisions

The space time evolution of a heavy ion collision is represented in Figure 1.4 [29]-[31]. The vertical and horizontal axis respectively represents the time and spatial direction. Two nuclei approach each other with speeds close to the speed of light and collide thereby creating a hot dense fireball. The system expands, increasing in energy and temperature, and eventually forming the QGP in which quarks and gluons are deconfined. The system later expands and cools down to a critical temperature T_c upon which hadrons are formed from quarks and gluons, and interact inelastically until the system reaches chemical freeze-out. The energy density continues to decrease and hadrons interact elastically until thermal (or kinetic) freeze-out in which the hadron interaction stops and the particles can fly off to reach the detectors [29]- [31].

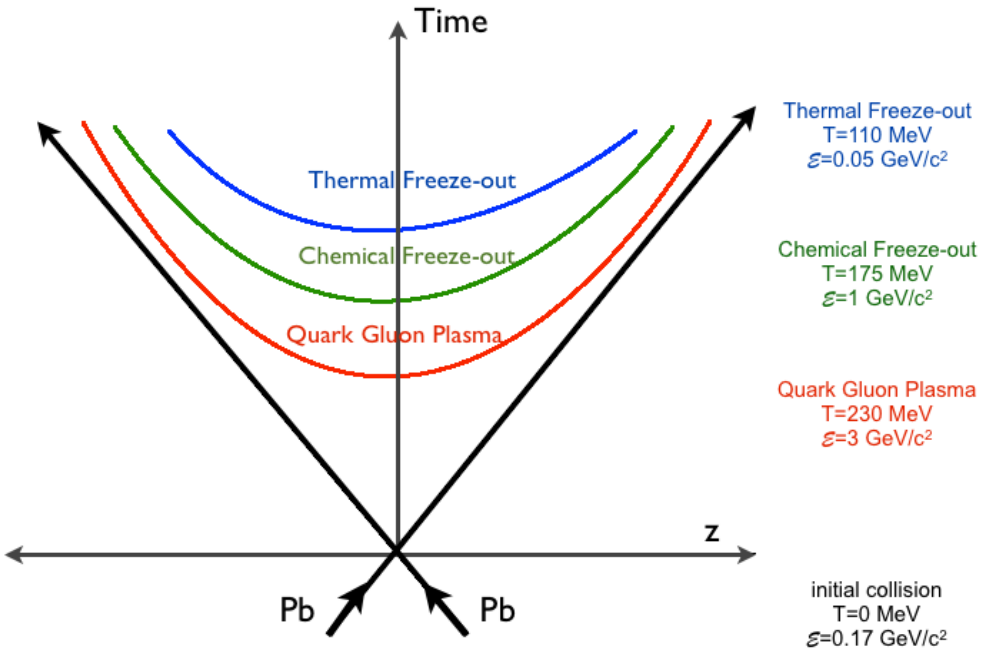

Figure 1.4: Space time diagram of a heavy ion collision

Determining the collision centrality is essential for all heavy-ion measurements. In a collision, the impact parameter b has a range $0 \leq b \leq R_1 + R_2$, where R_1 and

R_2 are the diameters of the two nuclei. A head-on collision has $b = 0$, whereas a peripheral collision has $b \leq R_1 + R_2$. The centrality of a collision allows one to study the particle production versus the density of the colliding system. The centrality classes are typically defined by a Glauber Model, which provides an estimate of N_{part}, the number of participating nucleons having at least one interaction per event, and reported N_{bin}, the number of interactions in an event. Observations are typically studied in bins of the fraction of total cross section per event, and reported as a function of N_{part} and N_{bin} for each centrality class [29].

Figure 1.5 shows an illustration of different centrality ranges: "central" collision 0-5% in Figure 1.5a, "mid-central" collision from 40-50% in Figure 1.5b, and "peripheral" collision 70-80% in Figure 1.5c.

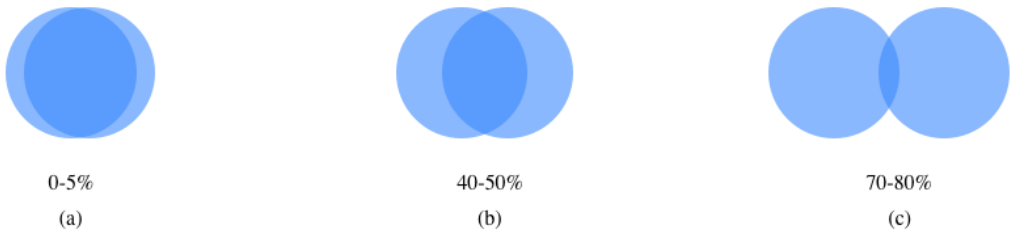

Figure 1.5: Illustration of Collision centrality

An example of centrality classes defined by Glauber model and fit to the data for Pb-Pb collisions at $\sqrt{s}$=2.76 TeV using the ALICE VZERO detector is shown in Figure 1.6. More information on the VZERO detector will be covered in Chapter 2.

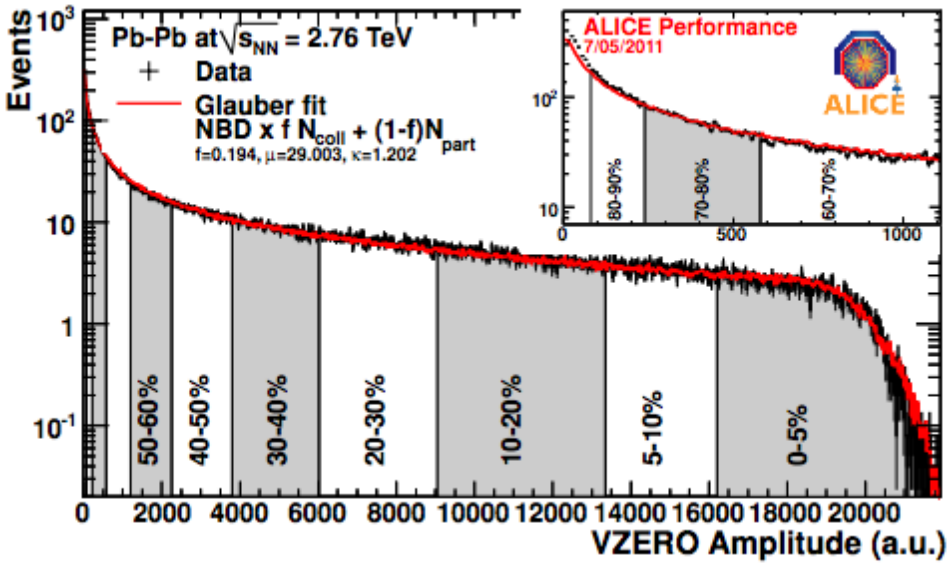

Figure 1.6: Centrality determination in ALICE. Glauber model fit to the amplitude of the VZERO detector with an zoomed portion of the most peripheral region (far left of plot) [30]

1.6 Signatures of QGP

In heavy-ion experiments, hadrons are measured as they hit the detector after the stage of thermal freeze-out in the collision process. However, the earliest stage of the collision, where the QGP is expected to form, is not directly accessible. Therefore observables are needed to provide information on the possible QGP phase, some of these measurements are discussed in this section. They are grouped in observable, which are characteristic of a certain stage of the heavy ion collision. Hard observables are those that probe the very early, initial stage of the collision, electromagnetic observables emerge after the initial stage, and hadronic observables emerge only in the final stages of the heavy ion collision.

1.6.1 Hard Physics Observables

1.6.1.1 J/Ψ Suppression

The measurement of quarkonia suppression, such as J/Ψ, gives information on properties of the stages of heavy ion collisions and the existence of the QGP [32]. Measuring the probability of different quarkonia states also allows us to estimate the temperature of the system [33].

In order to measure the amount of J/Ψ suppression, the nuclear modification factor R_{AA} is used:

$$R^i_{AA} = \frac{Y^i_{J/\Psi}(\Delta p_T, \Delta y)}{\langle T^i_{AA} \rangle \times \sigma^{pp}_{J/\Psi}(\Delta p_T, \Delta y)}, \tag{1.2}$$

where $Y^i_{J/\Psi}$ is the inclusive J/Ψ yield per centrality, $\langle T^i_{AA} \rangle$ is the average value of the nuclear overlap function per centrality, and $\sigma^{pp}_{J/\Psi}(\Delta p_T, \Delta y)$ is the J/Ψ cross section in p+p collisions. In Figure 1.7, a measurement of inclusive J/Ψ suppression is shown versus $\langle N_{part} \rangle$, the number of participating nucleons in a heavy ion collision. The centrality ranges are from 0-80% The "most peripheral" events are shown as

having low $\langle N_{part} \rangle$, and the "more central" events have high $\langle N_{part} \rangle$. The value of R_{AA} decreases less than unity, showing possible evidence of a medium created [33]. Comparing the two experiments shown, we see that R_{AA} is larger by a factor of three at the LHC energy than at RHIC energy for $\langle N_{part} \rangle \gtrsim 180$ [34].

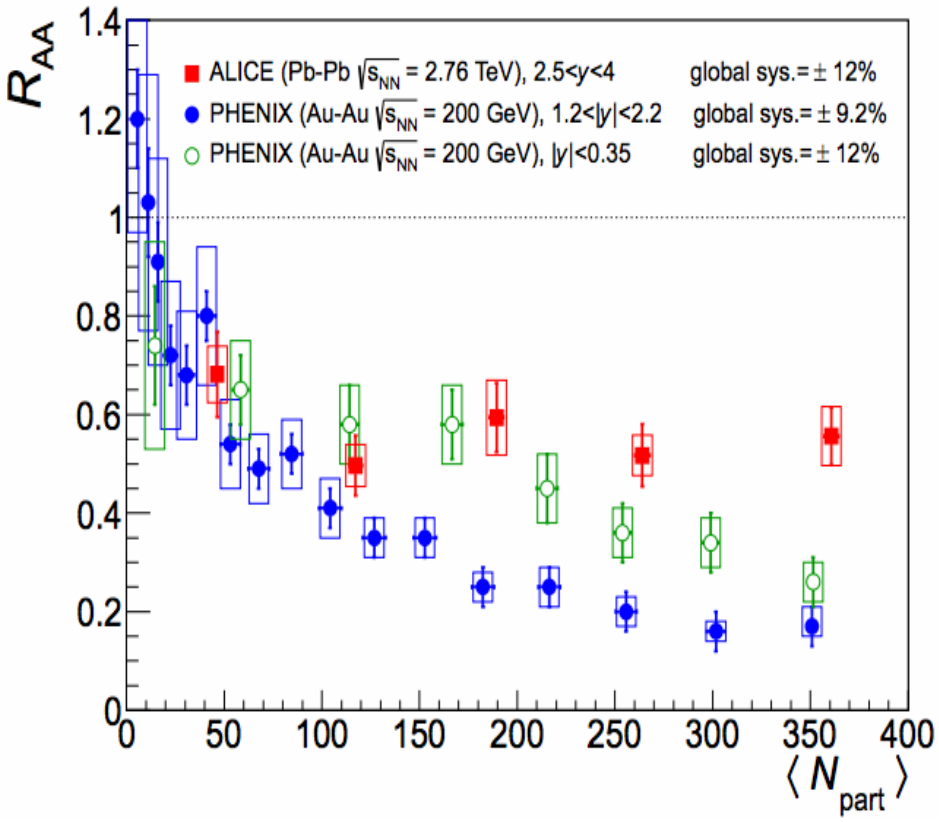

Figure 1.7: Inclusive J/Ψ R_{AA} as a function of $\langle N_{part} \rangle$ measured in Pb-Pb collisions at $\sqrt{s}_{NN}$=2.76 TeV by the Collaboration and measured by $Au - Au$ collisions at $\sqrt{s}_{NN}$=200 GeV by the PHENIX Collaboration. Inclusive J/Ψ R_{AA} as a function of the mid-rapidity charged-particle density (top) and the number of participating nucleons (bottom) measured in Pb-Pb collisions at $\sqrt{s}_{NN}$ = 2.76 TeV compared to PHENIX results in Au-Au collisions at $\sqrt{s}_{NN}$=200 GeV at mid-rapidity and forward rapidity [34]

1.6.2 Electromagnetic Physics Observables

1.6.2.1 Direct photons

In a thermalized QGP, photons are produced, as a result of quark interactions. Given they readily escape the fireball without further rescattering. Photons are created at all stages of a heavy ion collision. It is consequently very challenging to identify photons from the QGP, making direct photon measurement (photons not created from decays) challenging. In Figure 1.8, we see the direct photon invariant yield in Pb-Pb collisions at $\sqrt{s}_{NN} = 2.76$ TeV for 0-40% centrality [39] measured by the ALICE Collaboration. The nuclear modification factor R_{AA} of direct photons measured by the PHENIX Collaboration is shown in Figure 1.9 [40]. R_{AA} for direct photons is shown to be close to one, a possible indication of direct photons unmodified by the medium.

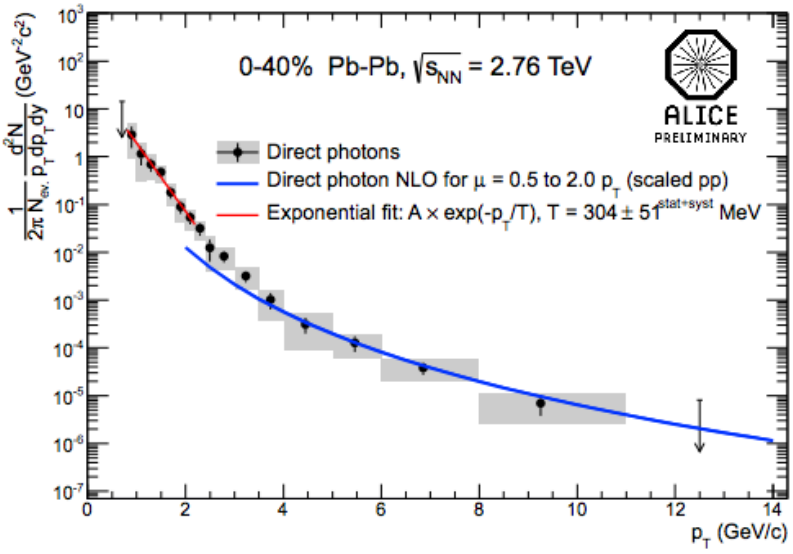

Figure 1.8: Direct photon of Pb-Pb collisions of charge particles at $\sqrt{s}$=2.76 TeV [39]

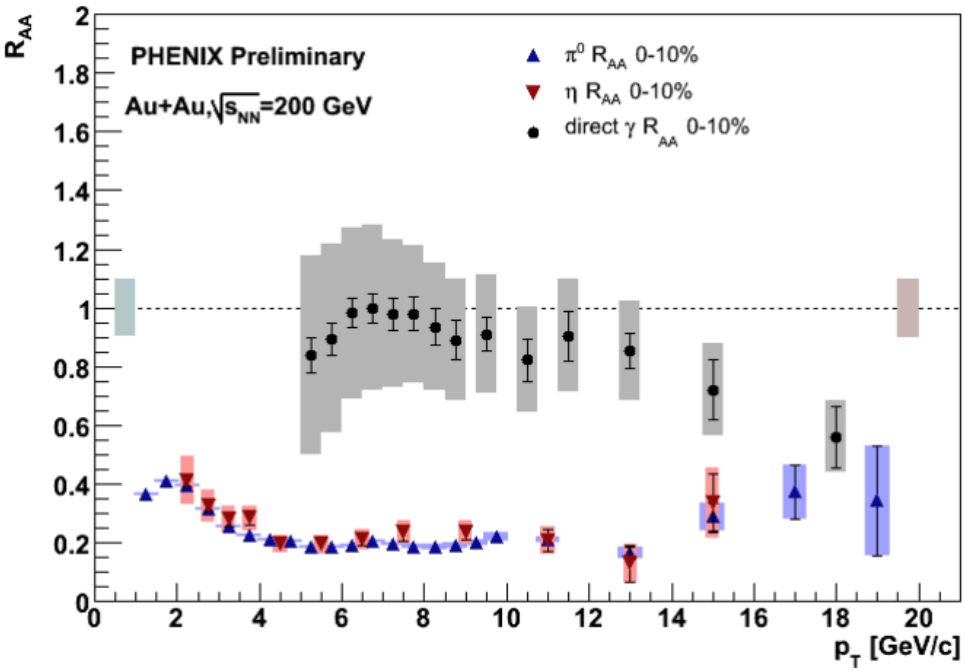

Figure 1.9: Nuclear modication factors (RAA for photons, π^0, and η in 0-10 % central Au+Au collisions at $\sqrt{s_{NN}} = 200$ GeV. [40]

1.6.3 Soft Physics Observables

We will discuss and focus primarily on two types of soft physics observables: flow and femtoscopy.

1.6.3.1 Flow

Flow involves a measurement of the azimuthal momentum distribution of emitted matter from a heavy ion collision,first proposed by S. Voloshin and Y. Zang [41] in 1994, and modified by Poskanzer and Voloshin [42] in 1998. The term *collective flow* represents the correlation between spatial location and direction of movement of emitted matter. *Radial flow* describes expanding matter parallel in the radial direction. *Anisotropic flow* refers to the nonuniform azimuthal distribution expanded in terms of a Fourier series:

$$\begin{aligned} \frac{dN}{d\varphi} = \frac{N}{2\pi}\left[1 + 2v_1\cos(\varphi) + 2v_2\cos(2\varphi) + ...\right] \\ v_n = \langle\cos(n\varphi)\rangle, \end{aligned} \tag{1.3}$$

where φ is the azimuthal angle of momentum, v_n are the Fourier coefficients, and n is the harmonic number. v_1 is called *directed* flow, and v_2 is called *elliptic* flow. An illustration o elliptic flow and directed flow are shown in Figure 1.10. Elliptic flow shows the initial spatial anisotropy which is almond-shaped and greater in the y direction (out-of-plane) than in the reaction plane in the x direction (in-plane) [**?**].

Results on elliptic flow from the RHIC experiments constitutes larger elliptic flow for mid-central collisions than for central collisions. The results of the first paper on flow from the ALICE Collaboration is presented shown in Figure 1.11 and compared to elliptic flow results obtained by the STAR Collaboration at RHIC, shown in the solid lines. We see the that the integrated elliptic flow increases by 30% from RHIC $\sqrt{s_{NN}} = 200$ GeV to the LHC $\sqrt{s_{NN}} = 2.76$ TeV. This topic will be revisited later

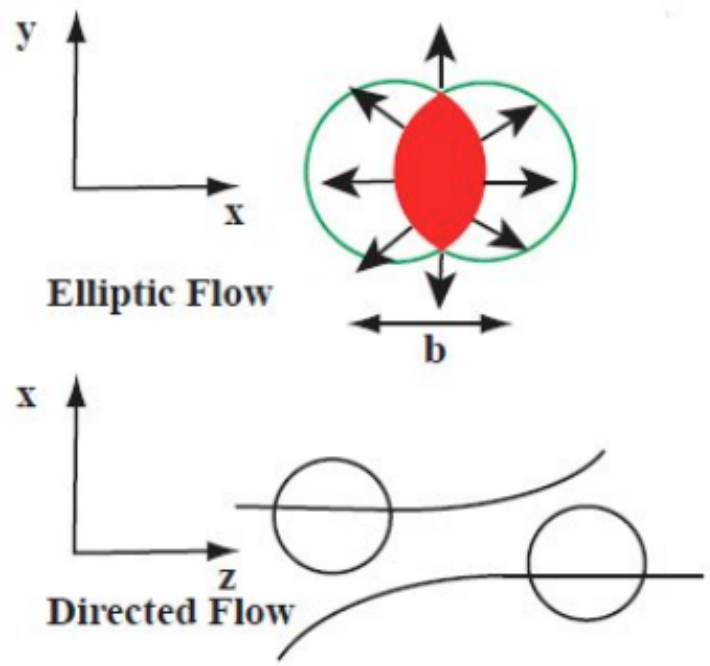

Figure 1.10: Schematic representation of elliptic flow v_2 and direct flow v_1, in the transverse plane

in Chapter 3.

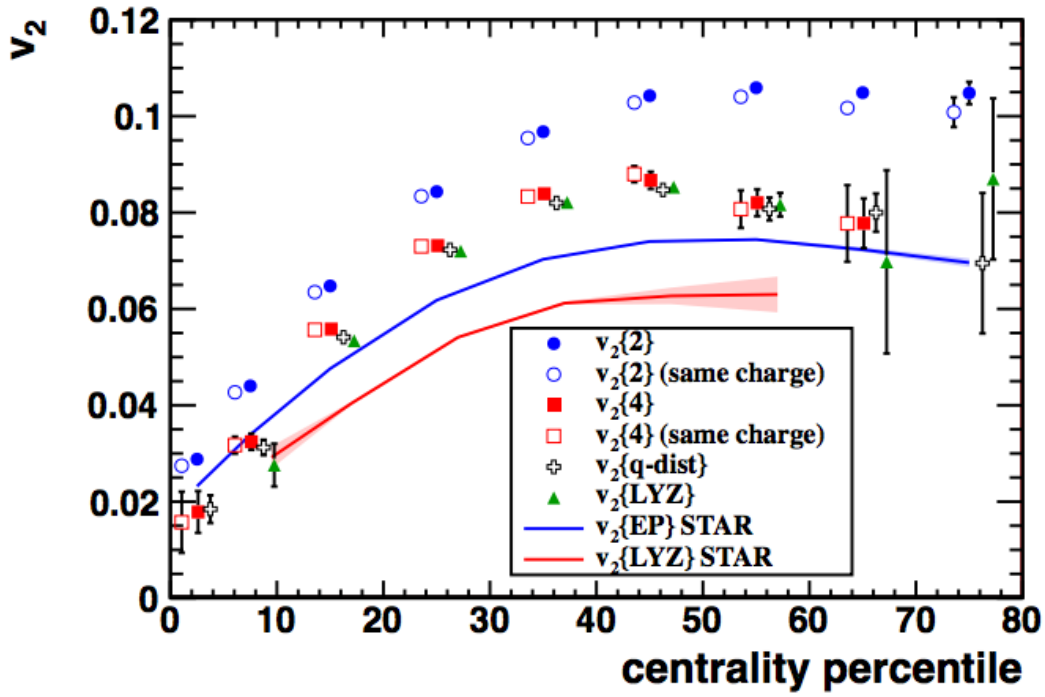

Figure 1.11: Elliptic Flow integrated over the $0.2 < p_T < 5.0$ GeV/c as a function of event centrality for Pb-Pb collisions at $\sqrt{s_{NN}}$=2.76 TeV, compared with RHIC results for Au-Au collisions at $\sqrt{s_{NN}} = 200$ GeV, integrated over the p_T range of $0.15 < p_T < 2.0$ GeV/c [43]

1.6.3.2 Femtoscopy

Femtoscopy is the study of the space-time characteristics of the system created in heavy ion collisions. The entire source of emitting identical particles in a heavy ion collision cannot be measured. However, a region in which pairs of particles with similar velocities, called the region of homogeneity, can be measured [44]. The source shape is assumed (usually Gaussian) and the correlation function can be fit for pairs of identical particles with the following function:

$$C(\mathbf{q}) = N[(1-\lambda) + \lambda K(q_{inv})(1 + \exp(-R^2_{out}q^2_{out} - R^2_{side}q^2_{side} - R^2_{long}q^2_{long}]B(\mathbf{q}), \quad (1.4)$$

where N is the normalization factor, $K(q_{inv})$ is the Coulomb wave function averaged over the Gaussian source to estimate the Coulomb correction, q is the pair relative momentum, and $B(\mathbf{q})$ are non-femtoscopic correlations. Figure 1.12 shows the results of femtoscopic measurements for proton-proton (pp) collisions and heavy ion collisions as a function of multiplicity. The pp results on the left show that there is a linear scaling of the radii with multiplicity for each direction. On the right, it is shown that the heavy ion data and pp data scale differently. In comparing RHIC and LHC data, the same behavior holds showing that there is no dependence on energy. This topic be revisited in Chapter 4 where further development of femtoscopic measurements will be discussed and an azimuthal reference included.

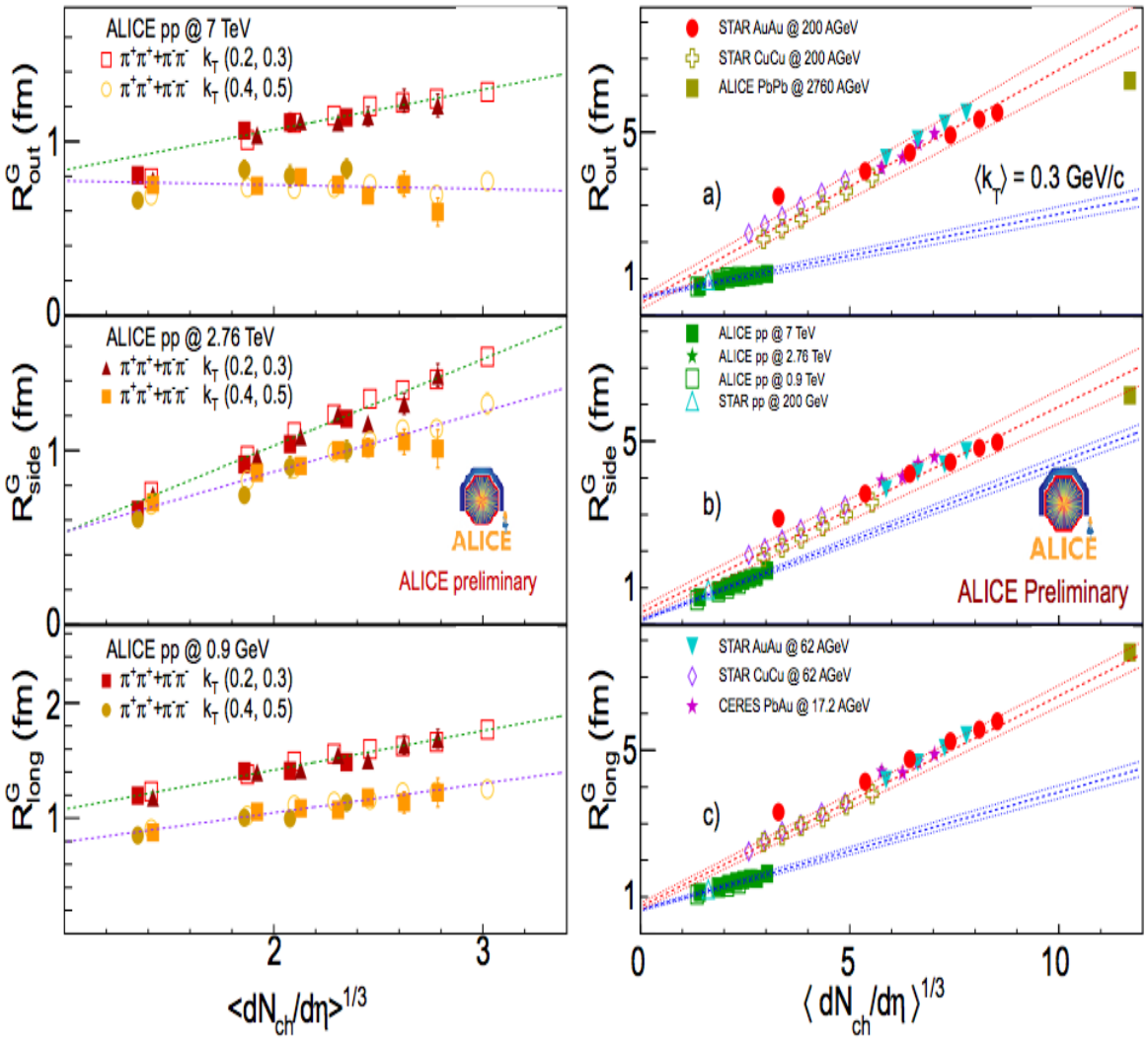

Figure 1.12: The femtoscopic radii as a function of event multiplicity in p+p collisions (left) and the femtoscopic radii as a function of event multiplicity for p+p and the heavy-ion collisions at a selected k_T (right). The lines are linear fits to all the data for two momentum ranges. [46]

1.7 Dissertation Outline

This chapter has introduced the basic concepts of particle physics, the quark gluon plasma (QGP), heavy ion collisions, and QGP signatures. This was an attempt to give a proper background of the heavy ion research and to preview topics that will be discussed in the remainder of this dissertation. Chapter 2 will give an overview of the Large Hadron Collider (LHC) and will focus primarily on the ALICE detector and sub detectors that are used in the analysis.

One motivation of this dissertation is a study of *non-flow* estimates using proton-proton (pp) collisions, presented in Chapter 3. The problem with obtaining flow measurements is in addition to flow, there are correlations not related to the reaction plane, non-flow contribution. A method is presented to remove non-flow using a two-particle correlator and also a three-particle correlator. The flow measurements are analyzed using Pb-Pb collisions, while the non-flow estimates are analyzed using pp collisions. Another motivation of this dissertation is two-pion femtoscopy, introduced in this chapter. The femtoscopic radii dependence on transverse momentum gives evidence of flow. The analysis extends to include azimuthal information, the angle of the pair of particles relative to the reaction plane, called azimuthally differential pion femtoscopy, presented in Chapter 4. This analysis is key in estimating the shape of the source of pairs of identical particles being emitted from a heavy ion collision. Chapter 5 will summarize all results.

Chapter 2

Experiment Overview

In this chapter we will introduce the Large Hadron Collider (LHC) accelerator at CERN and the layout and subsystems of the A Large Ion Collider (ALICE) detector.

2.1 The Large Hadron Collider (LHC)

The LHC [47, 51] is the world's largest and most powerful accelerator and collider for particle physics research. The LHC project was approved in 1994 by the CERN council and after years of design and construction, was ready for operation in 2008. Operation began September 10, 2008 and ran for nine days until an unfortunate magnet quench caused damage to the machine and running was postponed for another year. The first proton-proton collisions were achieved November 23, 2009 at a center of mass energy of 0.9 GeV. The maximum center of mass energy for proton-proton collisions occurred in 2010 at 7 TeV. The first lead-lead collisions also occurred the same year on November 8, 2010 at 2.76 TeV per nucleon pair.

The LHC is located at CERN and borders France and Switzerland. The LHC ring [47] has a circumference of 26.7 km and was constructed between 1984 and 1989 for the CERN LEP machine. An aerial image of the LHC along with a picture of the tunnel can be seen in Figure 2.1. The LHC is designed to collide protons beams at a maximum energy of $\sqrt{s_{NN}} = 14$ TeV and lead ion beams at a maximum center of mass energy of 5.5 TeV per nucleon pair. This corresponds to the maximum energy

of each beam, 7 TeV.

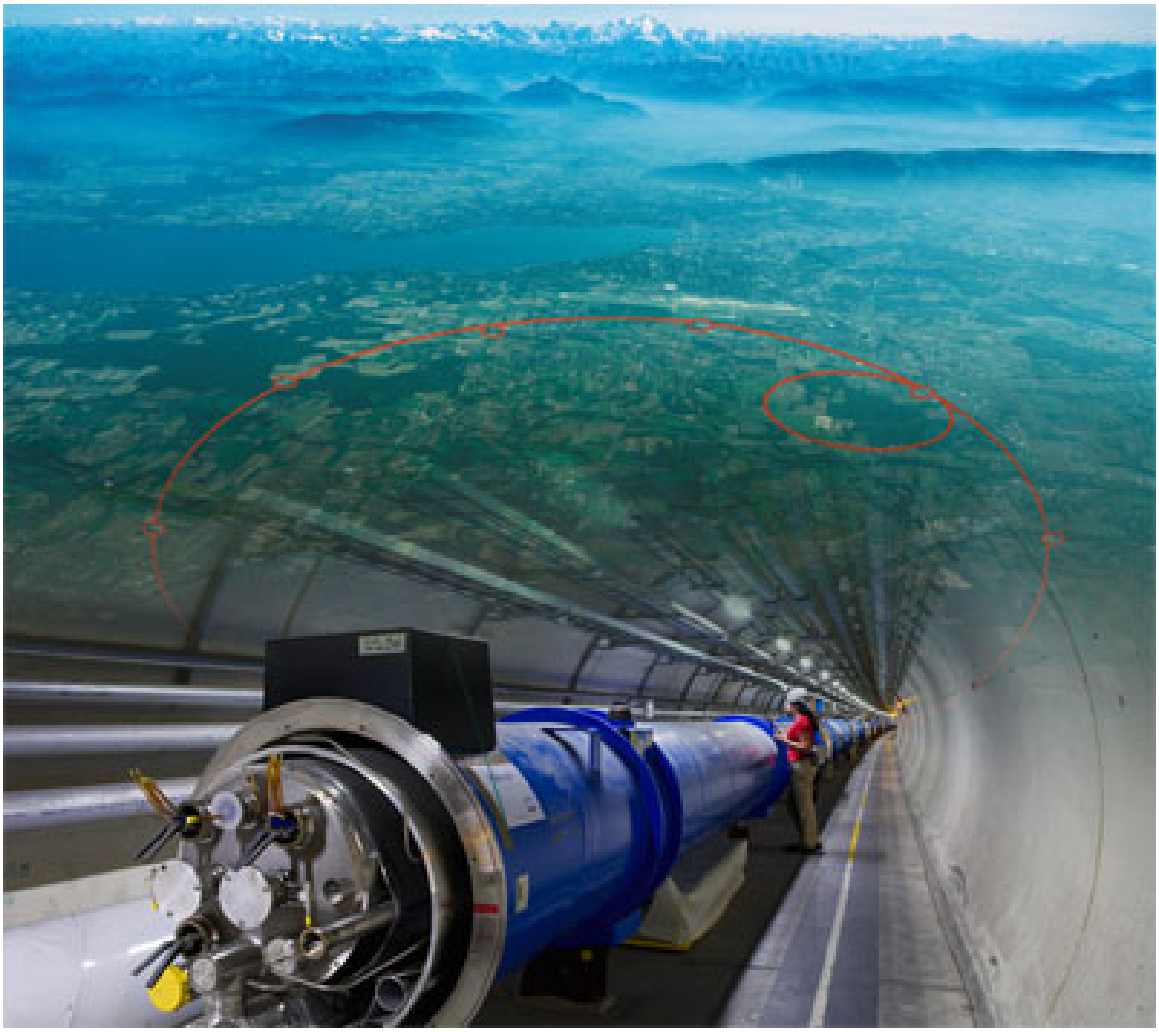

Figure 2.1: Aerial view of the LHC and view of the LHC tunnel [49]

The motivation for the LHC design comes from many unanswered questions in particle physics. One of the main topics, the Higgs boson existence, has been answered recently at CERN on July 4, 2012 [50]. Two experiments, ATLAS and CMS (details on experiments later in this chapter), and later confirmed by further measurements to have a mass region of 125-126 GeV. However, even after this discovery other questions still remain such as: whether supersymmetric particles exist, and what constitutes dark matter. A particular motivation for heavy ion physics, as mentioned in Chapter 1, is the Quark Gluon Plasma (QGP). By colliding nuclei, the conditions similar to

the early universe after the Big Bang were the QGP are recreated in order to study its properties.

2.1.1 LHC layout

The schematic of the LHC's injection chain [51] from multiple smaller accelerators is shown in Figure 2.2. Two beams of either protons or lead ions are created and injected in the LHC ring in opposite directions. They are made to collide at the detectors. The sequence of creation and acceleration of proton and lead ions is now described. At the Linear Accelerator (Linac2), hydrogen atoms have electrons stripped away and the protons that remain are then accelerated to 50 MeV. The proton beam then travels through the Proton Synchrotron Booster, and reaches an energy of 1.4 GeV. The proton beam then goes into the Proton Synchrotron (PS) and reaches an energy of 25 GeV. The proton beam then travels to the Super Proton Synchrotron (SPS) where it is accelerated to an energy of 450 GeV. From the SPS, the proton beam is accelerated to the final energy of 7 TeV. In addition to protons the LHC also collides lead ions. Leads are created by stripping off electrons at each stage of acceleration. The lead (Pb) ions are produced by the Electron Cyclotron Resonance (ECR) and then travel to the Linear Accelerator (Linac3) where they are accelerated to 4.2 MeV/nucleon. The lead ion beam then travels to the Low-Energy Ion Ring (LEIR) and is accelerated to 72.2 MeV/nucleon. The lead ion beam then moves to the PS and is accelerated to 5.9 GeV/nucleon, and the SPS where it is accelerated to 176.4 GeV/nucleon. The lead ion beam then moves to the LHC where it is accelerated to the final energy of 2.76 TeV/nucleon.

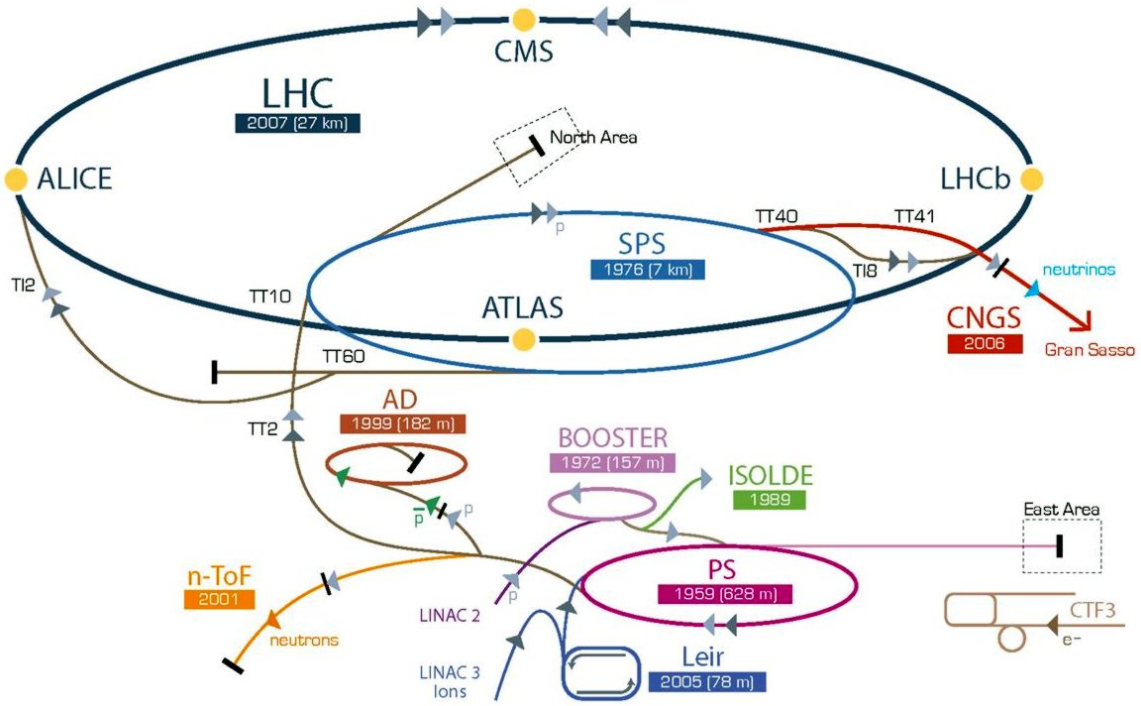

Figure 2.2: Schematic of LHC's injection chain consisting of smaller accelerators [52]

2.1.2 LHC experiments

There are a total of seven LHC experiments: ALICE, ATLAS, CMS, and LHCb, which are the four main experiments (see Figure 2.2), and three smaller experiments, LHCf, TOTEM, and more recently MOEDAL.

ALICE (A Large Ion Collider Experiment) [53] is the only dedicated heavy ion experiment at the LHC. ALICE however also collects data for proton-proton collisions as a reference for the heavy ion studies. The primary goal of the ALICE experiment is the study of the Quark Gluon Plasma (QGP). The main focus of this dissertation is data analysis from this experiment and more detail will be given regarding its sub-detectors.

ATLAS (A Toroidal LHC ApparatuS) & CMS (Compact Muon Solenoid) are two experiments were designed for proton-proton collisions and dedicated to search for the Higgs boson, which was discovered in 2012. They are also interested in the discovery of particles that can make up dark matter as well as testing many predictions of extensions of the standard model. These experiments also have heavy ion programs and also focus on measuring properties of the QGP [54], [55].

The LHCb (Large Hadron Collider beauty experiment) experiment has the primary goal of discovering the difference between matter and anti-matter by studying the decays of "b-quark", also referred to as the "beauty quark". The b-quark and its anti-matter counterpart are unstable and short lived particles. Therefore the tracking detectors of the LHCb are located close to the beam line for more accurate measurement [56].

The LHCf (Large Hadron Collider forward experiment) experiment is designed to primarily measure neutral particles produced forward by collisions. This simulates cosmic rays which are charged particles from outer space that hit the Earth's atmosphere and cascade down to ground level. Results from LHCf will enable the calibration of large scale cosmic ray experiments. LHCf has two detectors located on

either side of the ATLAS collision point [57].

The TOTEM (TOTal Elastic and diffractive cross section Measurement) experiment estimates the size of the proton by measuring the total proton-proton cross section, elastic scattering, and diffractive processes. TOTEM also monitors the total luminosity of the LHC. TOTEM detectors are also located close to the beam line, on ether side of the CMS collision point [58].

The MOEDAL (Monopole and Exotics Detector at the LHC) experiment is dedicated to the search for the production magnetic monopoles, a hypothetical particle with a magnetic charge. MOEDAL consists of sheets of plastic nuclear-track detectors in which monopoles would break the plastic molecules, forming a trail though all the sheets. Another motivation for MOEDAL is the search for highly ionizing Stable Massive Particles (SMPs) which were predicted in theories beyond the Standard Model. MOEDAL is located around the interaction region of the LHCb [59].

2.2 ALICE Experiment

ALICE [53] is a general purpose detector dedicated to the study of heavy-ion collisions. ALICE was built and is now operated by a collaboration of over 1200 members from in 36 countries [60]. The ALICE detector is 26 m long, 16 m high, and weighs 10,000 tons. It consists of central detectors that measure hadrons, electrons, and photons, and a forward spectrometer, which measured muons.

The layout of the ALICE detector is shown in Figure 2.3. The central portion of the detector covers $|\eta| < 0.9$ (a spatial coordinate describing the relation of a particle's angle relative to the beam line) and features a magnetic field up to 0.5 T. The four central detectors are: the Time Projection Chamber (TPC), the Inner Tracking System (ITS), the Time-Of-Flight (TOF), and the Time Radiation Detector (TRD). Three detectors in the central portion of the detector are the Electromagnetic Calorimeter (EMCAL), the High-Momentum Particle Identification Detector (HMPID), and the Photon Spectrometer (PHOS). In the forward region of the detector $-4.0 < \eta < 2.5$, several small detectors operate, used primarily for triggering and event characterization: the Zero Degree Calorimeter (ZDC), the Photon Multiplicity Detector (PMD), the Forward Multiplicity Detector (FMD), the T0 detector, and the V0 (or VZERO) detector. The ALICE COsmic Ray DEtector (ACORDE) (located above the ALICE detector) measures cosmic rays. The detectors that will be used in this analysis are the following: TPC, used for particle identification; TOF, used for particle identification; VZERO, used for determining the event plane (discussed in Chapter 3); ITS, used for vertex determination; and the ZDC, used for centrality definition. The remainder of this chapter provides a brief description of the detectors used in this analysis.

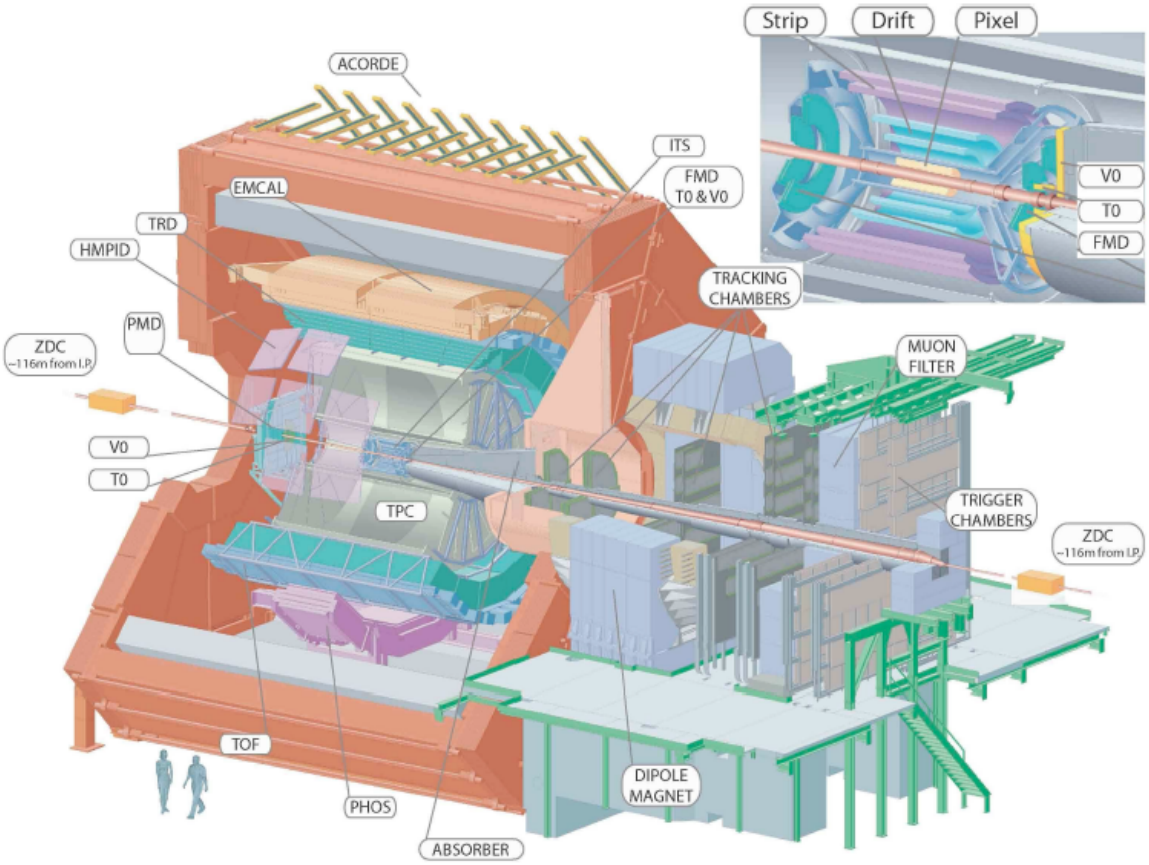

Figure 2.3: Schematic of the ALICE detector

2.3 ALICE Central detectors

2.3.1 The Inner Tracking System (ITS)

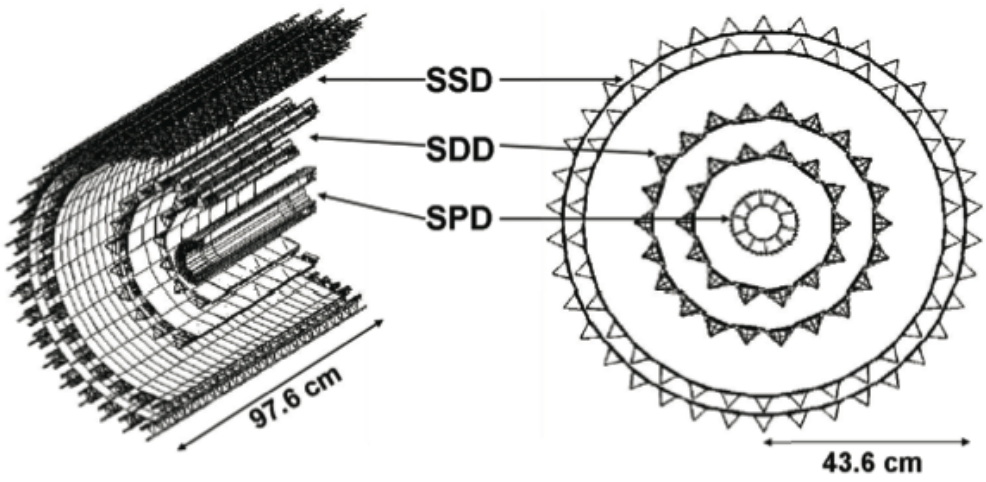

Figure 2.4: ITS schematic

The ITS [61] is made of silicon and is located within 10.6 cm of the interaction point along the direction of the beam. It has 6 cylindrical layers ranging from a radius $r = 3.9$ cm to a radius of $r = 44$ cm, covering a pseudorapidity range of $|\eta| < 0.9$. The first two layers, Silicon Pixel Detector (SPD) cover $|\eta| < 2$ and $|\eta| < 1.4$, respectively. ITS is responsible for the determination of the primary vertex, with resolution better than 100 μm, and identifying secondary vertices from decays of hyperons and heavy flavor hadrons. The ITS also tracks and identifies particles with momentum less than 200 MeV/c. Information on the geometry of all layers of the ITS, including the two outer layers, the Silicon Drift Detector (SDD), and the Silicon Strip Detector (SSD) is shown in Table 2.1. Particle identification using the ITS is presented in Figure 2.5.

Table 2.1: Characteristics of the ITS layers [62]

Layer	Type	Number of Modules	r(cm)	±z (cm)	Resolution $r\phi$ x z (μm)
1	SPD	80	3.9	14.1	12 x 100
2		160	7.6	14.1	12 x 100
3	SDD	84	15	22.2	35 x 25
4		176	23.9	29.7	35 x 25
5	SSD	748	38.0	43.1	20 x 830
6		950	43.0	48.9	20 x 830

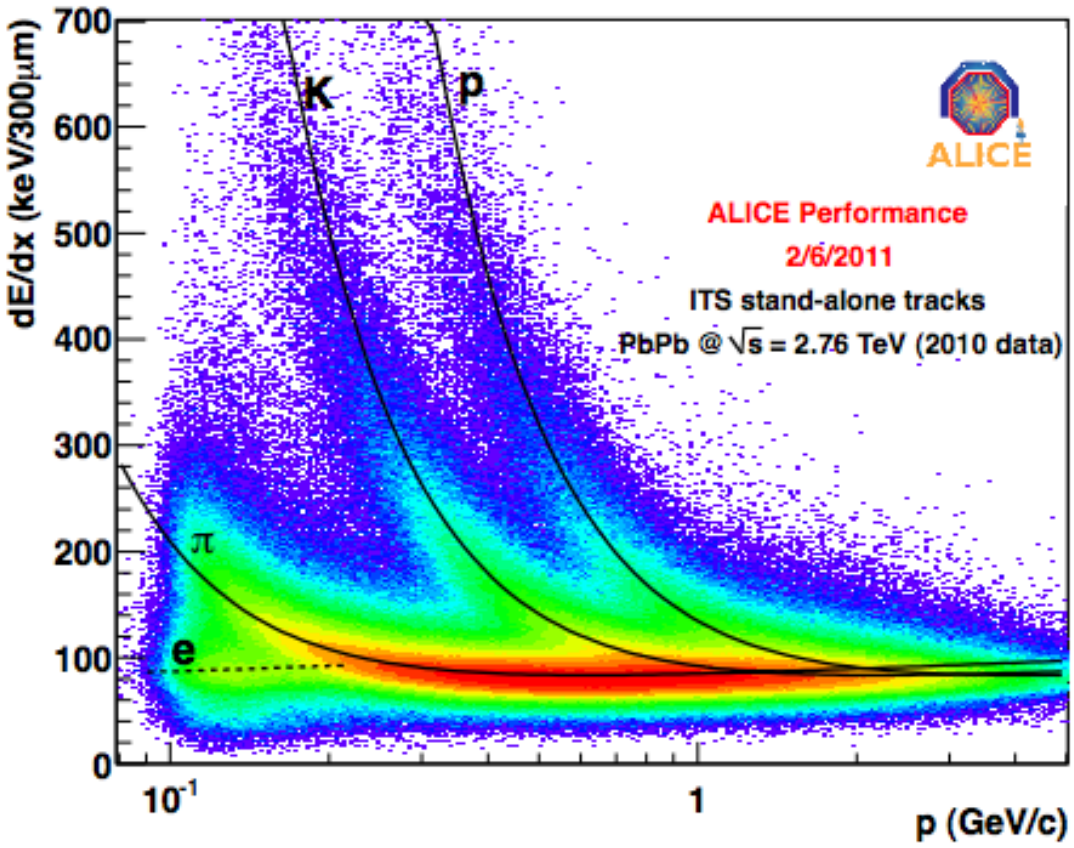

Figure 2.5: ITS particle identification, dE/dx spectrum [66]

2.3.2 The Time Projection Chamber (TPC)

The TPC [63] is the primary device used for tracking and identifying charged particles. The inner TPC radius is about 85 cm with $|\eta| < 1.5$, and the outer radius is about 250 cm with $|\eta| < 0.9$.The TPC has a volume of 90 m^3 and is designed to handle a maximum $dN_{ch}/d\eta$ of approximately 8000, or 20000 tracks including secondaries in the TPC acceptance. Tracks are measured by ionized electrons created when the particles pass through the gas volume ($N_e/CO_2/N_2$). The components of the TPC are seen in Figure 2.6. The TPC identifies by the energy loss dE/dx,see Figure 2.7.

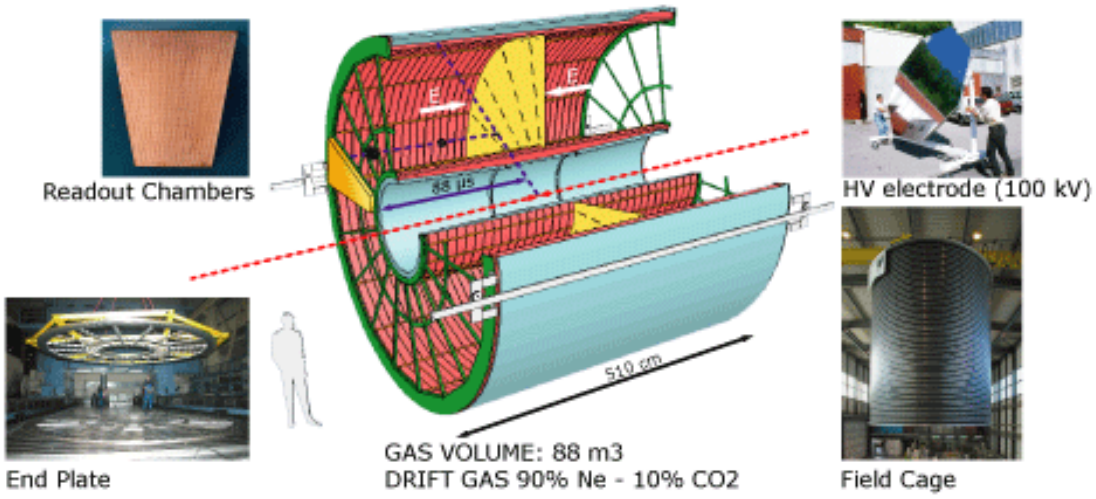

Figure 2.6: TPC layout

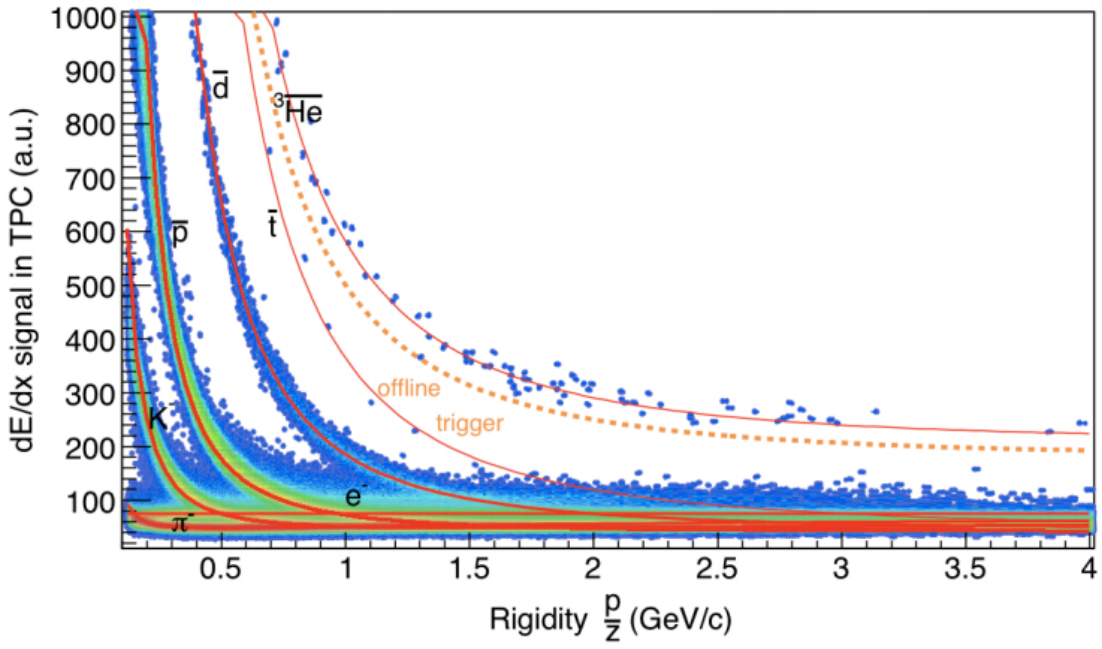

Figure 2.7: dE/dx spectrum of the ALICE TPC from 2.2 million Pb-Pb events [66]

2.3.3 The Time of Flight Detector (TOF)

The TOF covers pseudorapidity range $|\eta| < 0.9$, it has an inner radius of 3.7 m, an outer radius of 3.9 m, and a length of 7.4 m. The TOF consists of 18 sectors in ϕ, with 5 segments in z (90 modules total) of double stack glass resistive plates separated by gas gaps (MRPCs). Figure 2.8 shows an image of two sectors of the TOF being installed [64].

Figure 2.8: ALICE detector showing the first two TOF sectors inserted in the frame [64]

I

The TOF [65] is designed to identify particles from the difference in time-of-flight (t) for particles with different mass (m), but same momentum (p). The TOF gives the time when tracks reach the detector, and determines the velocity of the tracks by $m^2 = p^2(\frac{t^2}{l^2} - 1)$, where l^2 are the track lengths calculated from momentum. Figure 2.9 illustrates an example of TOF particle identification showing the track velocity β versus momentum p measured by TOF for Pb-Pb data at $\sqrt{s}$=2.76 TeV minimum bias data.

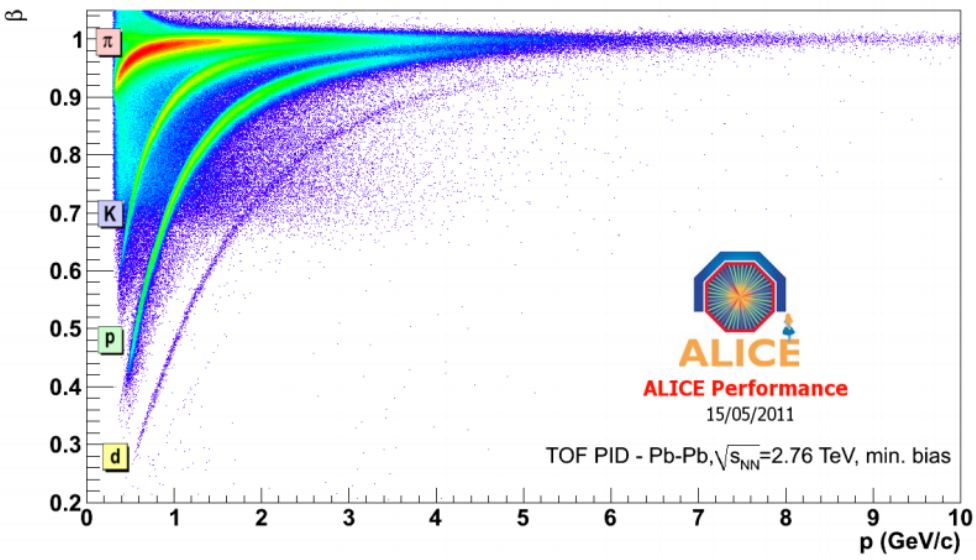

Figure 2.9: Track velocity β vs. momentum for Pb-Pb data at $\sqrt{s}$=2.76 TeV [66]

2.4 Forward Detectors

2.4.1 VZERO Detector

The VZERO Detector [69] is small-angle detectors with two arrays of scintillator counters, V0A and V0C on both sides of the collision vertex. The purpose of this detector, is to provide a minimum bias trigger for the central barrel detector in proton and heavy ion collisions. It is used to infer the centrality of a collision by the multiplicity recorded in an event. The V0A covers $2.8 < |\eta| < 5.1$, and the V0C covers the pseudo-rapidity range of $-3.7 < |\eta| < -1.7$. The V0A is located about 340 cm from the interaction point at the positive z-direction. The V0C is located about 900 mm from the interaction point in the negative z-direction. The V0A and V0C arrays each have 32 counters separated into four rings, see Figure 2.10. The full listing of pseudo-rapidity and angular coverage is listed in Table 2.2.

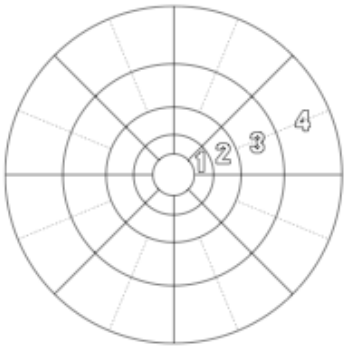

Figure 2.10: Segmentation of V0A/V0C Arrays [69]

Table 2.2: V0A/V0C η & ϕ ranges [69]

	V0A		V0C	
	η_{max}/ η_{min}	ϕ_{max}/ ϕ_{min}	η_{max}/ η_{min}	ϕ_{max}/ ϕ_{min}
Ring 1	5.1 / 4.5	0.7 / 1.3	-3.7 / -3.2	177.0 / 175.3
Ring 2	4.5 / 3.9	1.3 / 2.3	-3.2 / -2.7	175.3 / 172.4
Ring 3	3.9 / 3.4	2.3 / 3.8	-2.7 / -2.2	172.4/ 167.5
Ring 4	3.4 / 2.8	3.8 / 6.9	-2.2 / -1.7	167.5/ 159.8

2.4.2 Zero Degree Calorimeter (ZDC)

The ZDC [70] measures forward energy, which is inferred to correspond to the number of neutrons from spectators and this provides another tool to estimate the centrality of collisions.

The number of participant nucleons is estimated as N_{part}=A-$N_{spectators}$, where A is the total number of nucleons in the nucleus (mass number), and is used to estimate the collision centrality. The ZDC is located 116 cm from the beam interaction point, at a distance between beam pipes of 8 cm. This distance allows spectator protons and neutrons to separate by the magnetic elements of the beam. The ZDC has three calorimeters, two hadronic, the ZN (which measures neutrons) and the ZP (which measures protons), and an electromagnetic ZEM (which measures the total forward energy).

Chapter 3

Anisotropic Flow

3.1 Introduction

As already stated in the introduction, the study of transverse anisotropic flow in relativistic nuclear collisions by Fourier analysis of the particle azimuthal distribution was first proposed by S. Voloshin and Y. Zang [41] in 1994; the method was summarized by Poskanzer and Voloshin [42] in 1998. This finding was significant for many reasons. One reason was that anisotropic flow was observed both at the Brookhaven Alternate Gradient Synchrotron (AGS) [71]-[74] and at the at the Super Proton Synchroton (SPS) [75]-[76] at CERN. Another reason was understanding and relating the development of flow that occurs during the collision evolution with the creation of the quark gluon plasma (QGP) and processes such as thermalization [77] and the study of mean field effects. Other reasons were relating flow to analyses such as two particle correlations and developing techniques for flow analysis at higher energies such as at RHIC and at the LHC.

Anisotropic flow is defined as azimuthal asymmetry with respect to the reaction plane, which is the plane spanned by the beam direction (or longitudinal direction) and the center of the target nucleus to the center of the beam nucleus, the impact parameter [78]. The main importance of anisotropic flow is its relation to the early evolution of the system. Particle momentum asymmetries are due to the initial asymmetries of the system, which diminish as the system evolves. During the system

evolution, the azimuthal symmetry in the interaction volume is broken and spatial anisotropy is converted to momentum anisotropy. The collective motion of the reaction volume becomes azimuthally dependent, leading to an azimuthally anisotropic distribution of particles in the final state.

3.2 Definitions

There exists several techniques to evaluate the collective flow and will now be defined.

3.2.1 Particle Azimuthal Distribution

The particle azimuthal distribution with respect to the reaction plane is shown using the following Fourier expansion [79]:

$$E\frac{d^3N}{d^3p} = \frac{1}{2\pi}\frac{d^2N}{p_T dp_T dy}(1+\sum_{n=1}^{\infty}2v_n\cos(n(\phi-\Psi_{RP})), \tag{3.1}$$

where v_n are the flow coefficients, and n is the harmonic number.

The first few Fourier coefficients have a special name, v_1 (*directed* flow), v_2 (*elliptic* flow), v_3 (*triangular* flow), and v_4 (*quadratic* flow). Flow coefficients are defined are in principle determined according to The expression for the flow coefficients is the following:

$$v_n = \langle\cos(n(\varphi_i - \Psi_{RP})\rangle, \tag{3.2}$$

where the angle brackets indicate the average over all particles in an event. Due to the symmetry with respect to the reaction plane, there is equal probability to emit a particle in the ϕ direction then in the $-\phi$ directionThe expression for v_n as a function of p_T and rapidity y is called differential flow.

3.2.2 Flow Vector

Particle flow is evaluated, collision by collision, using a two-dimensional vector **Q** [79] defined as:

$$\begin{aligned} Q_{n,x} &= \mathbf{Q_n}\cos(n\Psi_n) = \sum_{j=1}^{M} w_j \cos(n\varphi_j) \\ Q_{n,y} &= \mathbf{Q_n}\sin(n\Psi_n) = \sum_{j=1}^{M} w_j \sin(n\varphi_j), \end{aligned} \tag{3.3}$$

where Ψ_n is the azimuthal angle of Q_n and is an estimate of the reaction plane angle Ψ_{RP}. The sum runs over all azimuthal particle angles φ_j in the event and w_j is a weight designed to optimize the measurement by minimizing statistical error. w_j depends on transverse momentum, particle mass, and rapidity. The complex form of the flow vector Q_n is,

$$\mathbf{Q_n} = Q_{n,x} + iQ_{n,y} = Qe^{in\Psi_n} = \sum_{j=1}^{M} w_j e^{in\varphi_j} \tag{3.4}$$

3.2.3 Scalar Product Method

The scalar product method [80] is an anisotropic flow measurement that can be measured without using the reaction plane. In this method, each event is divided into two sub-events, labeled a and b. The sub-events are chosen such that they are equal in size, for example choosing them on the basis of equal pseudorapidity windows, charge, or randomly. The correlation between the two sub-events is given by:

$$\langle Q_n^a Q^{b^*} \rangle = \langle v_n^2 M^a M^b \rangle \tag{3.5}$$

where M^a and M^b are multiplicities of the two sub-events and Q_n is the "full event" flow vector $Q_n^a + Q_n^b$.

The scalar product of a particle unit vector with n harmonic number, defined as $u = e^{in\varphi}$ and depends on particle transverse momentum and pseudorapidity, and the complex conjugate of the flow vector Q^*,

$$\langle \mathbf{u} \cdot \mathbf{Q}^* \rangle = \frac{1}{M_Q} \sum_{i=k}^{M} \mathbf{u_k} \sum_{j=1, j\neq k}^{M} \mathbf{u_j^*}. \tag{3.6}$$

In order to remove autocorrelation, the particle $\mathbf{u}$ is subtracted from $\mathbf{Q}$ before the scalar product is calculated. An estimate of v_n, with the scalar product method, is obtained with

$$v_n\{SP\} = \frac{\langle Q_n \cdot u(\eta, p_T) \rangle}{2\sqrt{\langle Q_n^a Q_n^b \rangle}}. \tag{3.7}$$

The scalar product involves two particle correlations and is sensitive to non-flow correlations, which are correlations that are not related to the event plane [79]. Non-flow contributions to the evaluation of the flow coefficients can be reduced by separating the sub-events in pseudorapidity.

3.2.4 Cumulant method

The cumulant method [81] consists of a multi-particle correlation approach used measure flow, which is a means of reducing non-flow. Here we will concentrate on two-particle correlations $c_n\{2\}$ to give an estimate of flow coefficients v_n, however the fourth order cumulant $c_n\{4\}$ gives an estimate on v_n using four particle cumulants, which is a more accurate because the higher the number of particles correlated the better the chance of reducing non-flow. The two and four particle cumulants are listed in the following equations:

$$\begin{aligned} c_n\{2\} &= \left\langle \frac{|\mathbf{Q_n}|^2 - M}{M(M-1)} \right\rangle \\ c_n\{4\} &= \left\langle \frac{|\mathbf{Q_n}|^4 + |\mathbf{Q_{2n}}|^2 - 2 \cdot Re[\mathbf{Q_{2n}} \mathbf{Q_n^*} \mathbf{Q_n^*}]}{M(M-1)(M-2)(M-3)} - 2\frac{2(M-2) \cdot |\mathbf{Q_n}|^2 - M(M-3)}{M(M-1)(M-2)(M-3)} \right\rangle. \end{aligned} \tag{3.8}$$

Only the even cumulants, i.e. $c_n\{2k\}$ (where k is an integer), are evaluated because odd order cumulants vanish over many events. For example, $c_n\{3\}$ contains $\langle \cos(\Psi_{RP}) \rangle$, which is zero for a detector with perfect acceptance.

The cumulants are related to flow by the following manner. Two and four particle correlations yield:

$$\begin{aligned} \left\langle e^{ni(\phi_1 - \phi_2)} \right\rangle &= v_n\{2\}^2 \\ \left\langle e^{ni(\phi_1 + \phi_2 - \phi_3 - \phi_4)} \right\rangle &= v_n\{4\}^4, \end{aligned} \tag{3.9}$$

and may be related to cumulants according to

$$\begin{aligned} v_n\{2\} &= \sqrt{c_n\{2\}} \\ v_n\{4\} &= \sqrt[4]{-c_n\{4\}}. \end{aligned} \tag{3.10}$$

The above flow expressions for two and four particle cumulants also contain a non-flow δ_n and a flow fluctuation component σ_{v_n}.

$$\begin{aligned} v_n\{2\}^2 = & \quad \langle v_n^2 \rangle = \langle v_n \rangle^2 + \sigma_{v_n}^2 + \delta_n \\ v_n\{4\}^2 = & \quad (2\langle v_n^2 \rangle^2 - \langle v_n^2 \rangle^4)^{\frac{1}{2}} = \langle v_n \rangle^2 - \sigma_{v_n}^2 + \delta_{2n} \end{aligned} \tag{3.11}$$

The non-flow (δ_n) can not be calculated analytically but may be estimated. The second order estimate of non-flow (δ_2) is larger than the fourth order estimate of non-flow (δ_4). For elliptic flow, for example, if there are $M/2$ pairs of particles in an event emitted randomly, and a total of $M(M-1)/2$ particle pairs with $M/2$ correlated pairs, the two and four particle correlations are the following [82]:

$$\begin{aligned} \left\langle e^{2i(\phi_1-\phi_2)} \right\rangle &= \frac{1}{(M-1)} \\ \left\langle e^{ni(\phi_1+\phi_2-\phi_3-\phi_4)} \right\rangle &= \frac{2}{(M-1)(M-3)} \end{aligned} \tag{3.12}$$

The non-flow contribution for elliptic flow is $c_2\{2\}$ is $\delta_2 \approx 1/(M-1)$ and for $c_2\{4\}$ is $\delta_4 \approx 2/(M-1)(M-3)$. The effects for non-flow and flow fluctuations cannot be separately measured, however studying different orders of cumulants provides upper and lower limits to true elliptic flow.

3.2.5 uQ Method {AA-pp}

In studying azimuthal correlation from *pp* collisions, the non-flow contribution of the heavy ion collisions is estimated [83]. Differential flow is studied, which is v_n as a function of rapidity and transverse momentum, and can be used to estimate the azimuthal correlation of a certain particle with the following equation:

$$\langle \mathbf{uQ}^* \rangle^{AA} = \langle \sum_{i=1} cos(n(\varphi_{p_T} - \varphi_i)) \rangle = M v_n(p_T) v_n^{'} + \text{non-flow}, \tag{3.13}$$

φ_{p_T} is the azimuthal angle of the particle in the given p_T bin, where $v_2(p_T)$ is the elliptic flow for a given p_T, and $v_2^{'}$ is the average for particles in a certain region, and M is the multiplicity which depends on the centrality. The centrality of the nuclear collision can be estimated by measuring the multiplicity of produced particles, more central collisions have higher multiplicity than more peripheral collisions which have lower multiplicity

The AA-pp method assumes that in proton-proton *pp* collisions only non-flow correlations are present whereas in *AA* collisions, or heavy ion collisions, a superposition of flow and non-flow effects take placemany *pp* collisions. If the scalar product of the unit vector $\mathbf{u_n}$ and the complex conjugate of the Q vector $\mathbf{Q_n}$ is expressed in terms of flow v_n, average flow $v_n^{'}$ and non-flow δ_n components, then we have the following definition:

$$\langle \mathbf{u_n Q_n^*} \rangle = \langle M \rangle \left(v_n\{2\} v_n^{'}\{2\} + \delta_n \right) = \langle M \rangle \, v_n\{2\} v_n^{'}\{2\} + \widetilde{\delta_n}, \tag{3.14}$$

and solving for $v_n\{2\}$,

$$v_n\{2\} = \frac{\langle \mathbf{u_n Q_n^*} \rangle - \widetilde{\delta_n}}{\langle M \rangle \, v_n^{'}\{2\}}, \tag{3.15}$$

where M is the multiplicity of the *AA* collisions, and $\widetilde{\delta_n} = \langle M \rangle \, \delta_n$. Using the *pp* to estimate the non-flow component, there is a new expression for $v_n\{2\}$ in terms of $AA - pp$,

$$v_n\{2\}\{uQ, AA - pp\} = \frac{\langle \mathbf{u_n Q_n^*} \rangle^{AA}}{\langle M^{AA} \rangle \, v_n^{'}\{2\}} - \frac{\langle \mathbf{u_n Q_n^*} \rangle^{pp}}{\langle M^{AA} \rangle \, v_n^{'}\{2\}}. \tag{3.16}$$

3.2.6 Event Plane Method

The event plane method was introduced by Danielewicz and Odyniec in 1985 [84]. The first prodecure in this method is to reconstruct the event plane angle Ψ_n on an event by event basis, where Ψ_n is

$$\Psi_n = \frac{1}{n} \cdot \arctan\left(\frac{Q_{n,y}}{Q_{n,x}}\right), \tag{3.17}$$

where the Q vectors where defined in Equation 3.3.

3.2.6.1 Event Plane Resolution

The event plane resolution is defined as:

$$R_n = \langle \cos\left[n\left(\Psi_n - \Psi_{RP}\right)\right] \rangle . \tag{3.18}$$

The resolution factor depends the number of particles N used in the Q-vector and the average flow of the event. The higher the value of N, the more precise the definition of the event plane and less sensitive to statistical fluctuations.

The event plane resolution is given by [78, 79]:

$$R\left(\chi\right) = \frac{\sqrt{\pi}}{2}\chi exp\left(-\chi^2/2\right)\left[I_0\left(\frac{\chi^2}{2}\right) + I_1\left(\frac{\chi^2}{2}\right)\right] \tag{3.19}$$

where I_0 and I_1 are the modified Bessel function and χ is the resolution parameter defined as:

$$\chi = v_n\sqrt{N}. \tag{3.20}$$

Experimentally, the resolution can be evaluated by applying the event plane method on two sub-events A and B and comparing the obtained results. Each sub-event is positively correlated since each is correlated with the reaction plane. The square root of this correlation gives the event plane resolution:

$$R_{n,sub} = \sqrt{\langle \cos\left[n\left(\Psi_n^A - \Psi_n^B\right)\right]\rangle}. \tag{3.21}$$

The two sub-events are obtained by dividing each event into two samples with equal multiplicities. This can be done by randomly choosing positive and negative charged particles, choosing particles within a certain rapidity region, or combinations of these results. The full event plane resolution is obtained using $R\left(\chi\right)$ from the resolution of the sub-events:

$$R_{full} = R\left(\sqrt{2}\chi_{sub}\right) \tag{3.22}$$

The first measurements from the ALICE Collaboration of anisotropic flow coefficients of $v_2 - v_5$ in Pb-Pb collisions at $\sqrt{s_{NN}}$=2.76 TeV are shown for data taken in November 2010 during the first heavy ion run. The flow coefficients $v_n\{2\}$ from two particle correlations using the cumulants method is shown in Figure 3.1 [86]. Results are presented for centrality classes 30-40%, 0-5%, and 0-2%. The 30-40% centrality class is compared to hydrodynamic predictions using Glauber initial conditions for different η/s [86]. Since this flow method involves two particle correlations, non-flow (particles uncorrelated with the reaction plane) are removed by introducing a separation in pseudorapidity, $\Delta\eta$. This motivated a comparison between the $v_n\{2\}$ from the ALICE published results and the $v_n\{2\}\{uQ, AA\}$ from this analysis.

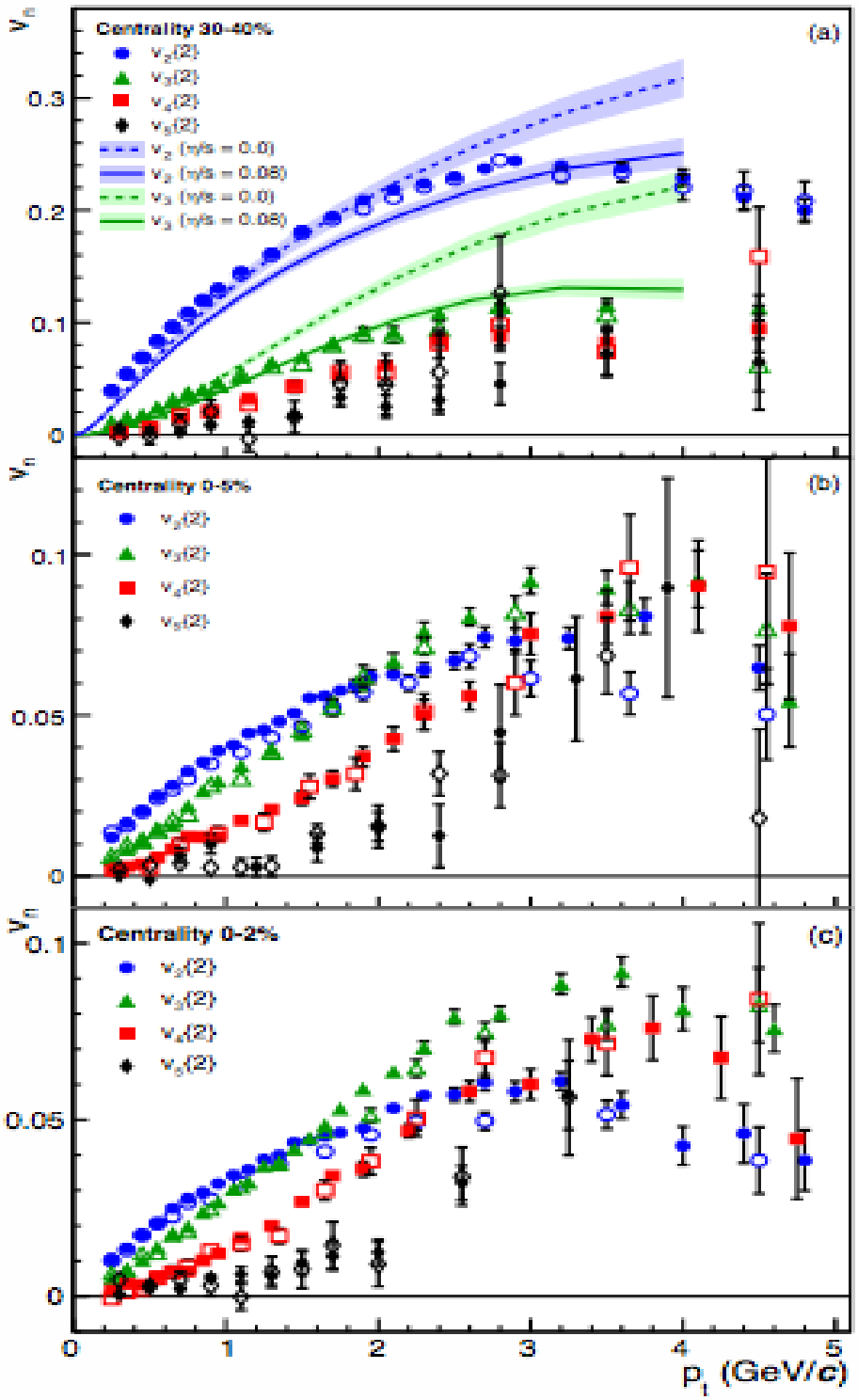

Figure 3.1: v_2, v_3, v_4, v_5 as a function of transverse momentum and for three event centralities. The full, open symbols are for $\Delta\eta > 0.2$ and for $\Delta\eta > 1.0$, respectively. a) 30%-40% compared to hydrodynamic model calculations b) 0-5% centrality percentile c) 0-2% centrality percentile. [86]

3.3 Results

3.3.1 Data Selection

In this analysis, flow coefficients are obtained using the $v_2\{2\}\{AA-pp\}$ method using the 2010 Pb-Pb heavy-ion data at $\sqrt{s_{NN}} = 2.76$ TeV and the 2010 pp data from 2010 at $\sqrt{s_{NN}} = 2.76$ TeV. The Time Projection Chamber (TPC) was used to reconstruct charged particle tracks, and to define centrality based on TPC multiplicity. The event sample was collected with a dedicated minimum bias trigger. Only events with a reconstructed primary vertex within ± 10 cm along the beam axis are selected for this analysis. The analysis was carried out based on14 million Pb-Pb charged particles with $p_T > 0.2$ GeV/c and pseudo-rapidity range $|\eta| < 0.8$ The full list of following event cuts and track cuts used to produce the Pb-Pb and pp data are listed in Table 3.3.

Table 3.1: Analysis Details of pp & Pb-Pb data at $\sqrt{s_{NN}} = 2.76$ TeV

Event cuts	Value
$\|vertex\|_z$	< 10 cm
Track cuts	Value
$\|\eta\|$	< 0.8
p_T	> 0.2 GeV/c
$N_{clusters}$	> 70
$\|dca\|_{xy}$	< 2.4 cm
$\|dca\|_z$	< 3.0 cm

The $v_n\{2\}$ flow coefficients from the published results are compared with that obtained from $v_n\{2\}\{AA\}$, the $AA-pp$ method without subtracting the pp non-flow estimate Figure 3.3. The results are comparable for v_2-v_5 without removing the non-flow component. This shows that $v_n\{2\}\{AA\}$ for $n \leq 4$ has similar values, however the $v_5\{2\}\{AA\}$ shows the most deviation from $v_5\{2\}$, however still falls within the

statistical limits. The second harmonic (n=2) flow results are significantly higher than the higher harmonics (n=3-5) in most central collisions (0-5%). Similar to the ALICE published results, a $|\eta|$ separation was used to reduce non-flow. Figure **??** shows a separation between the **u** vector and the **Q** vector, $\Delta\eta \leq 0.4$. In this example the **u** particle from η range $\in$ (-0.8,-0.2) is correlated with the **Q** vector from the η range $\in$ (0.2,0.8). Similarily, $\Delta\eta \leq 1.0$ would yield the **u** particle from η range $\in$ (-0.8,-0.5) is correlated with the **Q** vector from the η range $\in$ (0.5,0.8). In this work, $\Delta\eta$ separation is also referred to as $\Delta\eta$ gap.

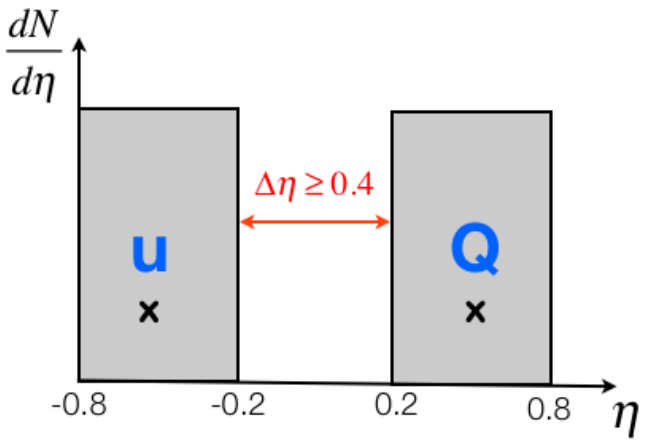

Figure 3.2: $\Delta\eta$ separation between the **u** vector and the **Q** vector to reduce autocorrelation

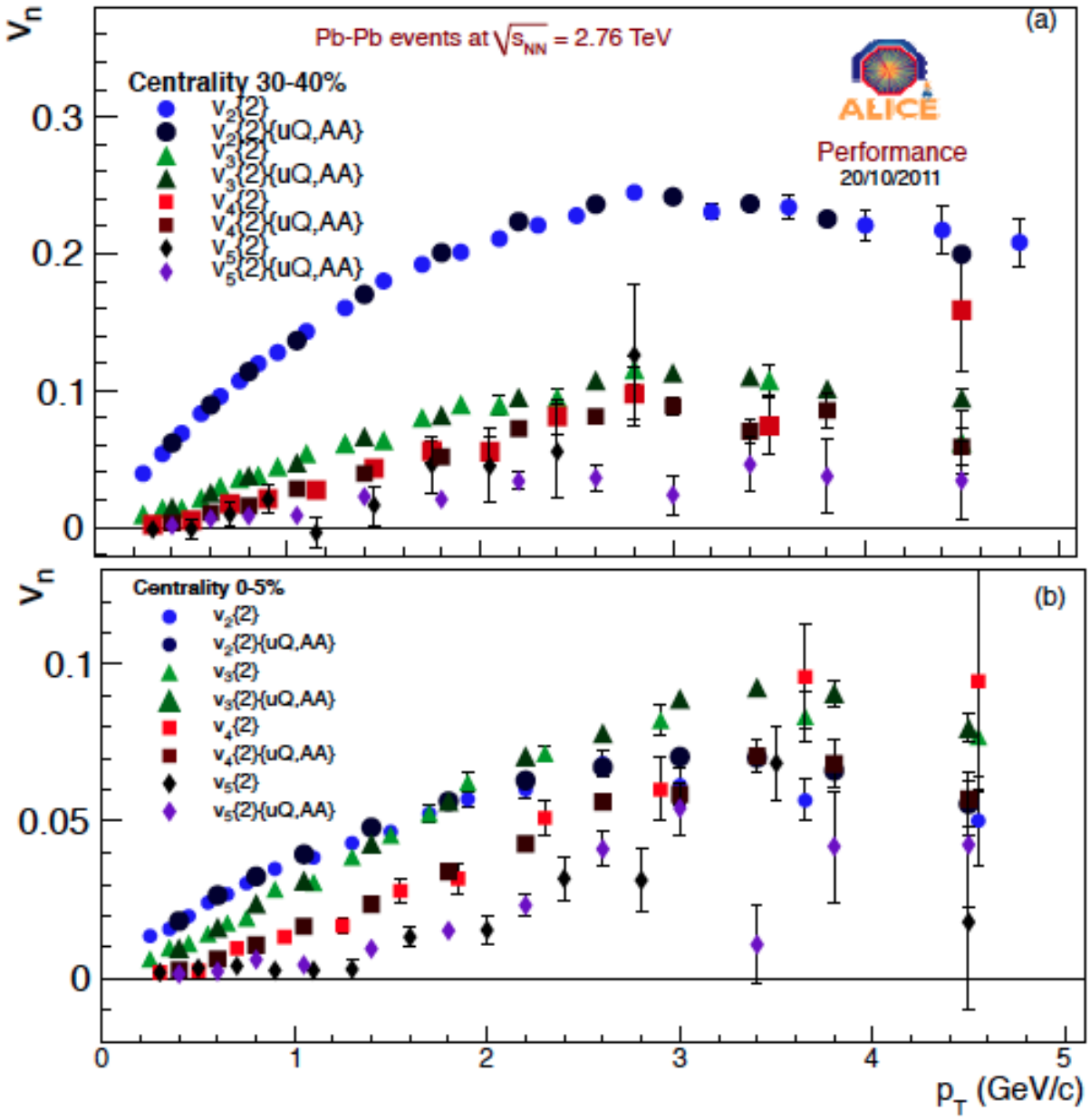

Figure 3.3: $v_2\{2\}\{AA\}$, $v_3\{2\}\{AA\}$, $v_4\{2\}\{AA\}$, and $v_5\{2\}\{AA\}$ as a function of transverse momentum and for 30-40% and 0-5%.$v_2\{2\}$, $v_3\{2\}$, $v_4\{2\}$, and $v_5\{2\}$ are from published data [86]

3.3.2 $\langle u_n Q_n^* \rangle^{pp}$

In this work, the non-flow component is estimated using *pp* data at $\sqrt{s_{NN}} = 2.76$ TeV, see Figures 3.4-3.8. Two separations in pseudorapidity were used, $|\Delta\eta| > 0.4$, where the **u** particle from η range $\in$ (-0.8,-0.2) is correlated with the **Q** vector from the η range $\in$ (0.2,0.8), and $|\Delta\eta| >$1.0, where **u** particle from η range $\in$ (-0.8,-0.5) is correlated with the **Q** vector from the η range $\in$ (0.5,0.8). The solid lines represent polynomial fits to the *pp* data without a $\Delta\eta$ gap, whereas the dotted and dashed lines show results obtained with $|\Delta\eta| >$0.4 and $|\Delta\eta| >$1.0 respectively. Figures 3.4-3.8 show that without the $\Delta\eta$ gap, the non-flow estimate is higher than with the $\Delta\eta$ gap. The strength of the correlation for $|\Delta\eta| > 1.0$ is lower than for $|\Delta\eta| > 0.4$ showing less of a non-flow estimate, which confirms expectations that a larger $|\Delta\eta|$ gap can reduce the contribution of non-flow effects.

These results indicate that with wider separation in $\Delta\eta$, the more reduced are the non-flow effects. This analysis is limited by the TPC optimal acceptance of $\in (-0.8, 0.8)$, and the larger the $\Delta\eta$ separation the less particles are used for correlation. The ratio of $\langle u_n Q_n^* \rangle^{pp}$ with an η gap of 0.4 divided by $\langle u_n Q_n^* \rangle^{pp}$ without a gap, see Figure 3.5, shows a decrease of 33%. This shows that including an η gap decreases the non-flow estimate.

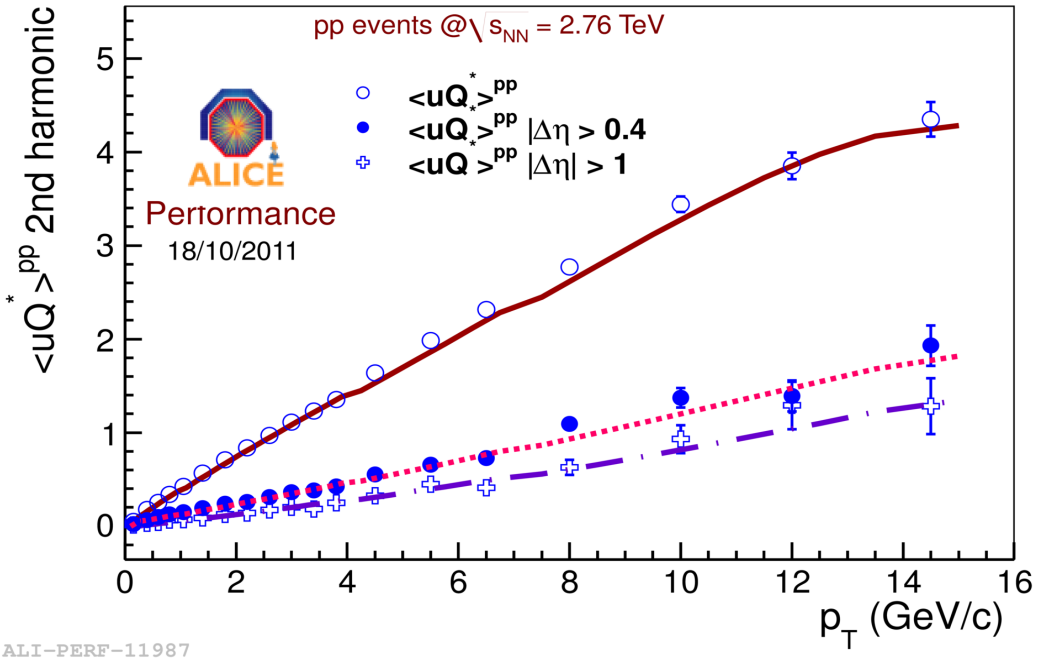

Figure 3.4: $\langle u_n Q_n^* \rangle^{pp}$, n=2, open circles (no $|\Delta\eta|$), full circles ($|\Delta\eta| \geq 0.4$), and open cross ($|\Delta\eta| \geq 1.0$). The solid and dotted line are polynomial fits to the data.

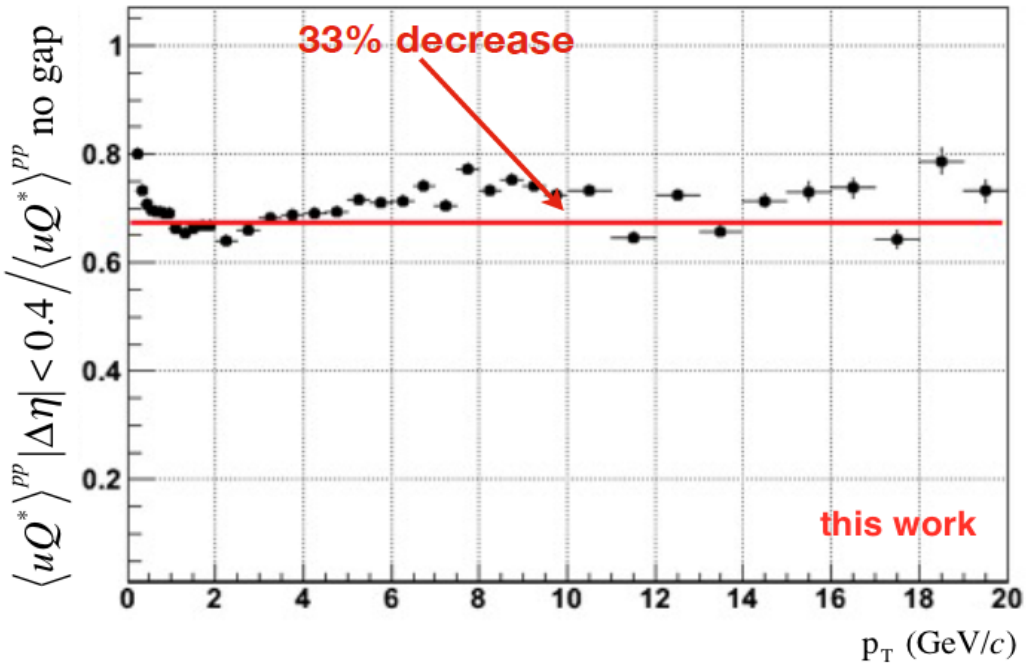

Figure 3.5: Ratio of $\langle u_n Q_n^* \rangle^{pp}$ $|\Delta\eta| > 0.4 / \langle u_n Q_n^* \rangle^{pp}$ no gap for n=2. The solid red line is a fit to a constant value to determine an estimate of the p_T averaged value of the ratio.

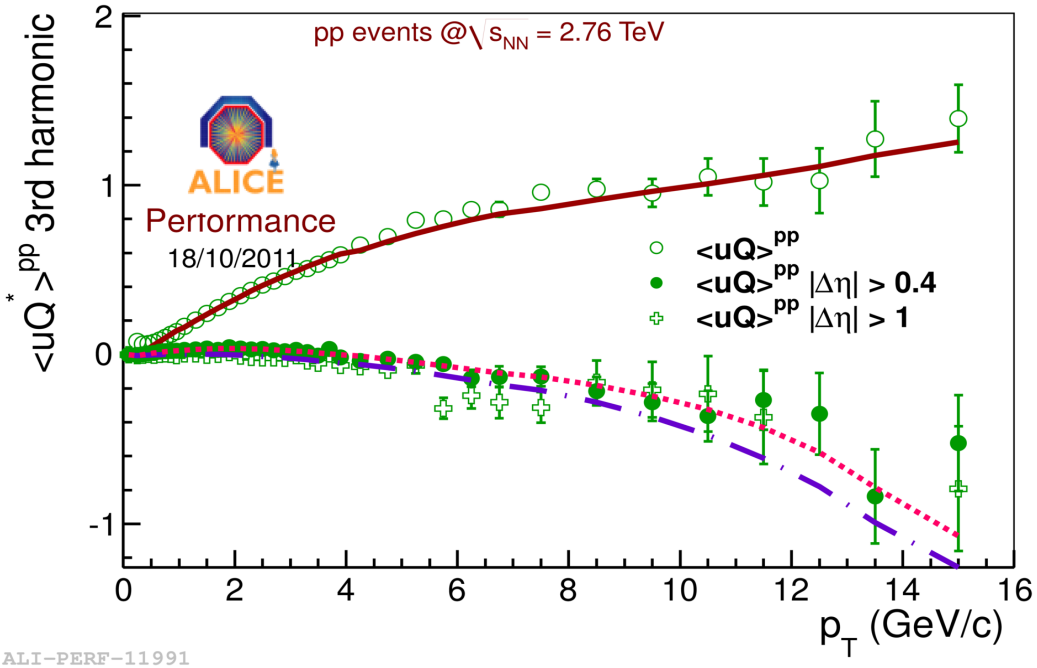

Figure 3.6: $\langle u_n Q_n^* \rangle^{pp}$, n=3, open circles (no $|\Delta\eta|$), full circles ($|\Delta\eta| \geq 0.4$), and open cross ($|\Delta\eta| \geq 1.0$). The solid and dotted line are polynomial fits to the data.

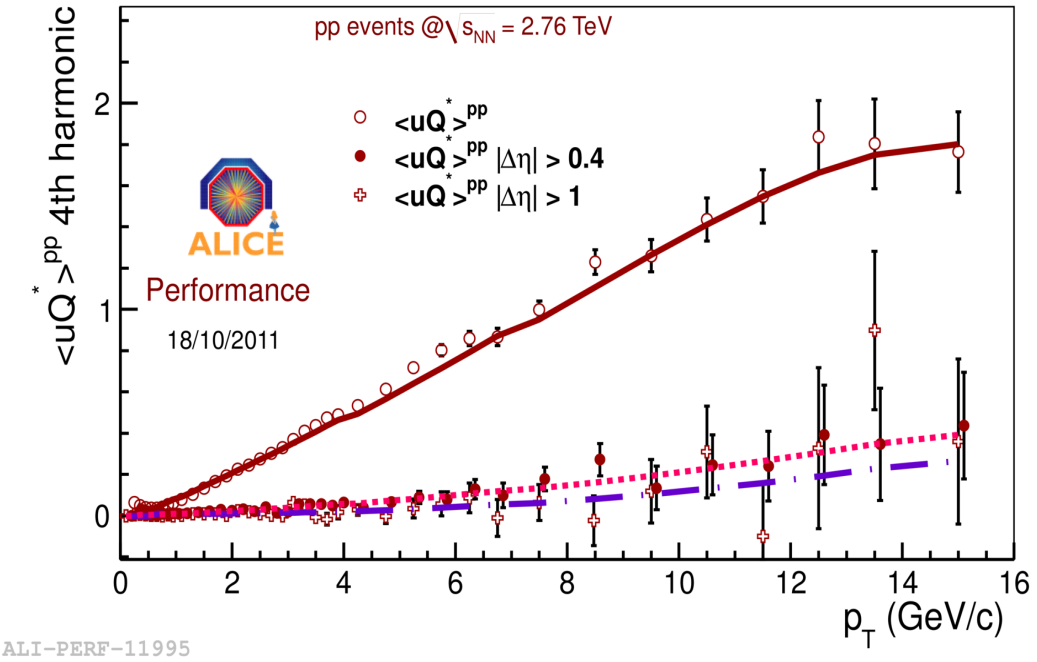

Figure 3.7: $\langle u_n Q_n^* \rangle^{pp}$, n=4, open circles (no $|\Delta\eta|$), full circles ($|\Delta\eta| \geq 0.4$), and open cross ($|\Delta\eta| \geq 1.0$). The solid and dotted line are polynomial fits to the data.

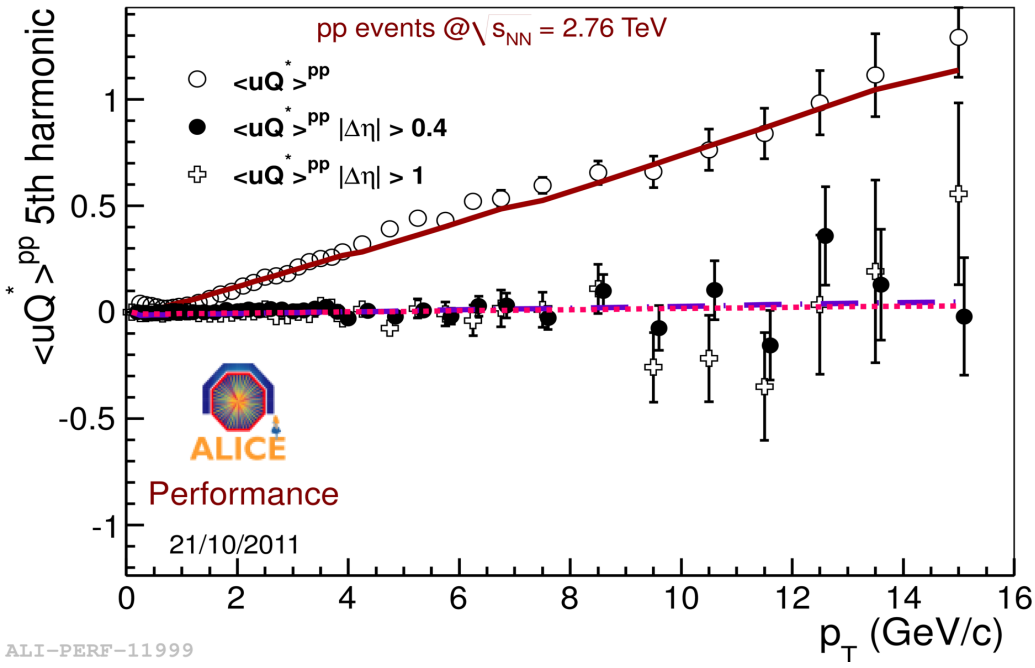

Figure 3.8: $\langle u_n Q_n^* \rangle^{pp}$, n=5, open circles (no $|\Delta\eta|$), full circles ($|\Delta\eta| \geq 0.4$), and open cross ($|\Delta\eta| \geq 1.0$). The solid and dotted line are polynomial fits to the data.

3.3.3 $v_2\{2\}\{uQ, AA\}$ and $v_2\{2\}\{uQ, pp\}$

In this work, the non-flow estimates $\langle u_n Q_n^* \rangle^{pp}$ are used as the correction $\frac{\langle u_n Q_n^* \rangle^{pp}}{\langle M^{AA} \rangle v_n'\{2\}}$ using pp data to the flow coefficients $\frac{\langle u_n Q_n^* \rangle^{AA}}{\langle M^{AA} \rangle v_n'\{2\}}$ using Pb-Pb data. The results are shown in Figure 3.9-3.11 for n=2. Figure 3.9 and Figure 3.10 show 0-5% most central and 50-60% centralities respectively where there is significant separation between the Pb-Pb and pp data at $p_T \leq 8$ GeV. Figure 3.11 shows that both Pb-Pb and pp data are in agreement. This indicates that for central (0-5%) and mid-central (50-60%) collisions, there are significant non-flow contributions and in the most peripheral collisions (80-90% mainly non-flow effects completely dominate in the correlation function. This result agrees with the measurements from STAR [83, 85] at $\sqrt{s}_{NN} =$ 200 GeV.

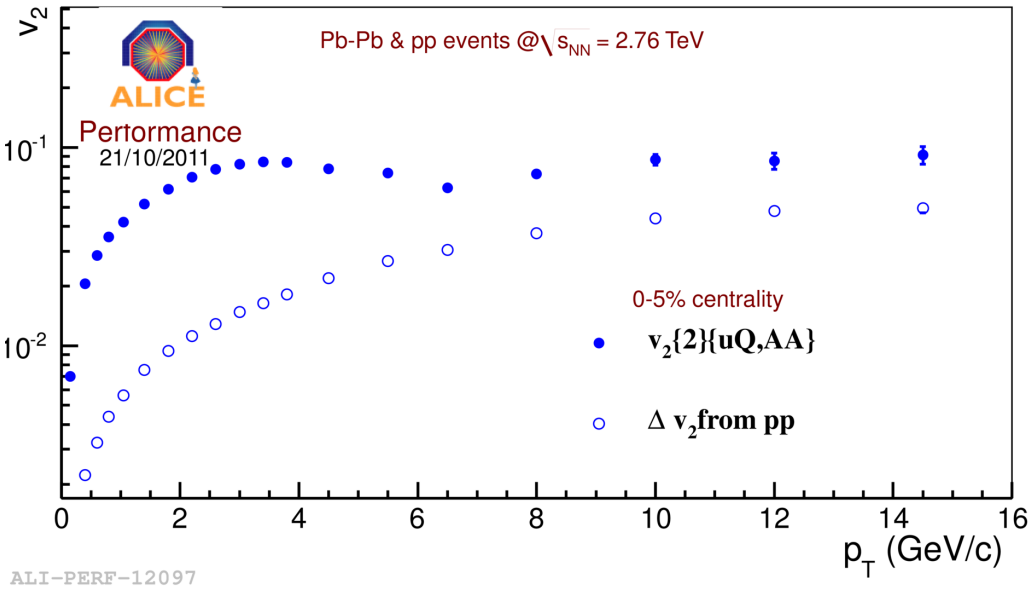

Figure 3.9: $v_2\{2\}\{AA\}$and $v_2\{2\}\{pp\}$ for Pb-Pb and pp collisions at $\sqrt{s_{NN}} =$ 2.76 TeV for 0-5% centrality

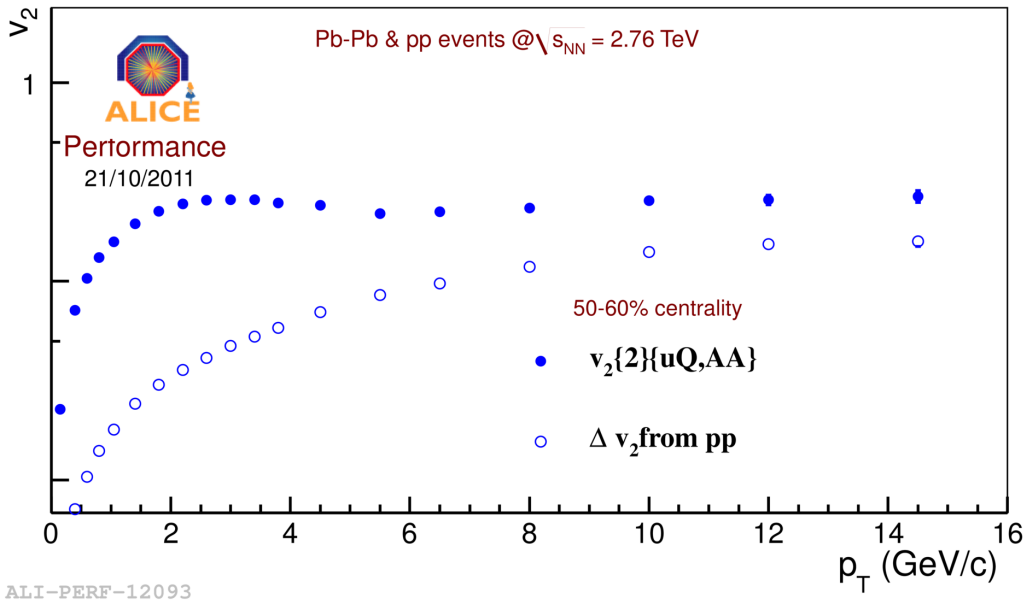

Figure 3.10: $v_2\{2\}\{AA\}$and $v_2\{2\}\{pp\}$ for Pb-Pb and pp collisions at $\sqrt{s_{NN}}$ = 2.76 TeV for 50-60% centrality

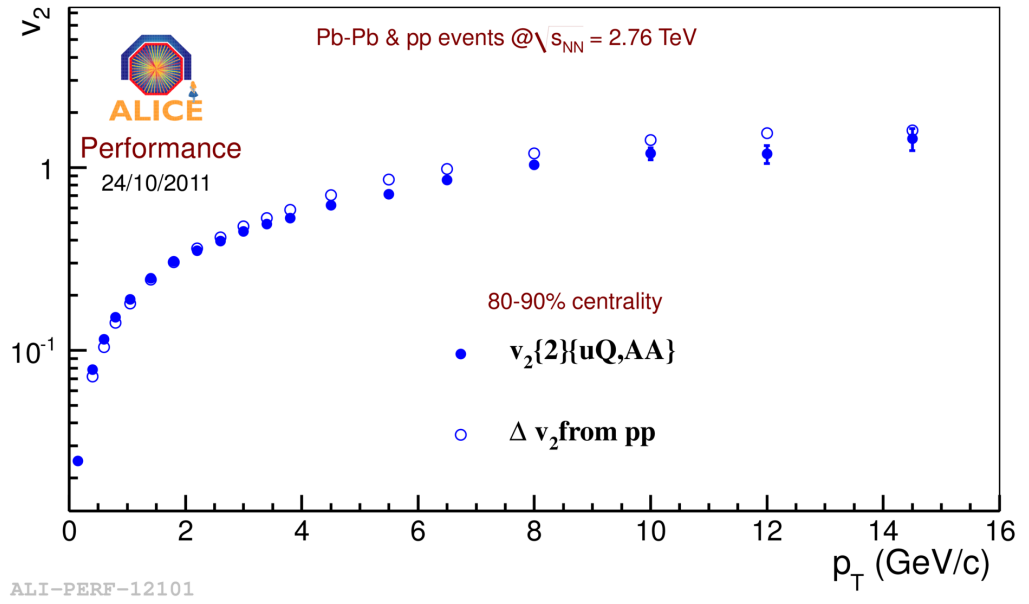

Figure 3.11: $v_2\{2\}\{AA\}$and $v_2\{2\}\{pp\}$ for Pb-Pb and pp collisions at $\sqrt{s_{NN}}$ = 2.76 TeV for 80-90% centrality

3.3.4 $v_n\{2\}\{uQ, AA\}$ and $v_n\{2\}\{uQ, pp\}$

In this section, higher harmonics (n=3, n=4, and n=5) are discussed and various separation in $\Delta\eta$ are used to reduce the non-flow contributions.

Odd harmonic flow coefficients are expected to be completely due to event-by-event fluctuations in the initial spatial geometry [86]. The (n=3) triangular flow coefficient, shown in Figures 3.1 and 3.3, is significantly smaller than the (n=2) elliptic flow coefficient. Little dependence on centrality is seen for triangular flow as compared to elliptic flow. The non-flow estimate $\langle u_n Q_n^* \rangle^{pp}$ in Figure 3.6 is divided by the Pb-Pb multiplicity $\langle M^{AA} \rangle$ and average flow $v_n^{'}\{2\}$ to obtain the non-flow estimate. In Figure 3.12, the solid line represents the non-flow estimate in pp without including an η gap, whereas the dotted and dashed lines show the estimate of non-flow including an η gap. One observes that the use of an $\Delta\eta$ gap significantly reduces the non-flow contribution. The corrected results removing the non-flow contribution are shown in Figure 3.13 and Figure 3.15 of $v_{3,correction} = \frac{\langle \mathbf{u_n Q_n^*} \rangle^{AA}}{\langle M^{AA} \rangle v_n^{'}\{2\}} - \frac{\langle \mathbf{u_n Q_n^*} \rangle^{pp}}{\langle M^{AA} \rangle v_n^{'}\{2\}}$. After removing the non-flow component, all $v_3\{2\}\{uQ, AA - pp\}$ results with and without the η gap are in agreement.

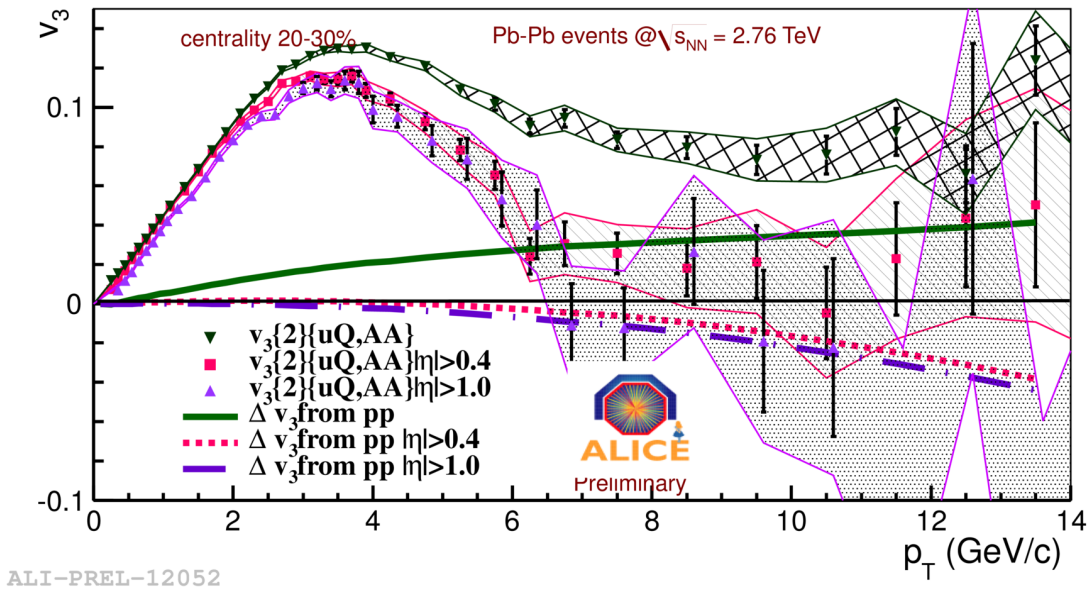

Figure 3.12: 20-30% centrality before removing non-flow ($v_3\{2\}\{AA\}$)

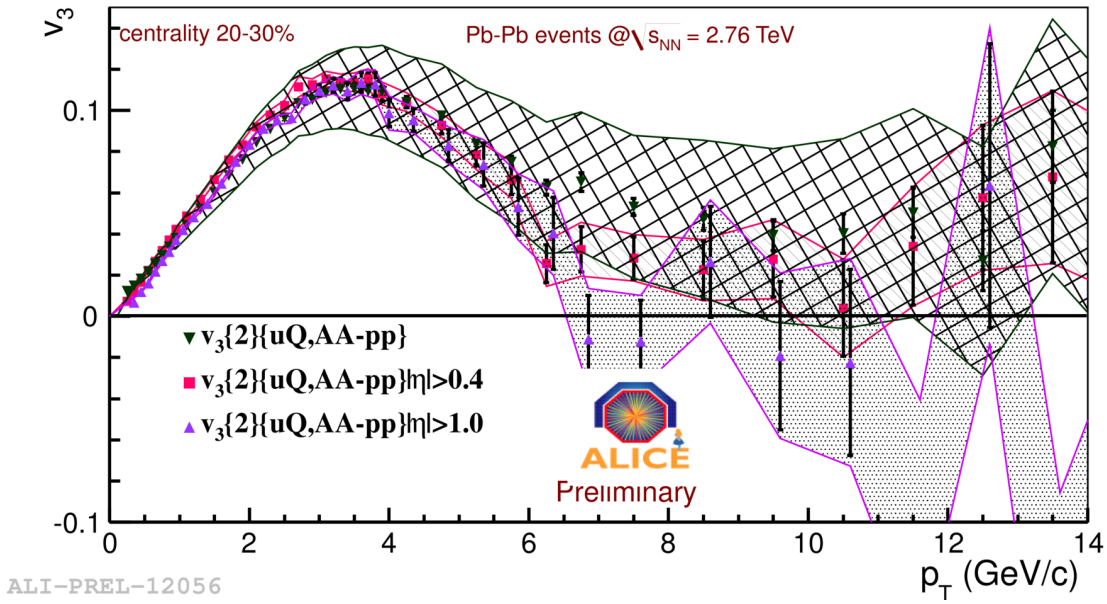

Figure 3.13: 20-30% centrality after removing non-flow ($v_3\{2\}\{AA-pp\}$)

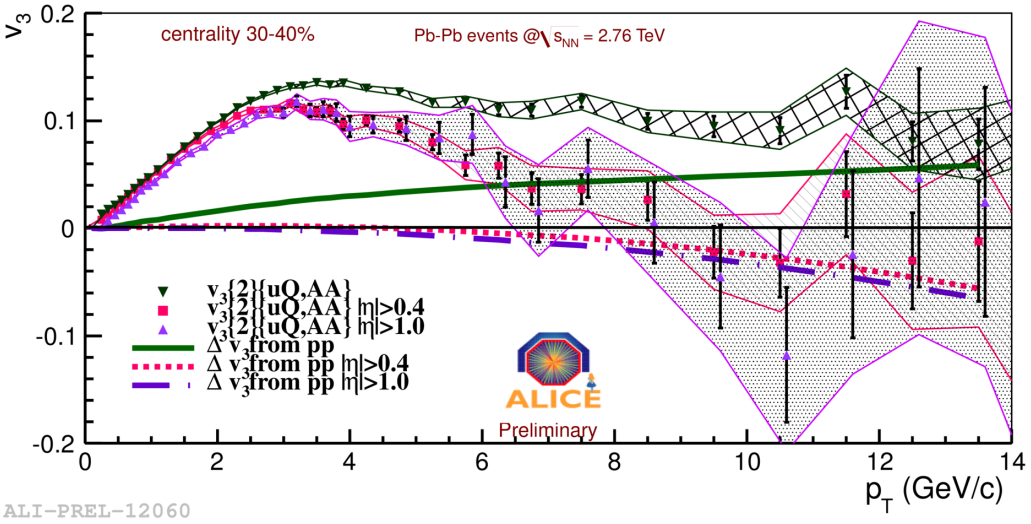

Figure 3.14: 30-40% centrality before removing non-flow ($v_3\{2\}\{AA\}$)

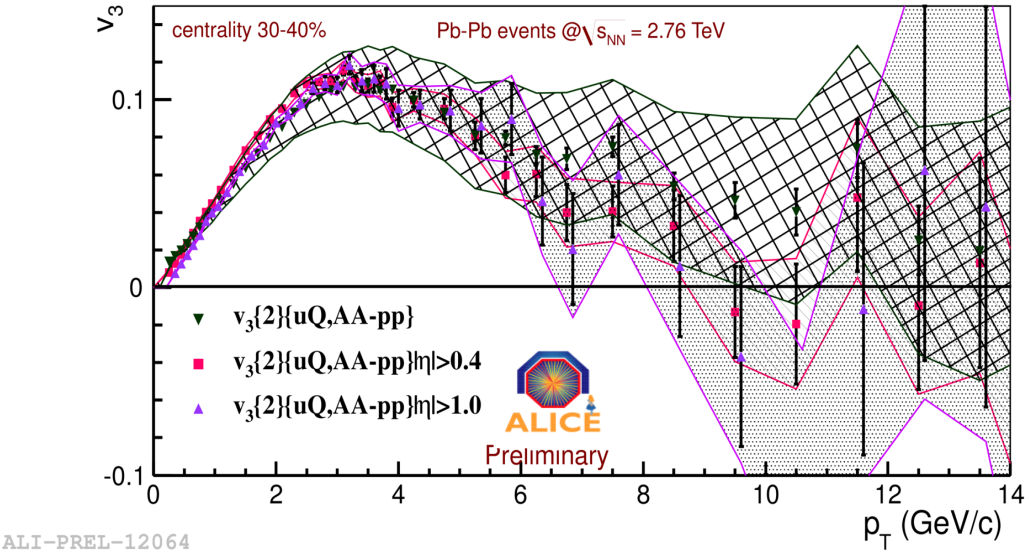

Figure 3.15: 30-40% centrality after removing non-flow ($v_3\{2\}\{AA-pp\}$)

Results for $v_4\{2\}\{AA-pp\}$ are shown with and without $\Delta\eta$ gap separation in Figures 3.16-3.17. In comparing the non-flow estimate for n=4 (see Figure 3.16) vs. n=3 (see Figures 3.14) at $p_T \geq 9$, the non-flow estimate is more significant for $v_4\{2\}\{AA\}$ than $v_3\{2\}\{AA\}$ (shown by the green lines). Including the $\Delta\eta$ gaps for this harmonic significantly suppresses nonflow effects (dotted and dashed lines are close to zero). Figure 3.18-3.19 shows $v_5\{2\}\{uQ, AA\}$ and $v_5\{2\}\{uQ, AA-pp\}$. The results for $v_5\{2\}\{uQ, AA-pp\}$ are similar to $v_4\{2\}\{uQ, AA-pp\}$, after removing the non-flow estimate. These results without an $\Delta\eta$ gap and including a $\Delta\eta$ gap are consistent.

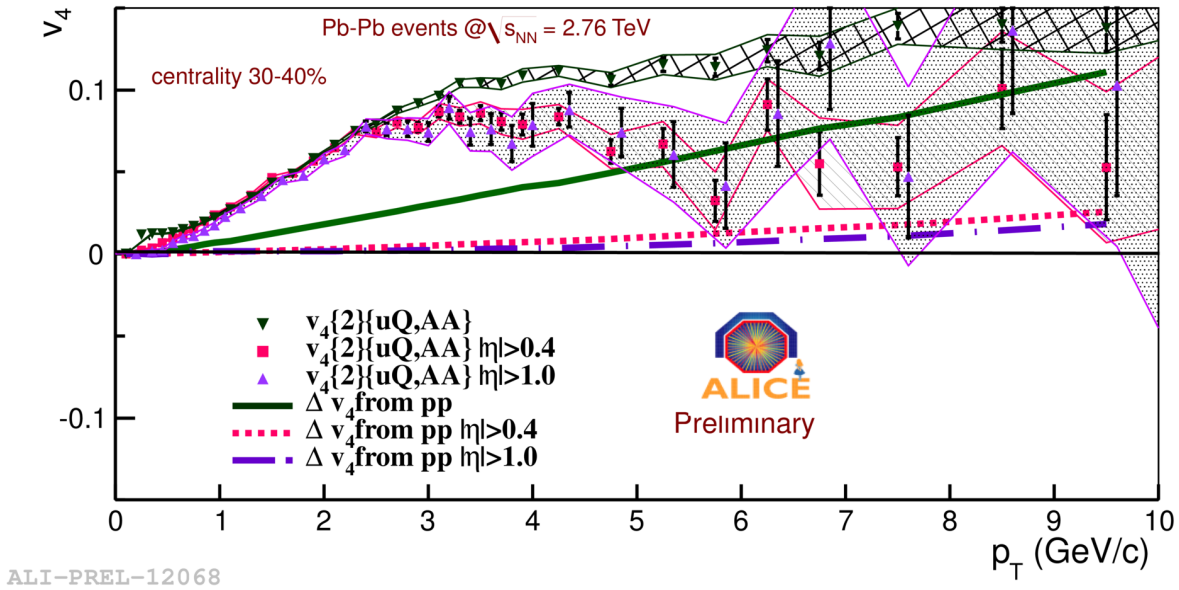

Figure 3.16: 30-40% centrality before removing non-flow ($v_4\{2\}\{AA\}$)

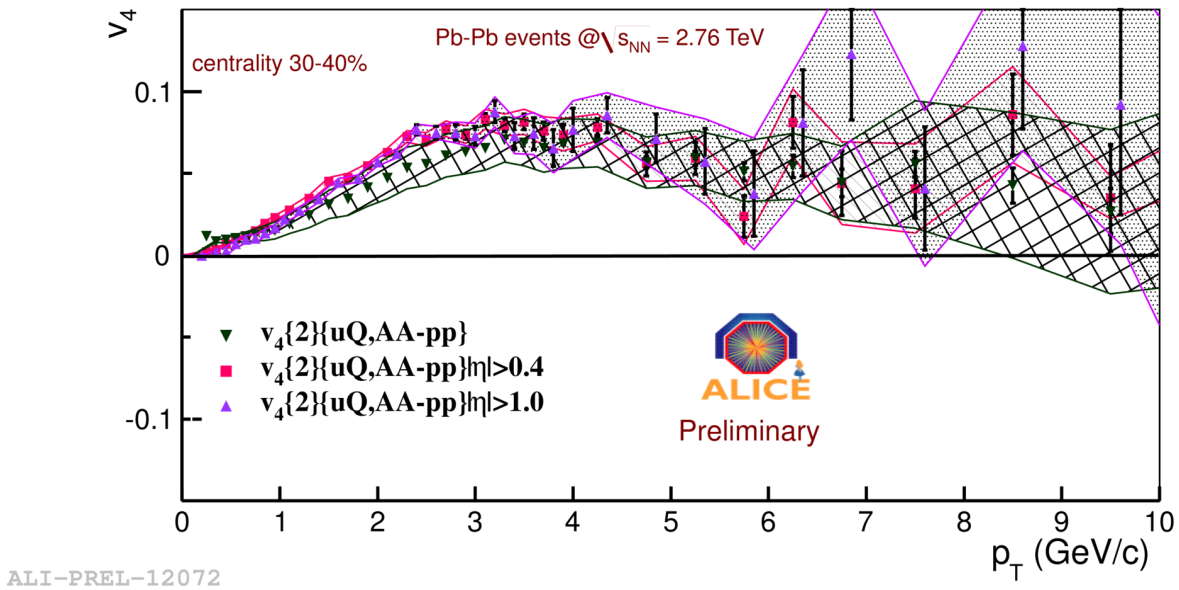

Figure 3.17: 30-40% centrality after removing non-flow ($v_4\{2\}\{AA-pp\}$)

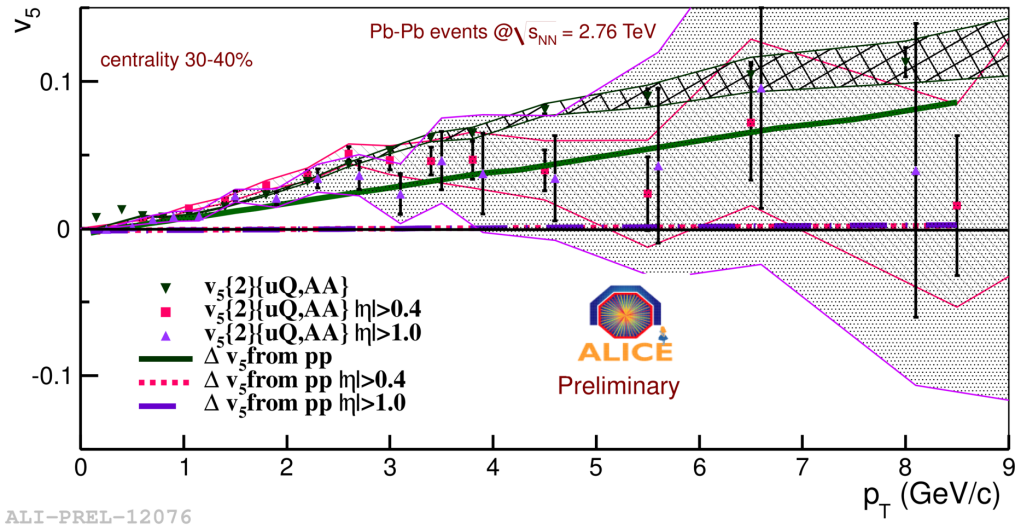

Figure 3.18: 30-40% centrality before removing non-flow ($v_5\{2\}\{AA\}$)

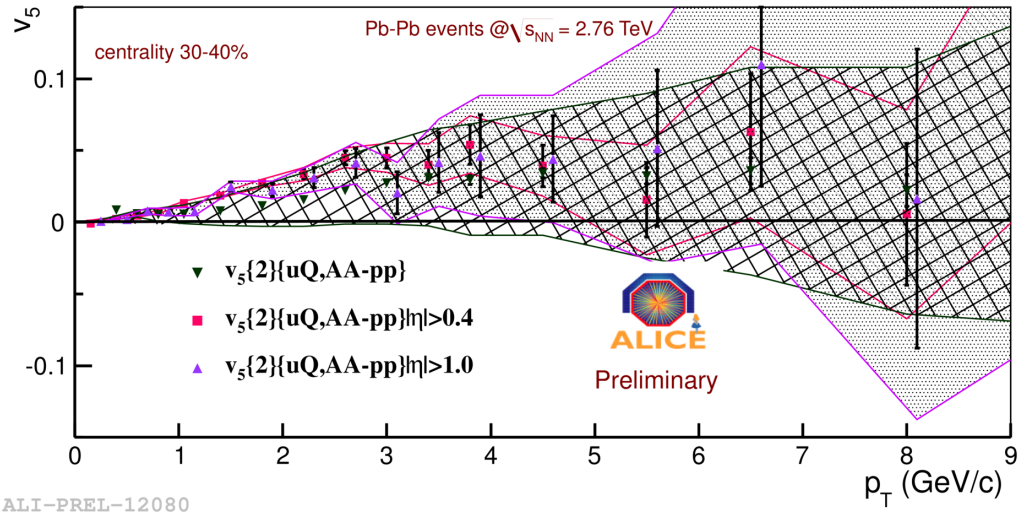

Figure 3.19: 30-40% centrality after removing non-flow ($v_5\{2\}\{AA-pp\}$)

3.3.5 uQ Method {AA-pp} vs. Scalar Product {AA-pp}

3.3.5.1 $v_n\{2\}\{uQ, AA\}$ and $v_n\{2\}\{SP, AA\}$

The results for $v_n\{2\}\{\text{uQ,AA}\}$ are now compared to $v_n\{2\}\{\text{SP,AA}\}$ for n=1-5, for different centralities and for higher p_T. The uQ method is the following:

$$v_n\{2\}\{uQ, AA\} = \frac{\langle \mathbf{u_n Q_n^*} \rangle^{AA}}{\langle M^{AA} \rangle \, v_n'\{2\}}, \tag{3.23}$$

whereas the SP method is defined below without removing the non-flow component:

$$v_n\{2\}\{SP, AA\} = \frac{\langle Q_n \cdot u(\eta, p_T) \rangle^{AA}}{2\sqrt{\langle Q_n^a Q_n^b \rangle}}. \tag{3.24}$$

Figure 3.20-3.22 shows results for v_n for $p_T < 8$ GeV/c. The SP method (open symbols) yields values that are slightly lower than those obtained with the uQ method (closed symbols). For $p_T > 8$ GeV/c, the statistical errors are large, therefore comparisons cannot be made in this region. Also in this region, there are other dominate effects, such as jet contribution.

3.3.5.2 $v_n\{2\}\{uQ, AA - pp\}$ and $v_n\{2\}\{SP, AA - pp\}$

The $v_n\{2\}\{uQ, AA - pp\}$ is seen in Equation 3.16, and the same method of non-flow subtraction is followed for the Scalar Product Method:

$$v_n\{2\}\{SP, AA - pp\} = \frac{\langle Q_n \cdot u(\eta, p_T) \rangle^{AA}}{2\sqrt{\langle Q_n^a Q_n^b \rangle}} - \frac{\langle Q_n \cdot u(\eta, p_T) \rangle^{pp}}{2\sqrt{\langle Q_n^a Q_n^b \rangle}}. \tag{3.25}$$

In Figures 3.20-3.22, $v_n\{2\}\{SP, AA\}$ is smaller than $v_n\{2\}\{uQ, AA\}$for $p_T \leq 4$ GeV/c. However, in this method of non-flow subtraction in Figure 3.23 (centrality 20-30%),

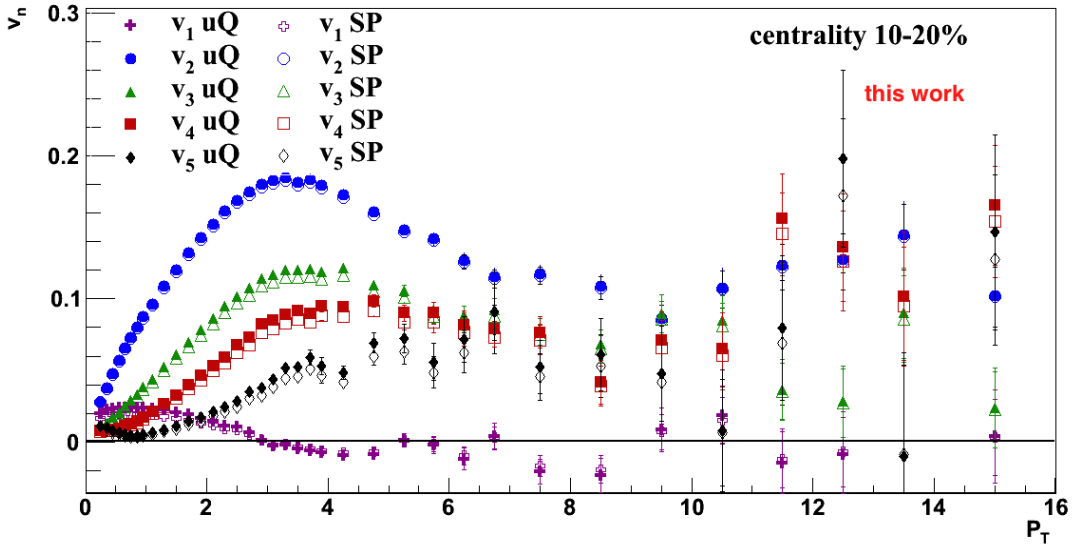

Figure 3.20: $v_n\{2\}\{uQ, AA\}$ and $v_n\{2\}\{SP, AA\}$ for centrality 10-20%. Closed data points are $v_n\{2\}\{uQ, AA\}$ and open points are $v_n\{2\}\{SP, AA\}$.

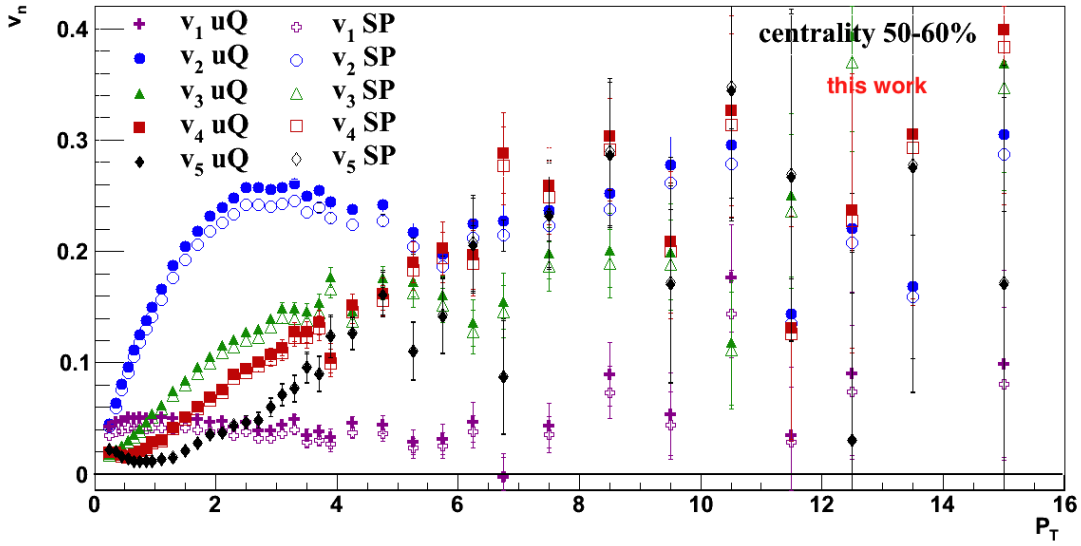

Figure 3.21: $v_n\{2\}\{uQ, AA\}$ and $v_n\{2\}\{SP, AA\}$ for centrality 50-60%. Closed data points are $v_n\{2\}\{uQ, AA\}$ and open points are $v_n\{2\}\{SP, AA\}$.

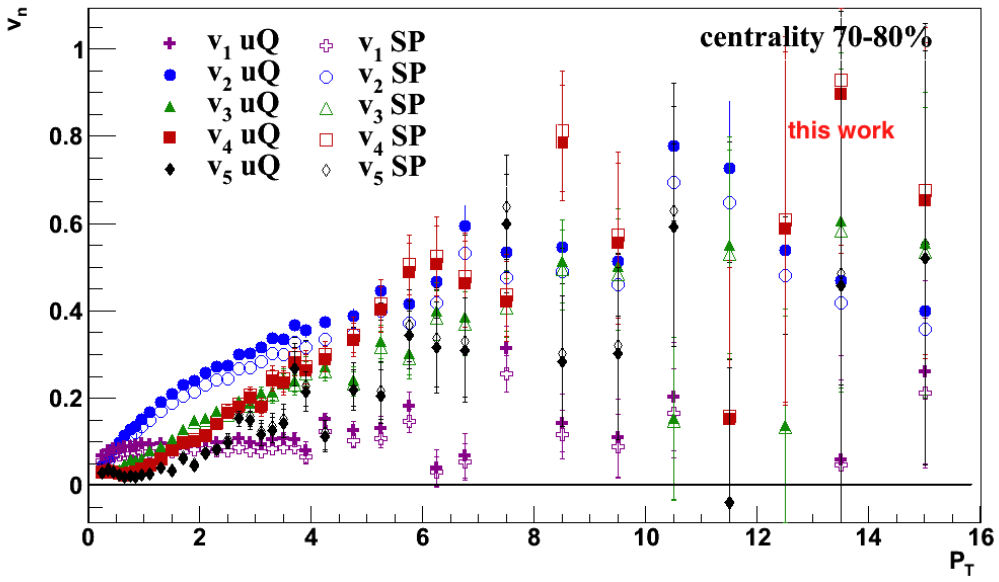

Figure 3.22: $v_n\{2\}\{uQ, AA\}$ and $v_n\{2\}\{SP, AA\}$ for centrality 70-80%. Closed data points are $v_n\{2\}\{uQ, AA\}$ and open points are $v_n\{2\}\{SP, AA\}$.

in Figure 3.24 (centrality 30-40%), $p_T \leq 4$ GeV/c, both the uQ and SP methods are within statistical errors for n=2. For $p_T > 4$ GeV/c both v_2\{uQ,|$\Delta\eta$|¿0.4, AA-pp\} and v_2\{uQ,|$\Delta\eta$|¿1.0, AA-pp\} are lower than v_2\{SP,|$\Delta\eta$| > 0.4, AA-pp\}. This is a possible indication that $v_2\{2\}\{uQ, AA - pp\}$ is comparable to the $v_2\{2\}\{SP, AA - pp\}$. For $p_T \geq 6$ GeV/c, $v_2\{2\}\{uQ, AA - pp\}$ is less than $v_2\{2\}\{SP, AA - pp\}$, indicating more non-flow contribution is removed.

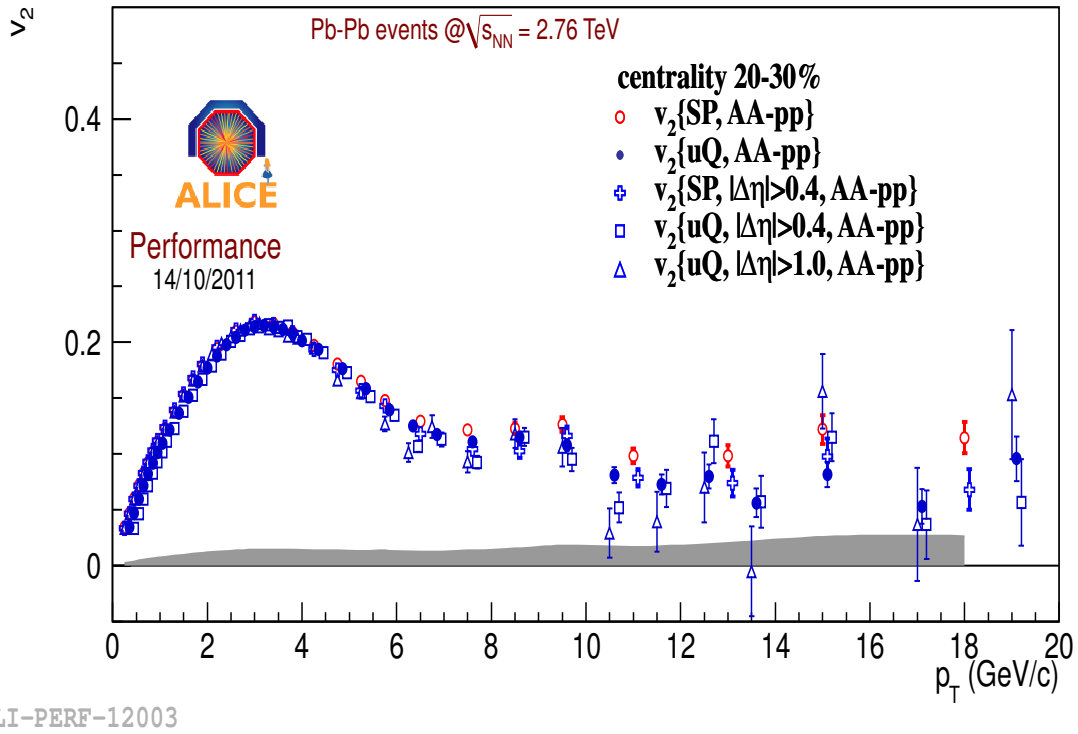

Figure 3.23: $v_2\{2\}\{uQ, AA{-}pp\}$ and $v_2\{2\}\{SP, AA{-}pp\}$ for centrality 20-30%. Blue open points show both $|\Delta\eta| > 0.4$,$|\Delta\eta| > 1.0$. The gray areas show the systematic errors.

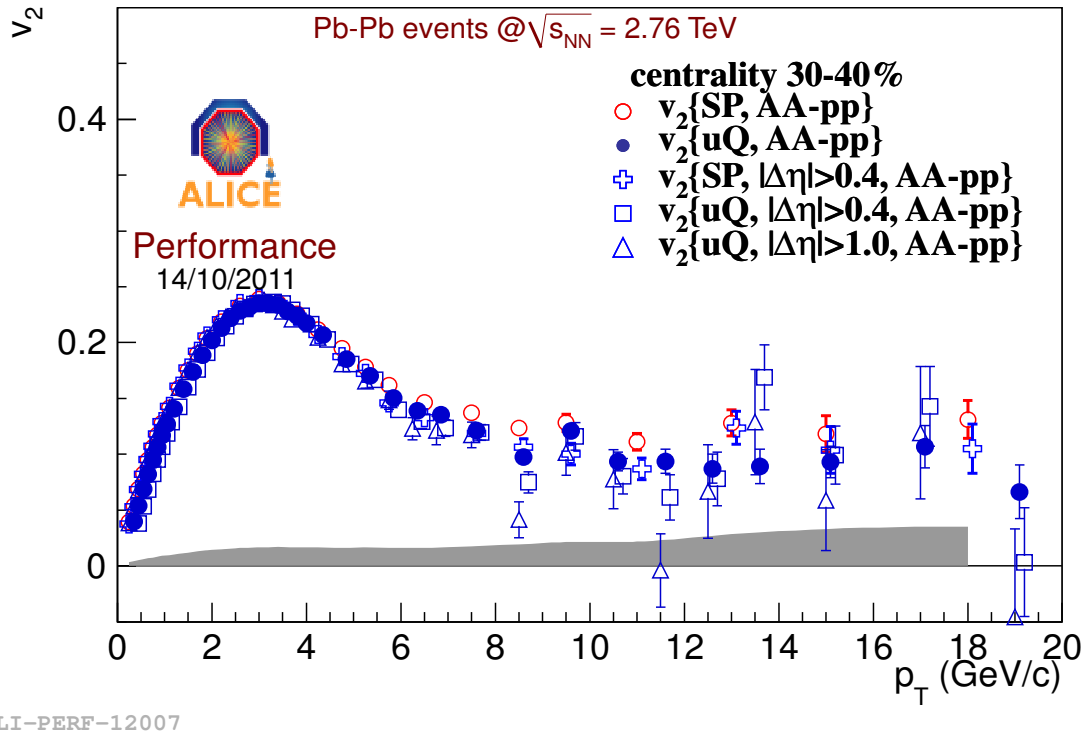

Figure 3.24: $v_2\{2\}\{uQ, AA-pp\}$ and $v_2\{2\}\{SP, AA-pp\}$ for centrality 30-40%. Blue open points show both $|\Delta\eta| > 0.4$,$|\Delta\eta| > 1.0$.

3.3.6 Charge dependence of $\langle\cos(n(\varphi_1 - \varphi_2))\rangle$

The measurements of the charge dependence of $\langle\cos(n(\varphi_1 - \varphi_2))\rangle$ are considered in order to seek an understanding of the non-flow effects. The correlation functions are plotted for "same" (or like) sign $(+,+)$ and $(-,-)$, and "opposite" (or unlike) sign $(+,-)$ or $(-,+)$, and "all" for all charge combinations.

3.3.6.1 Data Selection

In this work, the charge dependent analysis, *pp* collisions at $\sqrt{s}_{NN}$ =7 TeV are presented. The ALICE TPC was used to reconstruct charged particle tracks. The collision centrality determination is based on TPC multiplicity. Results presented in this section are based on the following event cuts and track cuts were used for this analysis:

Table 3.2: Analysis Details of *pp* data at $\sqrt{s}NN = 7$ TeV

Event cuts	Value
$\lvert vertex\rvert_z$	< 7 cm
Track cuts	Value
$\lvert\eta\rvert$	< 0.8
p_T	> 0.2 GeV/c
$N_{clusters}$	> 80
$\lvert dca\rvert_{xy}$	< 2.4 cm
$\lvert dca\rvert_z$	< 3.0 cm

Figures 3.25, 3.30, 3.33, 3.36, and 3.39 for n=1-5 display the correlator $\langle\cos(n(\varphi_1 - \varphi_2))\rangle$ as a function of p_T. One observes that for opposite sign correlations without the $\Delta\eta$ gap, the strength of the correlator are higher than for the same sign. When including the $|\Delta\eta| > 0.4$ and $|\Delta\eta| > 1.0$, as shown in Figures 3.26, 3.27, 3.29, 3.30, 3.32, 3.33, 3.35, 3.36, 3.38, and 3.39, the effect is reduced and the difference between same and opposite sign correlations becomes insignificant.

3.3.6.2 $\langle\cos(1(\varphi_1 - \varphi_2))\rangle$

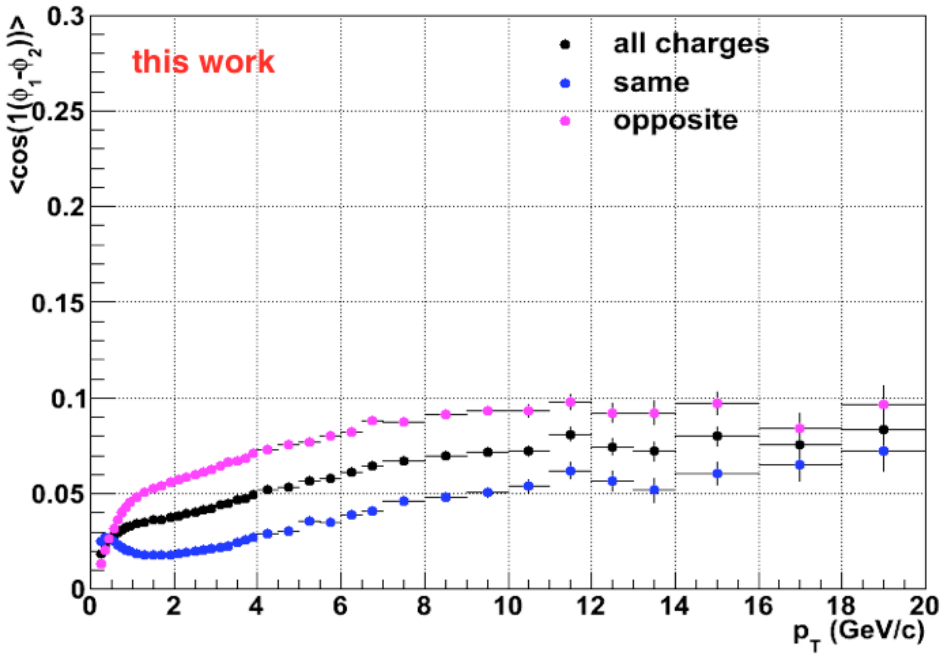

Figure 3.25: $\langle\cos(1(\varphi_1 - \varphi_2))\rangle$ for all charges (++,−−,+−,or −+), same charges (++ or −−), or opposite charges (+− or −+) for no $|\Delta\eta|$ separation for pp collisions at $\sqrt{s}_{NN}$ =7 TeV.

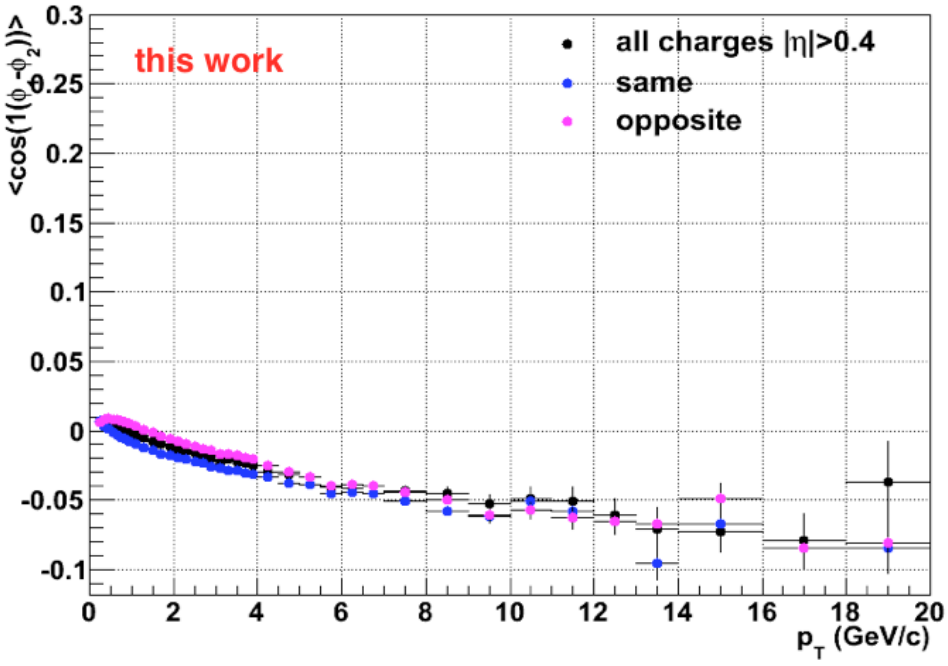

Figure 3.26: $\langle\cos(1(\varphi_1 - \varphi_2))\rangle$ for all charges (++,−−,+−,or −+), same charges (++ or −−), or opposite charges (+− or −+) for $|\Delta\eta| > 0.4$ for pp collisions at $\sqrt{s}_{NN}$ =7 TeV.

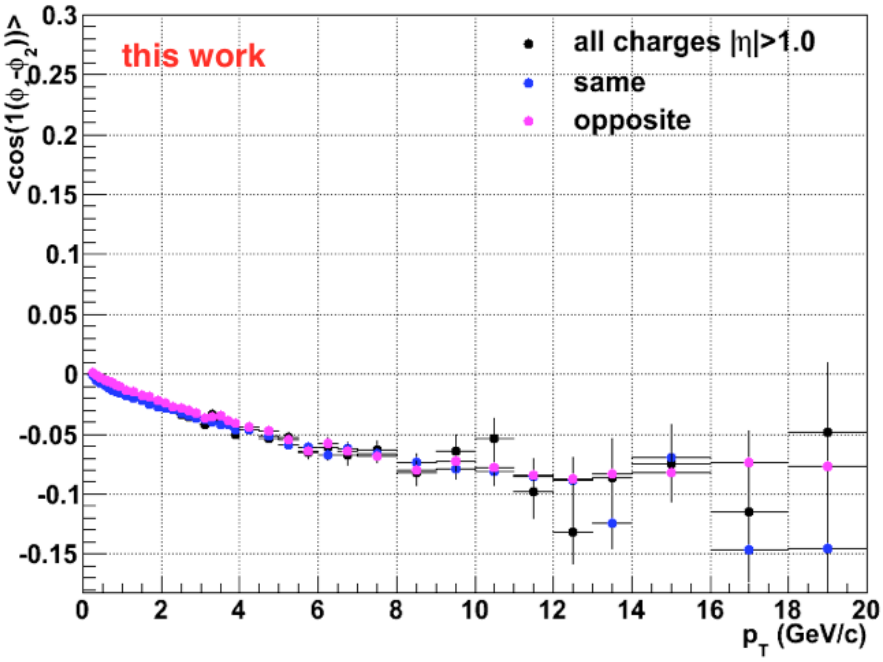

Figure 3.27: $\langle\cos(1(\varphi_1 - \varphi_2))\rangle$ for all charges (++,−−,+−,or −+), same charges (++ or −−), or opposite charges (+− or −+) for $|\Delta\eta| > 1.0$ for pp collisions at $\sqrt{s}_{NN}$ =7 TeV.

3.3.6.3 $\langle\cos(2(\varphi_1 - \varphi_2))\rangle$

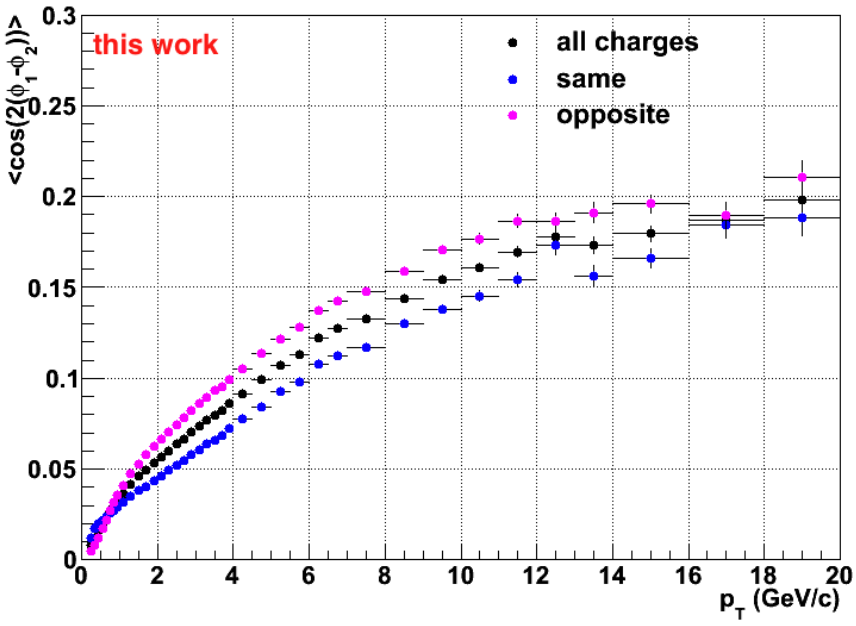

Figure 3.28: $\langle\cos(2(\varphi_1 - \varphi_2))\rangle$ for all charges (++,−−,+−,or −+), same charges (++ or −−), or opposite charges (+− or −+) for no $|\Delta\eta|$ separation for pp collisions at $\sqrt{s}_{NN}$ =7 TeV.

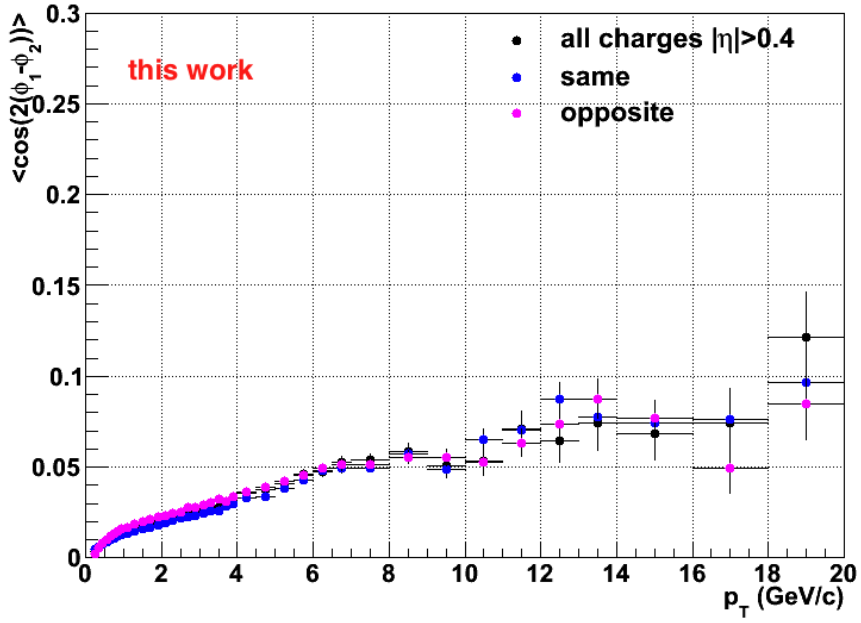

Figure 3.29: $\langle\cos(2(\varphi_1-\varphi_2))\rangle$ for all charges (++,−−,+−,or −+), same charges (++ or −−), or opposite charges (+− or −+) for $|\Delta\eta| > 0.4$ for pp collisions at $\sqrt{s}_{NN}$ =7 TeV.

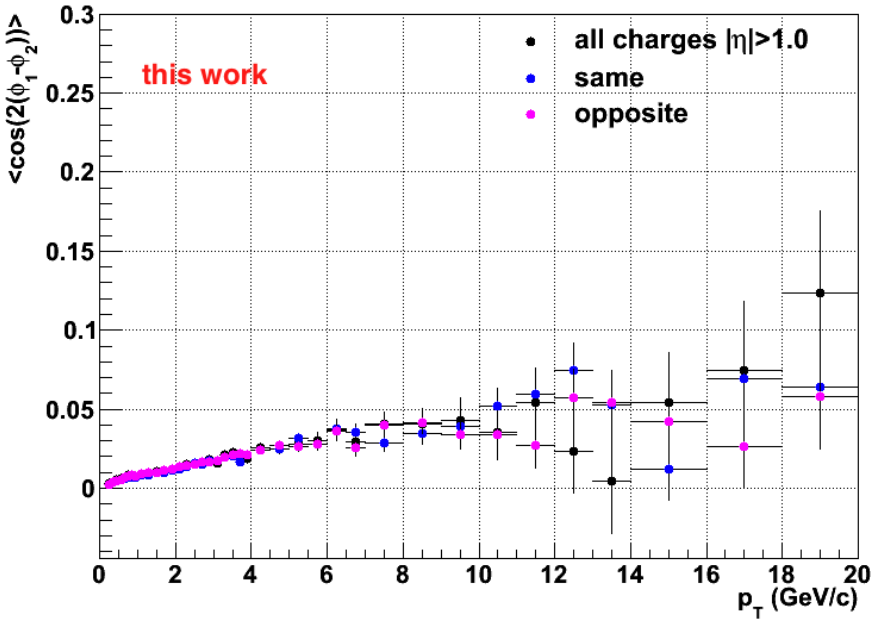

Figure 3.30: $\langle\cos(2(\varphi_1-\varphi_2))\rangle$ for all charges (++,−−,+−,or −+), same charges (++ or −−), or opposite charges (+− or −+) for $|\Delta\eta| > 1.0$ for pp collisions at $\sqrt{s}_{NN}$ =7 TeV.

3.3.6.4 $\langle\cos(3(\varphi_1 - \varphi_2))\rangle$

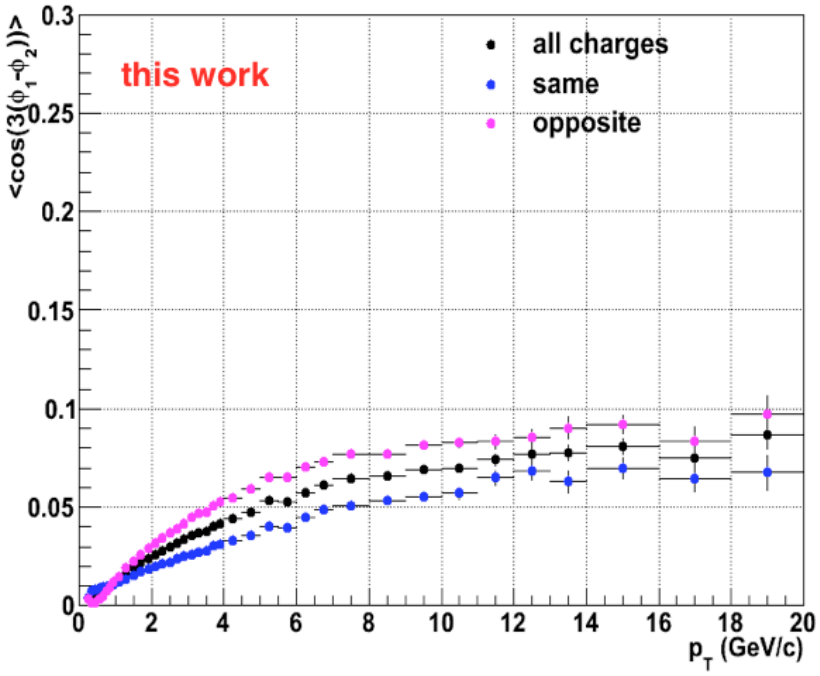

Figure 3.31: $\langle\cos(3(\varphi_1 - \varphi_2))\rangle$ for all charges (++,−−,+−,or −+), same charges (++ or −−), or opposite charges (+− or −+) for no $|\Delta\eta|$ separation for pp collisions at $\sqrt{s}_{NN}$ =7 TeV.

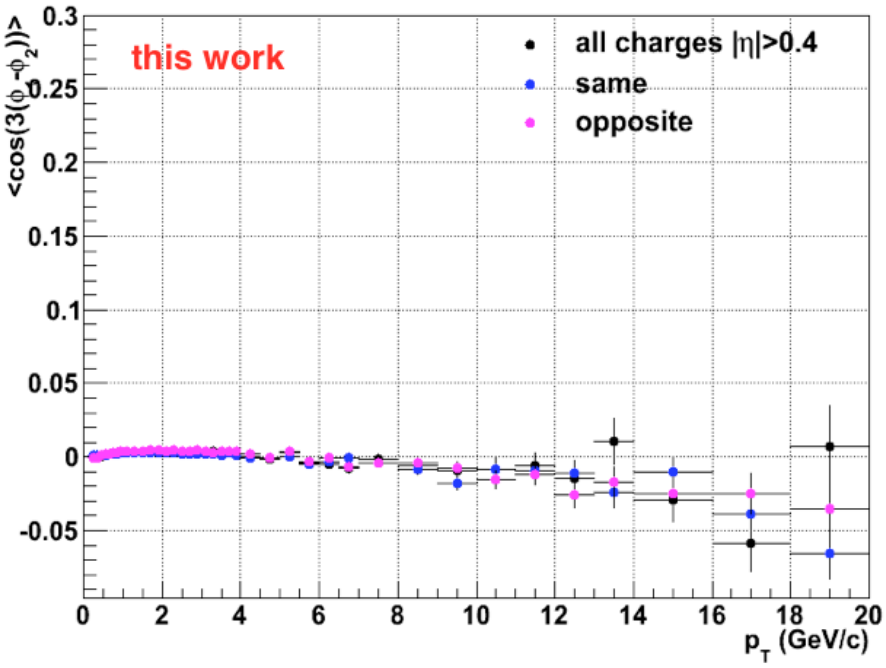

Figure 3.32: $\langle\cos(3(\varphi_1 - \varphi_2))\rangle$ for all charges (++,−−,+−,or −+), same charges (++ or −−), or opposite charges (+− or −+) for $|\Delta\eta| > 0.4$ for pp collisions at $\sqrt{s}_{NN}$ =7 TeV.

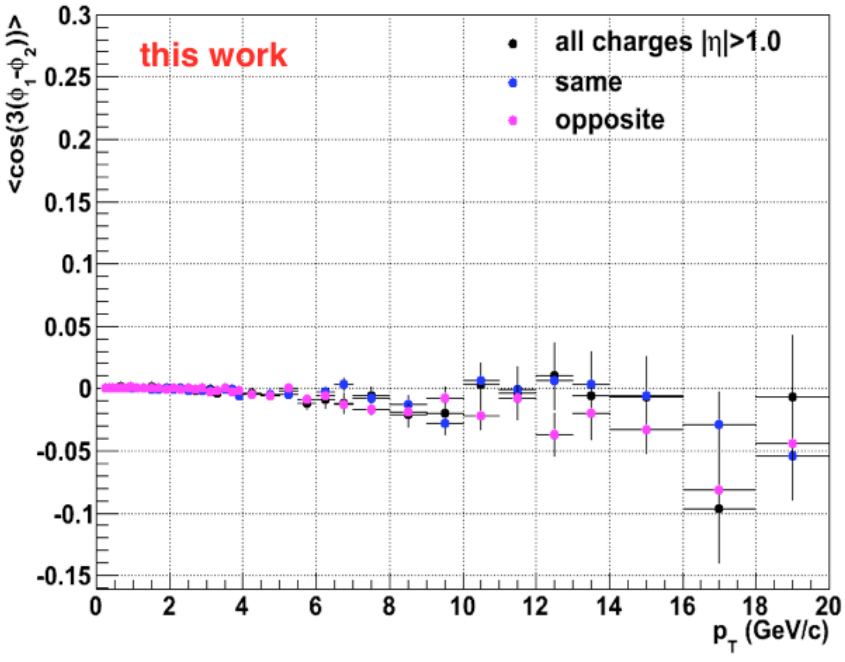

Figure 3.33: $\langle\cos(3(\varphi_1 - \varphi_2))\rangle$ for all charges (++,−−,+−,or −+), same charges (++ or −−), or opposite charges (+− or −+) for $|\Delta\eta| > 1.0$ for pp collisions at $\sqrt{s}_{NN}$ =7 TeV.

3.3.6.5 $\langle\cos(4(\varphi_1 - \varphi_2))\rangle$

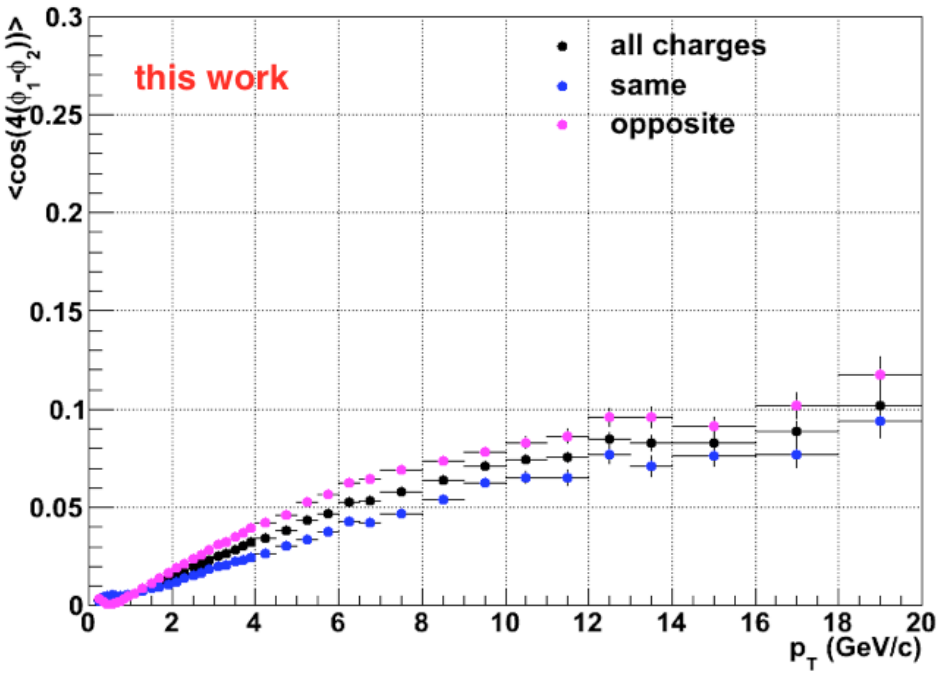

Figure 3.34: $\langle\cos(4(\varphi_1 - \varphi_2))\rangle$ for all charges (++,−−,+−,or −+), same charges (++ or −−), or opposite charges (+− or −+) for no $|\Delta\eta|$ separation for pp collisions at $\sqrt{s}_{NN}$ =7 TeV.

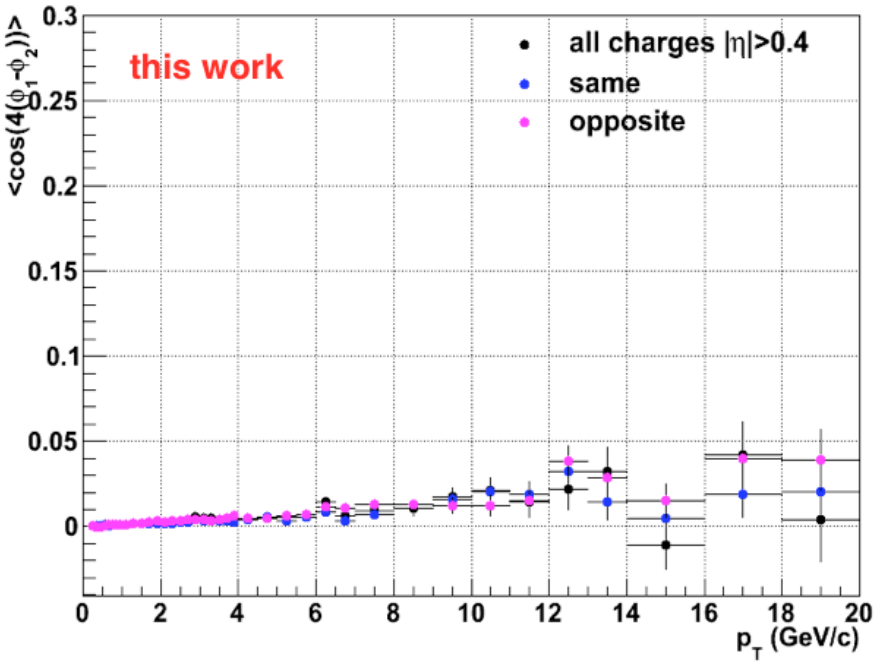

Figure 3.35: $\langle\cos(4(\varphi_1 - \varphi_2))\rangle$ for all charges (++,−−,+−,or −+), same charges (++ or −−), or opposite charges (+− or −+) for $|\Delta\eta| > 0.4$ for pp collisions at $\sqrt{s}_{NN}$ =7 TeV.

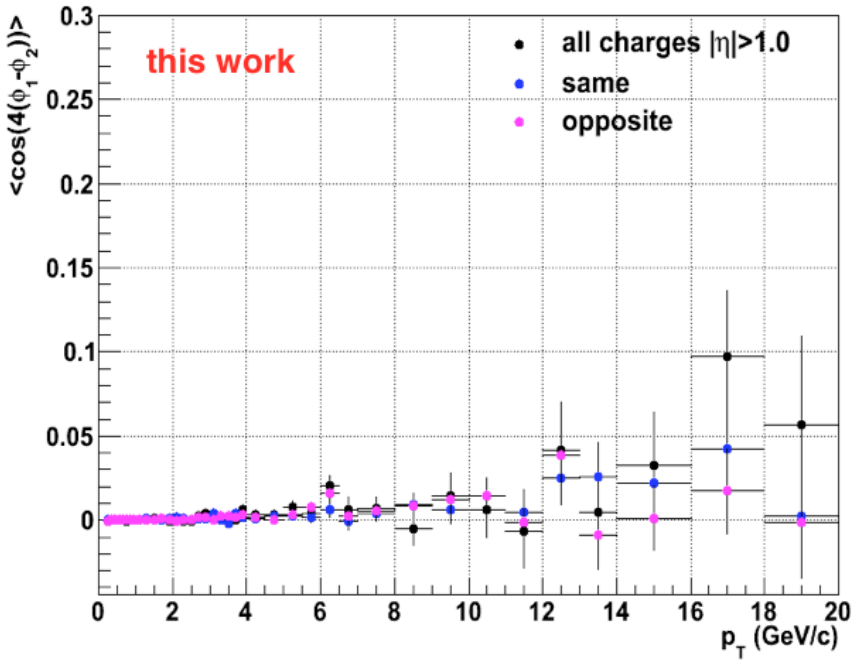

Figure 3.36: $\langle\cos(4(\varphi_1 - \varphi_2))\rangle$ for all charges (++,−−,+−,or −+), same charges (++ or −−), or opposite charges (+− or −+) for $|\Delta\eta| > 1.0$ for pp collisions at $\sqrt{s}_{NN}$ =7 TeV.

3.3.6.6 $\langle\cos(5(\varphi_1 - \varphi_2))\rangle$

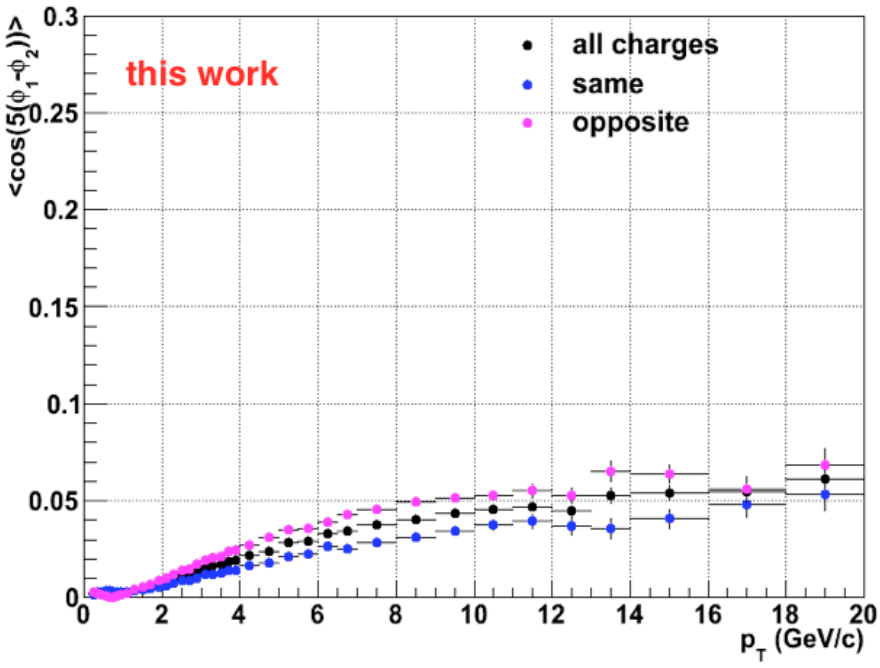

Figure 3.37: $\langle\cos(5(\varphi_1 - \varphi_2))\rangle$ for all charges (++,−−,+−,or −+), same charges (++ or −−), or opposite charges (+− or −+) for no $|\Delta\eta|$ separation for *pp* collisions at $\sqrt{s}_{NN}$ =7 TeV.

The effect of charge dependence correlations is the opposite charge correlations have a higher correlation which is more evident without the eta gaps, an effect due to resonance decays. The charge dependence of the non-flow *pp* correlations will be continued in the next section for further investigation.

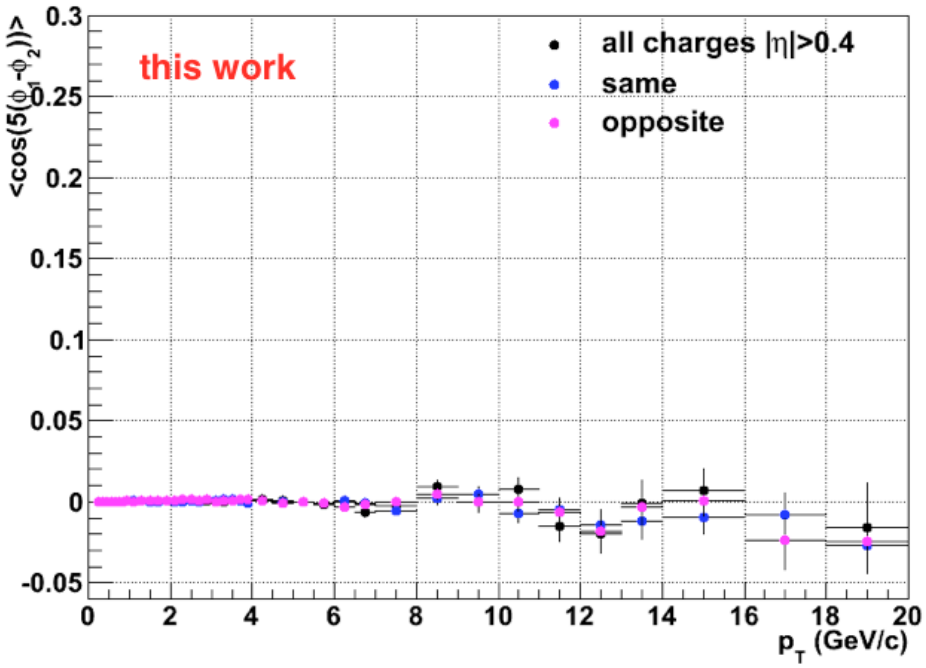

Figure 3.38: $\langle\cos(5(\varphi_1 - \varphi_2))\rangle$ for all charges (++,−−,+−,or −+), same charges (++ or −−), or opposite charges (+− or −+) for $|\Delta\eta| > 0.4$ for pp collisions at $\sqrt{s}_{NN}$ =7 TeV.

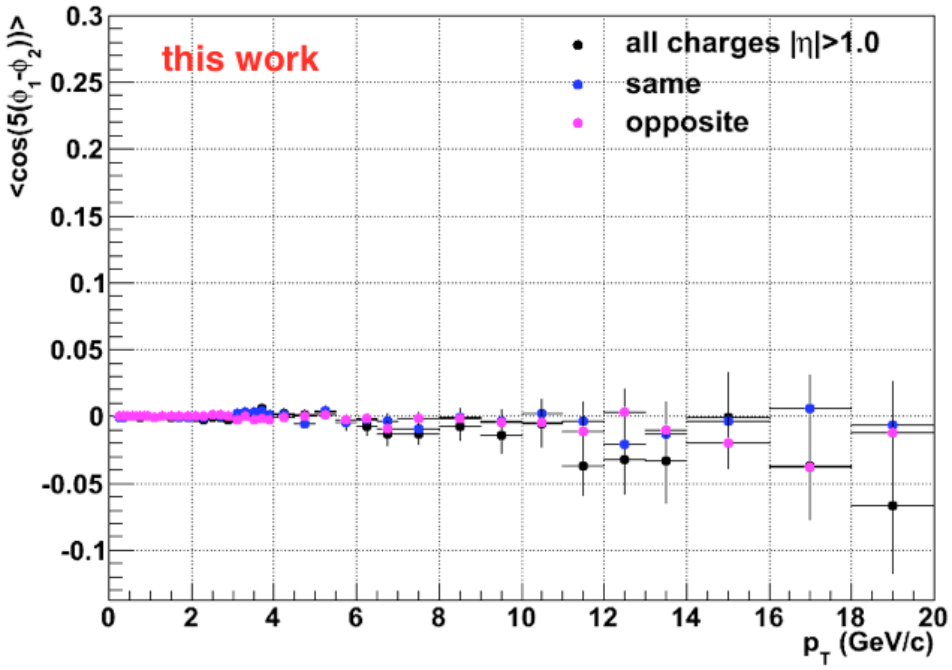

Figure 3.39: $\langle\cos(5(\varphi_1 - \varphi_2))\rangle$ for all charges (++,−−,+−,or −+), same charges (++ or −−), or opposite charges (+− or −+) for $|\Delta\eta| > 1.0$ for pp collisions at $\sqrt{s}_{NN}$ =7 TeV.

3.3.7 charge dependent 3-particle correlator in *pp* collisions

3.3.7.1 Motivation

Parity violation in strong interactions was first proposed by Kharzeev et al. in 1998 [87, 88]. When nuclei collide, there is a strong magnetic field present, and quark spins is aligned along the direction of the magnetic field. There is an imbalance of left-handed and right-handed quarks, generating an electromagnetic current. Few observables of CP- and P-symmetry related to flow studies [89, 90]. P- and CP-symmetry may indicate a larger than statistical difference of reaction planes constructed from different charges. For a symmetric collision, only one plane of symmetry should exist or else there is a P- or CP-violation. It was proposed by Kharzeev [91] that parity violation as a possibility of a preferred direction of particles or anti-particles into opposite sides of the reaction plane along the direction of angular momentum. The asymmetry with respect to the direction of angular momentum changes from event to event and can only be studied using correlation measurements since the average charge separation over many events is zero. This is due to fluctuations in the sign of the charge. The charge separation along the direction of the magnetic field, is called the Chiral Magnetic Effect (CME) [92], see Figure 3.40. The CME effect can only be observed for parity even observables using two and multi-particle correlations.

Local violation of parity symmetry can be described by adding sine terms to the following Fourier decomposition:

$$\frac{dN}{d\varphi_\alpha} \approx 1 + 2\sum_n [v_{n,\alpha}\cos(n(\varphi_\alpha - \Psi_{RP})) + a_{n,\alpha}\sin(n(\varphi_\alpha - \Psi_{RP}))], \tag{3.26}$$

where ϕ_α is the azimuthal angle of charged particle of type α. The azimuthal correlation between particles α and β is averaged over many events. The leading order coefficient $a_{1,\alpha}$ gives the magnitude of the effects of local parity violation, and $a_{n>1,\alpha}$

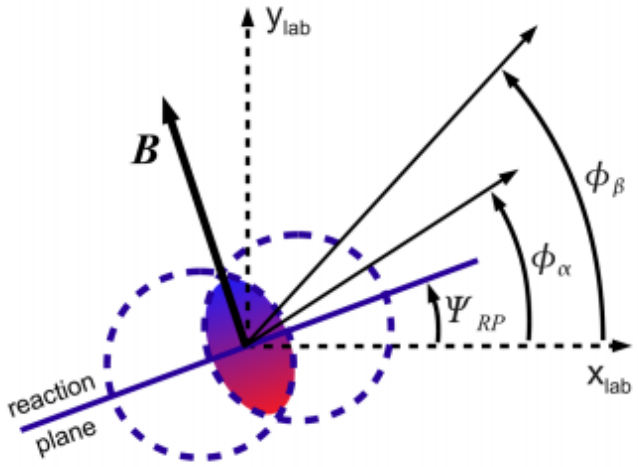

Figure 3.40: Schematic of the transverse plane in a heavy ion collision [94]

describes the shape. It was proposed in [93] that the following correlation is best to search for the CME because background particle production processes are expected to be suppressed with the decomposition,

$$\langle \cos(\phi_\alpha + \phi_\beta - 2\Psi_{RP})\rangle = \langle \cos(\phi_\alpha - \Psi_{RP})\cos(\phi_\beta - \Psi_{RP})\rangle - \langle \sin(\phi_\alpha - \Psi_{RP})\sin(\phi_\beta - \Psi_{RP})\rangle \tag{3.27}$$

In the above equation, $\langle \cos(\phi_\alpha - \Psi_{RP})\cos(\phi_\beta - \Psi_{RP})\rangle$ and $\langle \sin(\phi_\alpha - \Psi_{RP})\sin(\phi_\beta - \Psi_{RP})\rangle$ represent in-plane and out-of-plane correlations respectively. The above correlator is also sensitive to charge correlations from the CME effect .One can define the correlators as follows: $\langle a_+ a_+\rangle = \langle \cos(\phi_\alpha^+ + \phi_\beta^+ - 2\Psi_{RP})\rangle$, $\langle a_- a_-\rangle = \langle \cos(\phi_\alpha^- + \phi_\beta^- - 2\Psi_{RP})\rangle$, and $\langle a_+ a_-\rangle = \langle \cos(\phi_\alpha^+ + \phi_\beta^- - 2\Psi_{RP})\rangle$. The expected behavior is $\langle a_- a_-\rangle = \langle a_+ a_+\rangle = -\langle a_+ a_-\rangle > 0$ [94]. If the effect of final state interactions with the medium is included, a suppression is expected of particles traveling in opposite directions, $\langle a_+ a_+\rangle \gg |\langle a_+ a_-\rangle|$ [94].

3.3.8 $\langle\cos(\phi_\alpha + \phi_\beta - 2\Psi_{RP})\rangle$ in STAR

STAR has measured the centrality dependence of the correlation $\langle\cos(\phi_\alpha + \phi_\beta - 2\Psi_{RP})\rangle$ for both Cu+Cu and Au+Au collisions at $\sqrt{s}_{NN}$=200 GeV , see Figure 3.41. Open symbols represent Cu+Cu and closed symbols represent Au+Au. Blue line represent opposite sign correlation, and red represents same sign correlation. Same charge correlation is negative, while opposite charge correlation is positive. The magnitudes of both the same and opposite charge decrease with more central collisions (decreasing in percent centrality). This result agrees with the expectations of the CME [94]. The magnitude of the opposite charge correlation in Cu+Cu collisions is less suppressed than Au+Au, which can be due to a smaller medium in Cu+Cu collisions than in Au+Au collisions.

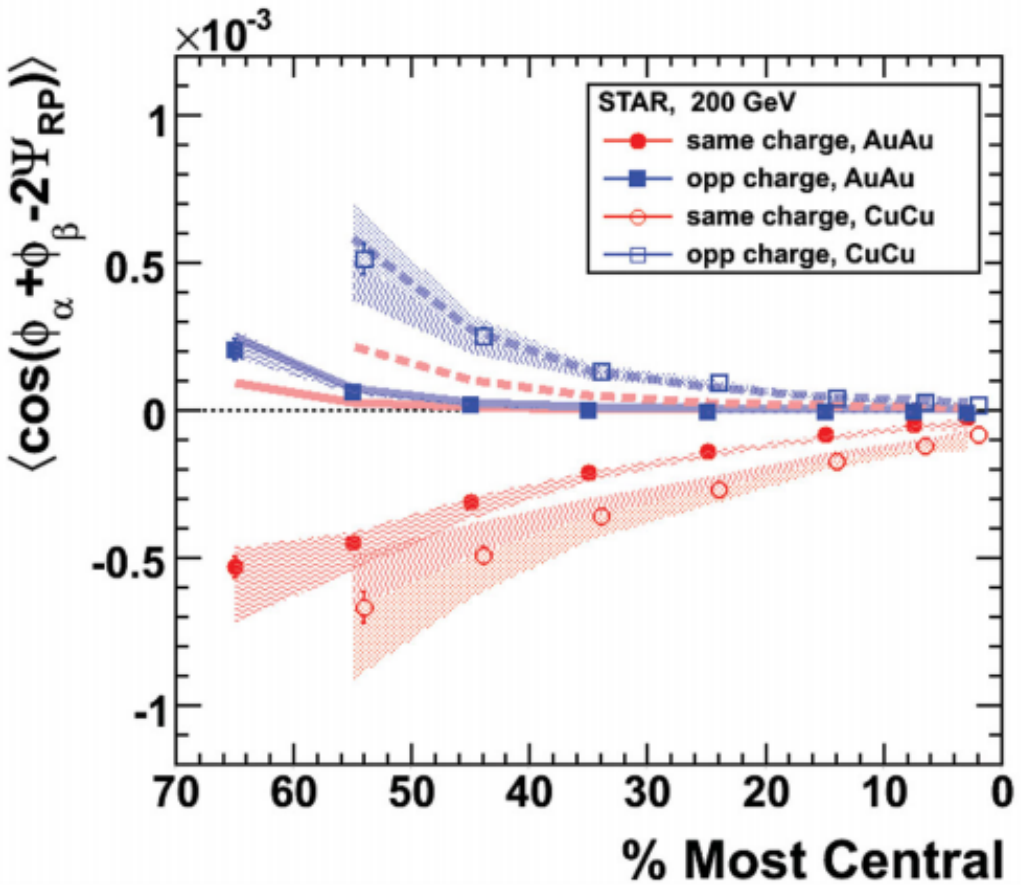

Figure 3.41: $\langle\cos(\phi_\alpha+\phi_\beta-2\Psi_{RP})\rangle$ measured by STAR at s_{NN}=200 GeV/c in Au-Au and Cu-Cu collisions [94]. Thick solid (Au+Au) lines and dashed solid (Cu+Cu) lines represent HIJING model expectations for the reaction plane independent background estimated by $\langle\cos(\phi_\alpha+\phi_\beta-2\varphi_\alpha)\rangle/v_2^{measured}$. The shaded bands represent the systematic errors. Blue line represent opposite sign correlation, and red represents same sign correlation. Open symbols represent Cu+Cu and closed symbols represent Au+Au.

3.3.9 $\langle\cos(\phi_\alpha + \phi_\beta - 2\Psi_{RP})\rangle$ in ALICE

The ALICE collaboration has also measured the $\langle\cos(\phi_\alpha + \phi_\beta - 2\Psi_{RP})\rangle$ and $\langle\cos(\phi_\alpha - \phi_\beta)\rangle$ in Pb-Pb at $\sqrt{s_{NN}}$ =2.76 TeV and compared to the STAR collaboration's Au-Au measurements. In Figure 3.42a, same charge pairs, $\pi^+\pi^+$ and $\pi^-\pi^-$, show a difference in correlation in comparison to opposite charge pairs, $\pi^-\pi^-$. This difference between correlations shows the charge dependence with respect to the reaction plane. In Figure 3.42b, $\langle\cos(\phi_\alpha - \phi_\beta)\rangle$ is shown which is P-even. The STAR collaboration shows negative behavior for same charges with a smaller magnitude than opposite sign, which has a stronger magnitude. ALICE, in comparison, shows positive correlation between same sign with a weaker magnitude than the opososite sign which shows a smaller magnitude than opposite charge. In Figure 3.42c, $\langle\cos(\phi_\alpha - \Psi_{RP})\cos(\phi_\beta - \Psi_{RP})\rangle$ and $\langle\sin(\phi_\alpha - \Psi_{RP})\sin(\phi_\beta - \Psi_{RP})\rangle$ is shown, where $\langle\sin(\phi_\alpha - \Psi_{RP})\sin(\phi_\beta - \Psi_{RP})\rangle$ is larger than $\langle\cos(\phi_\alpha - \Psi_{RP})\cos(\phi_\beta - \Psi_{RP})\rangle$ for pairs of same charge, and are of very close for opposite charge except for peripheral collisions.

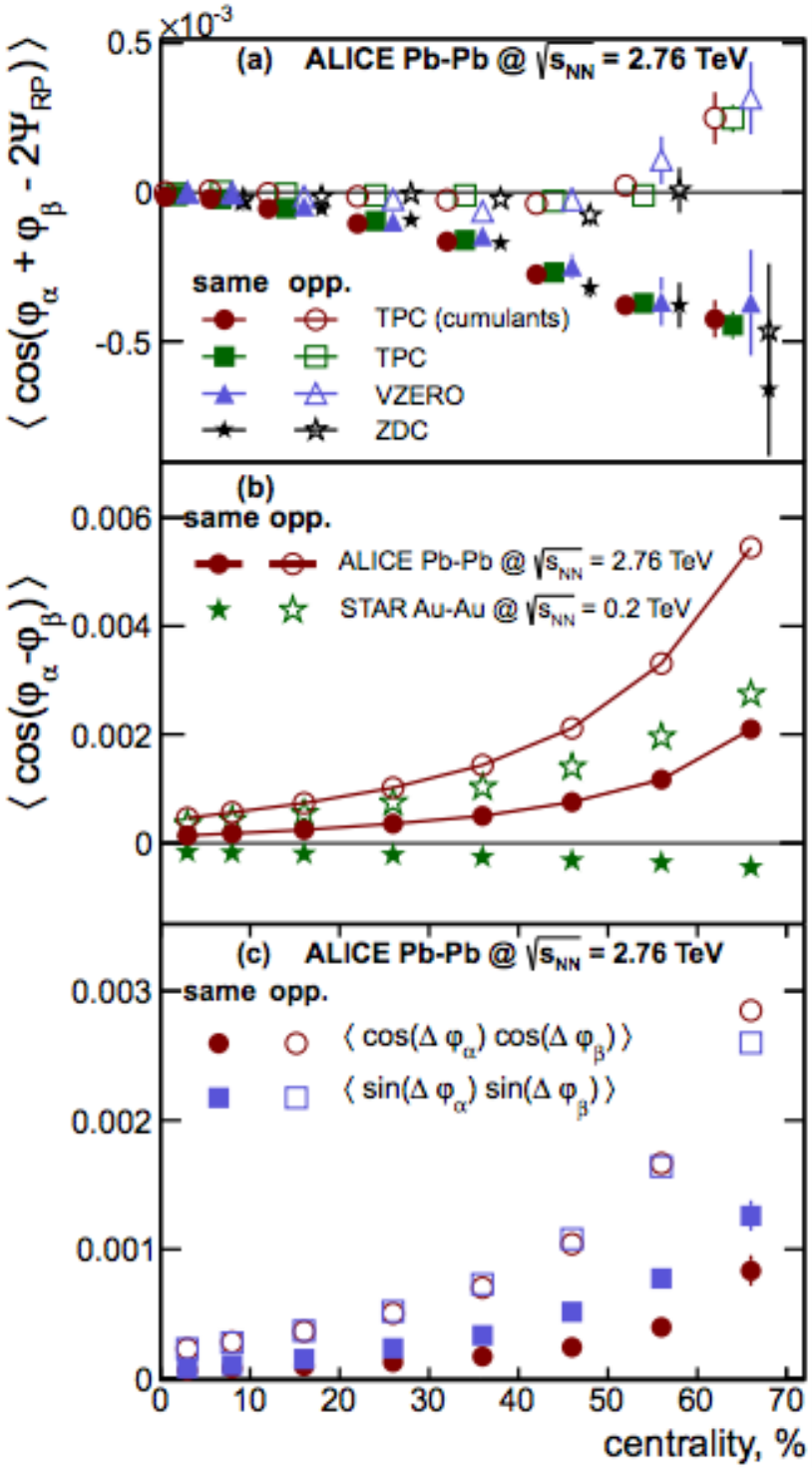

Figure 3.42: $\langle\cos(\phi_\alpha+\phi_\beta-2\Psi_{RP})\rangle$ measured by STAR at s_{NN}=200 GeV/c in Au-Au and ALICE in Pb-Pb at s_{NN}=2.76 TeV

3.3.10 $\langle\cos(\phi_\alpha + \phi_\beta - 2\Psi_{RP})\rangle$ in ALICE with pp data at $\sqrt{s}_{NN} = 7$ TeV

In this work, in order to understand the non-flow contribution to $\langle\cos(\phi_\alpha + \phi_\beta - 2\Psi_{RP})\rangle$, protons are used with same and opposite charge as a function of multiplicity. TPC tracks are also used for the (α and β particles) along with the event plane (Ψ_{RP}) estimated using the VZERO, in this manner auto-correlation is reduced, the correlation of particles with themselves.

3.3.10.1 Data Selection

The analysis details are as follows: 5 million pp min-bias events from proton data at 7 TeV. The event and track cuts are listed in the following table:

Table 3.3: Analysis Details of pp data at $\sqrt{s}NN = 7$ TeV

Event cuts	Value
$\lvert vertex\rvert_z$	< 10 cm
Track cuts	Value
$\lvert\eta\rvert$	< 0.8
p_T	> 0.2 GeV/c
$N_{clusters}$	> 70
$\lvert dca\rvert_{xy}$	< 2.4 cm
$\lvert dca\rvert_z$	< 3.0 cm

In $\langle\cos(\varphi_\alpha + \varphi_\beta - 2\Psi_{RP})\rangle$, φ_α and φ_β are the angles of the TPC tracks, and Ψ_{RP} is the event plane from the VZERO detector. For two particles of the same sign,

3.3.10.2 Definitions

$$\langle\cos(\varphi_\alpha^\pm + \varphi_\beta^\pm - 2\Psi_{RP})\rangle =$$

$$= \frac{1}{M_\pm(M_\pm+1)} \left[\begin{array}{c} \sum\limits_{n=1} \cos(\varphi_i^\pm)\cos(\varphi_i^\pm)\cos(2\Psi_{EP}) - \sum\limits_{n=1} \sin(\varphi_i^\pm)\sin(\varphi_i^\pm)\cos(2\Psi_{EP}) \\ + \sum\limits_{n=1} \cos(\varphi_i^\pm)\sin(\varphi_i^\pm)\sin(2\Psi_{EP}) + \sum\limits_{n=1} \sin(\varphi_i^\pm)\cos(\varphi_i^\pm)\sin(2\Psi_{EP}) \\ -\langle \sum\limits_{n=1} \cos(2\varphi_i^\pm)\cos(2\Psi_{EP}) + \sum\limits_{n=1} \sin(2\varphi_i^\pm)\cos(2\Psi_{EP})\rangle \end{array} \right] \tag{3.28}$$

If the tracks are of the opposite sign:

$$\langle\cos(\varphi_\alpha^+ + \varphi_\beta^- - 2\Psi_{RP})\rangle =$$

$$= \frac{1}{M_+M_-} \left[\begin{array}{c} \sum\limits_{n=1} \cos(\varphi_i^+)\cos(\varphi_i^-)\cos(2\Psi_{EP}) - \sum\limits_{n=1} \sin(\varphi_i^+)\sin(\varphi_i^-)\cos(2\Psi_{EP}) \\ + \sum\limits_{n=1} \cos(\varphi_i^+)\sin(\varphi_i^-)\sin(2\Psi_{EP}) + \sum\limits_{n=1} \sin(\varphi_i^+)\cos(\varphi_i^-)\sin(2\Psi_{EP}) \end{array} \right] \tag{3.29}$$

The $\left\langle\cos(2(\varphi_\alpha^\pm + \varphi_\beta^\pm - 2\Psi_{EP}))\right\rangle$ and $\left\langle\cos(2(\varphi_\alpha^+ + \varphi_\beta^- - 2\Psi_{EP}))\right\rangle$ need to be corrected for event plane resolution [42]. The following correlator $\langle\cos(2(\Psi_{TPC} - \Psi_{VZERO}))\rangle$ is used for the correction:

$$\langle\cos(2(\Psi_{TPC} - \Psi_{VZERO}))\rangle = \sqrt{\frac{\langle\cos[n(\Psi_{TPC} - \Psi_{V0A})]\rangle \langle\cos[n(\Psi_{TPC} - \Psi_{V0C})]\rangle}{\langle\cos[n(\Psi_{V0A} - \Psi_{V0C})]\rangle}} \tag{3.30}$$

where Ψ_{V0A} and Ψ_{V0C} are the event plane angles from the VZERO detector arrays and Ψ_{TPC} is the angle from the TPC. The correlation between the TPC and VZERO detector versus multiplicity is seen in Figure 3.43. For multiplicity less than 30, there is little difference between correlators, however the statistical errors are large.

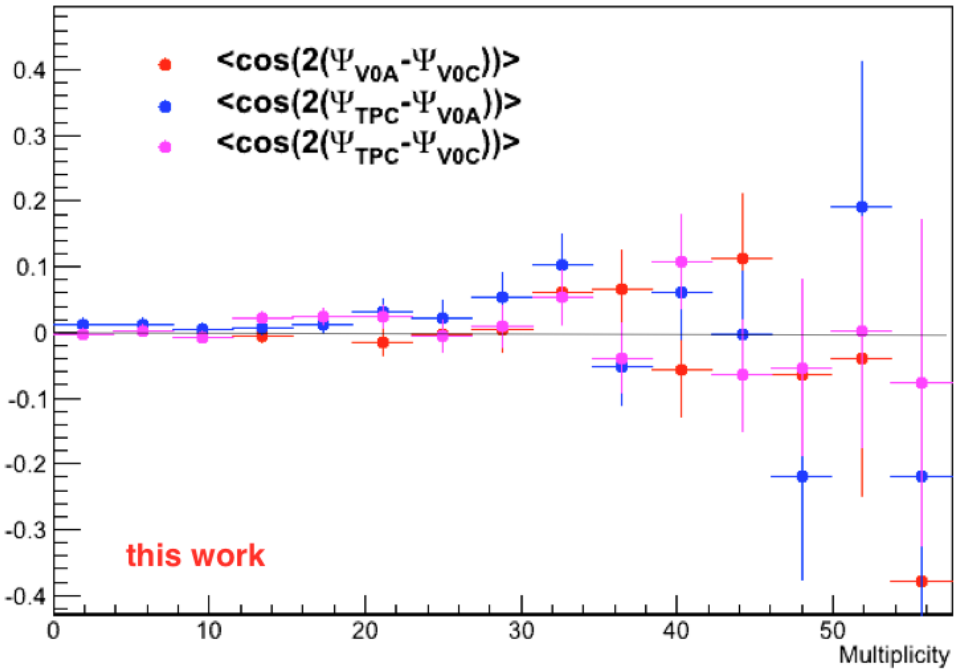

Figure 3.43: $\langle\cos(2(\Psi_{TPC} - \Psi_{V0A}))\rangle$,$\langle\cos(2(\Psi_{TPC} - \Psi_{V0C}))\rangle$, and $\langle\cos(2(\Psi_{V0A} - \Psi_{V0C}))\rangle$ used for the event plane resolution between the TPC and VZERO detector

3.3.10.3 Results

The charge dependent azimuthal correlations in *pp* data are shown in Figures 3.44-3.45 for same sign, and Figure 3.46 for opposite charges. Both same sign and opposite sign correlators show little dependence on multiplicity, as it is shown that the magnitude is a constant non-zero vale for multiplicity less than 40. The average values of each correlator can be seen in Table 3.4.

Figure 3.44: $\left\langle \cos(2(\varphi_\alpha^+ + \varphi_\beta^+)) - 2\Psi_{EP} \right\rangle$ versus multiplicity for *pp* data at $\sqrt{s_{NN}}$=7 TeV. A straight line fit is used to obtain the average value.

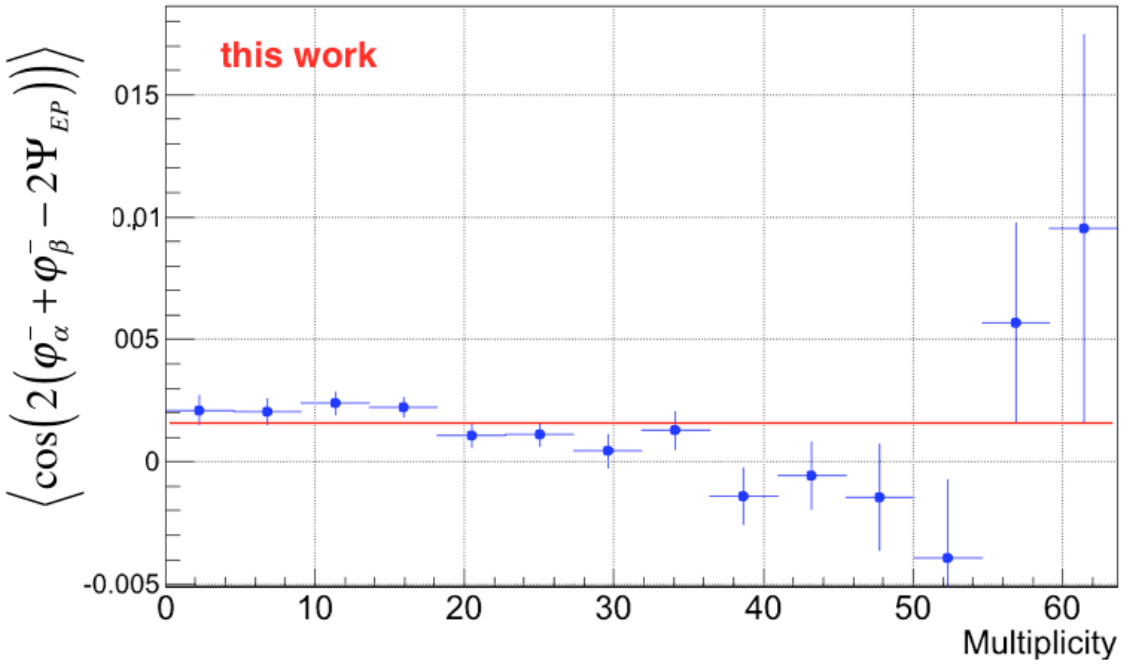

Figure 3.45: $\left\langle \cos(2(\varphi_\alpha^- + \varphi_\beta^-)) - 2\Psi_{EP} \right\rangle$ versus multiplicity for pp data at $\sqrt{s_{NN}}$=7 TeV. A straight line fit is used to obtain the average value.

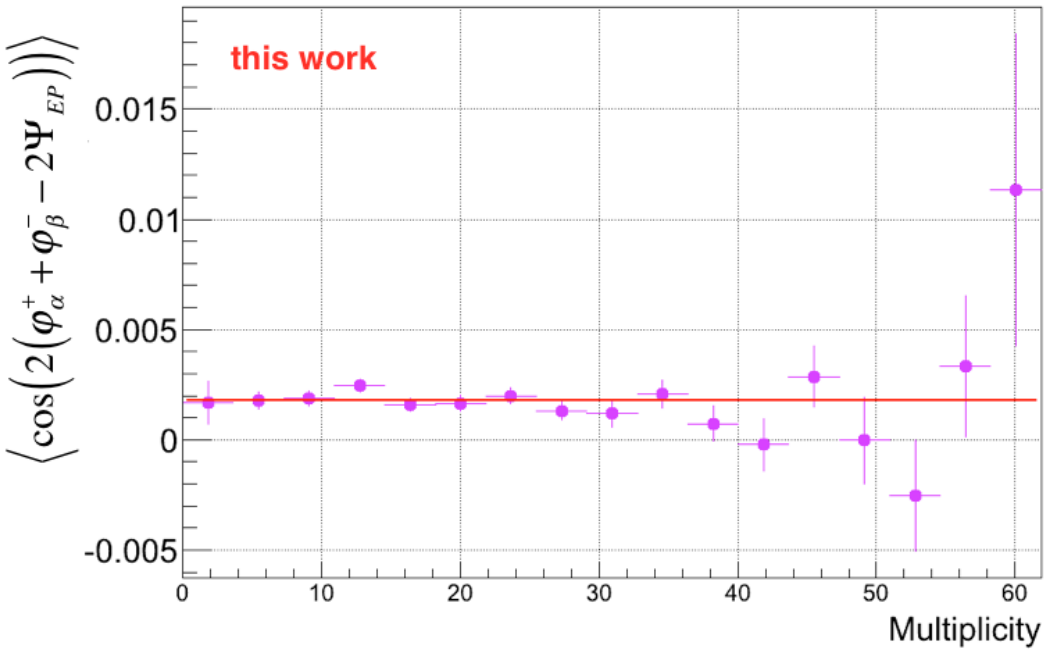

Figure 3.46: $\left\langle \cos(2(\varphi_\alpha^+ + \varphi_\beta^-)) - 2\Psi_{EP} \right\rangle$ versus multiplicity for pp data at $\sqrt{s_{NN}}$=7 TeV. A straight line fit is used to obtain the average value.

Table 3.4: Three particle charge dependent correlation averages

	Average
$\langle\cos(2(\varphi_\alpha^+ + \varphi_\beta^+ - 2\Psi_{EP}))\rangle$	0.00243
$\langle\cos(2(\varphi_\alpha^- + \varphi_\beta^- - 2\Psi_{EP}))\rangle$	0.000169
$\langle\cos(2(\varphi_\alpha^+ + \varphi_\beta^- - 2\Psi_{EP}))\rangle$	0.00181

The three particle correlation results from proton-proton data at $\sqrt{s}_{NN} = 7$ TeV need to be interpolated to $\sqrt{s_{NN}} = 2.76$ TeV, to match the energy of the Pb-Pb data, see Figure 3.47.

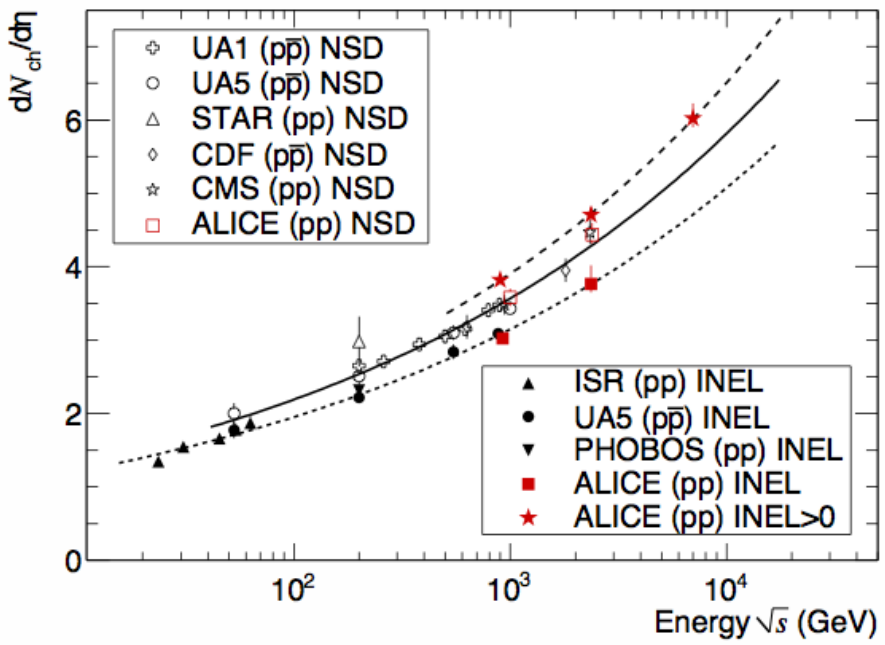

Figure 3.47: The charged-particle pseudo-rapidity density in the central pseudo-rapidity region $|\eta| < 0.5$ [96]

A power law fit is used:

$$\left\langle \frac{dN}{d\eta} \right\rangle \Big|_{s=0} = a(\sqrt{s})^b, \tag{3.31}$$

where a=0.7166, and b=0.2171. The change in energy from $\sqrt{s}_{NN}$ =7 TeV to $\sqrt{s}_{NN}$ =2.76 TeV is:

$$\left\langle \frac{dN}{d\eta} \right\rangle \Big|_{s=0}^{\sqrt{s}=2.76\ TeV} \Big/ \left\langle \frac{dN}{d\eta} \right\rangle \Big|_{s=0}^{\sqrt{s}=7\ TeV} = \frac{4.00}{4.89} = 0.82, \tag{3.32}$$

In order to correct the Pb-Pb correlators, all *pp* correlators are scaled with the multiplicity of Pb-Pb to estimate the correction for each centrality bin:

$$\left\langle \cos(2(\varphi_\alpha^\pm + \varphi_\beta^\pm - 2\Psi_{EP})) \right\rangle_{correction} = \langle \cos(2(\varphi_\alpha + \varphi_\beta - 2\Psi_{EP})) \rangle \left[\frac{M^{pp}_{\sqrt{s_{NN}}=7\ TeV} 0.82}{M^{Pb-Pb}_{\sqrt{s_{NN}}=2.76\ TeV}} \right]^2 \tag{3.33}$$

The multiplicity of each centrality bin in Pb-Pb and for *pp* at $\sqrt{s}_{NN}$ =7 TeV is listed in Table 3.5.

Table 3.5: Average Multiplicities for *pp* and Pb-Pb collisions

collision type	centrality	$\langle M \rangle$
Pb-Pb $\sqrt{s}_{NN}$ =2.76 TeV	0-5%	2165
	5-10%	1770
	10-20%	1330
	20-30%	893
	30-40%	577
	40-50%	353
	50-60%	202
	60-70%	104
	70-80%	48
	80-90%	19
	90-100%	9
pp $\sqrt{s}_{NN}$ =7 TeV		7

The *pp* correlators versus centrality are scaled using Equation 3.33, see Figure 3.48. There is a general increase of each correlator versus centrality as the collisions become more peripheral. For each centrality bin there is little difference between $(-,-)$ and $(+,-)$ correlators, and $(+,+)$ is higher in all centrality bins.

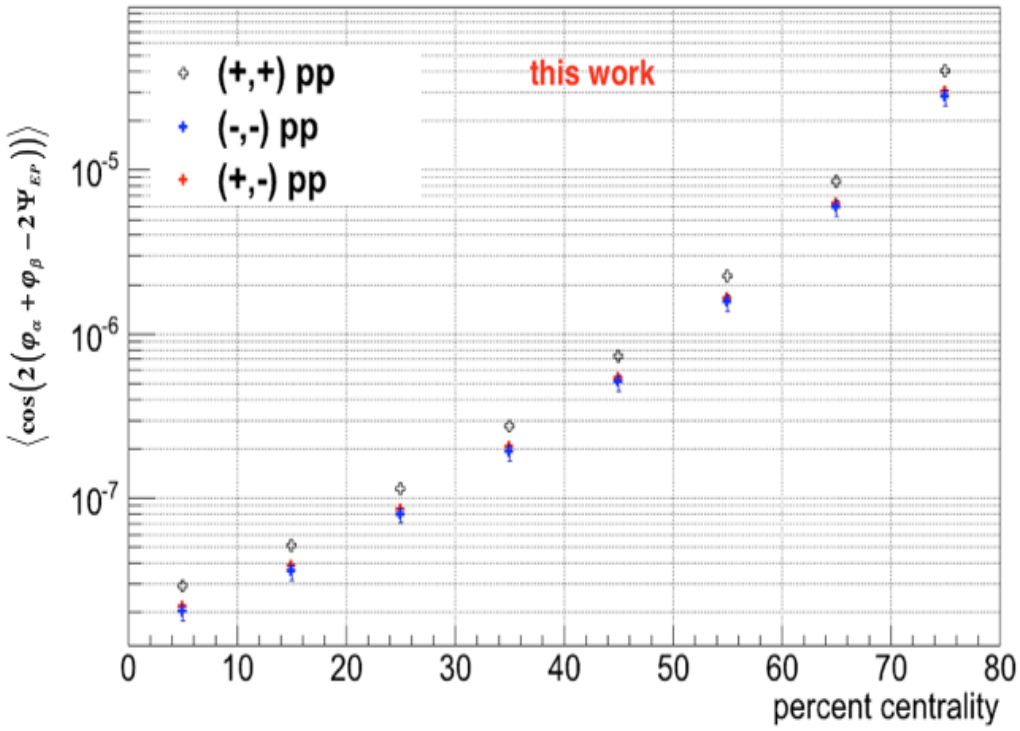

Figure 3.48: The *pp* correlators for same and opposite sign are scaled with the average multiplicities from each Pb-Pb centrality bin. $(+,+)$ represents $(\varphi_\alpha^+, \varphi_\beta^+)$, $(-,-)$ represents $(\varphi_\alpha^-, \varphi_\beta^-)$, and $(+,-)$ represents $(\varphi_\alpha^+, \varphi_\beta^-)$.

The charge dependent correlator $\langle\cos(2(\varphi_\alpha + \varphi_\beta - 2\Psi_{EP}))\rangle$ for Pb-Pb collisions at $\sqrt{s}_{NN}$ =2.76 TeV are shown in Figure 3.49 calculated by Yasuto Hori [97]-[98]. The opposite sign correlator is positive and the same sign correlator is negative showing clear charge dependence. The *pp* correction is shown along with the Pb-Pb results, see Figure 3.50, and is scaled with the multiplicity of the Pb-Pb correlators, Eq. 3.33.

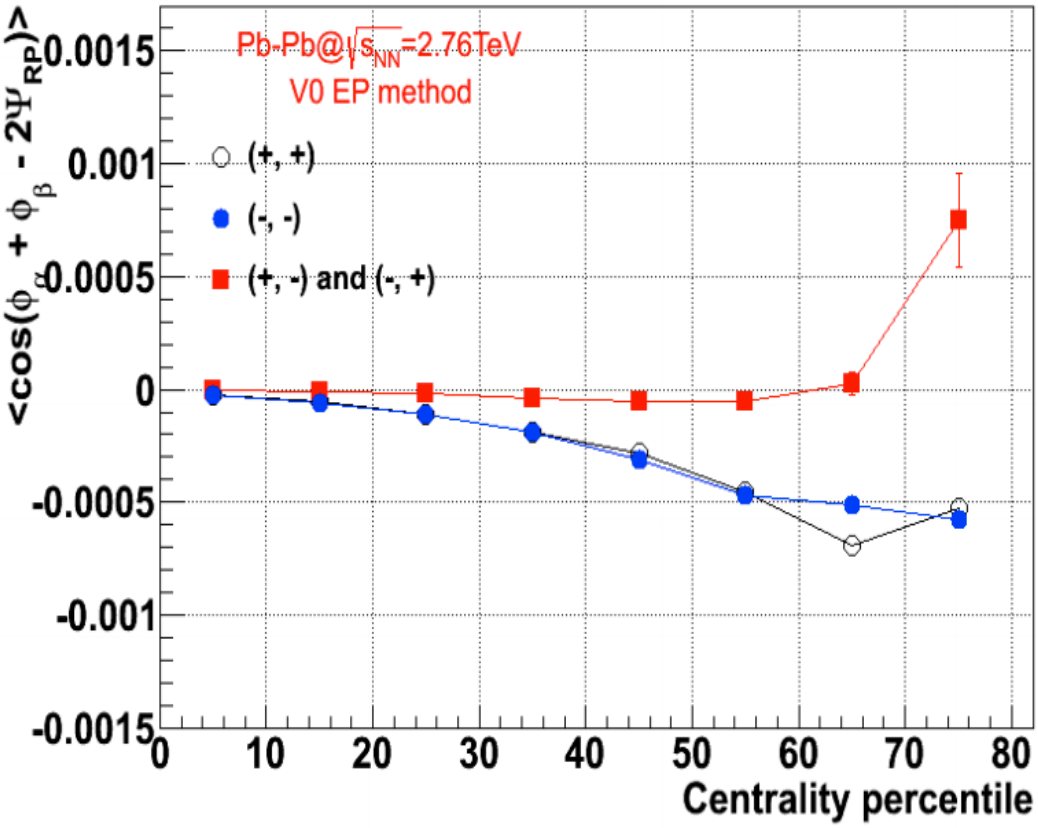

Figure 3.49: The charge dependent correlator $\langle\cos(2(\varphi_\alpha + \varphi_\beta + 2\Phi_{EP}))\rangle$ is shown for Pb-Pb collisions at $\sqrt{s}_{NN}$ =2.76 TeV calculated by Yasuto Hori [97]-[98]. $(+,+)$ represents $(\varphi_\alpha^+, \varphi_\beta^+)$, $(-,-)$ represents $(\varphi_\alpha^-, \varphi_\beta^-)$, and $(+,-)$ represents $(\varphi_\alpha^+, \varphi_\beta^-)$.

The $\langle\cos(2(\varphi_\alpha + \varphi_\beta + 2\Phi_{EP}))\rangle$ using *pp* data is directly compared to the Pb-Pb data, assuming that the *pp* data is the non-flow estimate. The *pp* data does not contribute to the Pb-Pb correlator except at peripheral bins (70-80%).

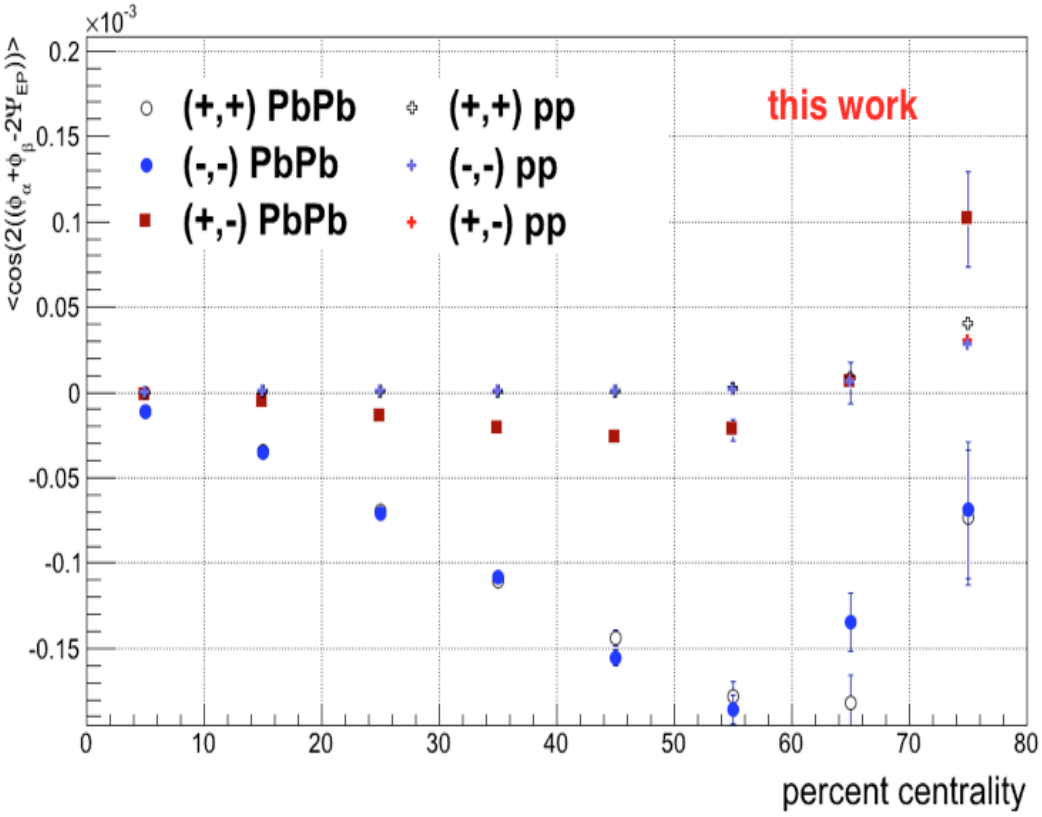

Figure 3.50:
The charge dependent correlator $\langle\cos(2(\varphi_\alpha + \varphi_\beta + 2\Phi_{EP}))\rangle$ is shown for both Pb-Pb collisions at $\sqrt{s}_{NN}$ =2.76 TeV calculated by Yasuto Hori [97]-[98] and *pp* collisions at $\sqrt{s}_{NN}$ =7 TeV. $(+,+)$ represents $(\varphi_\alpha^+, \varphi_\beta^+)$, $(-,-)$ represents $(\varphi_\alpha^-, \varphi_\beta^-)$, and $(+,-)$ represents $(\varphi_\alpha^+, \varphi_\beta^-)$.

3.4 Conclusion

In summary, both two particle correlations are studied in Pb-Pb and *pp* data. The non-flow component of flow with *pp* data has been estimated using the $v_n\{2\}\{\text{uQ,AA-pp}\}$ and compared with $v_n\{2\}\{\text{SP,AA-pp}\}$, and also the charge dependence for flow coefficients v_1 through v_5. According to the results in Figures 3.4-3.8, even harmonic numbers estimates ($\langle u_2 Q_2^* \rangle^{pp}$,$\langle u_4 Q_4^* \rangle^{pp}$) have the higher magnitude than the odd harmonic numbers ($\langle u_3 Q_3^* \rangle^{pp}$,$\langle u_5 Q_5^* \rangle^{pp}$). In examining the charge dependence in Figures **??-??** opposite charges have a higher magnitude then same charges for the non-flow estimates. The CME effect for three particle correlation in *pp* data has also been investigated and compared to Pb-Pb correlators $\left\langle \cos(2(\varphi_\alpha^\pm + \varphi_\beta^\pm - 2\Psi_{EP})) \right\rangle$ for same and opposite charge. The non-flow correction to the correlator is found to be negligible except for in peripheral collisions.

Chapter 4

Femtoscopy

4.1 Motivation

Correlation femtoscopy (intensity interferometry) is a direct method to measure small spatial scales, around 10^{-15} m, and temporal scales, around 10^{-23} sec in particle and heavy ion collisions. It is based on Fermi-Dirac or Bose-Einstein quantum statisitcs [99]-[102], and in many respects is similar to the intensity interferometry by Hanbury-Brown and Twiss (HBT), proposed to measure the angular size of stars [103]. In femtoscopy measurements, the correlation function is used, a ratio of two and single particle momentum spectra, to obtain information on the source of emitted particles. From the fitted correlation functions, the radii are extracted which is interpreted as the geometrical size of system. Since heavy ion collisions are inhomogeneous [104], the entire source cannot be measured, only a certain region, called the homogeneity region, from which particles of a similar momentum are emitted. An angular reference to the collisions is used to obtain the azimuthal angle of the emitted particles with respect to the reaction plane. In this manner, the final spatial eccentricity of source of emitted particles at freeze-out is obtained [44, 105]. The measurements of azimuthally differential pion femtoscopy will be described and compare to previous measurements and theoretical models.

4.2 Theoretical Background

Identical particle correlations in heavy ion correlations are used as a means of extracting the space-time information about the emission region. The two-particle correlation function is composed of the ratio of two particle to a product of single particle spectra. The following section will discuss this approach in detail.

4.2.1 Correlation Function

The two particle correlation function [44] is defined as:

$$C(\vec{p_1}, \vec{p_2}) = A\frac{P_2(\vec{p_1}, \vec{p_2})}{P_1(\vec{p_1})P_1(\vec{p_2})}, \tag{4.1}$$

where A is the normalization factor, $P_1(\vec{p})$ is a single particle spectrum and $P_2(\vec{p_1}, \vec{p_2})$ is a two-particle spectrum. We now describe the correlation function in terms of a source function $S(x, p)$,the probability of creating a particle with momentum p at space-time point x of a single particle spectra is given as:

$$P_1(\vec{p}) = \int d^4x S(x, p). \tag{4.2}$$

If the source emits two identical particles from positions x_1 and x_2, with momenta p_1 and p_2 that are measured at positions x_1' and x_2', the pair wave function is given by [44, 45] :

$$\Psi(x_1, x_1', x_2, x_2', p_1, p_2; t) = \frac{1}{\sqrt{2}}[e^{i(x_1'-x_1)p_1}e^{i(x_2'-x_2)p_2} \pm e^{-i(x_1'-x_2)p_1}e^{-i(x_2'-x_1)p_2}] \tag{4.3}$$

The pair wave function must be anti-symmetric for fermions and symmetric for bosons since identical particles are indistinguishable. The probability of measuring

the particle pair is:

$$P_2(\vec{p_1},\vec{p_2}) = \int d^4x_1 d^4x_2 S(x_1,p_1)S(x_2,p_2)\left|\Psi(x_1,x_1',x_2,x_2',p_1,p_2;t)\right|^2 \tag{4.4}$$

The wave function squared is:

$$\begin{aligned}\left|\Psi(x_1,x_1',x_2,x_2',p_1,p_2;t)\right|^2 &= \frac{1}{2}\left[e^{-i(x_1'-x_1)p_1}e^{-i(x_2'-x_2)p_2} + e^{-i(x_1'-x_2)p_1}e^{-i(x_2'-x_1)p_2}\right] \\ &\quad\cdot\left[e^{i(x_1'-x_1)p_1}e^{i(x_2'-x_2)p_2} + e^{i(x_1'-x_2)p_1}e^{i(x_2'-x_1)p_2}\right] \\ &= \frac{1}{2}\left[2 + e^{-i(p_1x_1-p_1x_2-p_2x_1+p_2x_2)} + e^{i(p_1x_1-p_1x_2-p_2x_1+p_2x_2)}\right] \\ &= \left[1+\cos(p_1-p_2)(x_1-x_2)\right] = 1+\cos(q\cdot r)\end{aligned} \tag{4.5}$$

where $q = p_1 - p_2$ and $r = x_1 - x_2$.

Then, the correlation function can be written as following:

$$\begin{aligned}C(\vec{q},\vec{k}) &= \frac{\int d^4x_1 d^4x_2 S(x_1,p_1)S(x_2,p_2)\left|\Psi(x_1,x_1',x_2,x_2',p_1,p_2;t)\right|^2}{\int d^4x_1 S(x_1,p_1)\int d^4x_2 S(x_2,p_2)} \\ &\approx 1 + \frac{|d^4x S(x,k)e^{iqx}|^2}{|\int d^4x S(x,k)|^2} = 1+|\tilde{s}(q)|^2\end{aligned} \tag{4.6}$$

where $\tilde{s}(q)$ is the Fourier transform of the normalized source function $S(x,k)$.

The mass-shell constraint implies that only three of the four relative momentum components are independent.

$$\begin{aligned}k\cdot q = p_1^2 - p_2^2 = m_1^2 - m_2^2 = 0 \\ q^0 = \frac{\vec{k}}{k^0}\cdot\vec{q} = \vec{\beta}\vec{q}\end{aligned} \tag{4.7}$$

where m_i is the particle mass, $\vec{k}$ is the average momentum of the pair, defined as $k = (p_1+p_2)/2$, $\vec{q}$ is the momentum difference of the pair, $\vec{\beta}$ is the pair velocity, q^0 is the zeroth component of the pair momentum difference, and k^0 is the zeroth component of the pair average momentum.

4.2.2 Coordinate System

In this analysis, the longitudinally co-moving system (LCMS) is used, which is a coordinate frame moving along the longitudinal (beam) direction such that the total momentum of the pair along the z axis is zero [44]. The coordinate system is defined in the following manner: *Long*, is the direction parallel to the beam, *out* is the direction parallel to the transverse momentum of the pair, and *side* is perpendicular to the other two axes, see Fig. 4.1.

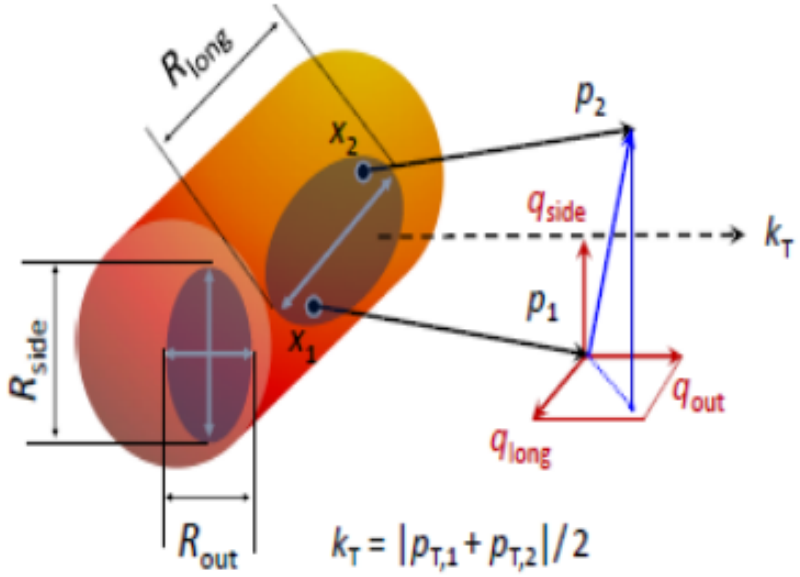

Figure 4.1: The Longitudinally Co-Moving System (LCMS) frame

The out-side-long components of any four vector V can be obtained using the four-momentum of the particle P.

$$\begin{aligned} V_{long} &= \frac{(P_0 V_z - P_z V_0)}{M_T} \\ V_{out} &= \frac{(P_x V_x + P_y V_y)}{P_T} \\ V_{side} &= \frac{(P_x V_x - P_y V_y)}{P_T} \end{aligned} \tag{4.8}$$

where ${P_T}^2 = {P_x}^2 + {P_y}^2$, and ${M_T}^2 = {P_0}^2 - {P_z}^2$

4.2.3 Gaussian Parameterization

To compute the correlation function $C(\vec{q}, \vec{k})$, Eq. 4.6, the source function $S(x, k)$ is often approximated by a Gaussian. The space-time point $\bar{x}$ is a point corresponding to the maximum probability of emiting a pair particle with momentum k [106]. The approximation of $S(x, k)$ at $\bar{x}$ is:

$$S(x,k) \approx N(k) S(\bar{x}(k), k) \exp\left[-\frac{1}{2}\tilde{x}^{\mu}(k) B_{\mu\nu}(k) \tilde{x}^{\nu}(k)\right], \tag{4.9}$$

where

$$\bar{x}^{\mu}(k) = \langle x \rangle, \tilde{x}^{\mu}(k) = x^{\mu} - \bar{x}^{\mu}(k), \ (B^{-1})_{\mu\nu}(k) = \langle \tilde{x}_{\mu} \tilde{x}_{\nu} \rangle. \tag{4.10}$$

and $(B^{-1})_{\mu\nu}(k)$ is the symmetric spatial correlation tensor. The expectation values are defined as space-time averages over the source function:

$$\langle f(x) \rangle = \frac{\int d^4x f(x) S(x,k)}{\int d^4x S(x,k)} \tag{4.11}$$

The two-particle correlation function is [104]:

$$C(\bar{k}, \bar{q}) = 1 + exp[-q^{\mu} q^{\nu} \langle \tilde{x}_{\mu} \tilde{x}_{\nu} \rangle (\bar{k})]. \tag{4.12}$$

$(B^{-1})_{\mu\nu}(k)$ has 10 independent parameters, however, due to the mass-shell constraint, this reduces to 6 parameters, the *radii*.

The Cartesian parameterization of the HBT radii are obtained by eliminating q^0 from the previous equation:

$$C(\bar{k}, \bar{q}) = 1 + exp\left[-\sum_{i,j=o,s,l} R^2_{i,j}(k) q_i q_j\right]. \tag{4.13}$$

The HBT radii are given by the covariances:

$$R^2_{i,j} = \langle(\tilde{x}_i - \beta_i\tilde{t})(\tilde{x}_i - \beta_i\tilde{t})\rangle \tag{4.14}$$

The out, side, and long radii are:

$$\begin{aligned} R^2_o &= \langle(\tilde{x}_i - \beta_T\tilde{t})^2\rangle \\ R^2_s &= \langle\tilde{y}^2\rangle \\ R^2_l &= \langle(\tilde{z}_i - \beta_L\tilde{t})^2\rangle \end{aligned} \tag{4.15}$$

β_T is the transverse pair velocity, and β_L is the pair longitudinal velocity. The radii R_o and R_l contain have a mixture of spatial and temporal information on whileR_s only has spatial dependence [106].

4.3 Experimental Techniques

The experimental correlation function for a given pair momentum $\vec{k}$ and relative momentum $\vec{q}$ is calculated as:

$$C(\vec{q},\vec{k}) = \frac{A(\vec{q},\vec{k})}{B(\vec{q},\vec{k})} \cdot \xi(\vec{q},\vec{k}), \tag{4.16}$$

where the numerator $A(\vec{q},\vec{k})$, is often called the signal, and the denominator $B(\vec{q},\vec{k})$, is the background. A correction factor $\xi(\vec{q},\vec{k})$ accounts for all the non-femtoscopic correlations present in the signal.

The signal is the momentum pair distribution selected from pairs of particles from the same event constructing the signal. The following criteria need to be considered: 1) event cuts and event binning; 2) single track cuts and single particle binning; and 3) two-track, or pair cuts and pair binning. The background is the momentum pair distribution of pairs of particles creating using the event-mixing technique, where a

particle from a given event is correlated with another particle from a previous event. The background must have the same cuts as the signal in order to avoid artificial structures in the correlation function.

4.3.1 Coulomb Wave Function

Coulomb interactions can distort correlations between charged particles The two-particle Coulomb wave function is [107] :

$$\psi_C = \Gamma(1+i\eta)e^{-\frac{1}{2}\pi\eta}e^{i\vec{q}\vec{r}}\left[1+\sum_{n=1}^{\infty}h_n\left(\frac{r}{a_0}\right)^n\right] \tag{4.17}$$

where $\eta = \mu e^2/\hbar q$, μ is the reduced mass, e is the elementary charge, a_0 is the two-pion Bohr radius, $h_1 = 1$, and $h_n = \frac{n-1-i\eta}{-in\eta}h_{n-1}$. When taking the limit from $r \to 0$, the squared wave function becomes the Gamow Factor:

$$G(\eta) = e^{-\pi\eta}|\Gamma(1+i\eta)|^2 = \frac{2\pi\eta}{e^{2\pi\eta}-1}. \tag{4.18}$$

The Gamow factor overestimates the Coulomb effect due to the $r \to 0$ approximation. It is assumed that the source is small, yet in heavy-ion collisions this may not be valid. The Gamow factor has been replaced by a calculation of a squared unsymmeterized Coulomb wave for a finite Gaussian source. More details of the Coulomb correction is described in section 4.7.6.2.

4.3.2 Log-Likelihood Fitting

Under the assumption of Gaussian source, the correlation function can be parameterized as:

$$G(q) = 1 + \exp(-R_o^2 q_o^2 - R_s^2 q_s^2 - R_l^2 q_l^2 - 2R_{os}^2 q_o q_s - 2R_{ol}^2 q_o q_l - 2R_{sl}^2 q_s q_l), \quad (4.19)$$

where $R_o = R_{out}$, $R_s = R_{side}$, $R_l = R_{long}$, $R_{os} = R_{out-side}$, $R_{ol} = R_{out-long}$, and $R_{sl} = R_{side-long}$. Including the Coulomb correction, as prescribed by Bowler and Sinyukov [110], provides the following correlation function that can be fit to the data:

$$C(q) = N[\lambda G(q) F(q) + (1 - \lambda)]. \quad (4.20)$$

where N is the normalization, $G(q)$ the above Gaussian fit function, and $F(q)$ is the Coulomb source. In order to fit the correlation function, a simple χ^2 minimization is inappropriate because the ratio of two Poisson distributions is not itself Poisson distributed. This is especially true when taking the ratio of small numbers. For this reason a log-likelihood fit function is used [44]:

$$\chi^2_{PML} = -2\left[A \ln\left(\frac{C(A+B)}{A(C+1)}\right) + B \ln\left(\frac{(A+B)}{B(C+1)}\right)\right], \quad (4.21)$$

where A is the signal distribution, B is the background distribution, and C is the ratio of signal to background which is the correlation function. This equation is used directly in ROOT using the MINUIT algorithm and log-likelihood fitting method.

4.4 Event Plane Azimuthal Reference

Azimuthally differential pion femtoscopy measurements performed relative to the reaction plane provide means to measure the source shape (or eccentricity) at freeze-out [45, 108, 109]. The collision geometry generates a greater pressure gradient in

the reaction plane than in the direction perpendicular, see Figure 4.2. Therefore, there is a stronger *in-plane* expansion (elliptic flow) than *out-of-plane*, and the initial *out-of-plane* spatial anisotropy is diminished. The source shape at freeze-out should be sensitive to pressure gradients and the lifetime of the system. A long-lived system should be less *out-of-plane* and more *in-plane* extended.

To perform this measurement, the event plane is estimated since the reaction plane is not directly accessible, see Chapter 3 for discussion on the Event Plane Method. This gives information on the azimuthal direction for the azimuthally differential femtoscopy analysis.

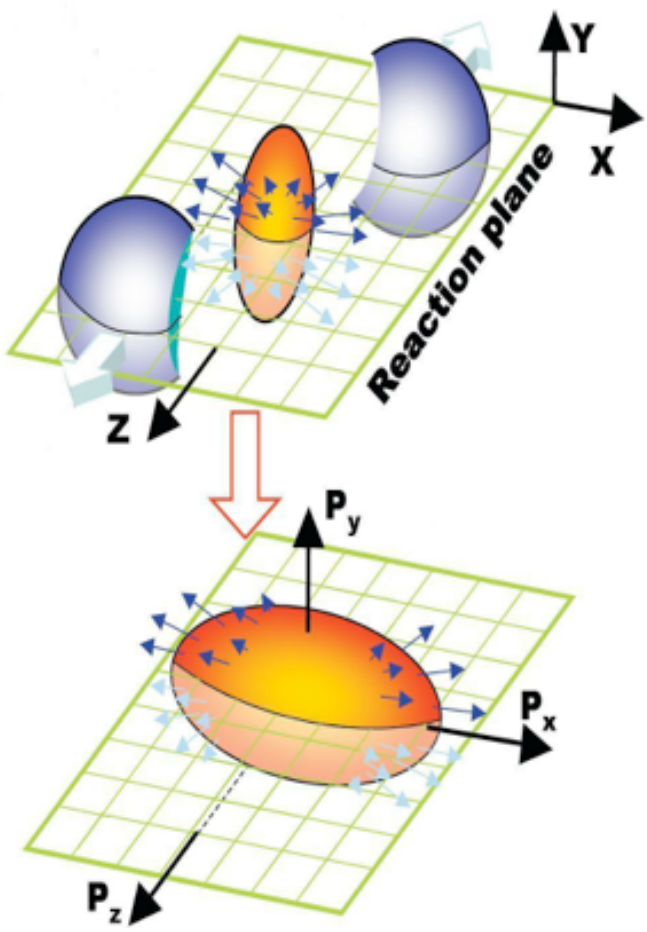

Figure 4.2: sketch of reaction plane and pressure gradients in non-central collisions

4.5 Systematic Studies

4.5.1 $\Delta\eta\Delta\phi^*$ pair cuts: Two Dimensional Ratio of $C(\Delta\eta, \Delta\phi^*)$

Pairs from tracks with similar momentum and small angular distance have the following reconstruction effects: *track splitting* and *track merging*. *track splitting* is an effect when one track is falsely reconstructed as two tracks. This results in an enhancement of tracks at low pair momentum. *track merging* is an opposite effect, when two tracks are falsely reconstructed as one track or not reconstructed at all. This results in a depletion of pairs close in momentum.

Both these effects bias the correlation function at low relative momentum q and effect the extraction of the HBT radii. Monte Carlo HIJING, tuned for the LHC11h dataset production is used to study the effect of the pair cuts.

Two track reconstruction effects such as *track splitting* and *track merging* as a function of angular distance between a pair of tracks is discussed, (also previously studied [111]). The angular distance between two tracks at a certain value of radius R is described:

$$\Delta\varphi^*_{min} = \varphi_1 - \varphi_2 + arcsin\left(\frac{z \cdot e \cdot B_z \cdot R}{2p_{T1}}\right) - arcsin\left(\frac{z \cdot e \cdot B_z \cdot R}{2p_{T2}}\right), \qquad (4.22)$$

where φ_1 and φ_2 are the azimuthal angles of the tracks at the vertex, p_{T1} and p_{T2} are the transverse momenta, e is the elementary charge, and Bz is the magnetic field in the z direction. R is the radius of either the TPC or ITS. For radii between 0.2 m and 0.8 m, R is inside the ITS, while for radii between 0.8 m and 2.5 m, R is inside the TPC. The value of R is fixed to 1.6 m corresponding to the center of the TPC. $\Delta\varphi^*_{min}$ defined in Eq.(4.22) is shown in Figure 4.3:

One of the cuts intended to remove undesired *track splitting* and *track merging* is called *share fraction*. Each TPC cluster is labeled as "shared" if it is used to reconstruct more than one track. Pairs that share more than 5% TPC clusters are

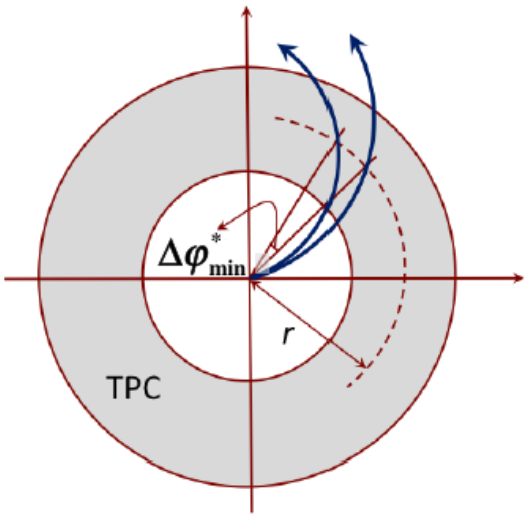

Figure 4.3: Definition of $\Delta\varphi^*_{min}$

removed. Another cut, called *share quality* removes pairs of tracks in which a single track splits into two segments in the TPC.

Table 4.1: $\Delta\eta$ and $\Delta\phi^{*min}$ cuts

$\Delta\varphi^*_{min}$	$\Delta\eta$
0	0
0.017	0.015
0.04	0.02
0.06	0.02

The distance of closest approach is varied along with the $\Delta\eta$ and $\Delta\phi^{*min}$ cuts to select the optimal two-track cuts to minimize both *track splitting* and *track merging*.

Table 4.2: DCA values

DCA_{xy}	DCA_z
0.2 cm	0.15 cm
0.4 cm	0.3 cm
2.4 cm	3.0 cm

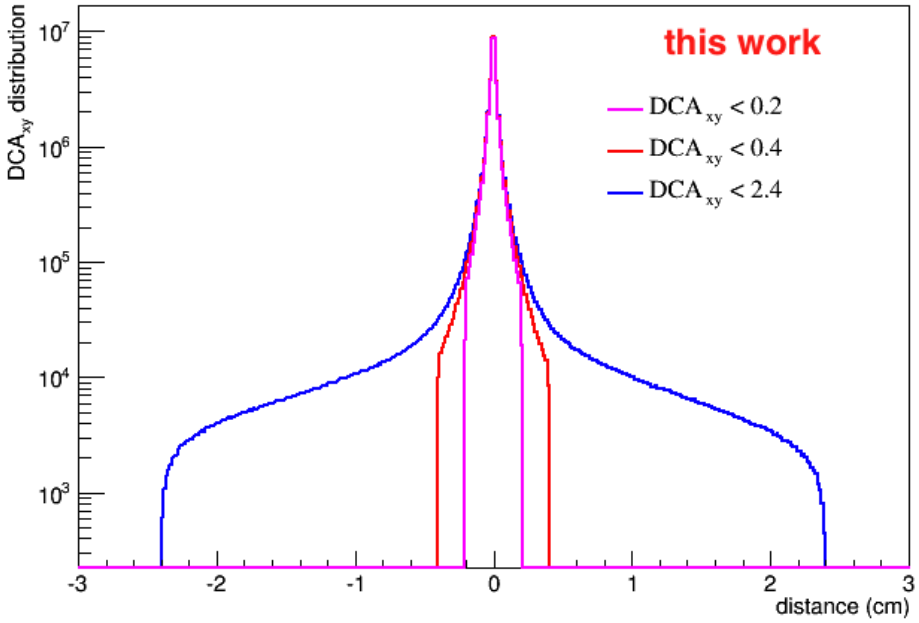

Figure 4.4: DCA_{xy} distribution

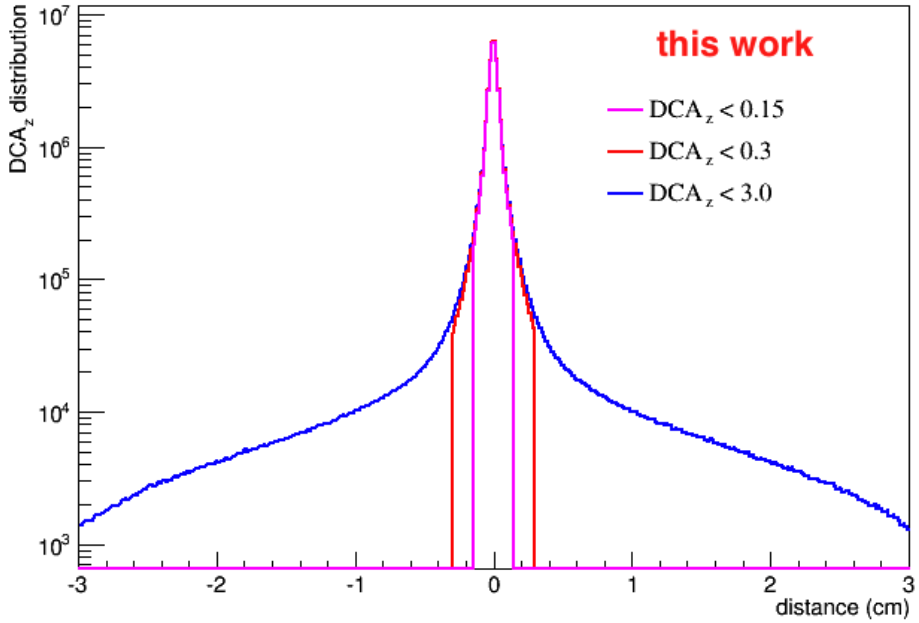

Figure 4.5: DCA_z distribution

The two dimensional ratio of the correlation function $C(\Delta\eta,\Delta\phi)$ is shown in the HIJING MC for the LHC11h dataset production, LHC12a17a_fix . There are three sets of DCA values. In Figure 4.6 and Figure 4.7 a depletion in the ratio near $\Delta\eta = 0$ and $\Delta\varphi^*_{min} = 0$ is shown. In order to estimate the values to use for the pair cut on $\Delta\eta$ and $\Delta\varphi^*_{min}$, the projections in Figures 4.8 and 4.9 are used for the k_T range 0.2-0.5 GeV/c, and then again for the higher k_T range 0.5-1.0 GeV/c. For this Hijing data, the ratio should have a value close to 1.0, otherwise this is evidence of undesirable *track splitting* and *track merging*.

$DCA_{xy} < 0.2cm$, $DCA_z < 0.15cm$

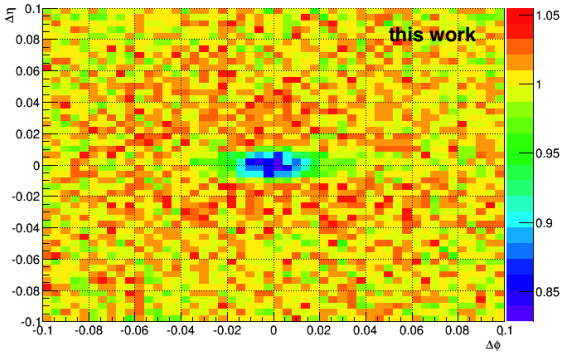

Figure 4.6: Two dim. ratio $\Delta\eta\Delta\phi^*$ for k_T range 0.2-0.5 GeV/c

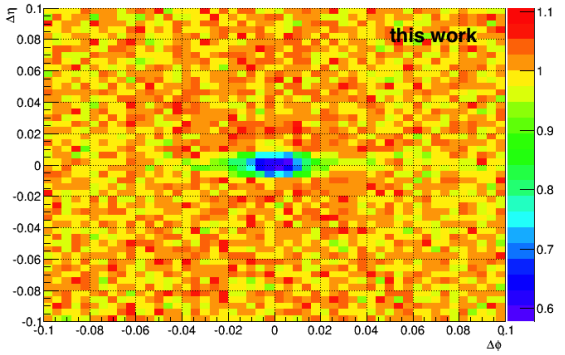

Figure 4.7: Two dim. ratio $\Delta\eta\Delta\phi^*$ for k_T range 0.5-1.0 GeV/c

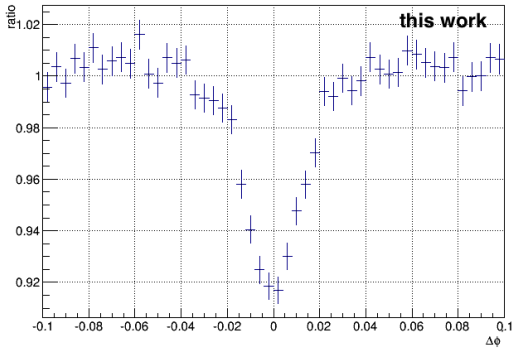

Figure 4.8: $\Delta\varphi^*_{min}$ projection for k_T range 0.2-0.5 GeV/c

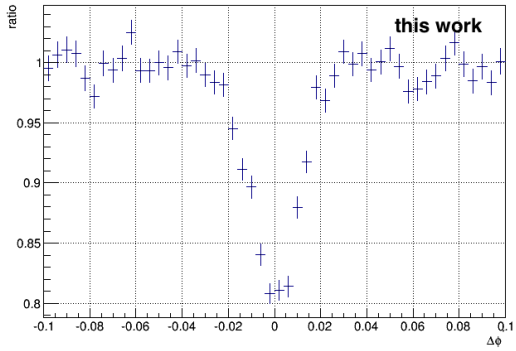

Figure 4.9: $\Delta\varphi^*_{min}$ projection for k_T range 0.5-1.0 GeV/c

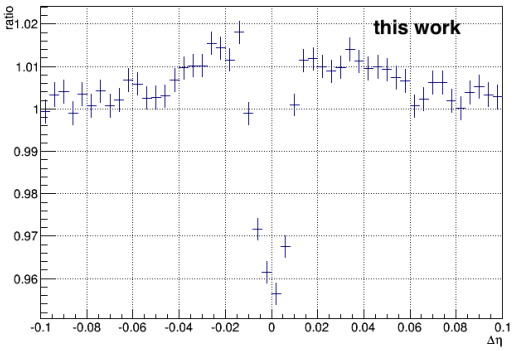

Figure 4.10: $\Delta\eta$ projection for k_T range 0.2-0.5 GeV/c

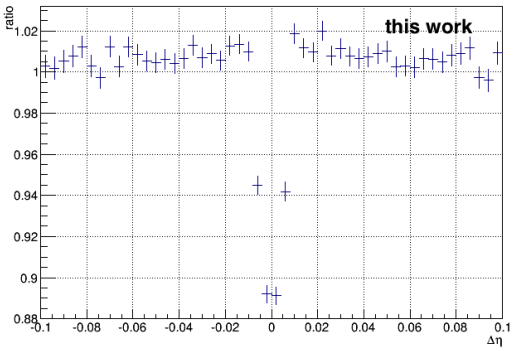

Figure 4.11: $\Delta\eta$ projection for k_T range 0.5-1.0 GeV/c

$DCA_{xy} < 0.4cm$, $DCA_z < 0.3cm$

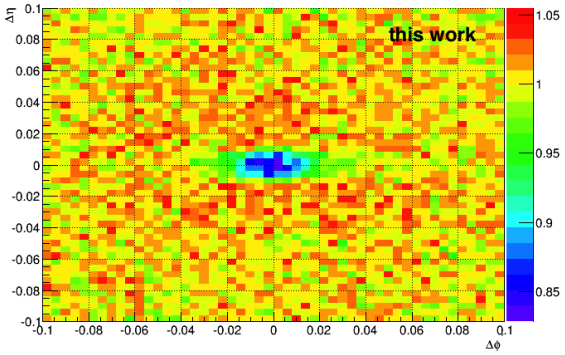

Figure 4.12: Two dim. ratio $\Delta\eta\Delta\phi^*$ for k_T range 0.2-0.5 GeV/c

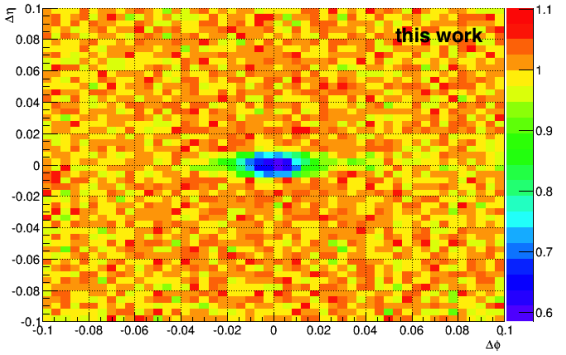

Figure 4.13: Two dim. ratio $\Delta\eta\Delta\phi^*$ for k_T range 0.5-1.0 GeV/c

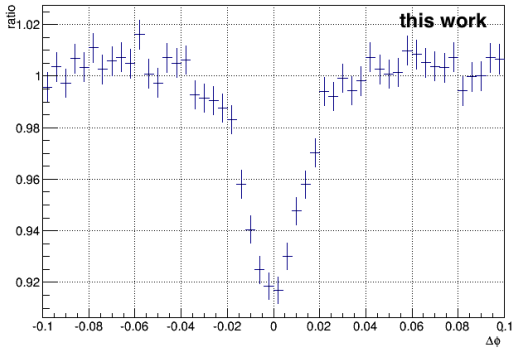

Figure 4.14: $\Delta\varphi^*_{min}$ projection for k_T range 0.2-0.5 GeV/c

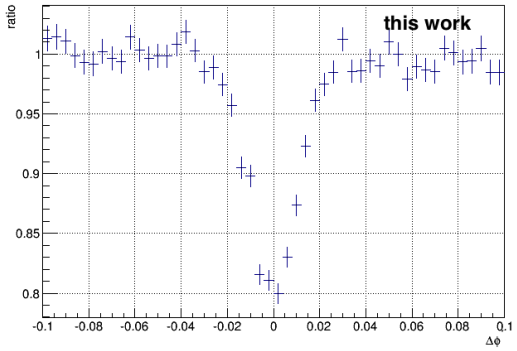

Figure 4.15: $\Delta\varphi^*_{min}$ projection for k_T range 0.5-1.0 GeV/c

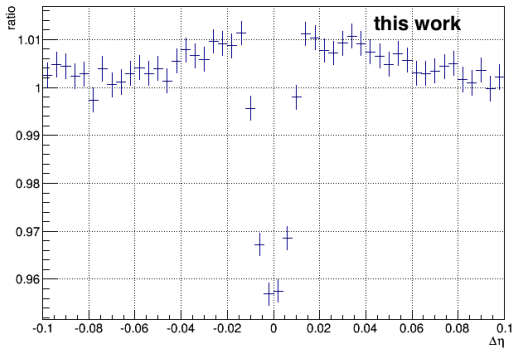

Figure 4.16: $\Delta\eta$ projection for k_T range 0.2-0.5 GeV/c

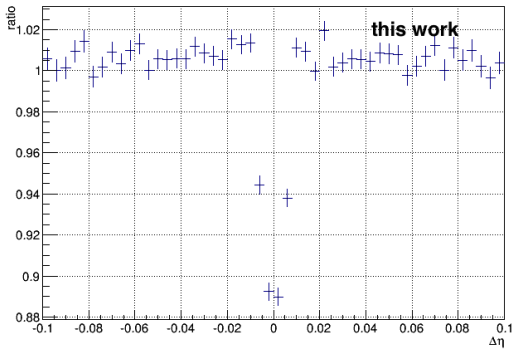

Figure 4.17: $\Delta\eta$ projection for k_T range 0.5-1.0 GeV/c

$$DCA_{xy} < 2.4cm,\ DCA_z < 3.0cm$$

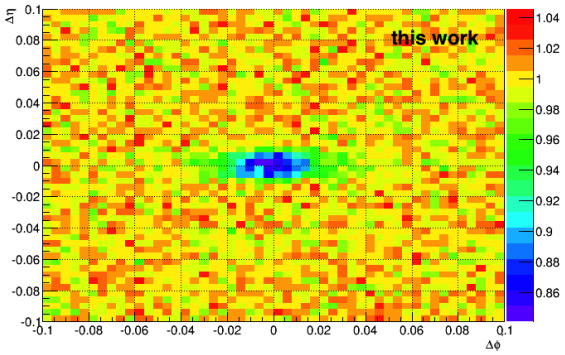

Figure 4.18: Two dim. ratio $\Delta\eta\Delta\phi^*$ for k_T range 0.2-0.5 GeV/c

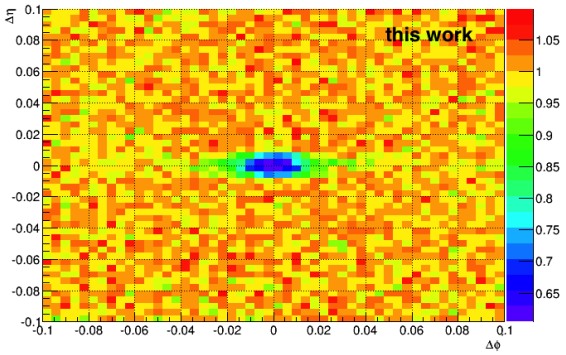

Figure 4.19: Two dim. ratio $\Delta\eta\Delta\phi^*$ for k_T range 0.5-1.0 GeV/c

In Figures 4.20-4.23 for $DCA_{xy} < 2.4$ cm, $DCA_z < 3.0$ cm, both the $\Delta\eta$ and $\Delta\varphi^*_{min}$ projections show a maximum value of the ratio is 1.0, as expected when no *track splitting* and *track merging* occurs. Next the one-dimensional correlation function is examined and pair cuts are applied on $\Delta\eta$ and $\Delta\varphi^*_{min}$ on the various DCA values.

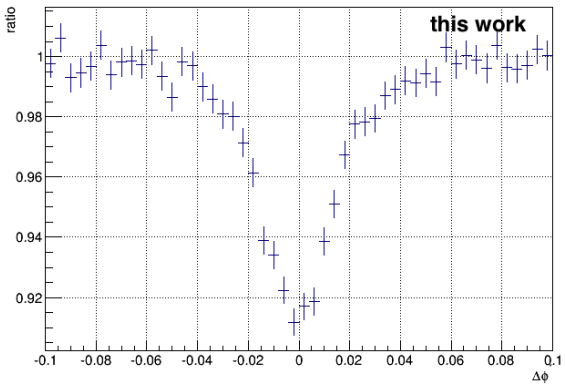

Figure 4.20: $\Delta\varphi^*_{min}$ projection for k_T range 0.2-0.5 GeV/c

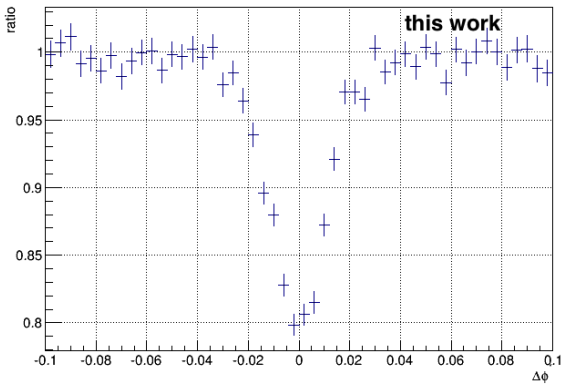

Figure 4.21: $\Delta\varphi^*_{min}$ projection for k_T range 0.5-1.0 GeV/c

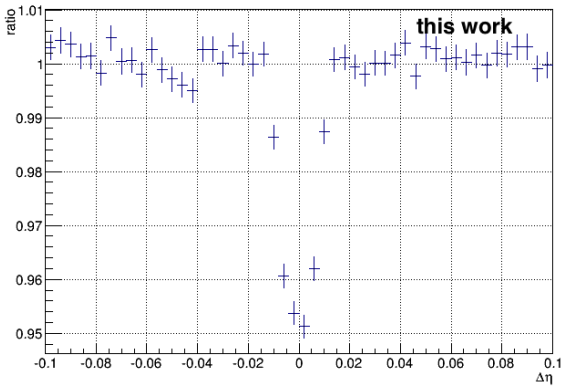

Figure 4.22: $\Delta\eta$ projection for k_T range 0.2-0.5 GeV/c

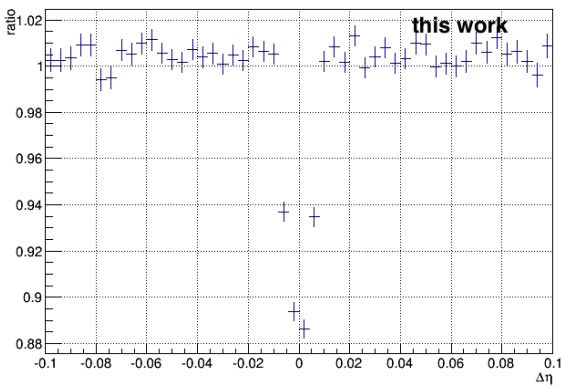

Figure 4.23: $\Delta\eta$ projection for k_T range 0.5-1.0 GeV/c

4.5.2 One Dimensional Correlation Function $C(q_{inv})$

The one dimensional correlation function as a function of Q_{inv} is given by

$$C(q,k) = 1 + \lambda(k) exp(-q_{inv}^2 R_{inv}^2(k)) \tag{4.23}$$

where q_{inv}^2 is the square of the spatial relative momentum in the pair rest frame, where $q_0 = 0$.

$$q_{inv}^2 = q^2 - q_0^2 \tag{4.24}$$

All $\Delta\eta\Delta\phi^*$ cuts are shown in Figure 4.24 - 4.27 for different DCA distributions.

$DCA_{xy} < 0.2cm$, $DCA_z < 0.15cm$

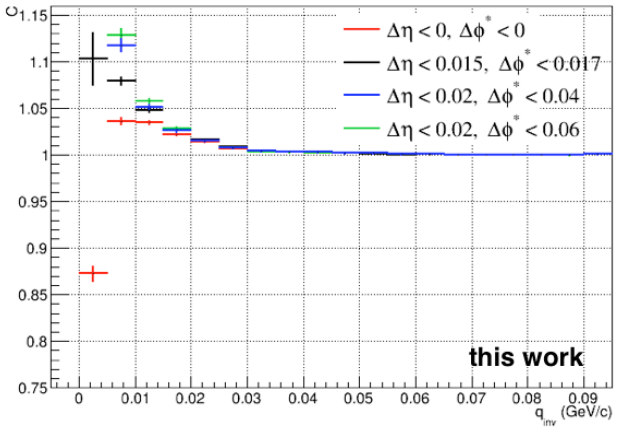

Figure 4.24: $C(q_{inv})$ for k_T range 0.2-0.5 GeV/c

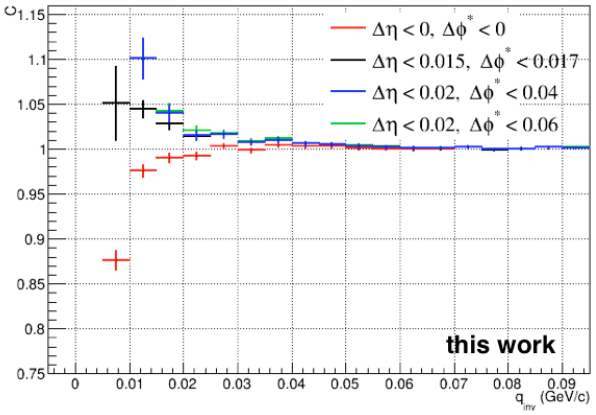

Figure 4.25: $C(q_{inv})$ for k_T range 0.5-1.0 GeV/c

$DCA_{xy} < 0.4cm$, $DCA_z < 0.3cm$

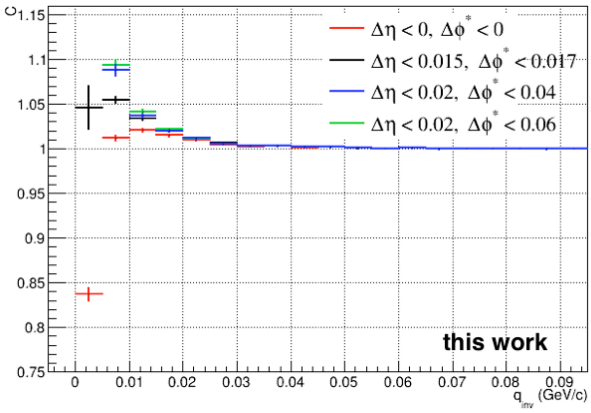

Figure 4.26: $C(q_{inv})$ for k_T range 0.2-0.5 GeV/c

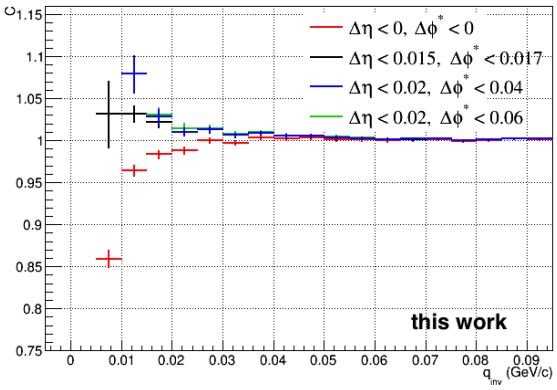

Figure 4.27: $C(q_{inv})$ for k_T range 0.5-1.0 GeV/c

Figure 4.25-Figure 4.27 show $q_{inv} < 0.3$, where there is *track splitting* and $C(q_{inv}) > 1$. *track merging* is also present for $\Delta\eta < 0, \Delta\phi^* < 0$ at $q_{inv} = 0.005GeV/c$ where $C(q_{inv}) < 1$. The effect of the pair cuts is a reduction in the *track merging* where $C_{qinv} < 0$, but also *track splitting* occurs where $C_{qinv} > 0$. A looser DCA cut range $DCA_{xy} < 2.4cm$, $DCA_z < 3.0cm$ is shown in Figure 4.28-Figure 4.29.

$$DCA_{xy} < 2.4cm,\ DCA_z < 3.0cm$$

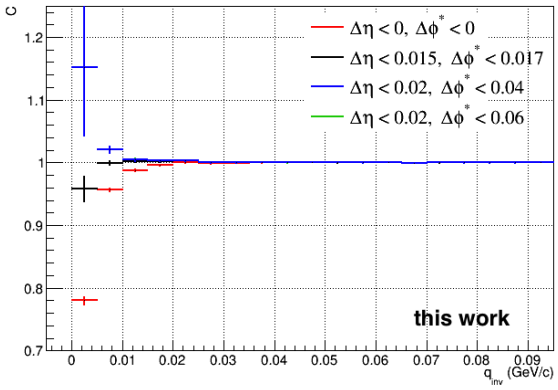

Figure 4.28: $C(q_{inv})$ for k_T range 0.2-0.5 GeV/c

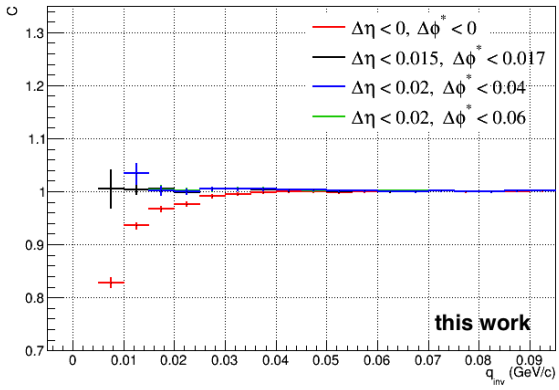

Figure 4.29: $C(q_{inv})$ for k_T range 0.5-1.0 GeV/c

4.6 Corrections

The corrections that are used in this analysis are the following: ϕ efficiency correction, which is needed to correct the ϕ distribution for detector effects; Coulomb correction, to correct the Coulomb interaction between particles; the momentum resolution correction, which is needed to broaden the correlation function caused by the detector; and the event plane resolution correction, is used correct for the event plane resolution. All corrections will be described in section 4.7, except the event plane resolution correction which will be discussed in this section.

4.6.1 Event Plane Resolution Correction

There are two methods for correcting the event plane resolution. One method, the so called bin-by-bin correction, involves correcting both the numerator and denominator for event plane resolution. Another method involves correcting the radii for event plane resolution. The correction for event plane resolution effects on the level of numerator and denominator are described here. The correction depends on the relative pair momentum q and the pair emission angle ϕ_j [114]. The correction

for the numerator is the following:

$$N(q,\phi_j) = N_{exp}(q,\phi_j) + 2\left(\sum_{n=1}^{n_{bins}} \xi_{n,m}(\Delta)[N_{c,n}^{exp}(q)\cos(n\phi_j) + N_{s,n}^{exp}(q)\sin(n\phi_j)]\right), \tag{4.25}$$

where N_{exp} is the experimentally determined distribution. The decompositions are:

$$\begin{aligned} N_{c,n}^{exp}(q) &= \langle N_{exp}(q,\phi_j)\cos(n\phi)\rangle = \frac{1}{n_{bins}}\sum_{n=1}^{n_{bins}} N_{exp}(q,\phi_j)\cos(n\phi_j), \\ N_{s,n}^{exp}(q) &= \langle N_{exp}(q,\phi_j)\sin(n\phi)\rangle = \frac{1}{n_{bins}}\sum_{n=1}^{n_{bins}} N_{exp}(q,\phi_j)\sin(n\phi_j). \end{aligned} \tag{4.26}$$

The correction factor ξ is:

$$\xi_{n,m}(\Delta) = \frac{n\Delta/2}{\sin(n\Delta/2)R_{EP}}, \tag{4.27}$$

where Δ is the bin width and R_{EP} is the measured event plane resolution, described in section 4.4. The results of this section are presented in section 4.7.

The second method for correcting for the event plane resolution is the so called "E895 method" [115]. This method corrects the radii oscillation term ($R_{j,2}^2$ where j=out, side,long, and out-side). The radii corrected for event plane resolution is the following:

$$\begin{aligned} R_{i,j,true}^2 &= R_{i,j,measured}^2/\rho \\ \rho &= \langle cos(\psi - \Phi_n)\rangle \frac{\sin(n\Delta/2)}{(n\Delta/2)} \end{aligned} \tag{4.28}$$

where n is the harmonic number, and $\langle\cos(n-\Psi_n)\rangle$ is the event plane resolution. $\Delta = \pi/n_{bins} = 0.349$, and $\frac{\sin(n\Delta/2)}{(n\Delta/2)} = 0.98$, for $n_{bins} = 9$. The results of this section are presented in section 4.7.

4.7 Azimuthally Differential Femtoscopy Results

The HBT analysis is performed in 9 bins of the pair emission angle with respect to the reaction plane: $-15°, 5°, 25°, 45°, 65°, 85°, 105°, 125°, 145°, 165°$, six bins of centrality: $0-5\%, 5-10\%, 10-20\%, 20-30\%, 30-40\%$, and $40-50\%$, and four k_T bin ranges (0.2-0.3 GeV/c, 0.3-0.4 GeV/c, 0.4-0.5 GeV/c, 0.5-0.7 GeV/c).

Pion pairs are identified using the energy loss in TPC and the TOF is used to reject pion pairs. The measurement of the specific energy loss dE/dx in the TPC allows to identify single particles in the region where the dE/dx is proportional to $1/\beta^2$, with $\beta = v/c$ being the velocity of the particles. TOF provides PID by measuring the time it takes for a particle to travel from the primary vertex to the TOF detector and is thus sensitive to the mass of the particle when the momentum measurement of the TPC gets included. It provides PID in the momentum region where the specic energy loss becomes the same for different particle species. Depending on the momentum of the particle, different PID techniques were chosen. Namely, the TPC for momenta $p <$ 0.75 GeV/c, TPC and TOF for $0.75 \leq p < 1.0$ GeV/c and TOF alone for $1.0 \leq p <$ 3.25 GeV/c. The pion selection for $p \leq 0.75$ GeV/c was done by applying an upper and lower cut on the measured dE/dx, which is based on a parametrization of the Bethe-Bloch curve. A clear separation of the pions is achieved for these momenta with the TPC alone. The purity of the pion sample was determined by tting the dE/dx distributions in slices of total momentum. A three sigma cut was used to select pions. Pion pairs within one bin of ϕ, range of k_T and centrality (see above description) are used to create the signal, pairs from the same event, and the background is created using event mixing, where a pion from a given event is paired with one from a different event.

4.7.1 Trigger Selection

The data used in this analysis was recorded in centrality ranges 0-50% using the following triggers: minimum bias, semi-central, and central.

4.7.2 Event, Track, and Pair Selection

The events were chosen such that the position of the vertex was within 8 cm. The remaining track cuts and pair cuts are listed:

Table 4.3: Track cuts

variable	cut value
$\|\eta\|$	< 0.8
p_T	$0.14 - 1.5$ GeV/c
Number of reconstructed TPC clusters	> 80
χ^2 per TPC cluster	< 4
distance of closest approach to primary vertex in z	3.0 cm
distance of closest approach to primary vertex in xy	2.4 cm

Pair cuts, in addition to the event and track cuts are also applied. All pair cuts are implemented using the variables described in Chapter 4.5 and summarized in Table 4.4 .

Table 4.4: Pair cuts

variable	cut value
$(\|\Delta\eta\|, \Delta\varphi^*_{min})$	$(> 0.015, > 0.017)$
k_T	$0.2 - 0.7$ GeV/c
Share Quality Max	< 1.0
Share Fraction Max	< 0.05

4.7.3 1-D Projections of $C(q_{out}, q_{side}, q_{long})$

In order to proceed with the radii extraction, the 3D correlation function is fit using the method described in section 4.3.2. The correlation function projections are shown for each dimension, $C(q_{out})$, $C(q_{side})$, and $C(q_{long})$, see Figures 4.30-4.37. The bin width is 20 MeV shown here and for all preliminary figures. Figures 4.30-4.31 show the quality of the fit with variation in reaction plane bins. The fit shows some differences, however the overall χ^2/NDF is similar, see Table 4.5. Figures 4.34-4.35 show the lowest centrality range and lowest k_T range used. When comparing Figure 4.35 to Figure 4.36, the effect is seen of the centrality variation. Figure 4.37 when compared to Figure 4.30 shows the effect of reducing the fit range from 100 MeV to 70 MeV, where there is little difference shown here. The fits are again repeated for a finer bin width of 10 MeV. All figures 4.30-4.45 show the total q range along with the fit range used.

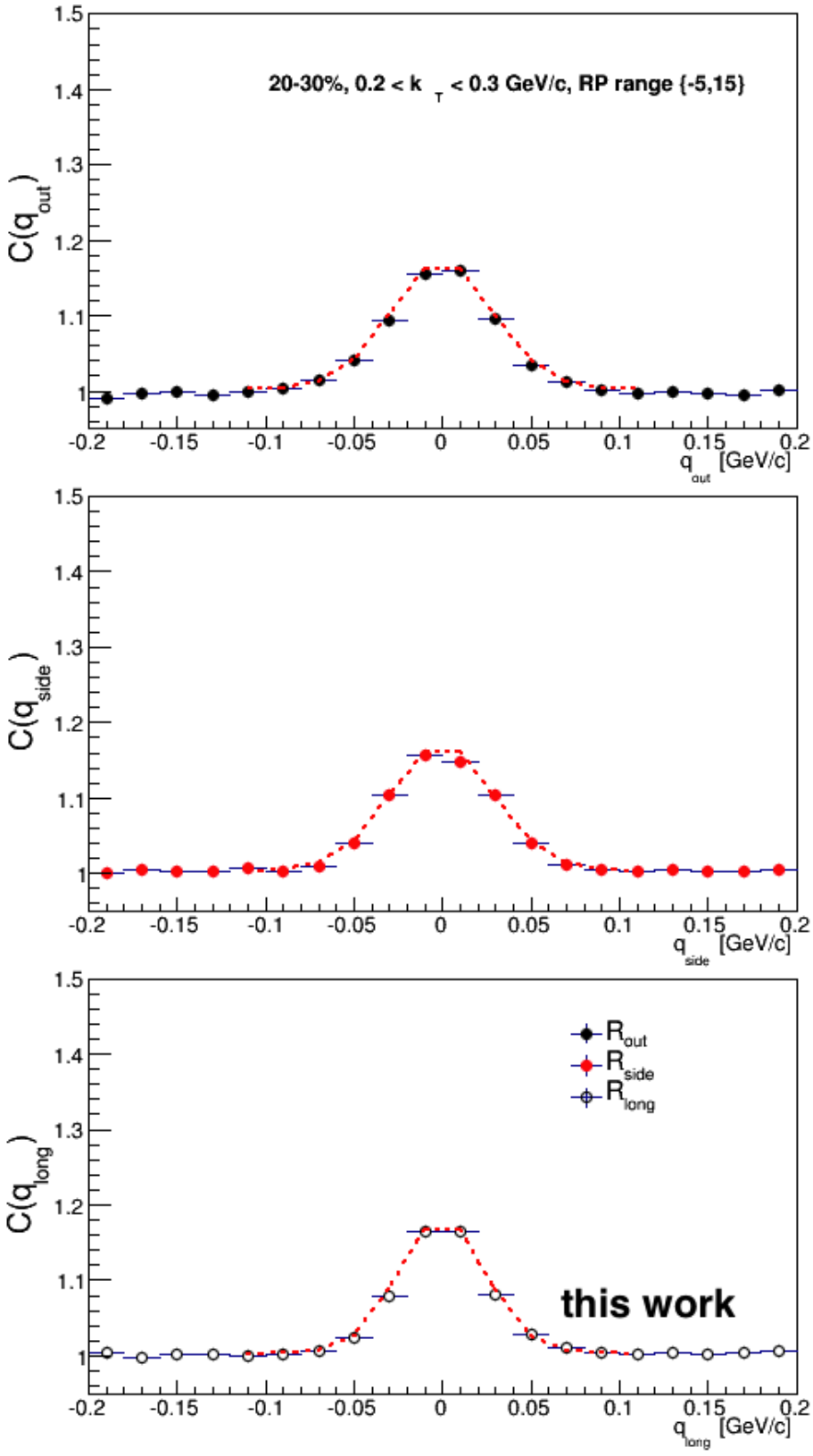

Figure 4.30: $C(q_{out})$, $C(q_{side})$, and $C(q_{long})$ 20-30% centrality, $0.2 < k_T < 0.3$ GeV/c, reaction plane angle $(-15°, 5°)$

Figures 4.32- 4.33 when compared to Figures 4.30- 4.31 show how the fit behaves when the range of k_T is varied from 0.2-0.3 GeV/c to 0.5-0.7 GeV/c.

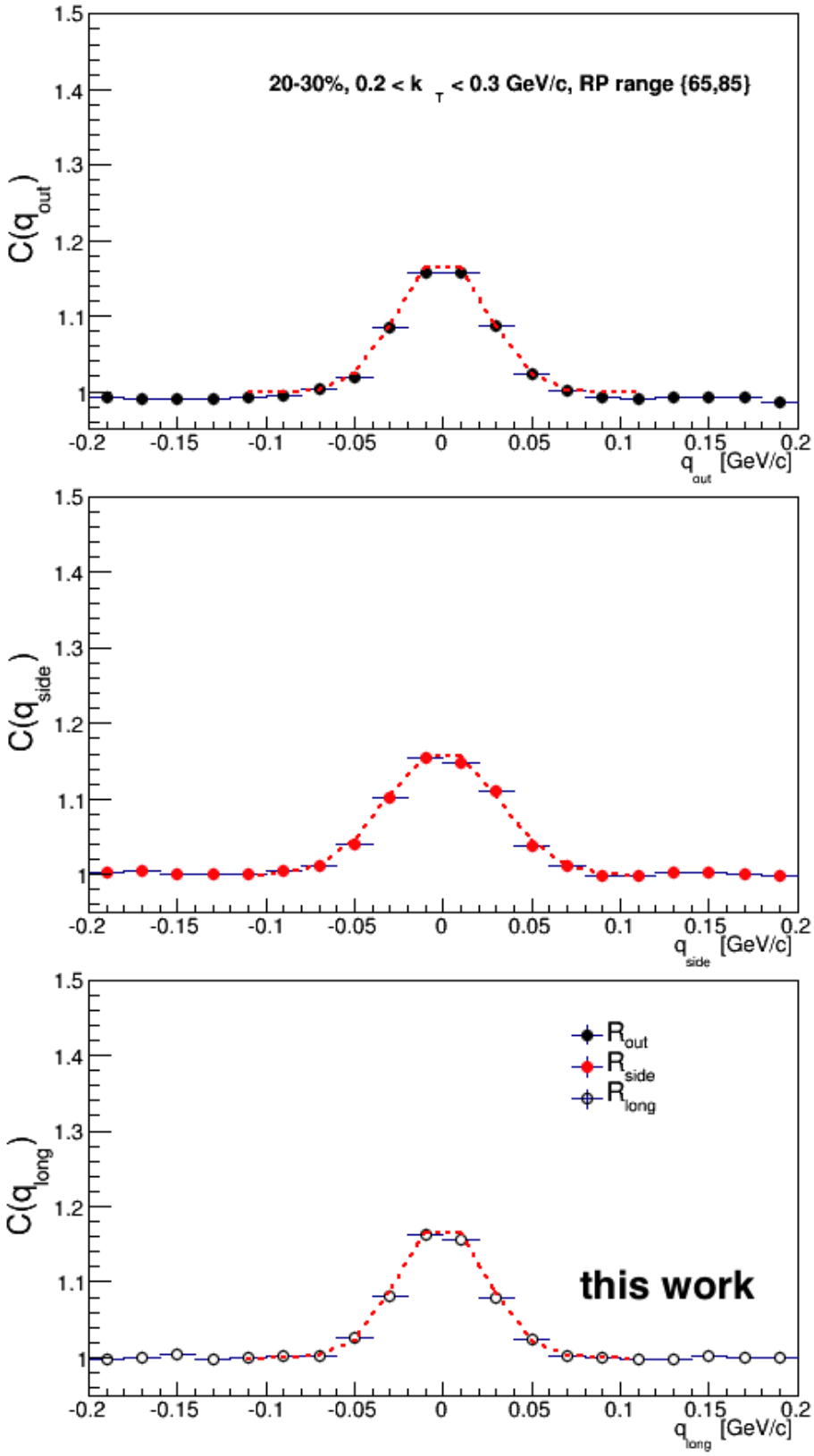

Figure 4.31: $C(q_{out})$, $C(q_{side})$, and $C(q_{long})$ 20-30% centrality, $0.2 < k_T <$0.3 GeV/c, reaction plane angle $(65°, 85°)$

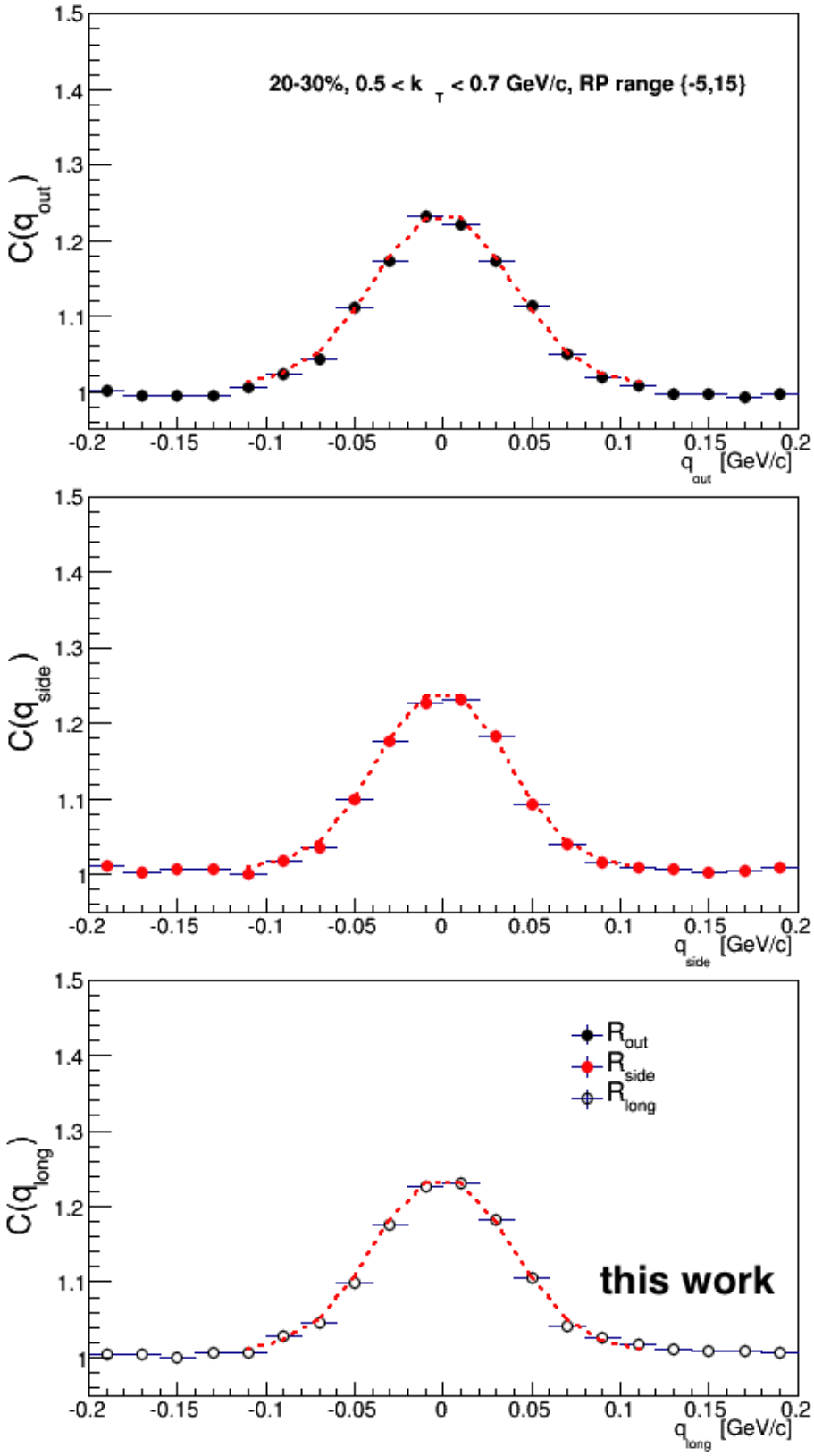

Figure 4.32: $C(q_{out})$, $C(q_{side})$, and $C(q_{long})$ 20-30% centrality, $0.5 < k_T < 0.7$ GeV/c, reaction plane angle $(-15°, 5°)$

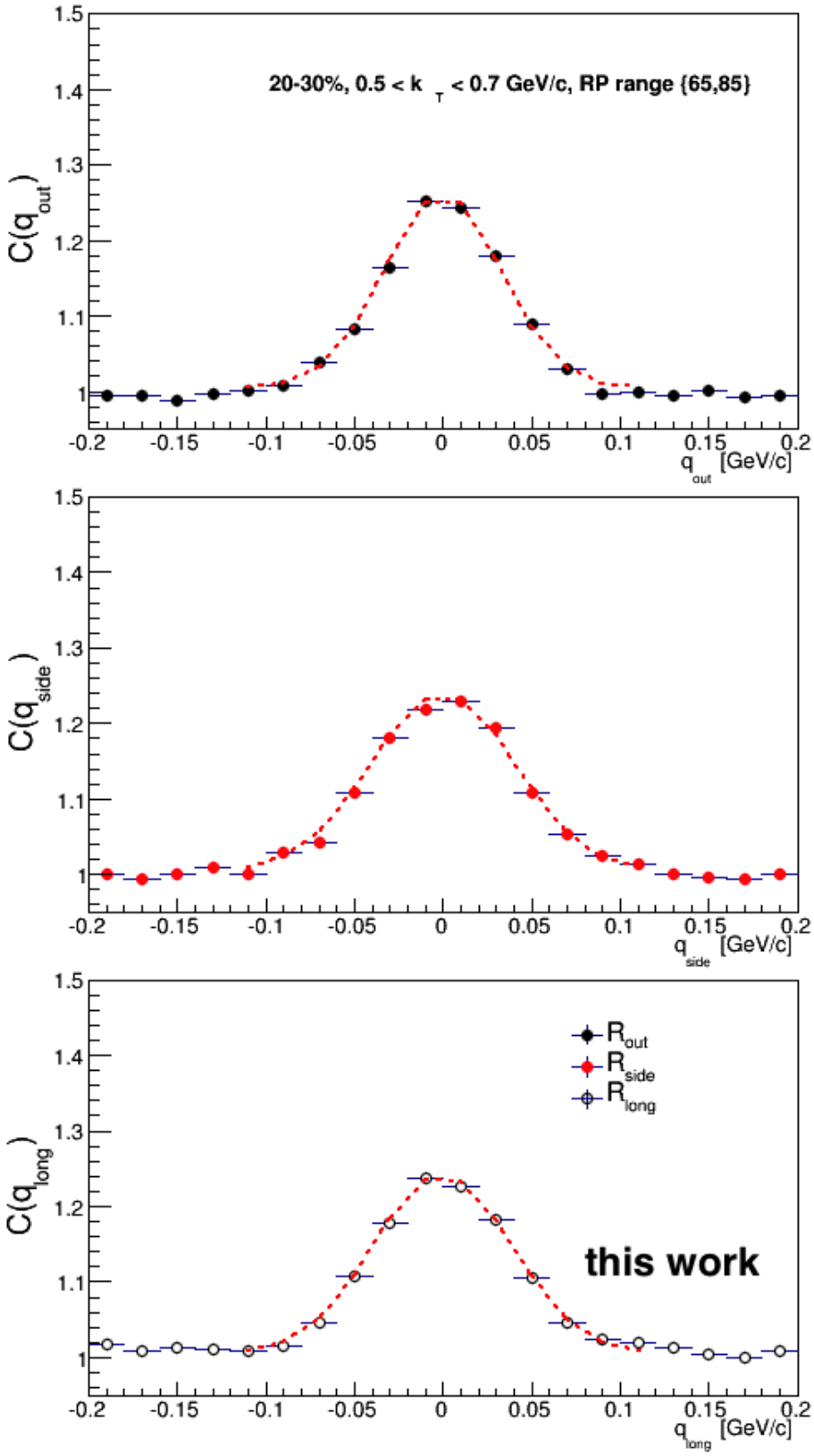

Figure 4.33: $C(q_{out})$, $C(q_{side})$, and $C(q_{long})$ 20-30% centrality, 0.5< k_T <0.7 GeV/c, reaction plane angle $(65°, 85°)$

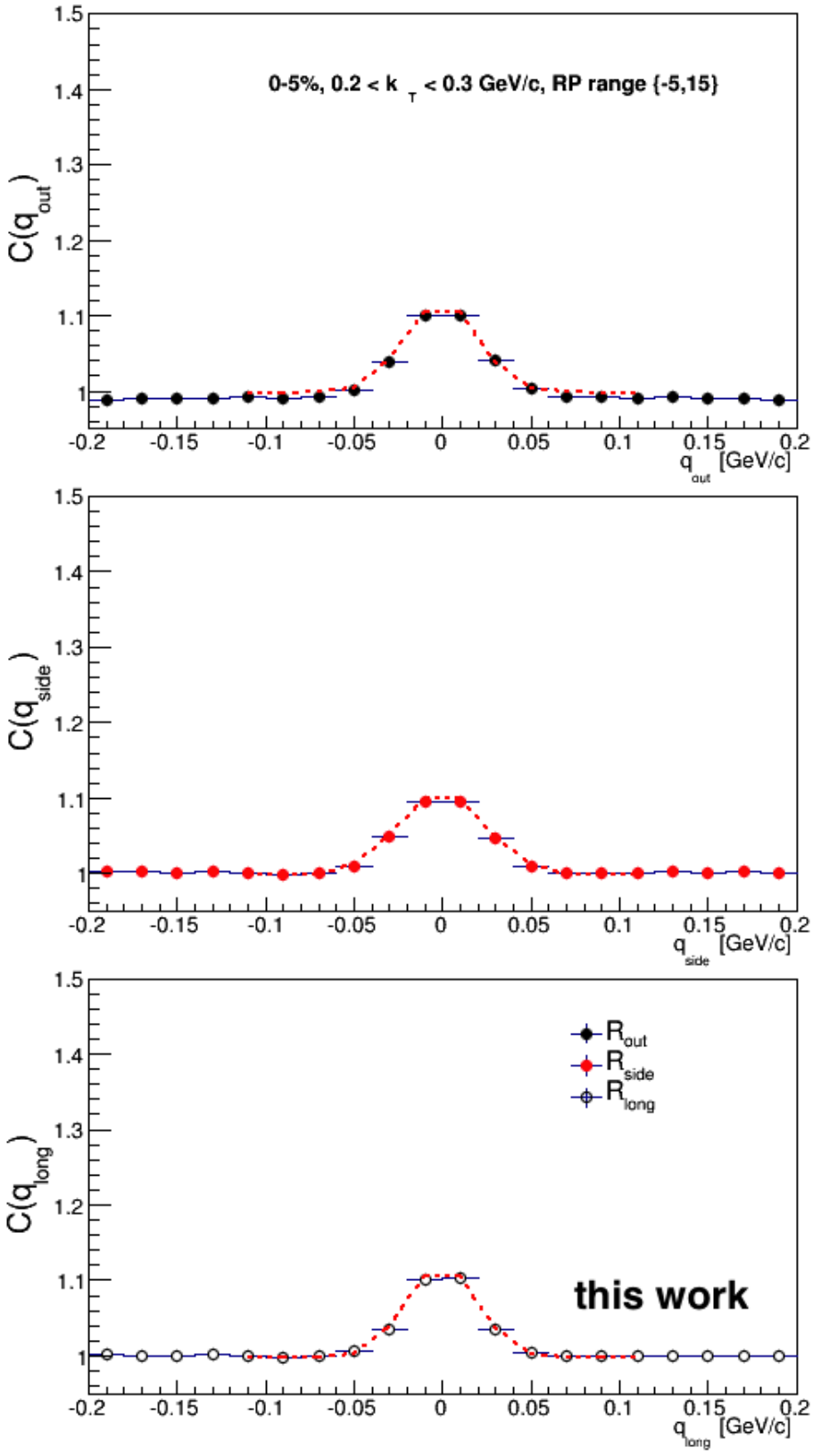

Figure 4.34: $C(q_{out})$, $C(q_{side})$, and $C(q_{long})$ 0-5% centrality, $0.2 < k_T <$0.3 GeV/c, reaction plane angle $(-15°, 5°)$

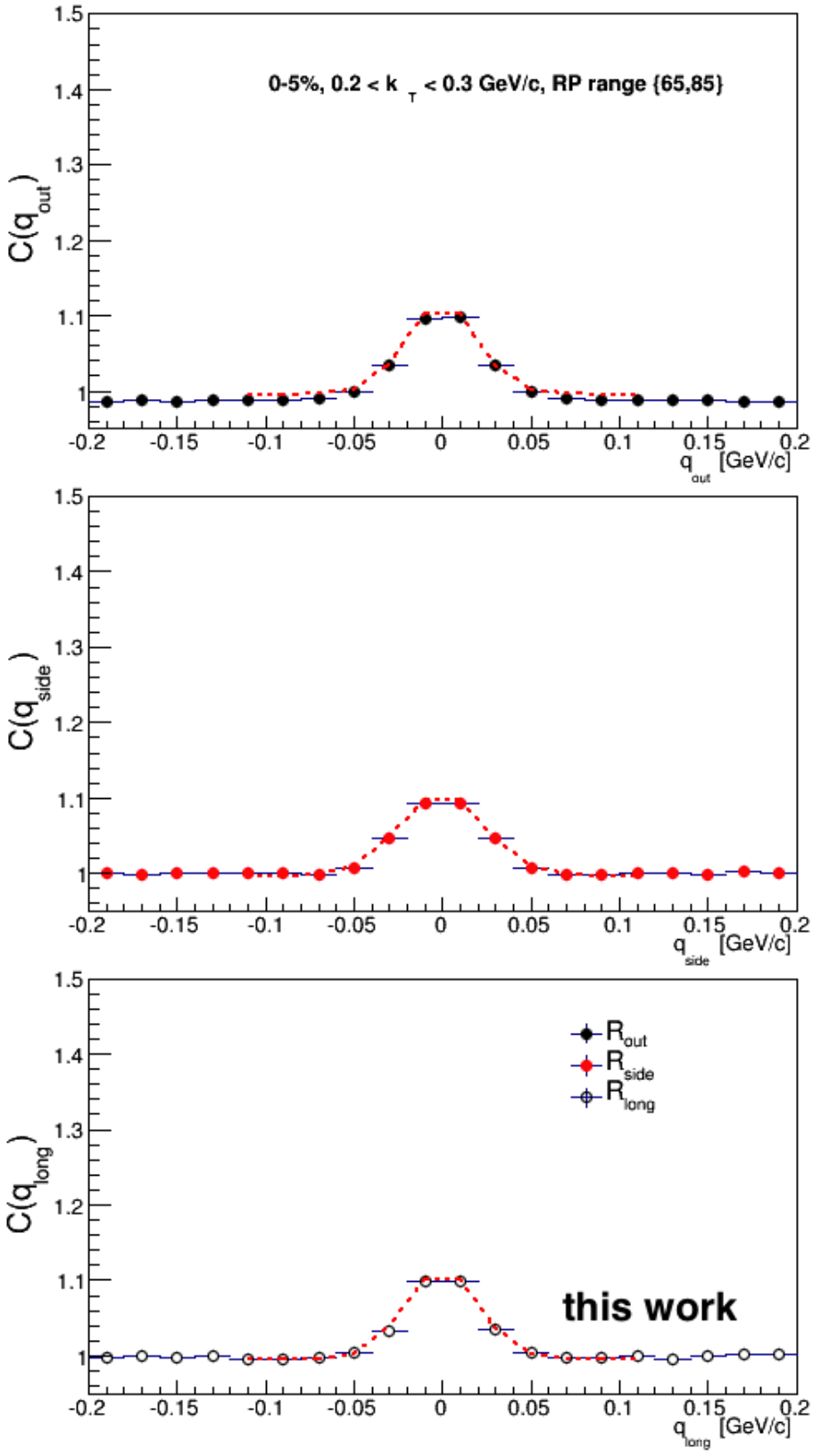

Figure 4.35: $C(q_{out})$, $C(q_{side})$, and $C(q_{long})$ 0-5% centrality, 0.2< k_T <0.3 GeV/c, reaction plane angle $(65°, 85°)$

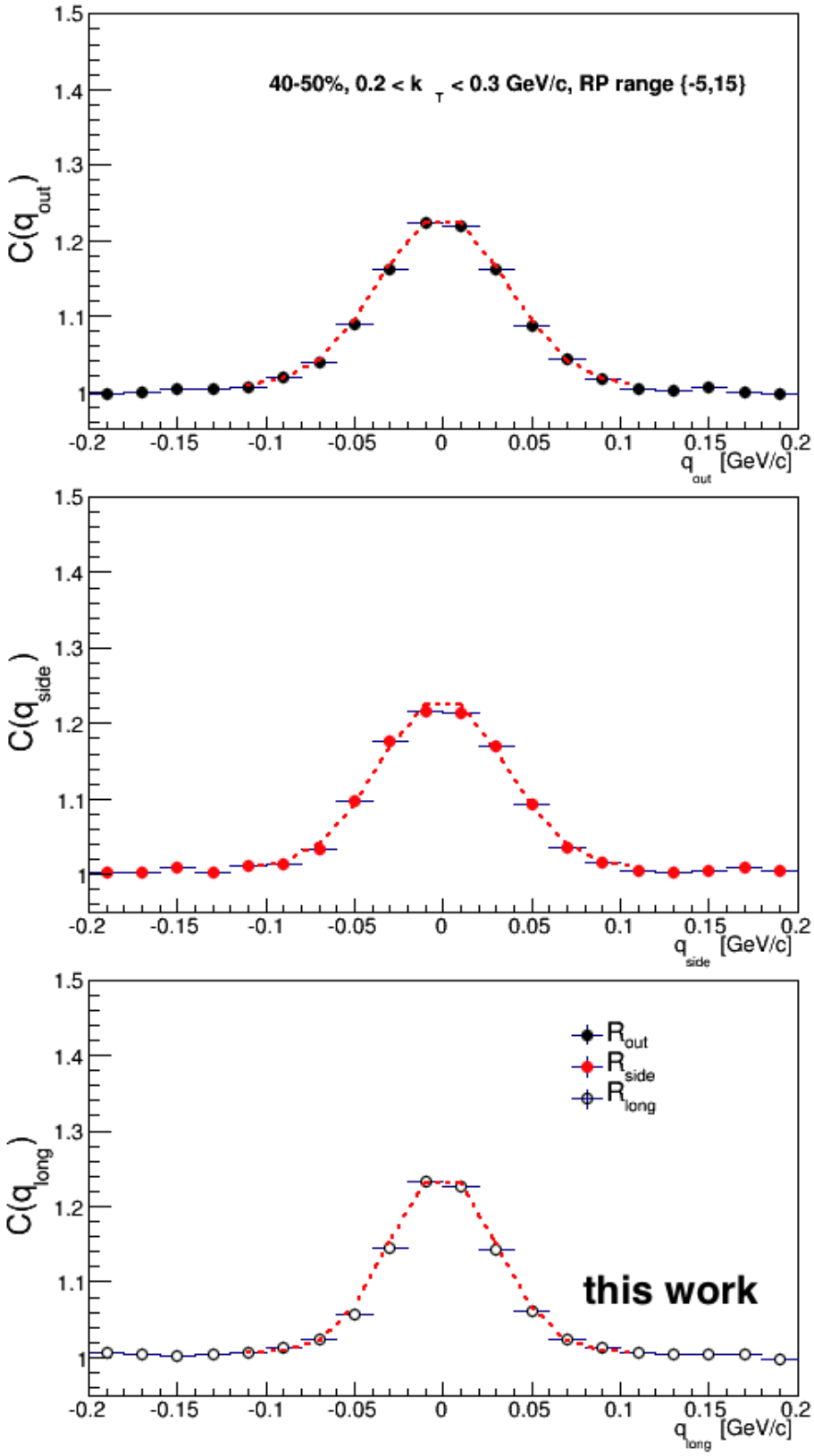

Figure 4.36: $C(q_{out})$, $C(q_{side})$, and $C(q_{long})$ 40-50% centrality, $0.2 < k_T < 0.3$ GeV/c, reaction plane angle $(-15°, 5°)$

The quality of the fit at low values of q_{out}, q_{side}, and q_{long} are examined by reducing the bin width from 20 MeV/c to 10 MeV/c, see Figures 4.38-4.45 and for the χ^2/NDF values, see Table 4.6.

Table 4.5: χ^2/NDF for 1D Projections of $C(q_{out}, q_{side}, q_{long})$, 20 MeV/c bin width

Figure	q range (MeV/c)	centrality	k_T range (GeV/c)	Reaction Plane Angle	χ^2//NDF	(+/-) bins (other dim.)	$R_{out}(fm)$	R_{side} (fm)	R_{long} (fm)
4.30	100	20-30 %	$0.2< k_T <0.3$	$\{-15°,\ 5°\}$	1.466	1	4.86	4.75	5.69
4.31	100	20-30 %	$0.2< k_T <0.3$	$\{65°,\ 85°\}$	1.543	1	5.58	4.48	5.59
4.32	100	20-30 %	$0.5< k_T <0.7$	$\{-15°,\ 5°\}$	1.428	2	3.61	3.95	3.73
4.33	100	20-30 %	$0.5< k_T <0.7$	$\{65°,\ 85°\}$	1.354	2	4.24	3.53	3.66
4.34	100	0-5 %	$0.2< k_T <0.3$	$\{-15°,\ 5°\}$	2.353	1	6.72	5.80	7.03
4.35	100	0-5 %	$0.2< k_T <0.3$	$\{65°,\ 85°\}$	2.492	1	6.956	5.74	6.86
4.36	100	40-50 %	$0.2< k_T <0.3$	$\{-15°,\ 5°\}$	2.00	1	3.83	3.92	4.66
4.37	70	20-30 %	$0.2< k_T <0.3$	$\{-15°,\ 5°\}$	1.415	1	5.03	4.88	5.93

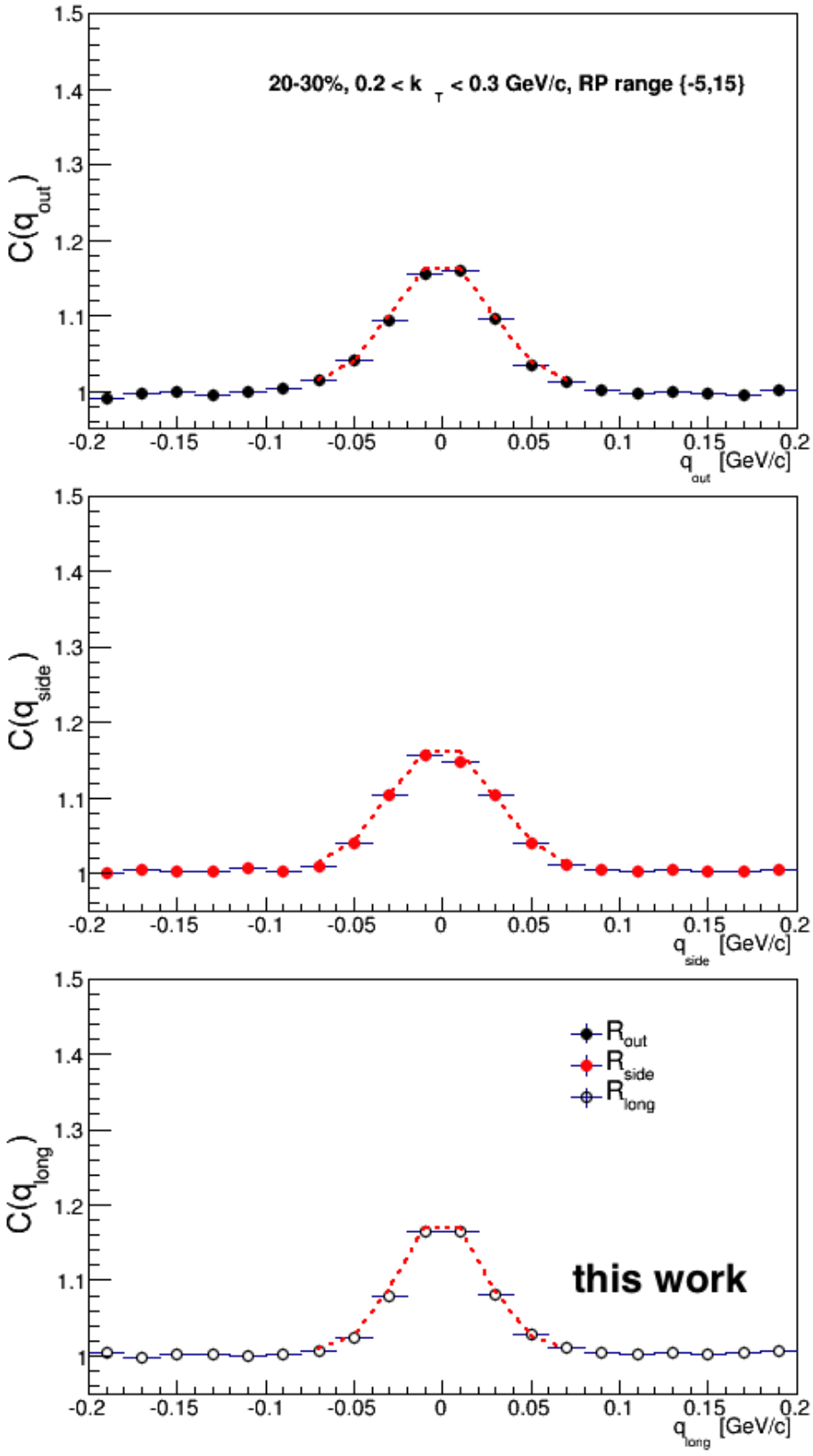

Figure 4.37: $C(q_{out})$, $C(q_{side})$, and $C(q_{long})$ q range 70 MeV/c, 20-30% centrality, $0.2 < k_T < 0.3$ GeV/c, reaction plane angle $(-15°, 5°)$

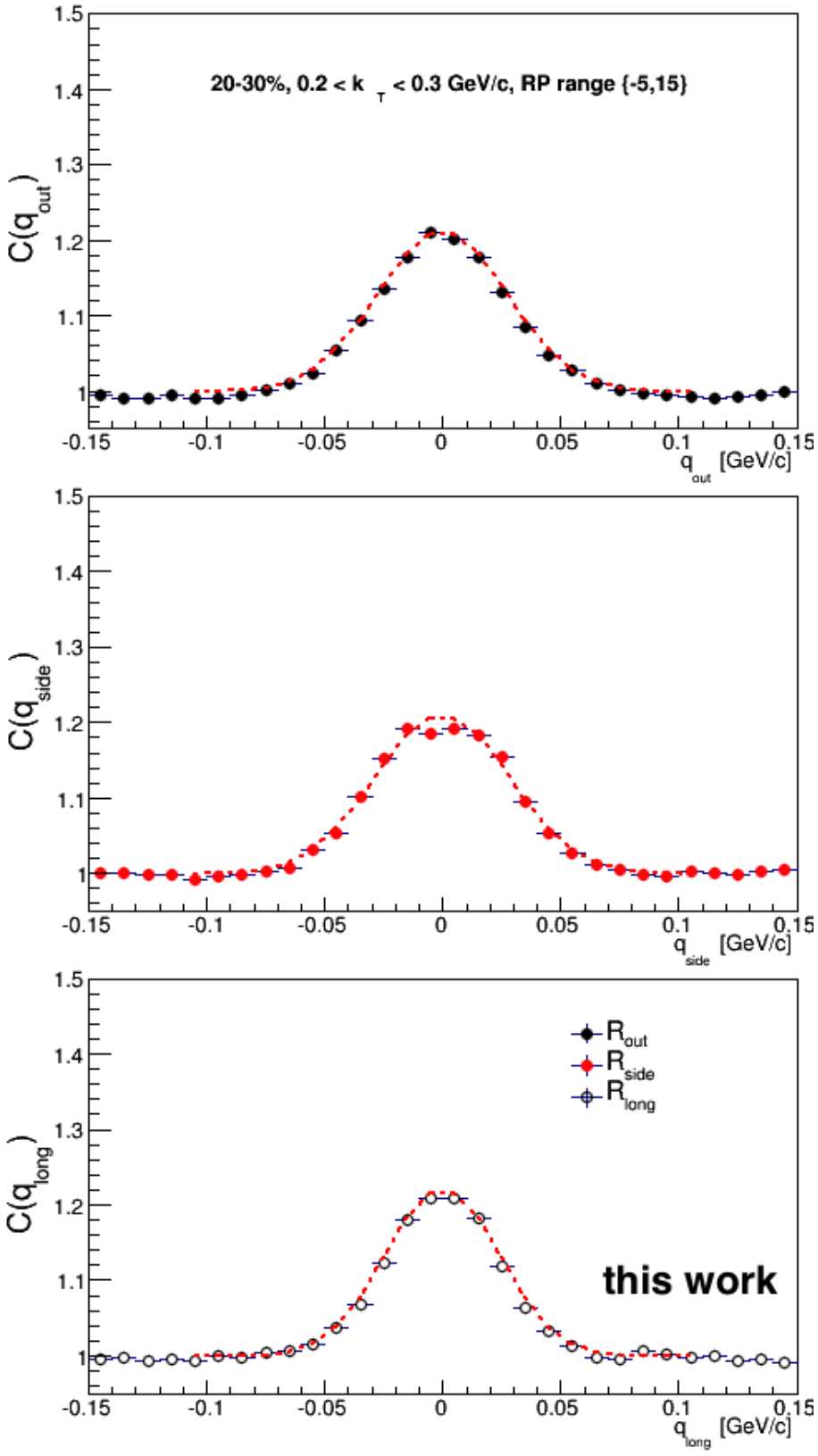

Figure 4.38: $C(q_{out})$, $C(q_{side})$, and $C(q_{long})$ 20-30% centrality, $0.2 < k_T < 0.3$ GeV/c, reaction plane angle $(-5°, 15°)$, 10 MeV/c bin width

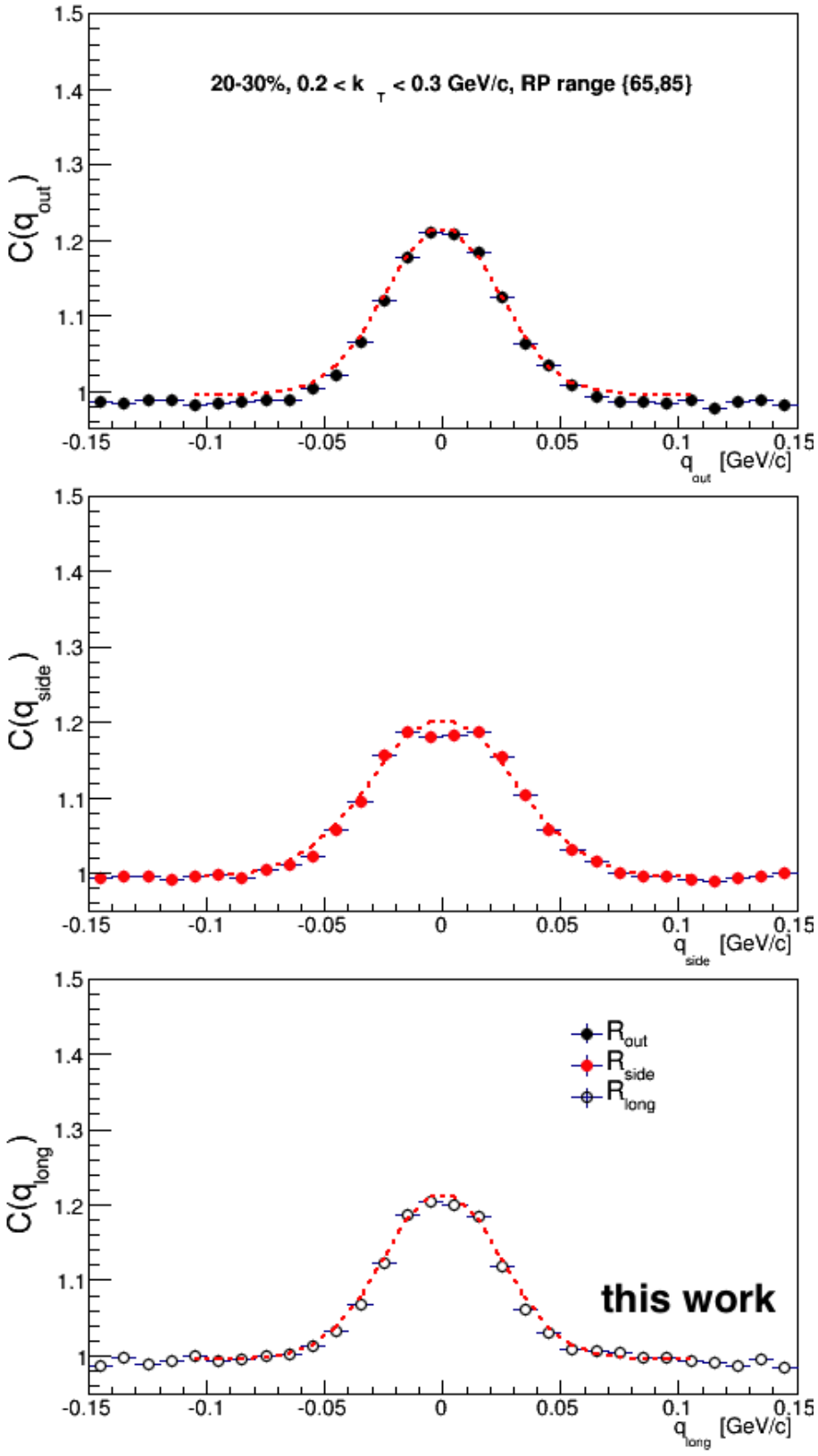

Figure 4.39: $C(q_{out})$, $C(q_{side})$, and $C(q_{long})$ 20-30% centrality, $0.2 < k_T < 0.3$ GeV/c, reaction plane angle $(65°, 85°)$, 10 MeV/c bin width

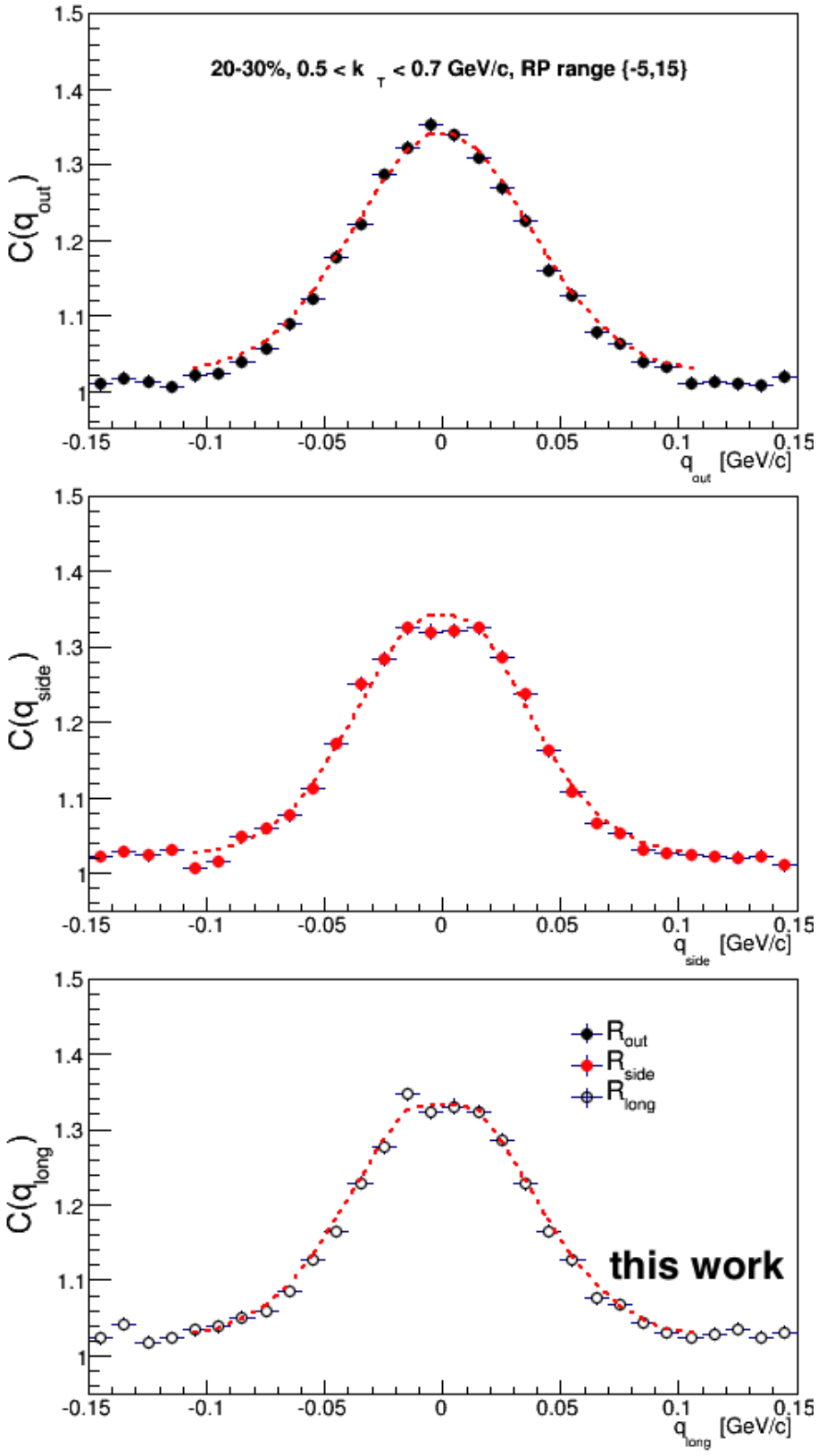

Figure 4.40: $C(q_{out})$, $C(q_{side})$, and $C(q_{long})$ 20-30% centrality, $0.5 < k_T < 0.7$ GeV/c, reaction plane angle $(-5°, 15°)$, 10 MeV/c bin width

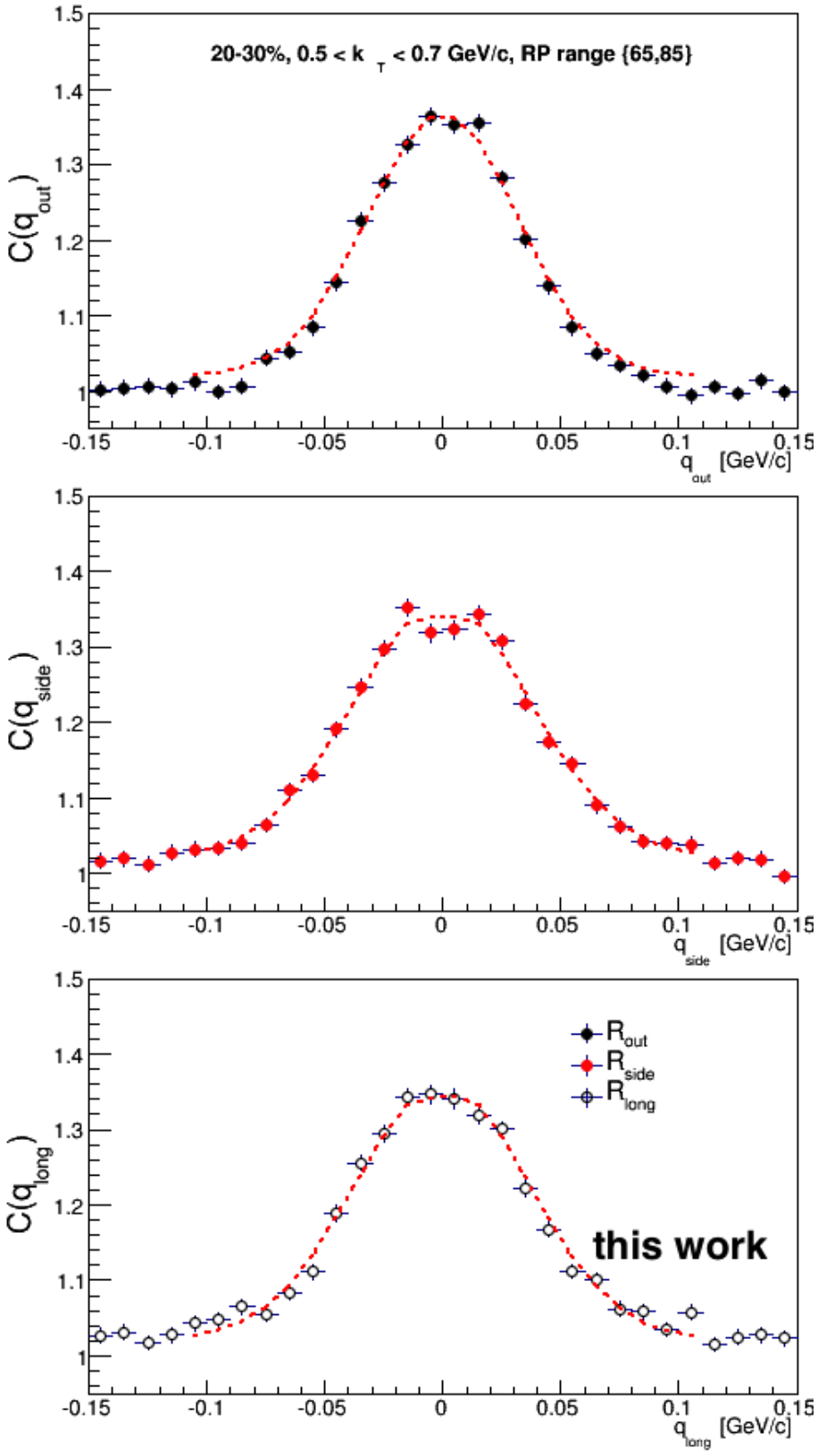

Figure 4.41: $C(q_{out})$, $C(q_{side})$, and $C(q_{long})$ 20-30% centrality, $0.5 < k_T < 0.7$ GeV/c, reaction plane angle $(65°, 85°)$, 10 MeV/c bin width

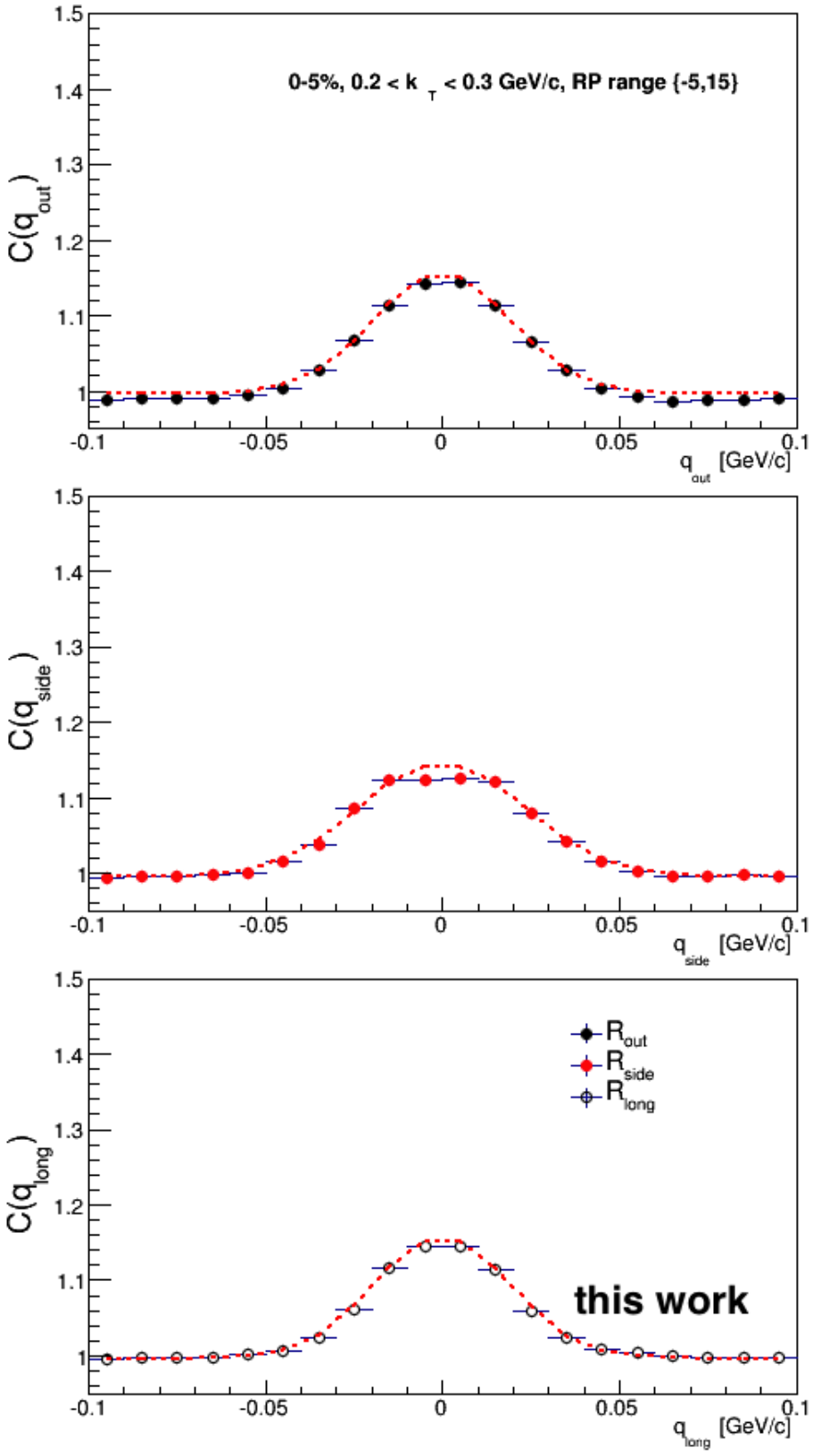

Figure 4.42: $C(q_{out})$, $C(q_{side})$, and $C(q_{long})$ 0-5% centrality, $0.2 < k_T <$0.3 GeV/c, reaction plane angle $(-5°, 15°)$, 10 MeV/c bin width

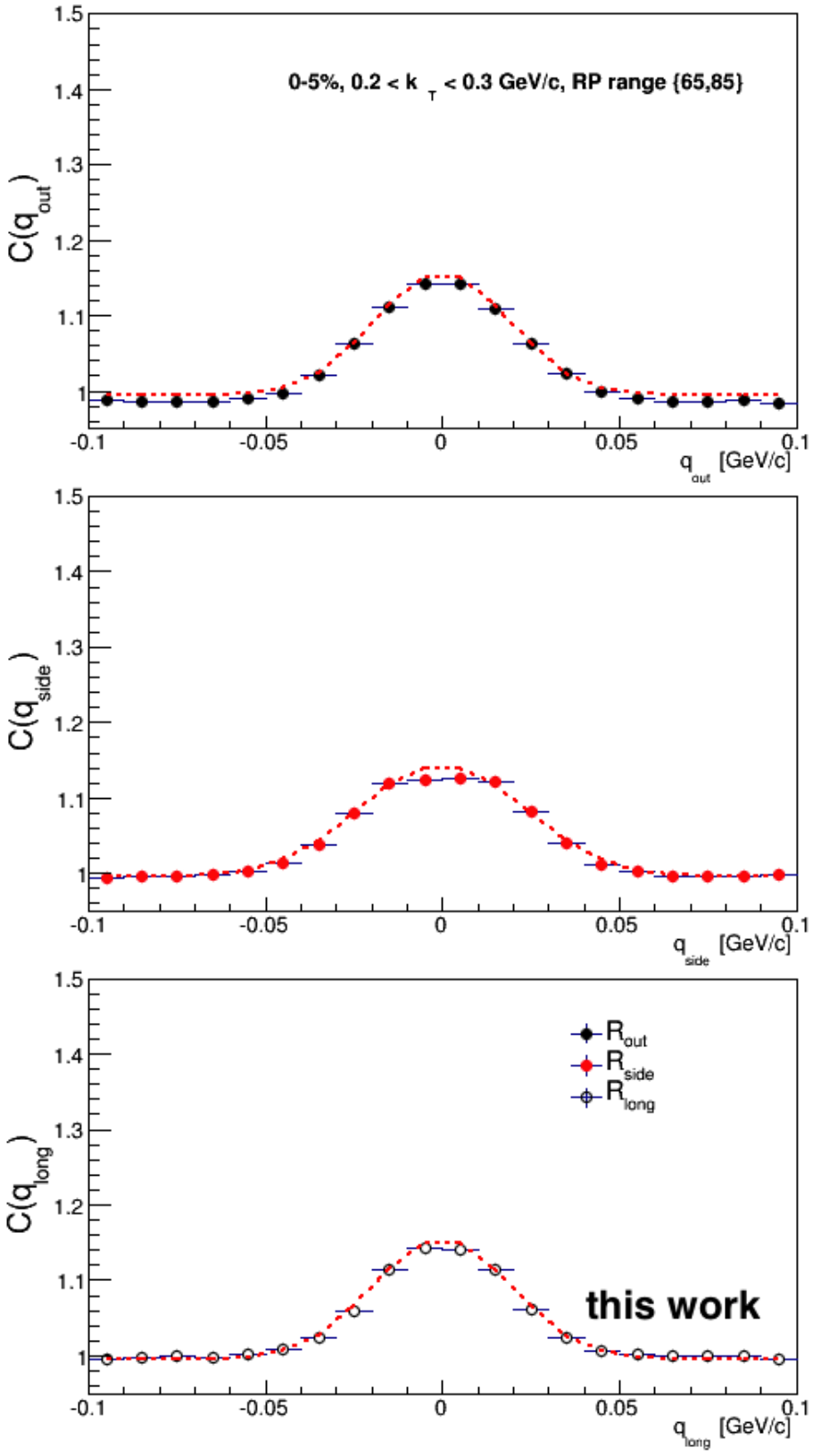

Figure 4.43: $C(q_{out})$, $C(q_{side})$, and $C(q_{long})$ 0-5% centrality, $0.2 < k_T <$0.3 GeV/c, reaction plane angle $(65°, 85°)$, 10 MeV/c bin width

4.7.4 Radii Oscillation

In case of an anisotropic source, the transverse radii oscillate as a function of the pair emission angle. To investigate the angular dependence, the radii are fit with the following formulas[45]:

$$\begin{aligned} R^2_{out}(\phi) &= R^2_{out,0} + 2R^2_{out,2}\cos(2\phi) \\ R^2_{side}(\phi) &= R^2_{side,0} + 2R^2_{side,2}\cos(2\phi) \\ R^2_{long}(\phi) &= R^2_{long,0} + 2R^2_{long,2}\cos(2\phi) \\ R^2_{outside}(\phi) &= R^2_{outside,2}\sin(2\phi) \end{aligned} \tag{4.29}$$

The HBT radii are extracted in bins of pair emission with respect to the second order reaction plane. The following figure shows the centrality dependence in the range 0-50% at the k_T range 0.3-0.4 GeV/c. The radii for R_{out}, R_{side}, and R_{long} are shown in Figure 4.46. The radii decrease from central to peripheral events. The λ parameter is also shown to ensure that the oscillations are not due to the fit fluctuation. Figure 4.47 shows the cross radii centrality dependence at a k_T range 0.3-0.4 GeV/c. The terms R_{sl} and R_{ol} are around zero, whereas R_{os} shows a sine oscillation.

Table 4.6: χ^2/NDF for 1D Projections of $C(q_{out}, q_{side}, q_{long})$, 10 MeV/c bin width

Figure	q range (MeV/c)	centrality	k_T range (GeV/c)	Reaction Plane Angle	χ^2//NDF	(+/-) bins (other dim.)	$R_{out}(fm)$	R_{side} (fm)	R_{long} (fm)
4.38	100	20-30 %	0.2< k_T <0.3	$\{-15°,\ 5°\}$	1.938	2	5.04	4.93	5.79
4.39	100	20-30 %	0.2< k_T <0.3	$\{65°,\ 85°\}$	1.898	2	5.91	4.68	5.81
4.40	100	20-30 %	0.5< k_T <0.7	$\{-15°,\ 5°\}$	1.838	3	3.76	4.05	3.78
4.41	100	20-30 %	0.5< k_T <0.7	$\{65°,\ 85°\}$	1.831	3	4.35	3.68	3.76
4.42	100	0-5 %	0.2< k_T <0.3	$\{-15°,\ 5°\}$	2.440	2	7.22	6.07	7.25
4.43	100	0-5 %	0.2< k_T <0.3	$\{65°,\ 85°\}$	2.409	2	7.40	6.03	7.18
4.44	100	40-50 %	0.2< k_T <0.3	$\{-15°,\ 5°\}$	1.958	3	3.93	3.96	4.59
4.45	70	20-30 %	0.2< k_T <0.3	$\{-15°,\ 5°\}$	1.875	2	5.15	5.03	5.94

4.7.4.1 k_T dependence

The k_T dependence at the centrality of 20-30% using all magnetic field polarities is shown in Figure 4.48. As k_T increases,the radii decrease, however, there is no dependence on k_T for the cross radii terms.

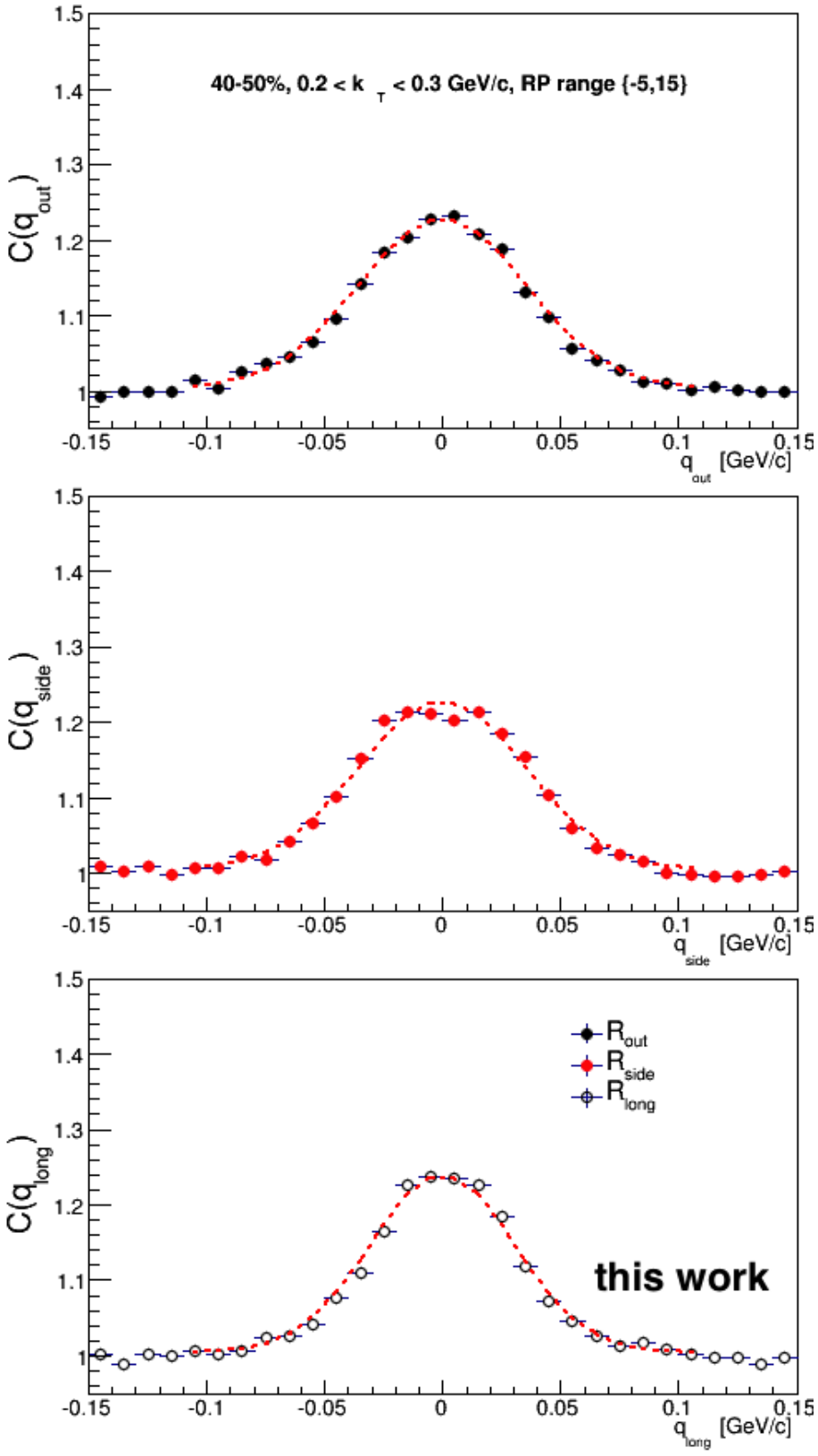

Figure 4.44: $C(q_{out})$, $C(q_{side})$, and $C(q_{long})$ 40-50% centrality, $0.2 < k_T < 0.3$ GeV/c, reaction plane angle $(-5°, 15°)$, 10 MeV/c bin width

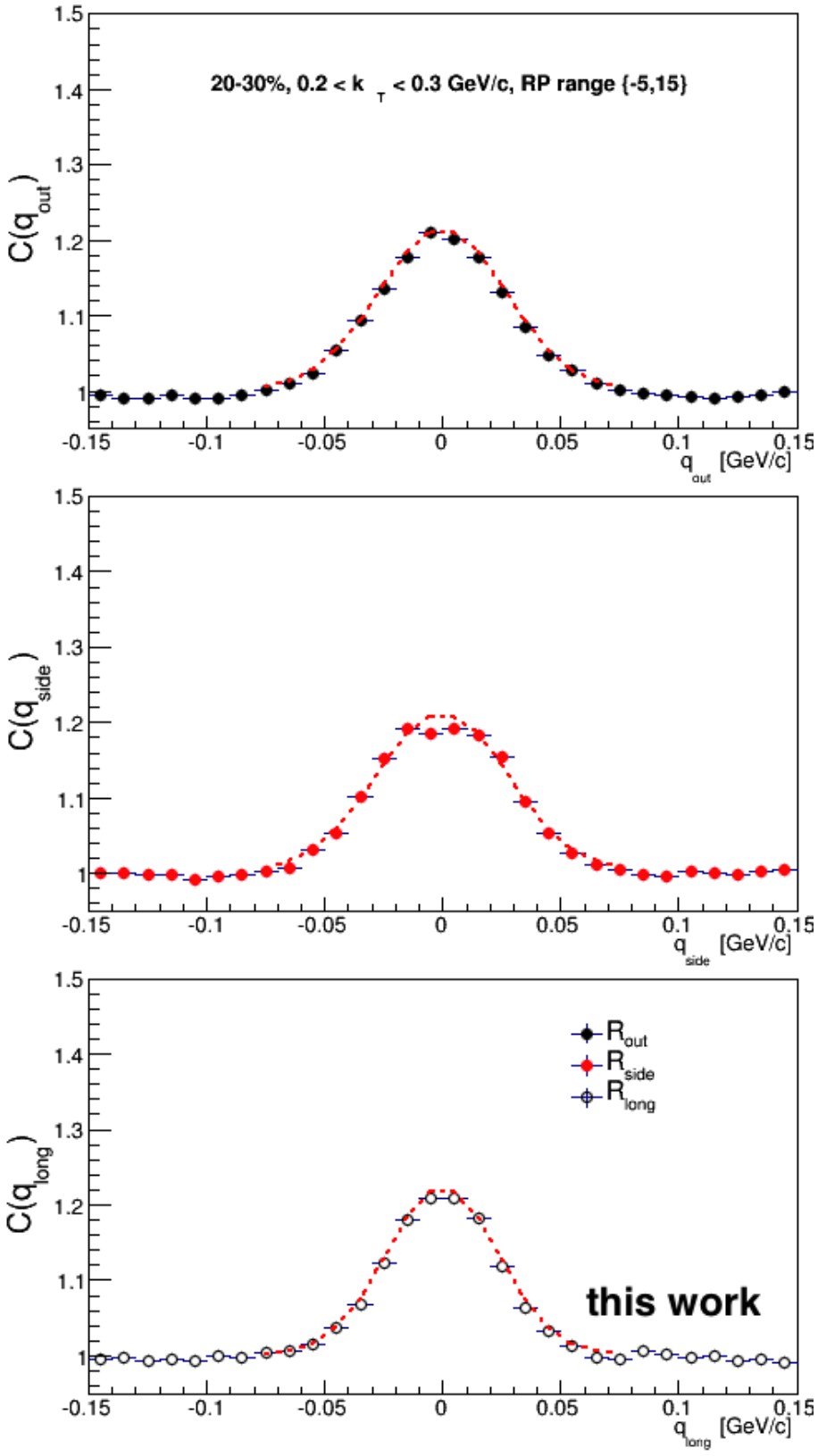

Figure 4.45: $C(q_{out})$, $C(q_{side})$, and $C(q_{long})$ q range 70 MeV/c, 20-30% centrality, $0.2 < k_T < 0.3$ GeV/c, reaction plane angle $(-15°, 5°)$,10 MeV/c bin width

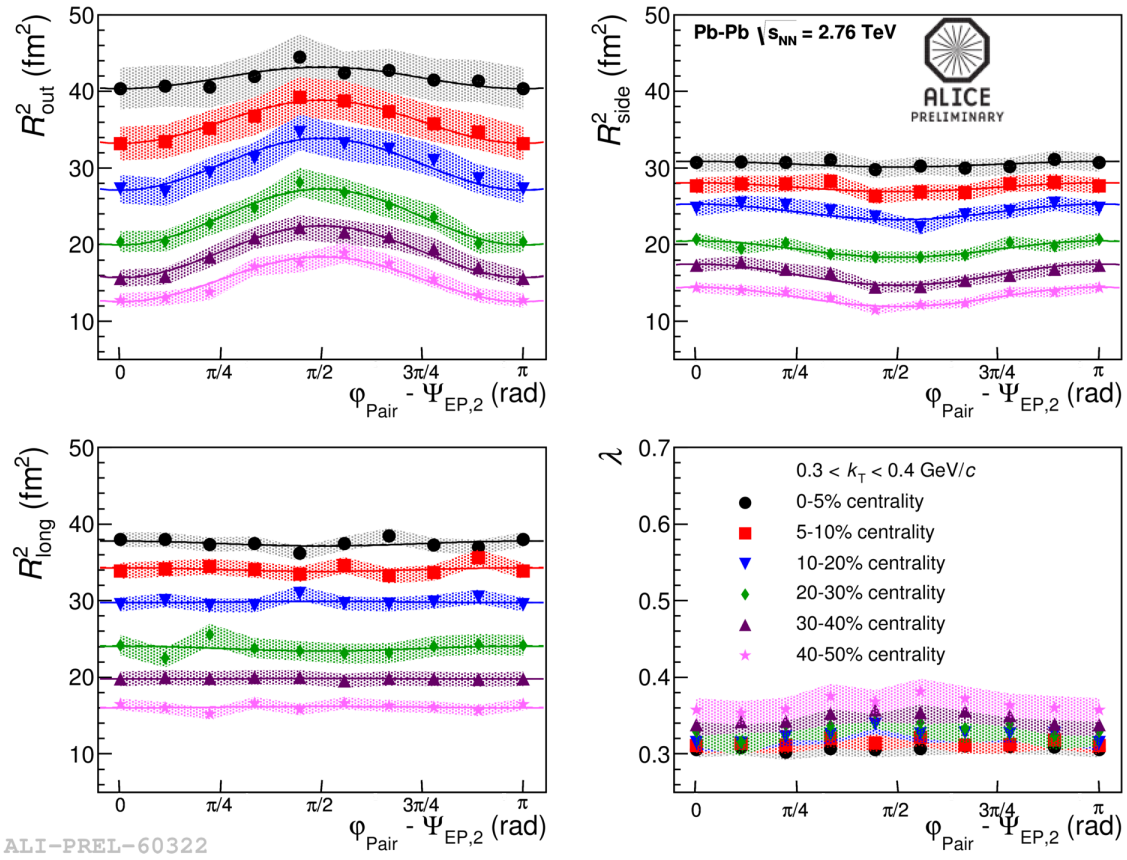

Figure 4.46: Centrality dependence of radii vs. pair emission angle at k_T range of 0.3-0.4 GeV/c

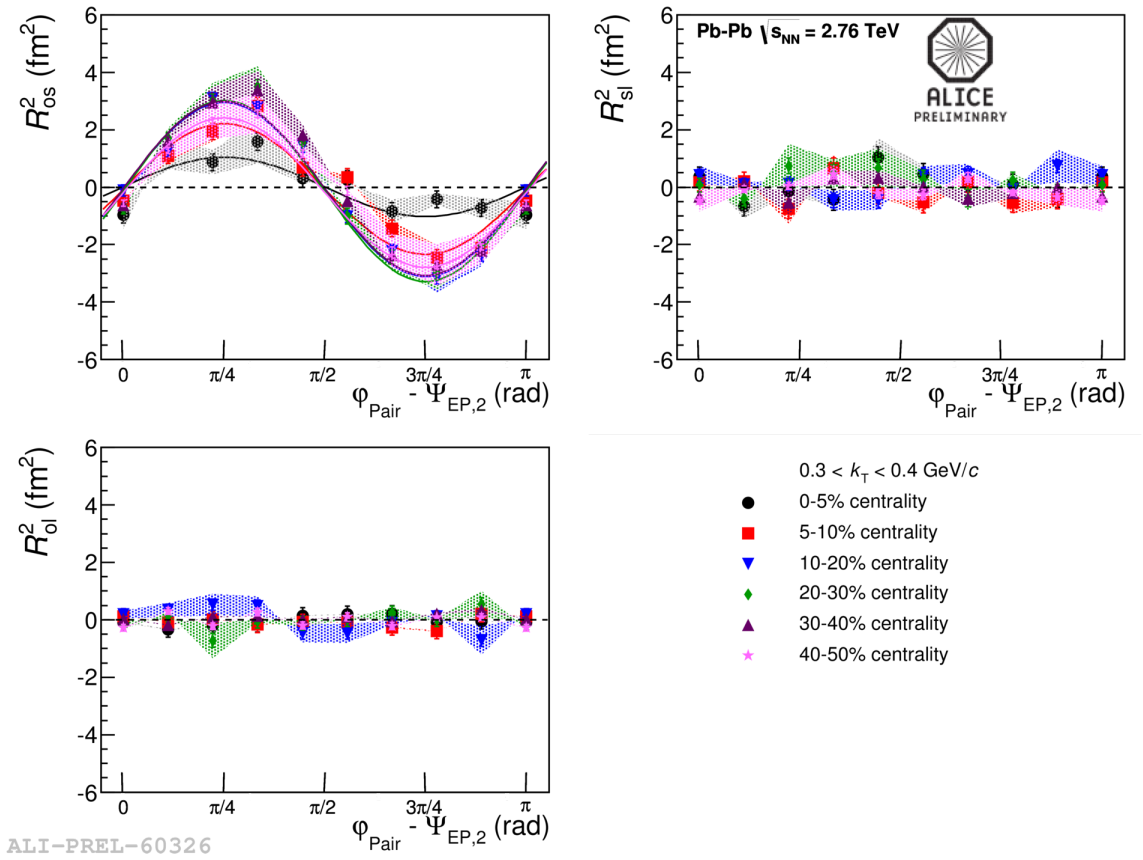

Figure 4.47: Centrality dependence of cross radii vs. pair emission angle at k_T range of 0.3-0.4 GeV/c

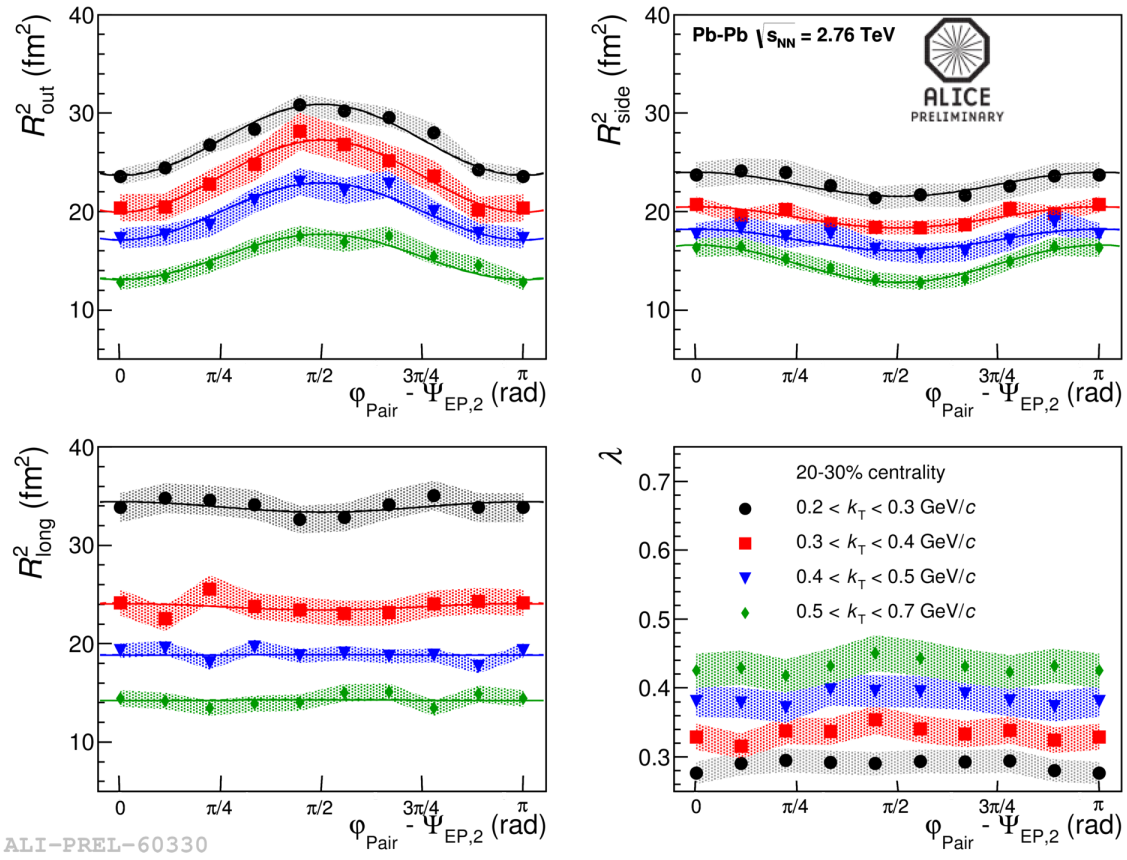

Figure 4.48: k_T dependence of radii vs. pair emission angle at centrality 20-30%

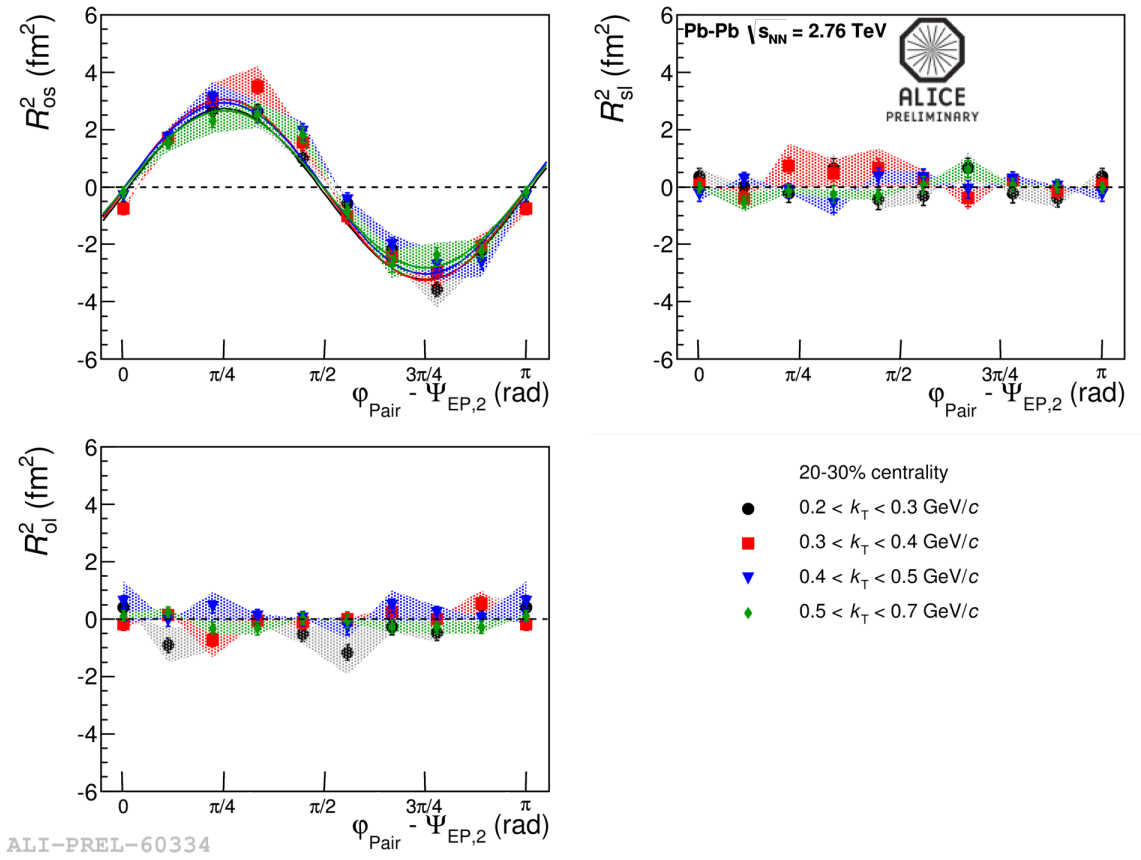

Figure 4.49: k_T dependence of cross radii vs. pair emission angle at centrality 20-30%

4.7.5 Average Radii and Normalized Oscillation Amplitudes

The average values R_{out}, R_{side}, and R_{long} decrease from central to peripheral, see Figure 4.50. The R_{os} average value is zero. The normalized oscillation amplitudes are shown in Figure 4.51.

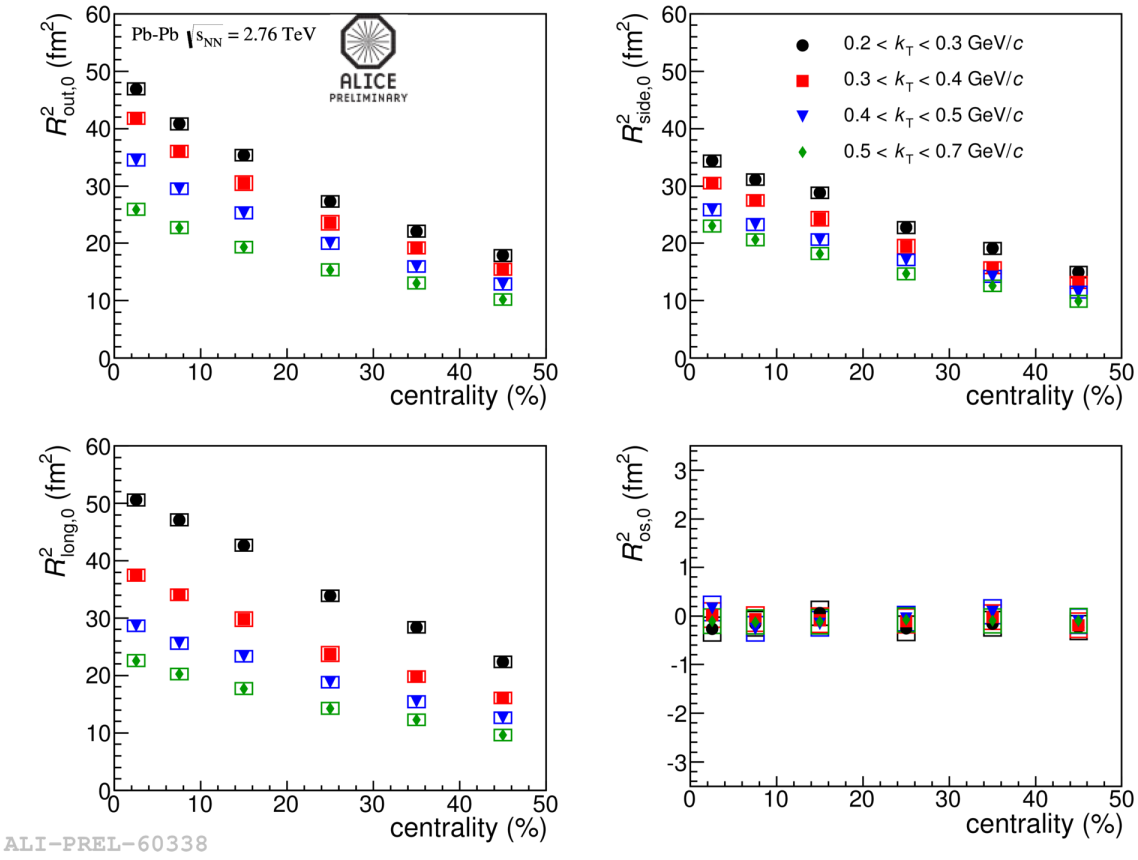

Figure 4.50: Average radii vs. centrality

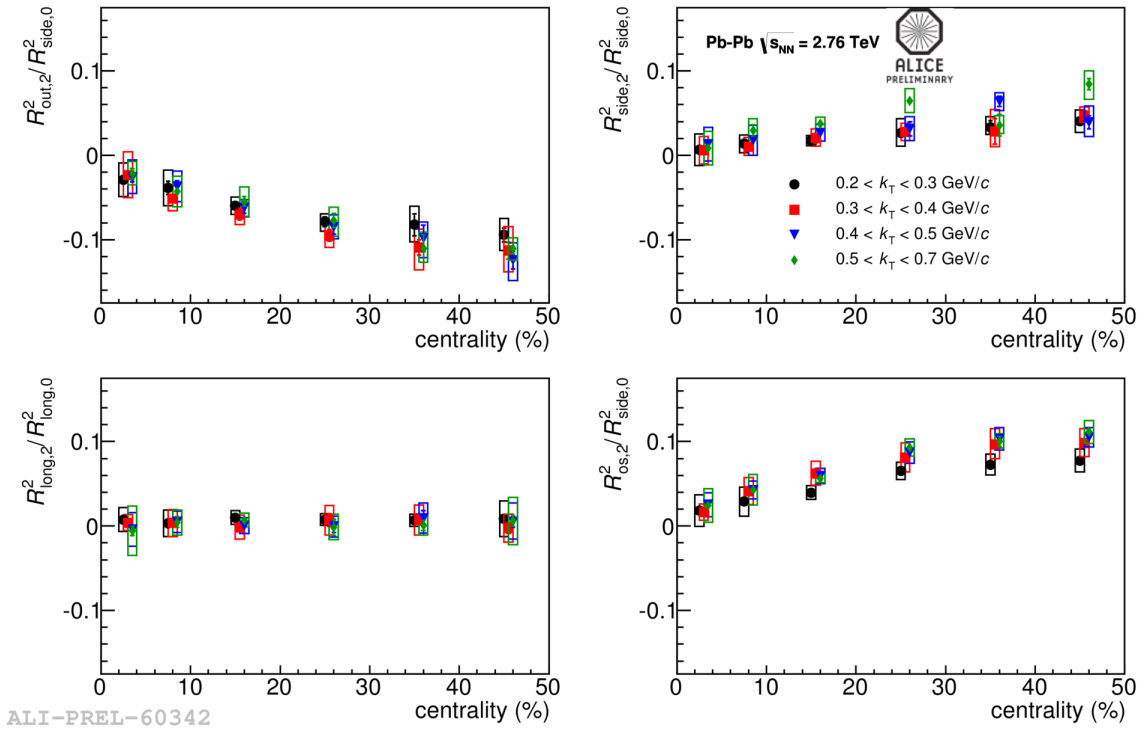

Figure 4.51: Oscillation amplitudes for different pair momenta depending on event centrality

In this analysis, non-azimuthally differential two pion femtoscopy is compared to the the azimuthally differential pion femtoscopy results. The Pb-Pb dataset is used for the non-azimuthal analysis from November and December of 2010 with 12 million min-bias events. There were seven centrality bins 0-5%, 5-10%, 10-20%, 20-30%, 30-40%, 40-50%, and 50-60%. The k_T (average pair momentum) ranges were grouped in seven groups, 0.2-0.3,0.3-0.4, 0.4-0.5, 0.5-0.6, 0.6-0.7, 0.7-0.8, and 0.8-1.0 GeV/c. The femtoscopic radii are obtained by fitting the Bowler-Sinyokov formula:

$$C(q) = (1-\lambda) + \lambda K_c[1 + exp(-R^2_{out}q^2_{out} - R^2_{side}q^2_{side} - R^2_{long}q^2_{long})] \qquad (4.30)$$

The non-azimuthally differential results are shown in Figure 4.52. Similar to the behavior shown in Figure 4.50, the radii are increasing for lower k_T and for more central collisions. The radii obtained with the azimuthally differential results were described in Eq. 4.29 were the zeroth order radii ($R^2_{out,0}$,$R^2_{side,0}$,$R^2_{long,0}$) do not depend on the event plane and therefore have no azimuthal dependence. These results should be comparable to the non-azimuthally differential results. The results are compared in Figure 4.53. The mid-central collisions, the azimuthal and non-azimuthally differential femtoscopy have the same values within statistics.

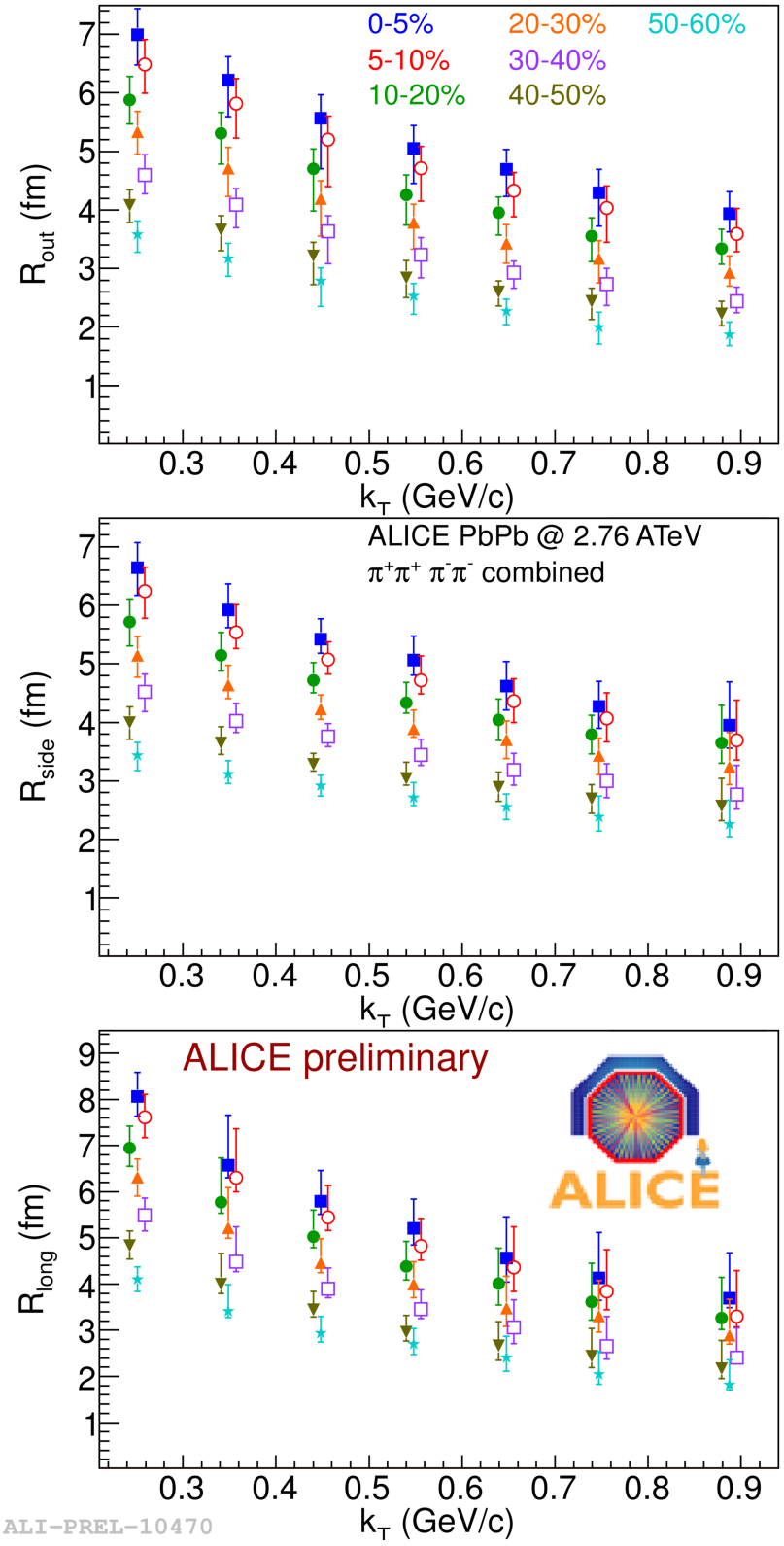

Figure 4.52: Centrality and k_T dependence of the Non-azimuthally differential pion femtoscopic radii in PbPb collisions at 2.76 ATeV. Vertical error bars show statistical+systematic error. R_{out}, R_{side}, and R_{long} are shown. Points are shifted slightly in the x direction for visibility. [112]

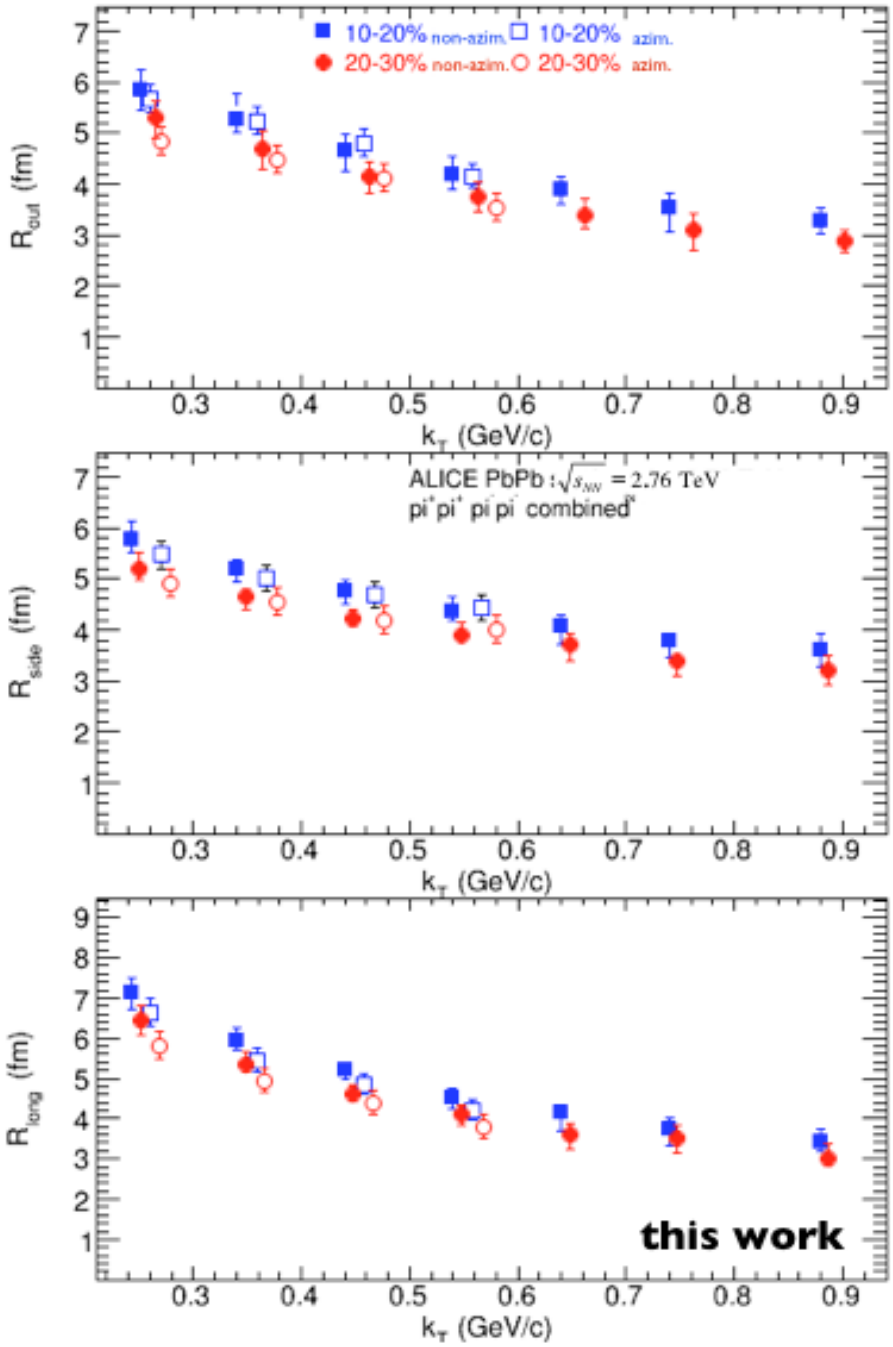

Figure 4.53: Comparison of azimuthally differential pion femtoscopy and non-azimuthally differential pion femtoscopy vs. k_T. Open symbols show the azimuthally differential results, Closed symbols show the non-azimuthally differential results. All points are shifted along the x-axis for visibility.

4.7.6 Corrections

4.7.6.1 ψ Efficiency Correction

The efficiency correction is applied to the ϕ distribution to correct for the uniformity in the detector. The uncorrected ϕ distribution is shown for the tracks from the TPC, see Figure 4.54. To perform the correction, the phi distribution is inverted and used as weights applied per bin for particles also used for the Q vector. Several runs with similar detector efficiency were taken together in order to increase statistics. The results of this efficiency correction is seen in Figure 4.55.

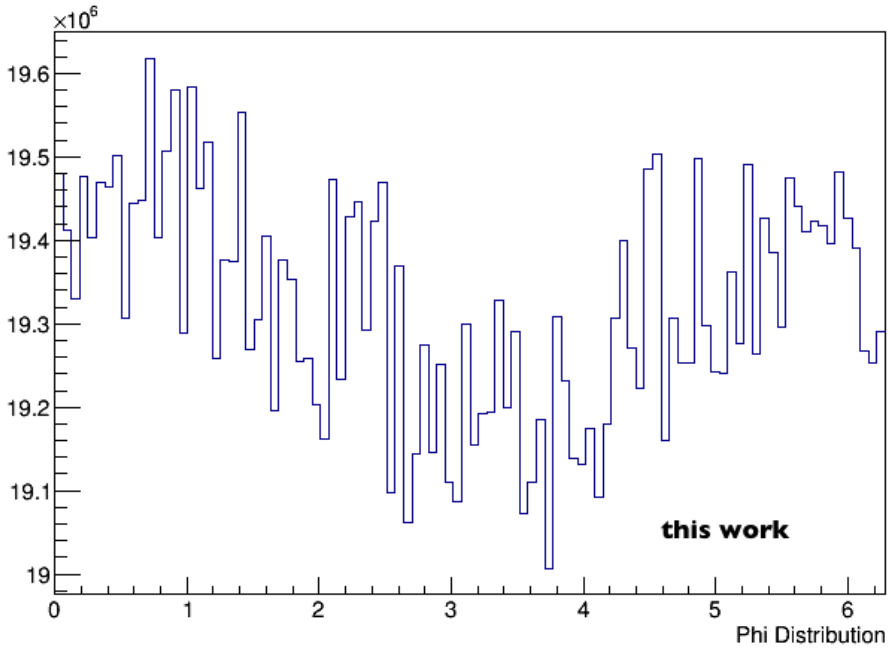

Figure 4.54: ψ distribution before efficiency correction

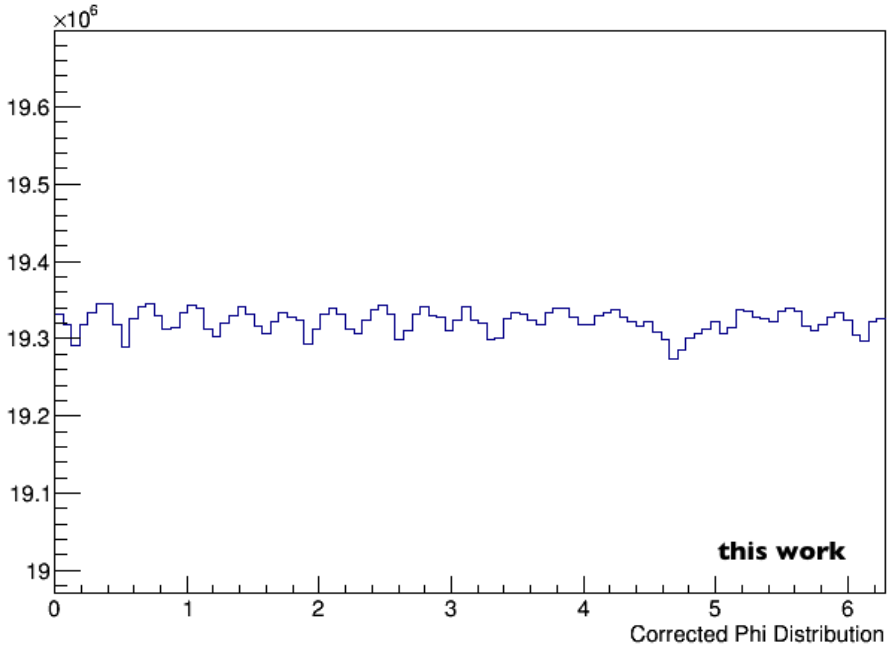

Figure 4.55: ψ distribution after efficiency correction

4.7.6.2 Coulomb Wave Function

The Coulomb interaction between two pions of the pair affects the extracted radii and must be included in the fit. The squared Coulomb wave function averaged over a Gaussian source with a comparable size to the mean of the extracted radii was calculated and included in the fit. The Coulomb source sizes used for each centrality bin are listed in Table 4.7:

Table 4.7: Coulomb source sizes per centrality bin

Event Centrality	Coulomb Source
0-5%	11 fm
5-10%	10 fm
10-20%	9 fm
20-30%	8 fm
30-40%	7 fm
40-50%	6 fm

4.7.6.3 Squared Coulomb wave function

The squared Coulomb wave function integrated over a source is shown with R=11 fm, see Figure 4.56, and R=6 fm, see Figure 4.57.

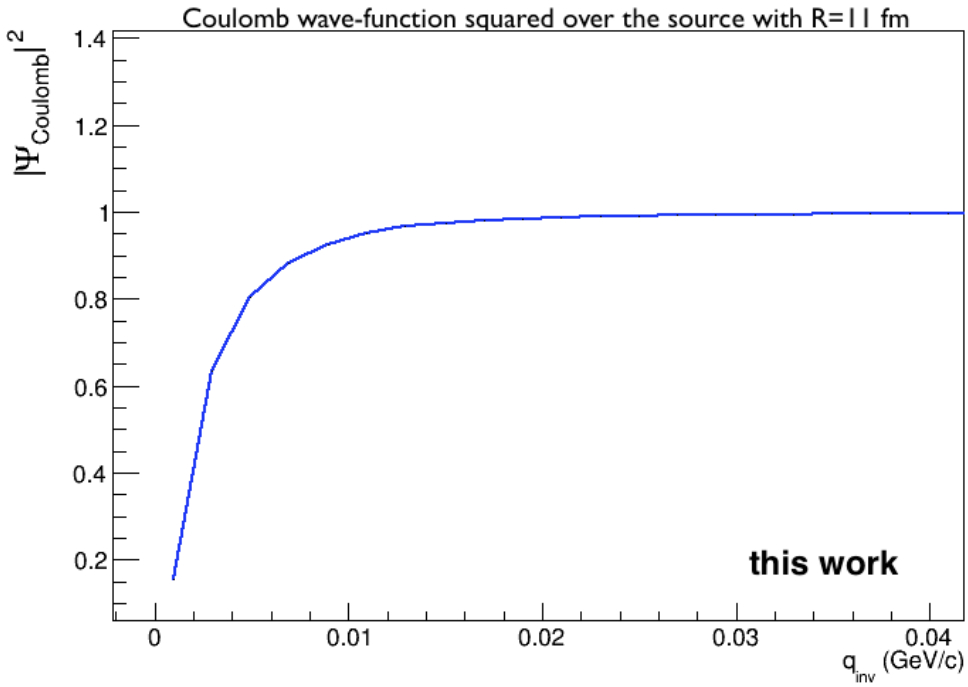

Figure 4.56: Squared Couloumb wave function with R=11 fm [113]

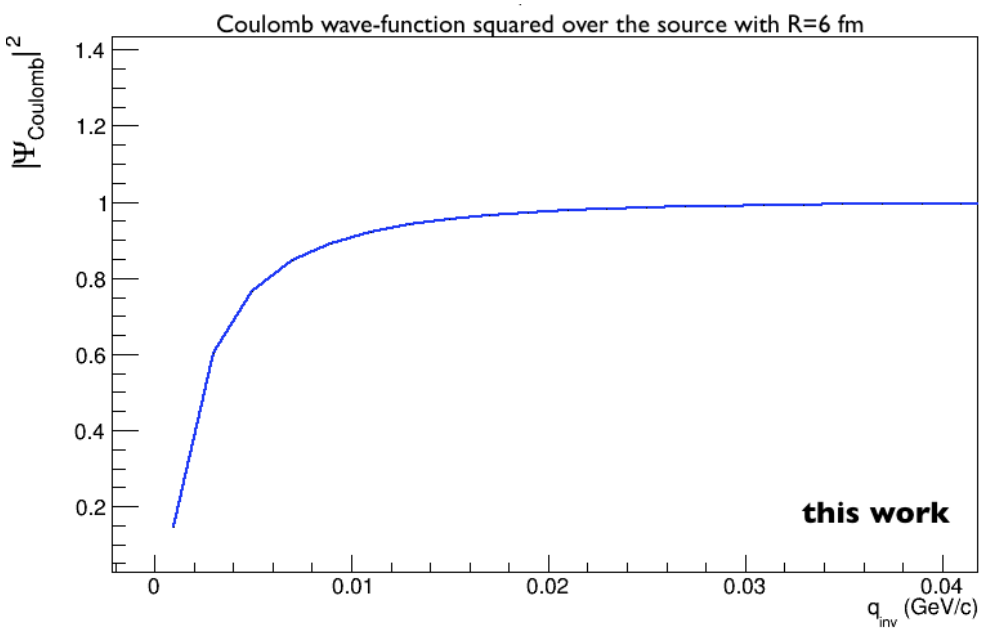

Figure 4.57: Squared Couloumb wave function for R=6 fm [113]

4.7.6.4 Momentum Resolution

The momentum resolution for the detector broadens the correlation peak and therefore reduces the extracted HBT radii. Using a Monte Carlo study for LHC10h, an artificial correlation is introduced by applying a Gaussian weight to the pairs according to the momentum difference. The input radii are compared to the result extracted from the reconstructed Monte Carlo tracks. The correction factors are determined in each bin of k_T and applied to the experimental HBT radii.

In Figure 4.58-4.59, the ratio is shown of the radii corrected and uncorrected radii for momentum resolution.

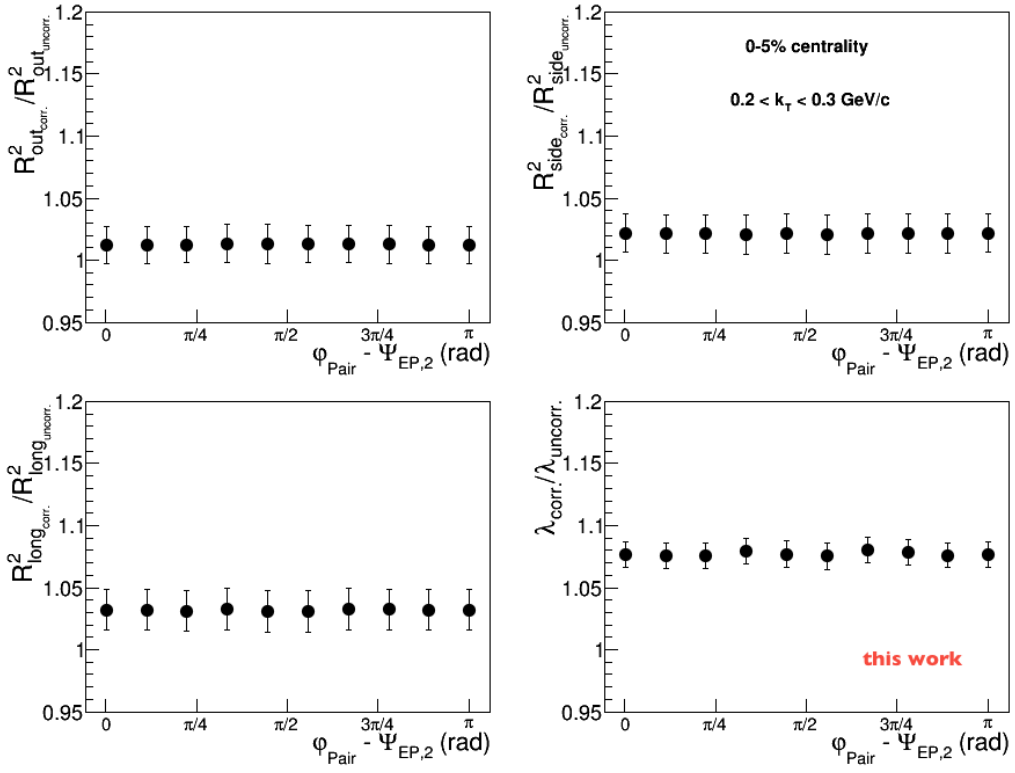

Figure 4.58: ratio of radii corrected/uncorrected for momentum resolution 0-5 % centrality $0.2 < k_T < 0.3$ GeV/c

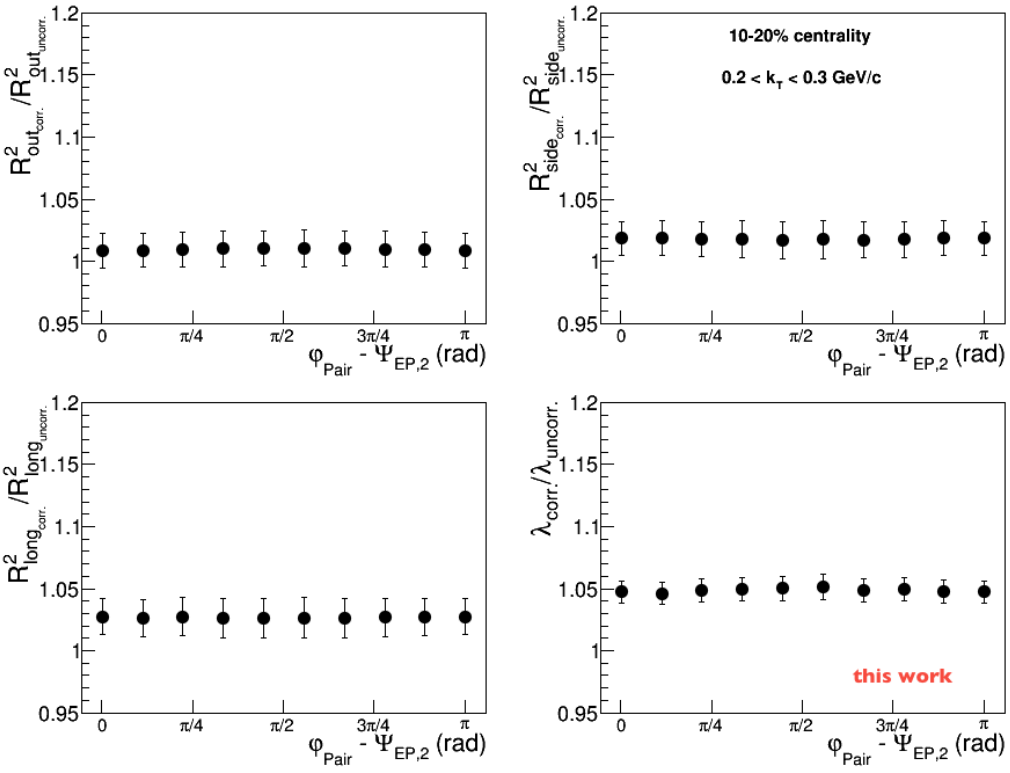

Figure 4.59: ratio of radii corrected/uncorrected for momentum resolution 10-20 % centrality $0.2 < k_T < 0.3$ GeV/c

4.7.6.5 Event Plane Resolution Correction

The event plane resolution corrections are described in Chapter 3. The centrality dependence of the 2nd order event plane resolution of the TPC using random sub events is given in the following Figure 4.60 and the values are in Table 4.8.

Table 4.8: TPC Event Plane Resolution using two random subevents

Event Centrality	TPC Resolution
0-5%	0.8809251
5-10%	0.897759
10-20%	0.93373
20-30%	0.944746
30-40%	0.934408
40-50%	0.904495

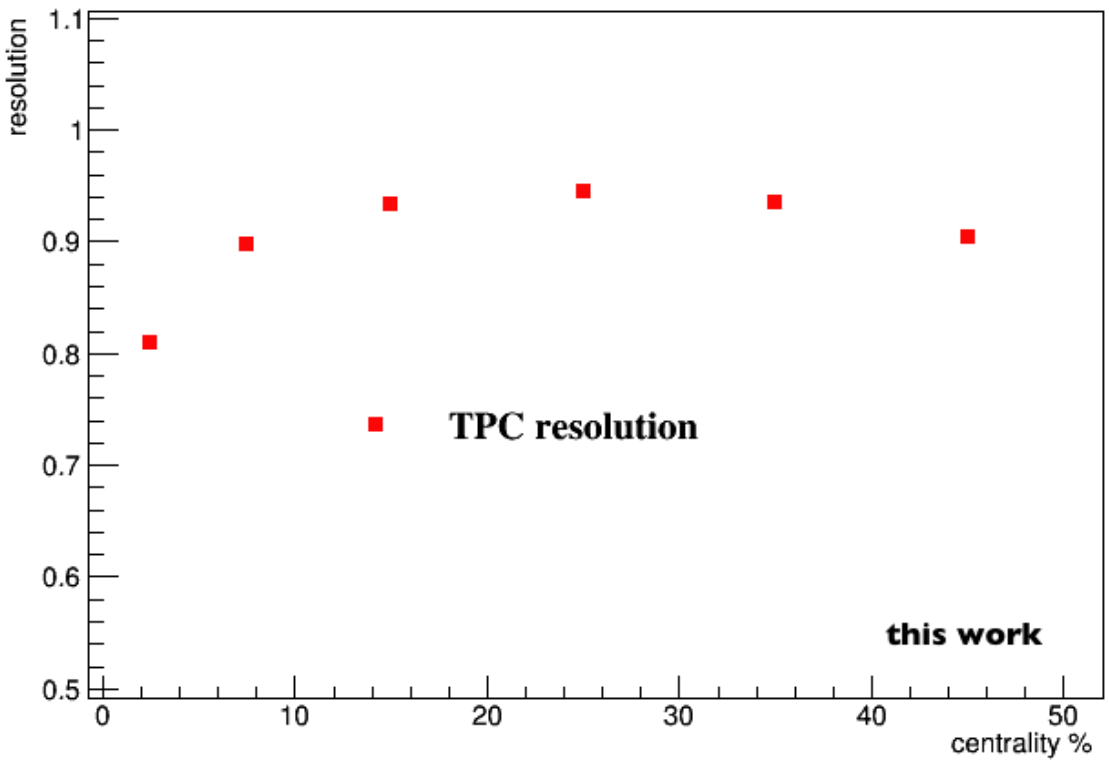

Figure 4.60: Centrality dependence of the event plane resolution

The bin-by-bin event plane correction on the radii can be seen in Figures 4.61-4.62. This method was not used for the final radii results.

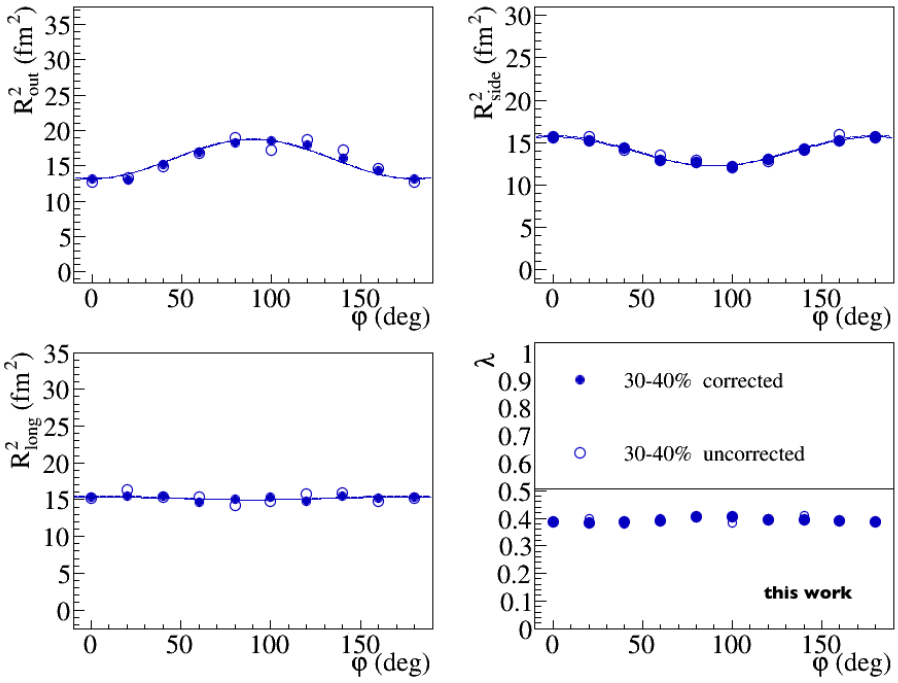

Figure 4.61: Bin-by-bin event plane resolution correction for radii at centrality 30-40% 0.3< k_T < 0.4

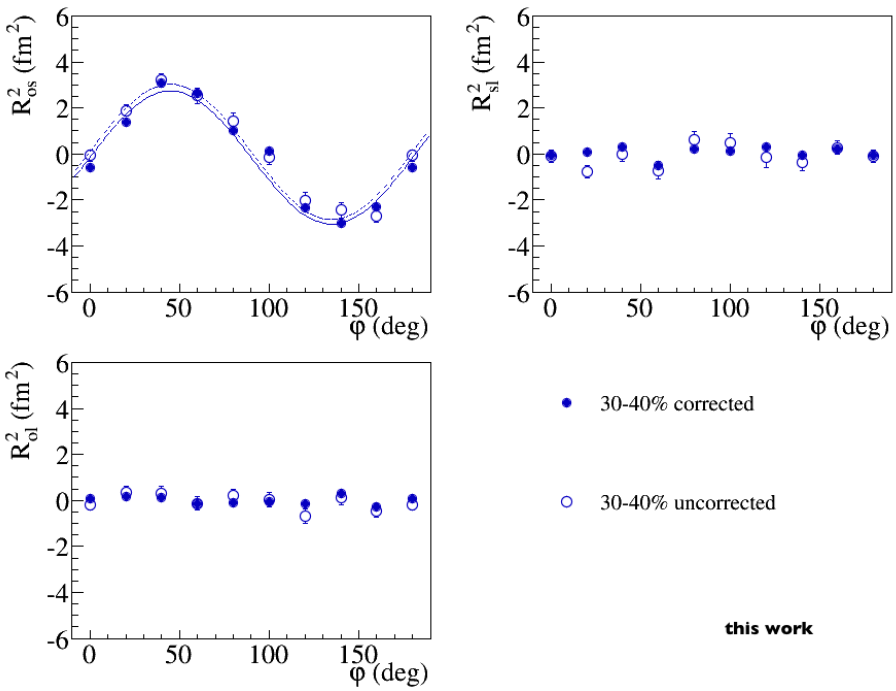

Figure 4.62: Bin-by-bin event plane resolution correction for cross radii for centrality 30-40%, $0.3 < k_T < 0.4$.

The E895 method is used for the event plane correction. This method will correct the radii oscillation term ($R^2_{j,2}$ where j=out, side,long, and out-side).

The systematics for correction to the event plane radii oscillation term was obtained by taking the % difference between three sub-events and two random sub events and obtained from the ALICE performance paper [116], see Figure 4.63.

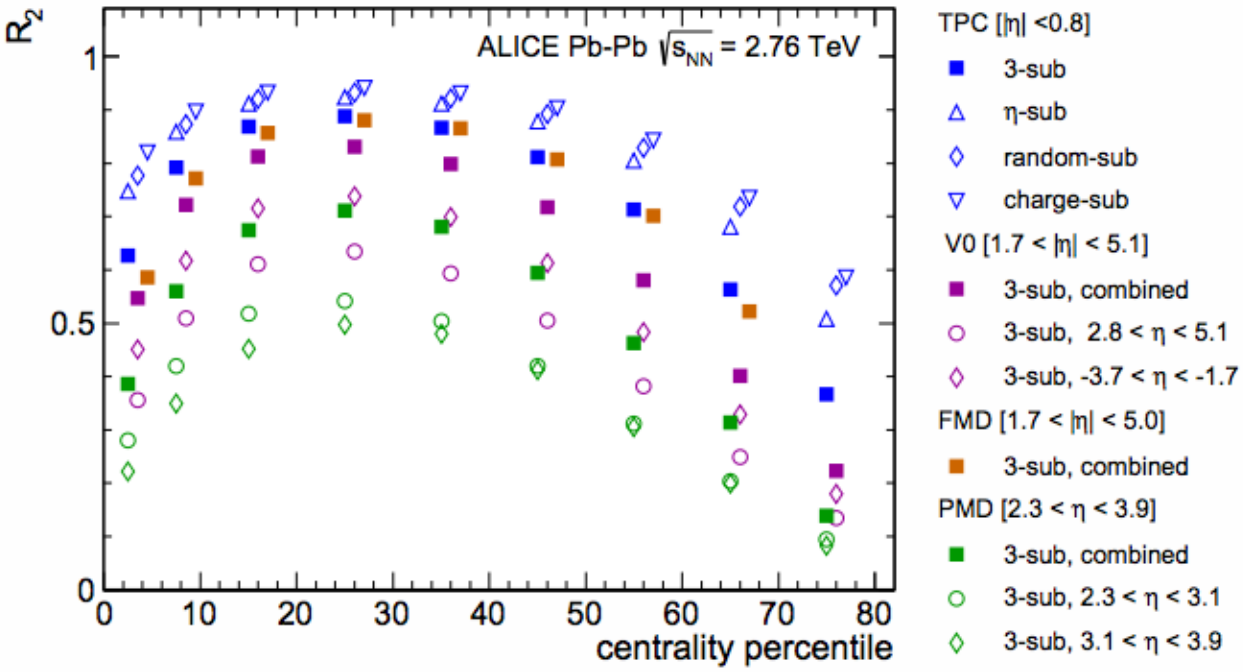

Figure 4.63: Resolution of the second-order event plane angle, Ψ_2^{EP}, vs. the collision centrality extracted from two and three-detector subevent correlations for TPC, V0, FMD, and PMD [116]

The values used for the systematic are shown in the table below:

Table 4.9: Systematic for Event Plane Resolution of the radii oscillation term $R^2_{j,2}$

Event Centrality	Systematic event plane
0-5%	17 %
5-10%	6 %
10-20%	2 %
20-30%	2 %
30-40%	5 %
40-50%	12 %

The systematics for the radii oscillations was estimated using the results from STAR in which the first method was applied, the correction to the numerators and denominators. The values from both ranges of k_T were averaged and used as a systematic for the radii oscillations. The data can be seen in Figure 4.64 and the values are in Table 4.10 [117].

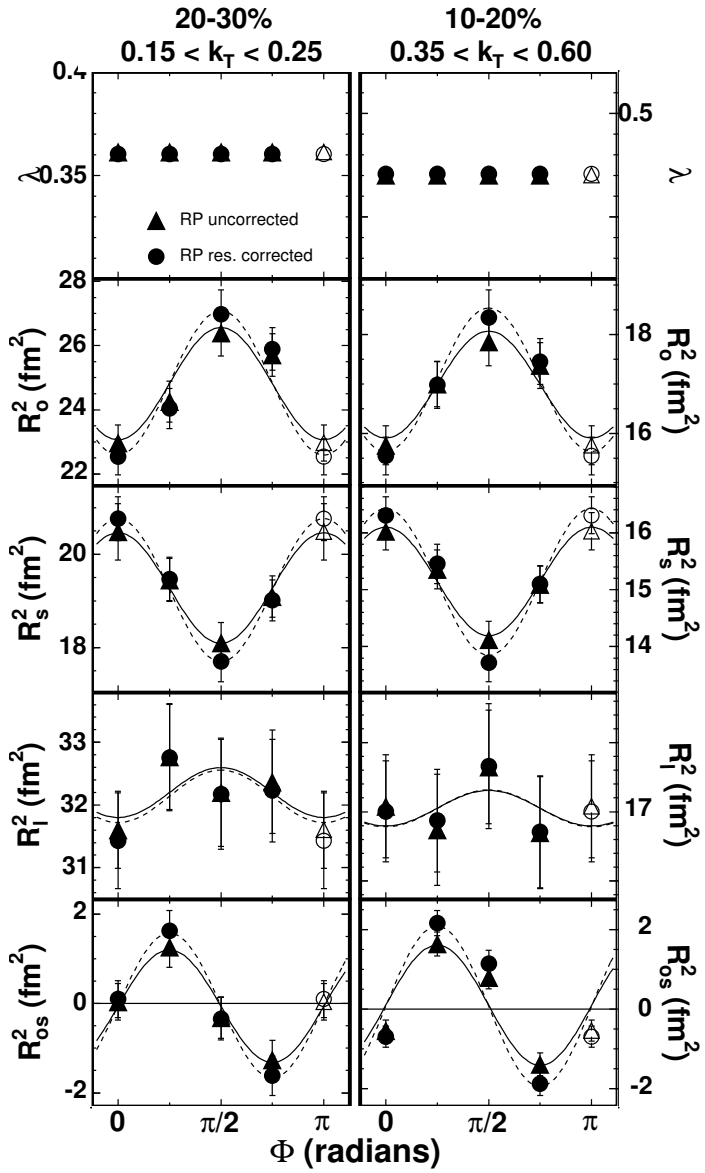

Figure 4.64: STAR bin-by-bin event plane resolution correction [117]

Table 4.10: Squared Radii vs Azimuthal Angle Uncorrected & Corrected EP resolution

			20-30%	$0.15 < k_T < 0.25$
Rout	0°	45°	90°	135°
uncorrected	22.96	24.25	26.4	25.71
corrected	22.54	24.04	27	25.9
% difference	1.85	0.87	2.25	0.74
			10-20%	$0.35 < k_T < 0.45$
Rout	0°	45°	90°	135°
uncorrected	0.54	1.63	0.8	1.38
corrected	0.69	2.16	1.14	1.88
% difference	24.39	27.97	35.05	30.67
			20-30%	$0.15 < k_T < 0.25$
Rside	0°	45°	90°	135°
uncorrected	20.48	19.45	18.1	19.09
corrected	20.77	19.47	17.7	19.01
% difference	1.41	0.10	2.33	0.42
			10-20%	$0.35 < k_T < 0.45$
Rside	0°	45°	90°	135°
uncorrected	16.03	15.36	14.12	15.09
corrected	16.3	15.45	13.72	15.1
% difference	1.67	0.58	2.87	0.07
			20-30%	$0.15 < k_T < 0.25$
Rlong	0°	45°	90°	135°
uncorrected	31.6	32.77	32.2	32.370
corrected	31.43	32.76	32.17	32.23
% difference	0.54	0.03	0.09	0.43
			10-20%	$0.35 < k_T < 0.45$
Rlong	0°	45°	90°	135°
uncorrected	17.04	16.87	17.32	15.09
corrected	17	16.94	17.33	15.1
% difference	0.24	0.41	0.06	0.07
			20-30%	$0.15 < k_T < 0.25$
Routside	0°	45°	90°	135°
uncorrected	0.03	1.26	0.32	1.26
corrected	0.1	1.62	0.34	1.62
% difference	107.69	25	6.06	25
			10-20%	$0.35 < k_T < 0.45$
Routside	0°	45°	90°	135°
uncorrected	0.54	1.63	0.8	1.38
corrected	0.69	2.16	1.14	1.88
% difference	24.39	27.97	35.05	30.67

4.7.7 Systematic Uncertainty

In this analysis, there were many variables to consider for the systematic uncertainties. They are listed in Table 4.11. The variables are: pair cuts, the $\Delta\eta$, $\Delta\phi^*$ cuts described in Table 4.1, the DCA cuts, mentioned in Table 4.2, q range, which is the fit range used varied from 100 MeV to 200 MeV, charge, the difference between positive and negative pairs, B field, the difference between positive and negative magnetic field, and event plane, the difference between the TPC and the VZero event planes.

Table 4.11: Systematic Table for Centralities 0-20 %

		0–5%			5–10%			10–20%		
	k_T bin	R_{out}	R_{side}	R_{long}	R_{out}	R_{side}	R_{long}	R_{out}	R_{side}	R_{long}
pair cut	0	0.1%	0.02%	1%	0.3%	0.5%	1%	1%	1%	1%
	1	4%	0.5%	1%	0.5%	2%	4%	1%	1%	1%
	2	5%	0.4%	1%	3%	0.6%	0.9%	3%	1%	1%
	3	5%	0.5%	1%	4%	0.9%	1%	4%	1%	1%
dca cut	0	0.1%	1%	1%	1%	0.9%	2%	1%	1%	1%
	1	2%	1%	2%	2%	0.4%	2%	2%	1%	2%
	2	3%	1%	3%	3%	0.2%	3%	3%	1%	2%
	3	3%	1%	3%	2%	0.2%	2%	2%	1%	2%
q range	0	1%	1%	1%	0.8%	1%	1%	1%	1%	1%
	1	2%	1%	2%	0.8%	2%	1%	1%	1%	1%
	2	1%	1%	1%	0.3%	1%	1%	1%	2%	2%
	3	1%	1%	1%	0.5%	1%	1%	1%	2%	2.5%
charge	0	0.2%	1%	1%	1%	2%	1%	1%	2%	1%
	1	0.5%	1%	1%	1%	1%	1%	1%	1%	1%
	2	1%	2%	2%	2%	4%	4%	3%	1%	2%
	3	1%	1%	1%	1%	2%	3%	1%	1%	1%
B field	0	2%	1%	5%	1%	2%	2%	1%	1%	2%
	1	2%	2%	2%	1%	3%	1%	1%	1%	4%
	2	2%	2%	2%	2%	1%	2%	1%	3%	1%
	3	2%	2%	2%	1%	2%	2%	1%	2%	1%
Event Plane	0	0.5%	2%	2%	1%	1%	0.5%	1%	1%	2%
	1	1%	2%	5%	0.6%	2%	1%	1%	2%	1%
	2	1.5%	1%	2%	3%	1%	1%	1%	2%	1%
	3	2%	1%	4%	1%	2%	1%	2%	1%	1%
Total	0	2.3%	2.8%	5.7%	2.3%	3.3%	3.4%	2.4%	3.0%	3.5%
	1	4.9%	3.4%	5.9%	3.3%	4.3%	5.2%	3.0%	3.0%	4.9%
	2	6.5%	3.3%	4.8%	6%	4.3%	5.6%	5.5%	4.5%	3.9%
	3	6.6%	2.9%	5.7%	4.9%	3.6%	4.8%	5.2%	3.5%	3.8%

Table 4.12: Systematic Table for Centralities 20-50 %

		20–30%			30–40%			40–50%		
	k_T bin	R_{out}	R_{side}	R_{long}	R_{out}	R_{side}	R_{long}	R_{out}	R_{side}	R_{long}
pair cut	0	1%	1%	1%	1%	1%	1%	2%	2%	2%
	1	1%	1%	1%	1%	2%	2%	1%	2%	2%
	2	3%	1%	1%	2%	2%	2%	1%	2%	1%
	3	4%	1%	1%	3%	2%	2%	1%	1%	3%
dca cut	0	1%	1%	2%	1%	1%	1%	1%	1%	1%
	1	2%	1%	2%	3%	1%	2%	2%	2%	1%
	2	3%	1%	2%	3%	1%	1%	4%	0.2%	2%
	3	3%	1%	2%	2.5%	1%	1%	3%	1%	2%
q range	0	1%	2%	3%	3%	3%	4%	5%	5%	6%
	1	1%	3%	3%	3%	5%	5%	4%	6%	8%
	2	0.9%	4%	3%	4%	5%	6%	5%	6%	8%
	3	1%	3%	3.5%	4%	5%	5%	4%	5%	6%
charge	0	1%	3%	1%	2%	0.2%	1%	2%	1%	1%
	1	2%	2%	2.5%	1%	1%	1%	1%	1%	1%
	2	1%	2%	1.5%	1%	3%	5%	4%	3%	1%
	3	2%	4%	1.5%	1%	4%	1%	2%	4%	1%
B field	0	2%	1%	1.5%	3%	0.5%	0.5%	1%	3%	2%
	1	2%	2%	1%	4%	2%	2%	1%	4%	2%
	2	2%	4%	2%	4%	0.2%	1%	2%	5%	4%
	3	2%	2%	1%	3%	1%	1%	3%	5%	2%
Event Plane	0	2%	1%	1%	4%	1%	1%	2%	1%	2%
	1	1%	1%	3%	2%	2%	2%	2%	2%	3%
	2	2%	2%	1%	1%	2%	4%	1%	1%	3%
	3	2%	1%	4%	4%	1%	0.1%	5%	2%	5%
Total	0	3.5%	4.1%	4.3%	6.3%	3.5%	4.5%	6.2%	6.4%	7.1%
	1	3.9%	4.5%	5.5%	6.3%	6.2%	6.5%	5.2%	8.1%	9.1%
	2	5.3%	6.5%	4.6%	6.9%	6.6%	9.1%	7.9%	8.7%	9.7%
	3	6.2%	5.7%	6.0%	7.6%	6.9%	5.7%	8.0%	8.5%	8.9%

4.8 Comparisons

4.8.1 ALICE vs. STAR

In studying the azimuthally differential femtoscopy radii for non-central collisions, we compare out results for Pb-Pb at $\sqrt{s_{NN}} = 2.76$ TeV to the experimental results of the STAR experiment for Au-Au at $\sqrt{s_{NN}} = 200$ GeV [117], see Figures 4.65-4.66. The solid points and lines indicate the ALICE data and fits to the Fourier expansion for second order oscillation, while the open points and dashed lines indicate the STAR data and fits. Similar second order oscillation are observed for both STAR and ALICE data. Both show opposite oscillation for R_{out} and R_{side}. The radii values for ALICE are higher than STAR, however the strength of amplitude is higher for STAR than ALICE. This can be due to the higher energy of the ALICE experiment.

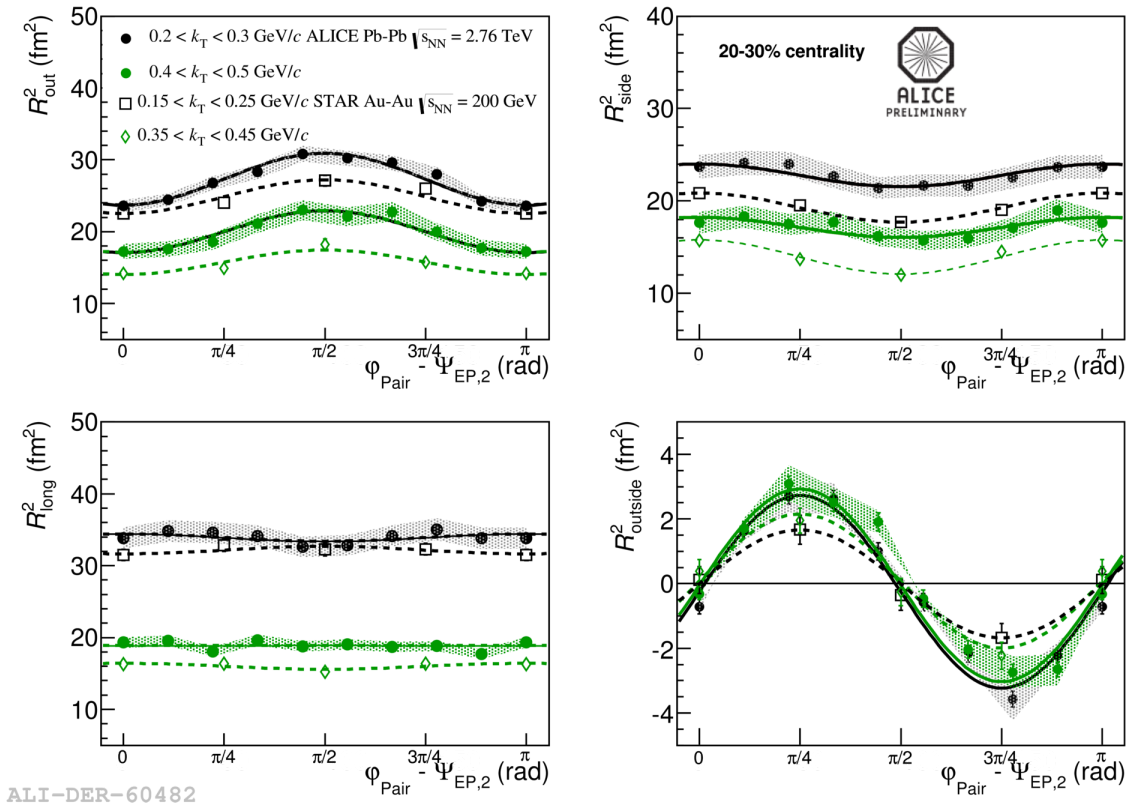

Figure 4.65: 20-30% centrality comparison of radii vs. pair emission angle at ALICE k_T of 0.2-0.3 GeV/c, 0.4-0.5 GeV/c, and STAR k_T ranges 0.15-0.25 GeV/c, and 0.35-0.45 GeV/c

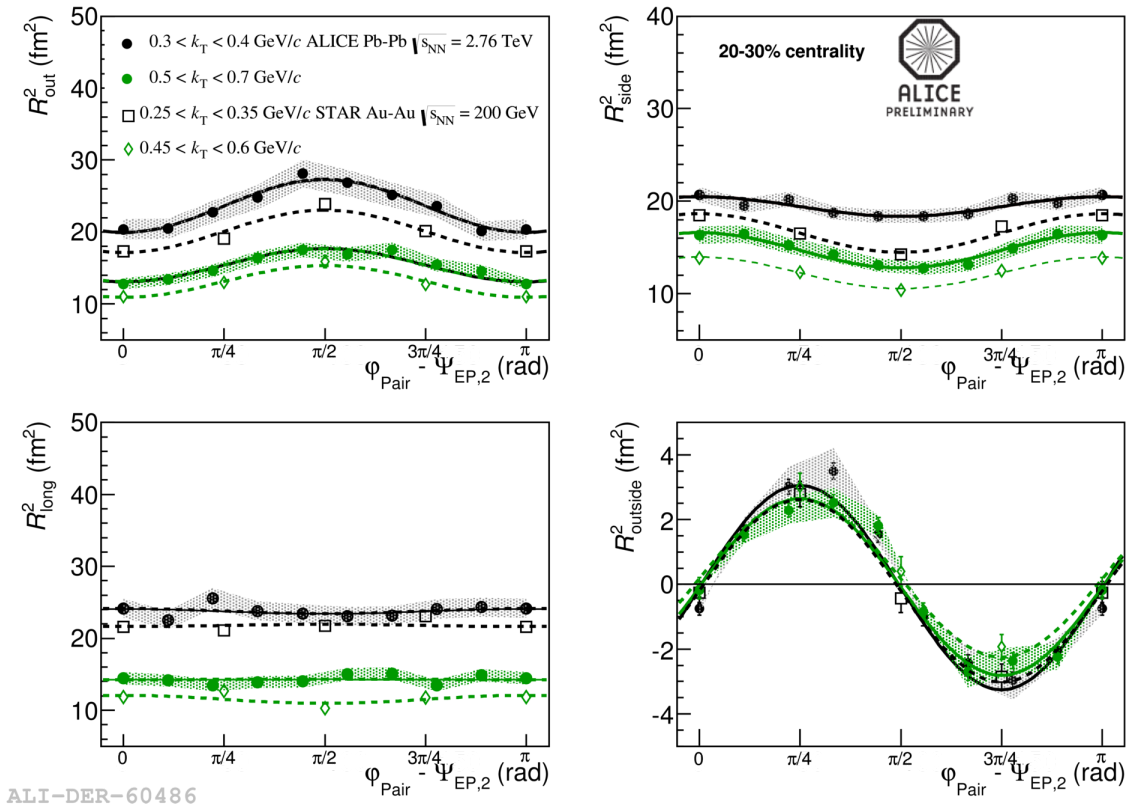

Figure 4.66: 20-30% centrality comparison of radii vs. pair emission angle at ALICE k_T of 0.3-0.4 GeV/c, 0.5-0.7 GeV/c, and STAR k_T ranges 0.35-0.45 GeV/c, and 0.45-0.60 GeV/c

4.8.2 Model Comparisons

4.8.2.1 Comparison of Radii to HYDRO-THERMINATOR Model

The azimuthally differential femtoscopy radii are compared to theoretical results of the HYDRO-THERMINATOR model calculated at $\sqrt{s_{NN}} = 5.5$ TeV for the LHC by Adam Kisiel et al. [118], see Figure 4.67. The model values shown in solid lines and open symbols are above the ALICE data points at $\sqrt{s_{NN}} = 2.76$ TeV, shown will closed symbols and boxes for systematic errors, for R_{side} and R_{long}. The model is more comparable to ALICE for R_{out}. The ratios for $R^2_{side,2}/R^2_{side,0}$ and $R^2_{outside,2}/R^2_{side,0}$ are also close to the ALICE data points. This comparison will again be revisited in the nedt LHC data taking period at the top energy of $\sqrt{s_{NN}} = 5.5$ TeV to better compare with the HYDRO-THERMINATOR model at the same energy.

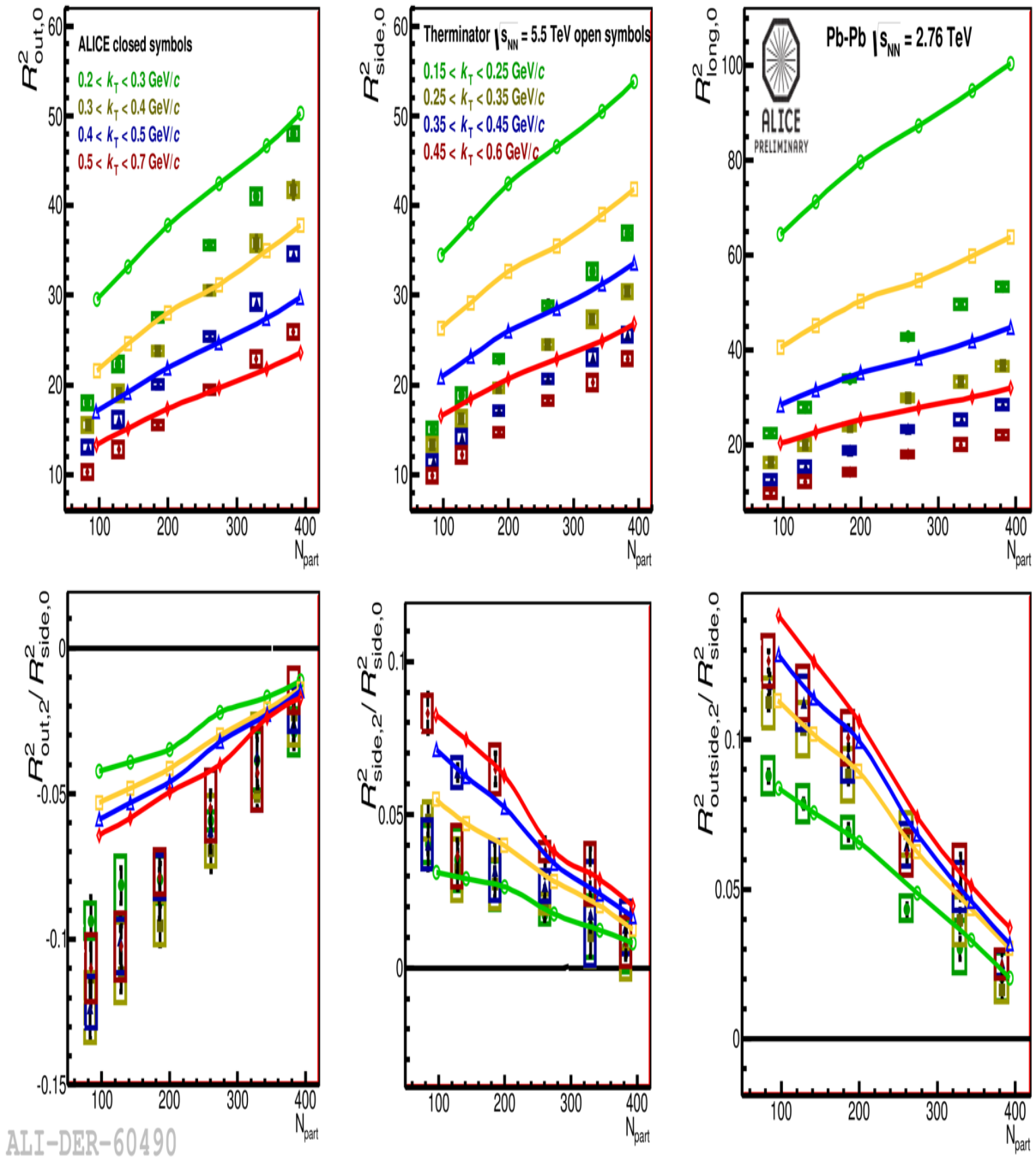

Figure 4.67: Predictions for the LHC calculated with the THERMINATOR at $\sqrt{s_{NN}} = 5.5$ TeV for the LHC. Open points are the model [118], closed points are ALICE data at $\sqrt{s_{NN}} = 2.76$ TeV. Circles: k_T range 0.2-0.3 GeV, squares: k_T range 0.3-0.4 GeV, triangles: k_T range0.4-0.5 GeV, and diamonds: k_T range 0.5-0.7 GeV.

4.8.2.2 Comparison of final eccentricity to MC-Glauber & MC-KLN

The results are compared of the relative oscillations to systematic hydrodynamic studies of pion azimuthal anisotropy to study the final shape of the source at freeze-out. The following models are compared: hydrodynamic models with Monte Carlo Glauber (MC-Glauber) initial conditions and with Monte Carlo Kharzeev-Levin-Nardi (MC-KLN) initial conditions by Ulrich Heinz and Chun Shen [119] , and Ultra Relativistic Quantum Molecular Dynamics (urQMD) by Mike Lisa et al. [120], see Figure 4.68. The data is compared to results from the following collaborations E895, CERES, and STAR. The data ranges in energies from 2.7 GeV to 2.76 TeV, whereas the models extend to 5.5 TeV. STAR data ranging from 7.7 GeV to 200 GeV are STAR preliminary by Christopher Anson. The models show predictions for the final spatial eccentricity, ϵ_f, which is related to the relative oscillations in all data in the following manner, $\epsilon_f \approx 2R^2_{side,0}/R^2_{out,0}$ for low values of k_T . The model with MC-Glauber and MC-KLN initial conditions shows a monotonic decrease in ϵ_f as the collision energy increases. At higher collision energies the fireball has a longer lifetime to transform from its original deformed shape to become more isotropic [119]. When comparing these models with the ALICE data, they both underestimate the data. The UrQMD model seems to follow the data points from the STAR energies to ALICE. A definite reason at this stage cannot be made without a more direct comparison of radii oscillations and average radii from the models. The ALICE data point at $\sqrt{s_{NN}} = 2.76$ TeV is lower than for most pervious experiments.

Since the magnitude of $2R^2_{side,0}/R^2_{out,0}$ remains positive, it is concluded that the source at the LHC remains out-of-plane extended at freeze-out and does not change to in-plane extended. It is also noted that this source behavior at freeze-out at the LHC energies is similar to the behavior of the previous experiments at lower energies.

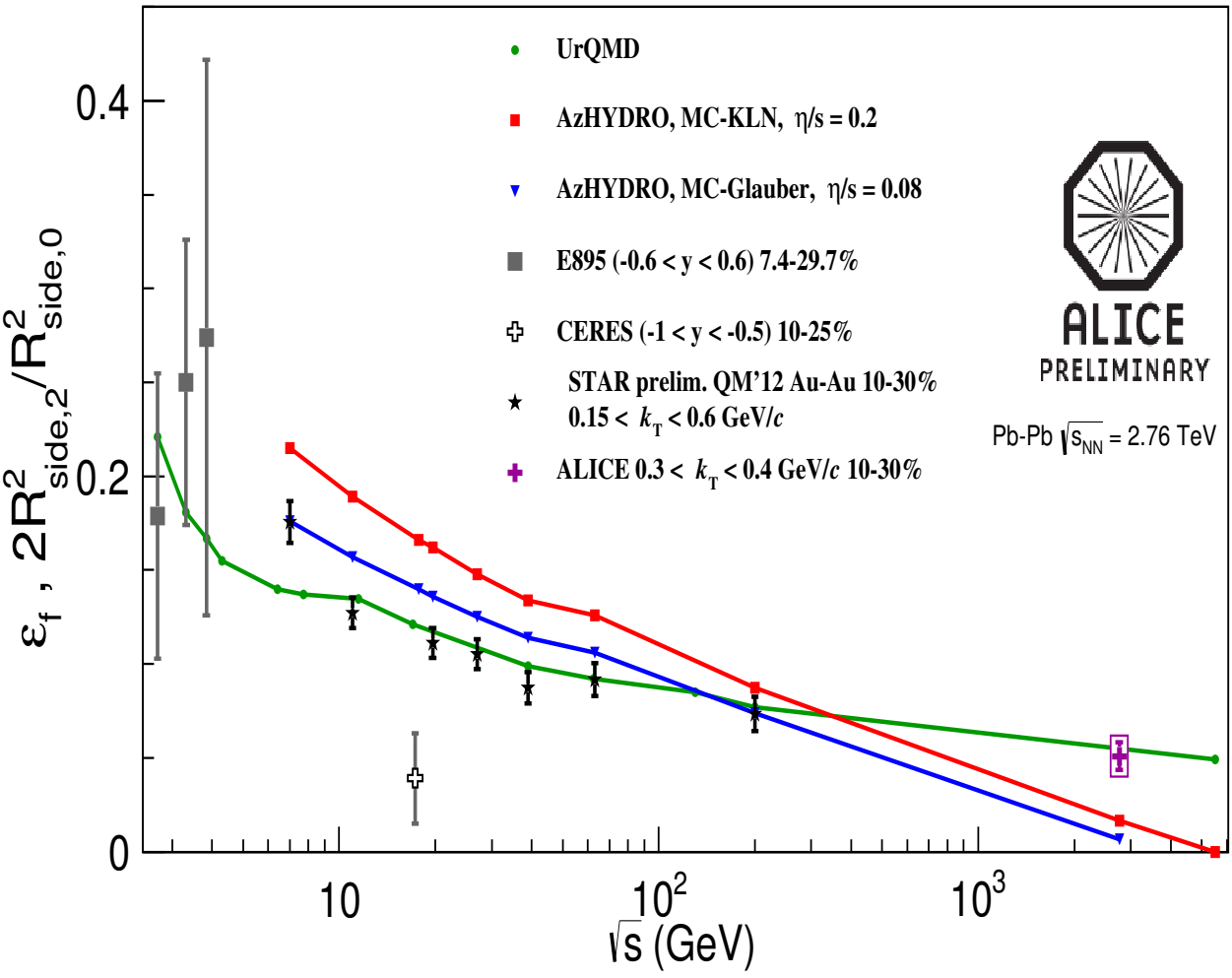

Figure 4.68: $\sqrt{s}$-dependence of the final spatial eccentricity ϵ_f of the isothermal kinetic freeze-out surface at $T_{dec} = 120$ MeV, for 10-30% centrality. [119] Experimental points from ALICE at $0.3 < k_T < 0.4$ GeV and STAR at $0.25 < k_T < 0.35$ GeV [117]

Chapter 5

Conclusion

In this thesis, the topics of the non-flow estimate in two particle azimuthal correlations is investigated, using the Scalar Product (SP) method and the uQ method in *pp* and Pb-Pb collisions at $\sqrt{s}_{NN} = 2.76$ TeV and $\sqrt{s}_{NN} = 7$ TeV, and in three particle correlations using the Chiral Magnetic Effect (CME) in *pp* collisions at $\sqrt{s}_{NN} = 7$ TeV. Also two particle azimuthally sensitive pion femtoscopy in Pb-Pb in collisions at 2.76 TeV was studied. The non-flow studies was motivated by the need to obtain the best estimate for flow removing any non-relating signal. It was found that most of the non-flow lies in the most peripheral centrality bins and is similar in magnitude to *pp* collisions. In comparing the uQ and SP methods, it was found that they give comparable results after subtracting the non-flow from *pp* collisions. The two particle charge dependence shows that opposite sign correlation is higher than the same sign correlations due to resonance decays. The CME three particle analysis shows that there is little non-flow estimated in correlation in the Pb-Pb collisions, and only occurs in the most peripheral bins.

Azimuthally sensitive pion femtoscopy was studied in order to obtain an estimate of the source shape at freeze-out. It was found that the radii in the out and side direction oscillate in opposite directions, and are comparable to results obtained from the STAR Collaboration in Au+Au collisions at $\sqrt{s}_{NN} = 200$ GeV. Results of the radii oscillations were compared to model calculations using hydrodynamics yielding com-

parable results. The ratio of the side radii is divided by the average side radii relates to the final spatial eccentricity, and was found to have a positive magnitude, indicating that the source shape remains out-of-plane extended at $\sqrt{s}_{NN} = 2.76$ TeV at the LHC. Further investigation is currently being done to extend the type of reaction plane from a second order (almond-shaped) reaction plane to a third order (triangular-shaped) reaction plane. Since odd harmonics are expected to be completely due to event-by-event fluctuations in the initial spatial geometry, the comparison between the second and third hold give more information about the source shape at freeze-out.

With the anticipated new heavy ion run scheduled at the LHC for spring 2015, this work will extend to the highest energy for heavy ion collisions at $\sqrt{s_{NN}} = 5.5$ TeV. With this energy, more is expected to be learned regarding how the non-flow effects the flow signals and about the final eccentricity of the source shape at freeze-out using azimuthally sensitive femtoscopy.

REFERENCES

[1] E. W. Kolb and M. S. Turner, *The Early Universe*, (Addison-Wesley, Redwood City, USA, 1990), Chapter 3.

[2] M. Roos, "Expansion of the Universe - Standard Big Bang Model," arXiv:0802.2005 [astro-ph].

[3] "Timeline of the Big Bang." Wikipedia. Wikimedia Foundation, 03 July 2014. Web. 02 Mar. 2014.

[4] Allday, Johnson, *Quarks, Leptons, and the Big Bang*; Taylor & Francis, 2002.

[5] Alice Physics. (2008), ("Free Quarks and Gluons"), Retrieved from http://aliceinfo.cern.ch/Public/en/Chapter1/Page2FreeQuarks-en.html.

[6] E. V. Shuryak, "Quark-gluon plasma and hadronic production of leptons, photons and pions," Phys. Lett. B. **78**, 150 (1978).

[7] M. Gell-Mann, "A schematic model of baryons and mesons," Phys. Lett. **8**, 214 (1964).

[8] Seagrave, Wyken, *History of the Universe*, Penny Press Ltd., 2012.

[9] Wojciech Florkowski, *Phenomenology of Ultra-Relativistic Heavy Ion Collisions*, World Scientific Publishing Co., 2010.

[10] C. Muntz [E802 Collaboration], "Recent results from E866 at BNL," nucl-ex/9806002.

[11] F. Wang, "Strangeness in dense nuclear matter: A Review of AGS results," J. Phys. G **27**, 283 (2001) [nucl-ex/0010002].

[12] M. Gazdzicki, "Quark gluon plasma in A + A collisions at CERN SPS," In

Les Houches 1998, Nuclear matter in different phases and transitions 293-302 [hep-ph/9806257].

[13] M. D. Oldenburg [STAR Collaboration], "Recent results from STAR," nucl-ex/0211033.

[14] W. A. Zajc *et al.* [PHENIX Collaboration], "Overview of PHENIX results from the first RHIC run," Nucl. Phys. A **698**, 39 (2002) [nucl-ex/0106001].

[15] G. Kane, *Modern Elementary Particle Physics: The Fundamental Particles and Forces*, Perseus Publishing, Cambridge (1993).

[16] J. F. Donoghue, E. Golowich, and B. R. Holstein, *Dynamics of the Standard Model*, Cambridge University Press, (1992).

[17] [ATLAS and CDF and CMS and D0 Collaborations], "First combination of Tevatron and LHC measurements of the top-quark mass," arXiv:1403.4427 [hep-ex].

[18] J. Beringer et al., (Particle Data Group), Phys. Rev. D **86**, 010001 (2012).

[19] O.W. Greenberg, "Spin and unitary spin independence in a paraquark model of baryons and mesons," Phys. Rev. Lett. **13**, 598 (1964).

[20] M. Y. Han and Y. Nambu, "Three-triplet model with double SU(3) symmetry," Phys. Rev. **139**, B1006 (1965).

[21] D. J. Gross and F. Wilczek, "Ultraviolet behavior of non-abelian gauge theories," Phys. Rev. Lett. **30**, 1343 (1973).

[22] D. J. Gross and F. Wilczek, "Asymptotically free gauge theories ," Phys. Rev. Lett. **30**, 1343 (1973).

[23] H. D. Politzer, "Reliable perturbative results for strong interactions?," Phys. Rev. Lett. **30**, 1346 (1973).

[24] K. G. Wilson, "Confinement of quarks," Phys. Rev. D **10**, 2445 (1974).

[25] G. 't Hooft, "On the phase transition towards permanent quark confinement," Nucl. Phys. B **138**, 1 (1978).

[26] G. 't Hooft, "Topology of the gauge condition and new confinement phases in non-abelian gauge theories," Nucl. Phys. B **190**, 455 (1981).

[27] S. Bethke, "The 2009 World Average of alpha(s)," Eur. Phys. J. C **64**, 689 (2009) [arXiv:0908.1135 [hep-ph]].

[28] M. A. Stephanov, "QCD phase diagram: An Overview," PoS LAT **2006**, 024 (2006) [hep-lat/0701002].

[29] M. Kliemant, R. Sahoo, T. Schuster and R. Stock, "Global Properties of Nucleus-Nucleus Collisions," Lect. Notes Phys. **785**, 23 (2010) [arXiv:0809.2482 [nucl-ex]].

[30] Y. Kharlov [ALICE Collaboration], "Physics with the ALICE experiment," arXiv:1203.1984 [nucl-ex].

[31] http://na49info.web.cern.ch/na49info/Public/Press/findings.html

[32] M. Bedjidian, D. Blaschke, G. T. Bodwin, N. Carrer, B. Cole, P. Crochet, A. Dainese and A. Deandrea *et al.*, "Hard probes in heavy ion collisions at the LHC: Heavy flavor physics," hep-ph/0311048.

[33] T. Matsui and H. Satz "J/Ψ Suppression by Quark Gluon Plasma Formation," Physics Letters B **178** , 4 (1986).

[34] B. Abelev *et al.* [ALICE Collaboration], "J/ψ suppression at forward rapidity in Pb-Pb collisions at $\sqrt{s_{NN}} = 2.76$ TeV," Phys. Rev. Lett. **109**, 072301 (2012) [arXiv:1202.1383 [hep-ex]].

[35] P. Braun-Munzinger and J. Stachel, "(Non)thermal aspects of charmonium production and a new look at J / psi suppression," Phys. Lett. B **490**, 196 (2000) [nucl-th/0007059].

[36] A. Andronic, P. Braun-Munzinger, K. Redlich and J. Stachel, "The thermal model on the verge of the ultimate test: particle production in Pb-Pb collisions at the LHC," J. Phys. G **38**, 124081 (2011) [arXiv:1106.6321 [nucl-th]].

[37] X. Zhao and R. Rapp, "Transverse Momentum Spectra of J/ψ in Heavy-Ion Collisions," Phys. Lett. B **664**, 253 (2008) [arXiv:0712.2407 [hep-ph]].

[38] X. Zhao and R. Rapp, "Medium Modifications and Production of Charmonia at LHC," Nucl. Phys. A **859**, 114 (2011) [arXiv:1102.2194 [hep-ph]].

[39] M. Wilde [ALICE Collaboration], "Measurement of Direct Photons in pp and Pb-Pb Collisions with ALICE," Nucl. Phys. A **904-905**, 573c (2013) [arXiv:1210.5958 [hep-ex]].

[40] Takao Sakaguchi (for the Phenix Collaboration), "Direct Photons: Flow, Thermal Yield and High pT RAA from the PHENIX experiment at RHIC," J. Phys.: Conf. Ser. **389** 012020, 2012.

[41] S. Voloshin and Y. Zhang, "Flow study in relativistic nuclear collisions by Fourier expansion of Azimuthal particle distributions," Z. Phys. C **70**, 665 (1996) [arXiv:hep-ph/9407282].

[42] A. M. Poskanzer and S. A. Voloshin, "Methods for analyzing anisotropic flow in relativistic nuclear collisions," Phys. Rev. C **58**, 1671 (1998) [nucl-ex/9805001].

[43] KAamodt *et al.* [ALICE Collaboration], "Elliptic flow of charged particles in Pb-Pb collisions at 2.76 TeV," Phys. Rev. Lett. **105**, 252302 (2010) [arXiv:1011.3914 [nucl-ex]].

[44] M. A. Lisa, S. Pratt, R. Soltz and U. Wiedemann, "Femtoscopy in relativistic heavy ion collisions," Ann. Rev. Nucl. Part. Sci. **55**, 357 (2005) [nucl-ex/0505014].

[45] S. A. Voloshin and W. E. Cleland, "HBT analysis of anisotropic transverse flow," Phys. Rev. C **53**, 896 (1996). [nucl-th/9509025].

[46] A. Kisiel [ALICE Collaboration], "Femtoscopy of Pb-Pb and pp collisions at the LHC with the ALICE experiment," J. Phys. G **38**, 124008 (2011) [arXiv:1109.5553 [nucl-ex]].

[47] L. Evans and P. Bryant (editors), JINST 3 (2008) S08001.

[48] Lyndon Evans and Philip Bryant, "LHC Machine," 2008 JINST 3 S08001 doi:10.1088/1748-0221/3/08/S08001.

[49] http://lhc-milestones.web.cern.ch/lhc-milestones/year2008-en.html.

[50] Davies, Lizzy, "Higgs Boson Announcement: Cern Scientists Discover Subatomic Particle," Theguardian.com Guardian News and Media 04 July 2012. http://www.theguardian.com/science/blog/2012/jul/04/higgs-boson-discovered-live-coverage-cern.

[51] Lyndon Evans and Philip Bryant, "LHC Machine," 2008 JINST 3 S08001 doi:10.1088/1748-0221/3/08/S08001.

[52] CERN-THESIS-2013-042 , arXiv:1306.0858.

[53] K. Aamodt et al., [ALICE Collaboration], JINST **3** (2008) S08002.

[54] http://atlas.ch/.

[55] http://cms.web.cern.ch/news/what-cms.

[56] http://lhcb-public.web.cern.ch/lhcb-public/.

[57] http://cds.cern.ch/record/887108/files/lhcc-2005-032.pdf.

[58] http://totem-experiment.web.cern.ch/totem-experiment/.

[59] http://moedal.web.cern.ch/.

[60] http://aliceinfo.cern.ch/Public/Welcome.html.

[61] ALICE Collaboration, "Technical Design Report of the Inner Tracking System," CERN/LHCC/1999-12 (1999), https://edms.cern.ch/document/398932/1.

[62] K. Aamodt et al. [ALICE Collaboration], JINST **3** (2008) S08002.

[63] ALICE Collaboration, "Technical Design Report of the Time Projection Chamber," CERN/LHCC/2000-01 (2000), https://edms.cern.ch/document/398930/1.

[64] E. Scapparone. "The Time of Flight detector of the ALICE experiment," J. Phys. G Nucl. Part. Phys. **34** (2007) S725S728.

[65] ALICE Collaboration, "Technical Design Report of the Time of Flight

System," CERN/LHCC/2000-12 (2000). Addendum CERN/LHCC/2002-16 (2002), https://edms.cern.ch/document/460192/1.

[66] A. Kalweit [ALICE Collaboration], "Particle Identification in the ALICE Experiment," J. Phys. G **38**, 124073 (2011), [arXiv:1107.1514 [hep-ex]].

[67] ALICE Collaboration, "Technical Design Report of the Transition Radiation Detector," CERN/LHCC/2001-021 (2001), https://edms.cern.ch/document/398057/1.

[68] U. Abeysekara *et al.* [ALICE EMCal Collaboration], "ALICE EMCal Physics Performance Report," arXiv:1008.0413 [physics.ins-det].

[69] ALICE Collaboration, Technical Design Report on Forward Detectors: FMD, T0 and V0," CERN/LHCC/2004-025 (2004), https://edms.cern.ch/document/498253/1.

[70] ALICE Collaboration, "Technical Design Report of the Zero Degree Calorimeter," CERN/LHCC/1999-5 (1999), https://edms.cern.ch/document/398933/1.

[71] E877 Collaboration, J. Barette *et al.*, "Measurement of transverse energy production with Si and Au beams at relativistic energy: Towards hot and dense hadronic matter," Phys. Rev. Lett. **70**, 2996 (1993).

[72] E877 Collaboration, J. Barette *et al.*, "Proton and pion production relative to the reaction plane in Au + Au collisions at 11A GeV/c," Phys. Rev. C **56**, 3254 (1997).

[73] E877 Collaboration, J. Barette *et al.*, "Energy and charged particle flow in 10.8A GeV/c Au + Au collisions," Phys. Rev. C **55**, 1420 (1997).

[74] E802 Collaboration, L. Ahle *et al.*, "Proton, deuteron, and triton emission at target rapidity in Au+Au collisions at 10.20A GeV: Spectra and directed flow," Phys. Rev. C **57**, 1416 (1998).

[75] NA49 Collaboration, T. Wienold *et al.*, "Stopping and collective effects at SPS energies," Nucl. Phys. A **610**, 76 (1996).

[76] NA49 Collaboration, H. Appelhauser *et al.*, "Directed and Elliptic Flow in 158 GeV/Nucleon Pb+Pb Collisions," Phys. Rev. Lett. **80**, 4136 (1998).

[77] J. Stachel, "Tests of thermalization in relativistic nucleus-nucleus collisions," Nucl. Phys. A **610**, 509 (1996).

[78] S. A. Voloshin, "Collective phenomena in ultra-relativistic nuclear collisions: anisotropic flow and more," Prog. Part. Nucl. Phys. **67**, 541 (2012) [arXiv:1111.7241 [nucl-ex]].

[79] S. A. Voloshin, A. M. Poskanzer and R. Snellings, "Collective phenomena in non-central nuclear collisions," arXiv:0809.2949 [nucl-ex].

[80] A. M. Poskanzer and S. A. Voloshin, "New Developments in Methods for Anisotropic Flow Analysis," LBNL Annual Report, R34,(1998), http://ie.lbl.gov/nsd1999/rnc/RNC.htm.

[81] A. Bilandzic, R. Snellings and S. Voloshin, "Flow analysis with cumulants: direct calculations," arXiv:1010.0233 [nucl-ex].

[82] N. Borghini, P. M. Dinh and J. -Y. Ollitrault, "Thermalization and elliptic flow at RHIC," hep-ph/0111402.

[83] J. Adams *et al.* [STAR Collaboration], "Azimuthal anisotropy and correlations at large transverse momenta in p + p and Au + Au collisions at s(NN)**(1/2) = 200-GeV," Phys. Rev. Lett. **93** (2004) 252301 [arXiv:nucl-ex/0407007].

[84] P. Danielewicz and G. Odyniec, " Transverse momentum analysis of collective motion in relativistic nuclear collisions", Phys. Lett. **B** 157, 146 (1985).

[85] P. Sorensen, "Elliptic Flow: A Study of Space-Momentum Correlations In Relativistic Nuclear Collisions," arXiv:0905.0174 [nucl-ex].

[86] K. Aamodt *et al.* [ALICE Collaboration], "Higher harmonic anisotropic flow measurements of charged particles in Pb-Pb collisions at $\sqrt{s_{NN}}$=2.76 TeV," Phys. Rev. Lett. **107**, 032301 (2011) [arXiv:1105.3865 [nucl-ex]].

[87] D. Kharzeev, R. D. Pisarski, and M.H.G. Tytgat, "Possibility of Spontaneous Parity Violation in Hot QCD," Phys. Rev. Lett. **81** 512 (1998).

[88] D. Kharzeev and R. D. Pisarski, "Pionic measures of parity and CP violation in high energy nuclear collisions," Phys. Rev. D **61** 111901 (2000).

[89] S. A. Voloshin, "Discussing the possibility of observation of parity violation in heavy ion collisions," Phys. Rev. C **62** 044901 (2000).

[90] L.E. Finch, A. Chikanian, R.S. Longacre, J. Sandweiss, and J.H. Thomas, "Observing spontaneous strong parity violation in heavy-ion collisions," "Phys. Rev. C **65** 014908 (2002).

[91] D. Kharzeev, "Parity violation in hot QCD: Why it can happen, and how to look for it," Phys. Lett. B **633**, 260 (2006) [hep-ph/0406125].

[92] B. I. Abelev *et al.* [STAR Collaboration], "Observation of charge-dependent azimuthal correlations and possible local strong parity violation in heavy ion collisions," Phys. Rev. C **81**, 054908 (2010) [arXiv:0909.1717 [nucl-ex]].

[93] Voloshin, Sergei A., "Parity violation in hot QCD: How to detect it," Phys. Rev. C **70**, 057901, (2004).

[94] B. I. Abelev et al. [STAR Collaboration], "Azimuthal Charged-Particle Correlations and Possible Local Strong Parity Violation," Phys. Rev. Lett. **103**, 251601 (2009).

[95] B. Abelev *et al.* [ALICE Collaboration], "Charge separation relative to the reaction plane in Pb-Pb collisions at $\sqrt{s_{NN}} = 2.76$ TeV," Phys. Rev. Lett. **110**, 012301 (2013) [arXiv:1207.0900 [nucl-ex]].

[96] K. Aamodt *et al.* [ALICE Collaboration], "Charged-particle multiplicity measurement in proton-proton collisions at $\sqrt{s} = 7$ TeV with ALICE at LHC," Eur. Phys. J. C **68**, 345 (2010) [arXiv:1004.3514 [hep-ex]].

[97] Hori, Yasuto. Alice Flow Meeting, Presentation February 3, 2012.

[98] Hori, Yasuto. "Mixed harmonic azimuthal correlations in $\sqrt{s}_{NN}$=2.76 TeV

PbPb collisions measured by ALICE at LHC," (PhD Thesis 2013), Department of Physics, Graduate School of Science, University of Tokyo.

[99] G. Goldhaber, S. Goldhaber, W. Lee, A. Pais, Phys. Rev. **120** , 325 (1960).

[100] G.I. Kopylov, M.I. Podgoretsky, Sov. J. Nucl. Phys. **15** , 219 (1972); **18**, 336 (1973); **19**, 215 (1974).

[101] G. Cocconi, "Second-order interference as a tool for the determination of hadron fireball dimensions," Phys. Lett. B **49** , 459 (1974).

[102] Y. .M. Sinyukov and V. M. Shapoval, "Correlation femtoscopy of small systems," Phys. Rev. D **87** (2013) 094024 [arXiv:1209.1747 [hep-ph]].

[103] R. Hanbury Brown and R. Q. Twiss, "A Test of a New Type of Stellar Interferometer on Sirius," Nature **178** ,1046 (1956)

[104] U. W. Heinz, "How to extract physics from HBT radius parameters," Nucl. Phys. A **610**, 264C (1996) [nucl-th/9608002].

[105] M. Lisa [STAR Collaboration], "Azimuthally sensitive pion HBT at RHIC," [nucl-ex/0301005].

[106] U. W. Heinz, B. Tomasik, U. A. Wiedemann and Y. F. Wu, "Lifetimes and sizes from two particle correlation functions," Phys. Lett. B **382**, 181 (1996) [nucl-th/9603011].

[107] M. G. Bowler, "Coulomb corrections to Bose-Einstein corrections have greatly exaggerated," Phys. Lett. B **270**, 69 (1991).

[108] U. A. Wiedemann, "Two particle interferometry for noncentral heavy ion collisions," Phys. Rev. C **57**, 266 (1998) [nucl-th/9707046].

[109] M. A. Lisa *et al.* [E895 Collaboration], "Azimuthal dependence of pion interferometry at the AGS," Phys. Lett. B **496**, 1 (2000) [nucl-ex/0007022].

[110] Y. Sinyukov, R. Lednicky, S. V. Akkelin, J. Pluta, B. Erazmus, "Coulomb corrections for interferometry analysis of expanding hadron systems," Phys. Lett. B **432**, 248 (1998).

[111] web: http://cds.cern.ch/record/960443/files/ALICE-INT-2005-031.pdf

[112] Łu. K. Graczykowski [for the ALICE Collaboration], "Pion femtoscopy measurements in ALICE at the LHC," arXiv:1402.2138 [hep-ex].

[113] Gramling, J. "Azimuthally Sensitive Hanbury Brown Twiss Interferometry measured with the ALICE Experiment," (Master's Thesis 2011), Department of Physics and Astronomy, University of Heidelberg.

[114] U. W. Heinz, A. Hummel, M. A. Lisa and U. A. Wiedemann, "Symmetry constraints for the emission angle dependence of HBT radii," Phys. Rev. C **66**, 044903 (2002) [nucl-th/0207003].

[115] Lisa et al (E895) Nucl. Phys. B 2000.

[116] web: https://twiki.cern.ch/twiki/pub/ALICE/PerformancePaper2012/perf-r515.pdf

[117] J. Adams *et al.* [STAR Collaboration], "Pion interferometry in Au+Au collisions at S(NN)**(1/2) = 200-GeV," Phys. Rev. C **71**, 044906 (2005) [nucl-ex/0411036].

[118] A. Kisiel, W. Broniowski, M. Chojnacki and W. Florkowski, "Azimuthally-sensitive femtoscopy from RHIC to LHC in hydrodynamics with statistical hadronization," Phys. Rev. C **79**, 014902 (2009) [arXiv:0808.3363 [nucl-th]].

[119] C. Shen and U. Heinz, "Viscous Flow in Heavy-Ion Collisions from RHIC to LHC," Nucl. Phys. A904-905 **2013**, 361c (2013) [arXiv:1210.2074 [nucl-th]].

[120] M. A. Lisa, E. Frodermann, G. Graef, M. Mitrovski, E. Mount, H. Petersen and M. Bleicher, "Shape analysis of strongly-interacting systems: The Heavy ion case," New J. Phys. **13**, 065006 (2011) [arXiv:1104.5267 [nucl-th]].

ABSTRACT

COLLECTIVE FLOW AND AZIMUTHALLY DIFFERENTIAL PION FEMTOSCOPY WITH THE ALICE EXPERIMENT AT THE LHC

by

VERA RENEE LOGGINS

May 2014

Advisor: Dr. Sergei Voloshin

Major: Physics

Degree: Doctor of Philosophy

Since 2009, the Large Hadron Collider (LHC) at European Organization for Nuclear Research (CERN) has been conducting experiments in *pp*, Pb-Pb, as well as *p*-Pb collisions with the center of mass energy ranging $\sqrt{s_{NN}} = 0.9 - 5.05$ TeV. In this thesis, both, estimates of background correlations in anisotropic flow, $v_1 - v_5$, measurements in Pb-Pb collisions at $\sqrt{s_{NN}} = 2.76$ TeV, and azimuthally differential pion femtoscopy of Pb-Pb collisions are reported.

Two particle azimuthal correlations are statistically the most precise method of measuring anisotropic flow. The main drawback of this method is its sensitivity to the non-flow correlations, which unlike real flow, do not have geometrical origin. Non-flow contribution can be estimated from two particle azimuthal correlations using *pp* data. Measurements of the non-flow contribution using the uQ method and Scalar Product (SP) method are reported for *pp* collisions at $\sqrt{s_{NN}} = 2.76$ TeV and $\sqrt{s_{NN}} = 7$ TeV for the first through fifth harmonics.

Femtoscopy of non-central heavy-ion collisions provides access to information on the geometry of the effective pion-emitting source. In particular, its shape can be studied by measuring femtoscopic radii as a function of the emission angle relative to the collision plane of symmetry. The first measurements of azimuthally differential femtoscopy in Pb-Pb collisions at $\sqrt{s_{NN}} = 2.76$ TeV are reported and compared to

results from RHIC experiments at lower energies. Oscillations of the extracted radii versus the emission angle are measured, and R_{side} and R_{out} oscillations are found to be out of phase. The relative amplitude of the R_{side} oscillations decreases in more central collisions, however always remains positive. This indicates that the source is out-of-plane extended, similar to that observed at RHIC energies. Results are compared to existing hydrodynamical and transport model calculations.

AUTOBIOGRAPHICAL STATEMENT

Vera Loggins is a native of Detroit, Michigan. She attended Mercy High School where she first thought to become a professional dancer after years of rigorous ballet classes, and numerous solos in school performances. However her love of science prevailed and she attended the University of Detroit Mercy (UDM), as a recipient of the Jessie Slaton Scholarship, to study Electrical Engineering. She was elected president of the Institute of Electrical and Electronics Engineers (IEEE) student chapter, and was an active member in the Society of Women Engineers (SWE) student chapter. She earned a B.S. in electrical engineering, graduating magna cum laude. Vera received her M.S. in electrical engineering at Wayne State University (WSU), with a scholarship from the American Association of University Women (AAUW). In addition to her engineering education, she has also earned a M.S. and Ph.D. in physics. She is the first African American woman to earn a Ph.D. in physics from WSU.

In addition to her academic accomplishments, Vera is committed to her community. She has led demonstrations of physics labs to excite elementary and middle school children about science. She is an active member of her church, Elevation Fellowship Temple of Light, and while teaching Sunday School, Vera has also found time to encourage young minds to further their education and perhaps take on an interest in science. She arranges musical productions with the youth department, and occasionally creates floats and dance numbers for her neighborhood annual parade.

Vera receives her inspiration from Albert Einstein who said "[t]he important thing is to never stop questioning." Vera intends to do just that, and pursue a career in academic research.